THÈSE

présentée pour obtenir

Le grade de docteur en sciences
de l'Université Paris. Diderot (Paris 7)

École Doctorale: Particules, Noyaux et Cosmos (ED517)
Spécialité: Physique

par

Homero MARTINEZ

Measurement of the Z boson differential cross-section in transverse momentum in the electron-positron channel with the ATLAS detector at LHC

Dirigée par Frédéric DERUE
Encadrée par Nathalie BESSON

Soutenue le 20 septèmbre 2013 devant la commission d'examen composée de:

Mme	Nathalie BESSON	encadrante de thèse
M.	Raphael GRANIER DE CASSAGNAC	examinateur
Mme	Fabienne LEDROIT	rapporteur
M.	José OCARIZ	président du jury
M.	Terence WYATT	rapporteur

A ma mère, Paulina.

Résumé

Ce travail présente la mesure de la section efficace différentielle du boson Z en impulsion transverse (p_T^Z), dans le canal de désintégration electron-positron, avec le détecteur ATLAS au LHC. La mesure utilise $4.64\,\mathrm{fb}^{-1}$ de données de collisions proton-proton, prises en 2011 avec une énergie du centre de masse de 7 TeV. Le résultat est combiné avec une mesure indépendante faite dans le canal muon-antimuon. La mesure est faite jusqu'à $p_\mathrm{T}^Z = 800$ GeV, et a une incertitude typique de 0.5 % pour $p_\mathrm{T}^Z < 60$ GeV, atteignant jusqu'à 5 % vers la fin du spectre. La mesure est comparée avec modèles théoriques et prédictions des générateurs Monte Carlo.

Abstract

This work presents the measurement of the Z boson differential cross section in transverse momentum (p_T^Z), in the electron-positron decay channel, using the ATLAS detector at the LHC. The measurement is done using 4.64 fb^{-1} of proton-proton collision data, collected in 2011 at a center-of-mass energy of 7 TeV. The result is combined with an independent measurement done in the muon-antimuon decay channel. The measurement is done up to $p_\mathrm{T}^Z = 800$ GeV, and has a typical uncertainty of 0.5 % for $p_\mathrm{T}^Z < 60$ GeV, rising up to 5 % towards the end of the spectrum. The measurement is compared to theoretical models and Monte Carlo generators predictions.

Contents

Introduction

The Large Hadron Collider (LHC), operated by the European Organization for Nuclear Physics (CERN), started operation in 2009, colliding protons at a center-of-mass energy of 7 TeV, inaugurating a new era for high energy physics. Since then, it has collected a large amount of data (around 25 fb^{-1} per experiment) which has already given many interesting results, among them the discovery of a new particle in 2012 with properties similar to the Higgs boson predicted by the Standard Model of particle physics (SM). The data delivered by the LHC represents an invaluable source of information that is being used to perform many kinds of measurements, allowing to test the validity of the predictions of the SM, improve the precision of its parameters and search evidence of new physics that can help to elucidate some aspects not addressed by the theory, like the nature of dark matter.

Four particle detectors are installed around the interaction points of the LHC which perform an exhaustive analysis of the collision products, revealing information on the behavior of nature at conditions never reached before in the laboratory. One of these detector is ATLAS (A Toroidal LHC Apparatus), a general purpose detector designed to be sensitive to many different physical signatures and perform a broad spectrum of physics studies. Among other characteristics, the ATLAS detector is designed to have very good calorimetry and tracking systems in order to reconstruct with high precision electrons, muons, photons, and hadrons.

One of the most interesting processes that can occur in the proton-proton collisions is the Drell-Yan process, i.e., the production of a pair of leptons with high transverse momentum (p_T), which represents a clear experimental signature that can be easily separated from the high amount of hadrons and non isolated leptons produced in the hadron interactions. In particular, when the Drell-Yan process involves the production and decay of a Z boson, the related measurements can reach very high precision, due to the low background and the large cross-section of production of Z bosons. Another important process, the production of W bosons, has a larger cross-section but is however affected by more experimental uncertainties due to the reconstruction of neutrino final state kinematics.

In particular the p_T spectrum of the Z boson (p_T^Z) is one of the observables of the Drell-Yan process that give insight into the dynamical effects of the strong interaction. The quantum chromodynamics (QCD) prediction of the spectrum is sensitive to perturbative effects at high p_T, and non perturbative effects at low p_T, like resummation and parton showers, which allows the measurement to test the predictions and constrain the parameters involved in the computations. The constraint of the models can in turn reduce the theoretical uncertainty on other measurements, for example the W mass, which is strongly dependent on the theoretical description of lepton kinematic distributions. In addition, the p_T^Z spectrum can be used to constrain the parton distribution functions (PDF) of the partons involved in the hard interaction, in particular of the gluon.

This thesis presents the measurement of the p_T differential cross-section of the Z boson produced in proton-proton collisions at a center-of-mass-energy of 7 TeV, measured with the ATLAS experiment using the data collected in 2011 (4.64 fb^{-1}), in the electron-positron decay channel. Due to the excellent electron reconstruction and identification in ATLAS, this decay channel allows to measure the p_T spectrum with high precision. The measurement is done in a fiducial region defined by the selection: electron $p_\mathrm{T} > 20$ GeV, absolute value of electron

pseudo-rapidity lower than 2.4 and invariant dilepton mass between 66 and 116 GeV. The differential cross-section is normalized, in order to reduce uncertainties arising from the luminosity and detector efficiencies. In order to probe different values of the momentum fraction of the partons entering the hard process, the measurement is repeated independently in three Z boson rapidity (y^Z) bins, which is made possible by the high amount of statistics collected in 2011. The normalized p_T^Z spectrum is combined with a similar measurement done in the muon decay channel, and the final combined measurement is compared to theoretical predictions.

Previous measurements of the normalized p_T^Z spectrum have been done by the D0 collaboration using 0.98 fb^{-1}of data [1] in proton-antiproton collisions, and by the ATLAS and CMS collaborations using approximately 36 pb^{-1}of data collected by the LHC in 2010 [2][3]. This measurement presents a more stringent test, going up to higher values of p_T than previous measurements and reaching an unprecedented precision due to the reduction of the statistical and systematic uncertainties.

The outline of the document is the following. In chapter 1 we present a summary of the theoretical foundation of particle physics given by the Standard Model, with emphasis on the properties of the Z boson. We describe briefly the physics of proton-proton collisions and the QCD related predictions, in particular of the p_T^Z spectrum, and comment on the MC event generators used later in the analysis.

In chapter 2 we summarize the experimental context of the measurement. First, we describe briefly the LHC and its main parameters, then we present some of the conventional variables and terms used in the context of the ATLAS experiment, followed by a general summary of the main components of the ATLAS detector, including the trackers, calorimeters, muon system, trigger and data acquisition systems.

Chapter 3 continues the description of the experimental part, describing in detail the physics of the ATLAS electromagnetic calorimeter and its performance. The reconstruction and identification of electrons are explained, starting from the processing of electronic signals up to the final energy and position measurement. In chapter 4 we present a complementary study done on the calorimeter part of the trigger system, which allows to evaluate the efficiency of the bunch-crossing identification.

In chapter 5 we present the details of the p_T^Z measurement in the electron channel: the event selection procedure, background estimation, unfolding and estimation of uncertainties. Next, the results are presented, and the measurement in y^Z bins is described. We perform a comparison with the muon channel measurement, and then describe briefly the combination procedure.

The results are interpreted in chapter 6, presented in the context of comparison with other measurements and theoretical predictions. First, we review briefly the previous measurements of the p_T^Z spectrum, showing the precision attained. Then we compare our measurement with theoretical predictions that include resummation, NNLO computations and MC generators. Finally, a preliminary parton shower tuning is presented, based on the p_T^Z measurement and the complementary measurement of the ϕ^* variable, which also shows the compatibility of these measurements that were done with the same dataset.

Chapter 1

Theoretical background

In this chapter we present a summary of the theoretical description of particle physics given by the Standard Model, with emphasis on the Z boson and its properties. We review the main ingredients of the theoretical predictions done by the SM in the context of proton-proton collisions, and introduce the Z boson production and its transverse momentum distribution as important observables. The chapter ends with a brief discussion of Monte Carlo (MC) generators.

1.1 The Standard Model of particle physics

The Standard Model of particle physics (SM) is a theory that describes effectively the kinematics and the interactions of the fundamental constituents of matter. It is a combination of quantum chromodynamics (QCD), the theory of quarks and the strong interaction, with the Glashow-Weinberg-Salam (GWS) theory of the electroweak interaction [4]. Its predictive power allows to probe quantum effects to a high degree of accuracy, and its predictions have passed all experimental tests to the present day.

In the SM, matter particles are represented by spin 1/2 fermions, and the interactions are mediated by spin 1 bosons. The force mediators arise as a consequence of the postulated local gauge symmetries. The matter particles are organized in three families or generations of fermions, each one composed of two quarks and two leptons. In addition to the matter fermions and the gauge boson, a Higgs boson with spin 0 is postulated, as a consequence of the mechanism of spontaneous symmetry breaking. In table 1.1 we summarize the particle content of the SM [5].

Matter (spin 1/2 fermions)		
	Leptons	Quarks
First generation	e, ν_e	u, d
Second generation	μ, ν_μ	c, s
Third generation	τ, ν_τ	b, t
Force mediators (spin 1 bosons)		
Electromagnetic	γ	
Strong	g (8)	
Weak	W^+, W^-, Z	
Higgs (spin 0 boson)		

Table 1.1: Particle content of the SM.

Each one of the matter particles of table 1.1 has its own antiparticle, with the same mass but opposite charge and quantum numbers. The quarks form bound states that are called baryons

(bound state of three quarks) and mesons (bound state of a quark and an antiquark), all of them grouped under the name "hadrons". The force mediators are also called vector bosons (due to the fact that they have spin 1), and the Higgs boson is called scalar (spin 0).

The SM dynamics is formulated in terms of a Lagrangian density, which is written as a function of quantum fields and their derivatives. The Lagrangian gives rise to Feynman rules that are used to compute probability amplitudes for different processes. The particles are represented in the Lagrangian by fields operators that reflect their transformation properties under Lorentz transformation. In the following sections we describe briefly the main ingredients of the SM Lagrangian.

1.1.1 QCD Lagrangian

In the SM, the strong interactions are described by a non-abelian gauge theory based on the symmetry group $SU(3)$. The charge associated to this group is called "color". The Lagrangian can be written as [4]:

$$\mathcal{L}_{QCD} = -\frac{1}{4}F^a_{\mu\nu}F^{\mu\nu}_a + \sum_k [i\bar{\psi}_k\gamma^\mu\partial_\mu\psi + g_s\bar{\psi}_k T_a G^a_\mu \psi] \tag{1.1}$$

where $F^a_{\mu\nu}$ is the gluon field tensor, G^a_μ are the gluon fields, T_a are the $SU(3)$ generators, g_s is the strong coupling constant and the sum in the second term is done over all the fermions with "color" charge, i.e., the quarks. Each spinor ψ is in the fundamental representation of $SU(3)$, so it has 3 components. The index a runs across the number of dimensions of the symmetry group, giving raise to eight different types of gluons. This lagrangian is invariant under local $SU(3)$ symmetry transformations.

Notice that the first term of equation (1.1) gives rise to the gluon self-interaction terms, and the second term originates the interaction between quarks and gluons, with a strength proportional to the strong coupling constant g_s.

1.1.2 Electroweak Lagrangian and symmetry breaking

The electroweak interactions description is based on a non-abelian gauge theory with symmetry group $SU(2) \otimes U(1)$, where the $SU(2)$ associated charge is called "weak isospin" and the $U(1)$ one is called hypercharge (denoted by Y). The dimension of the $SU(2)$ group is three, and of $U(1)$ is one, so this symmetry originates four gauge bosons.

The local gauge symmetry requires the gauge bosons to be massless. The Higgs mechanism is used in order to introduce mass terms in the Lagrangian without spoiling the symmetry and renormalizability of the theory [4]. The main idea is the introduction of a Higgs $SU(2)$ doublet in the theory, which allows to write a potential term with a degenerate ground state. One of this ground states is chosen, and the neutral component of the Higgs field acquires a vacuum expectation value (VEV), denoted by v.

The expansion of the Higgs field around this VEV introduces mass terms in the Lagrangian, for the gauge bosons through the covariant derivative of the Higgs field, and for the matter fermions trough their Yukawa couplings to the Higgs field. This process is called "spontaneous symmetry breaking" (SSB). The original symmetry group of the Lagrangian is broken to a single group $U(1)$, that is identified with the gauge group of quantum electrodynamics (QED). One of the original gauge bosons remains massless (photon), and the other three acquire mass (W^+, W^- and Z).

Table 1.2 shows a decomposition of the electroweak Lagrangian after SSB, with a short explanation of the content of each term. A complete discussion of the Lagrangian is out of the scope of this work, a summary of the main aspects and notation is given below:

- The fermion fields are denoted by ψ.

$$\mathcal{L}_{EW} = -\frac{1}{4}F^i_{\mu\nu}F_i^{\mu\nu} - \frac{1}{4}G_{\mu\nu}G^{\mu\nu} \qquad \text{kinetic terms and interactions of gauge bosons (1)}$$

$$+ i\sum_{fermions} \bar{\psi}\gamma^\mu\partial_\mu\psi \qquad \text{fermion kinetic terms (2)}$$

$$+ g\sin\theta_W \sum_{fermions} Q_f\bar{\psi}\gamma^\mu\psi A_\mu \qquad \text{fermion-photon interactions (3)}$$

$$+ \frac{g}{\sqrt{2}}\sum_{leptons} \bar{\psi}_{\nu_l}\gamma^\mu\frac{(1-\gamma^5)}{2}\psi_l W^+_\mu + h.c \qquad \text{lepton-W interactions (4)}$$

$$+ \frac{g}{\sqrt{2}}\sum_{quarks} \bar{\psi}_{q_u}\gamma^\mu\frac{(1-\gamma^5)}{2}V_{q_uq_d}\psi_{q_d} W^+_\mu + h.c \qquad \text{quark-W interactions (5)}$$

$$+ \frac{g}{\cos\theta_W}\sum_{fermions} \bar{\psi}\gamma^\mu\frac{(g_v - g_a\gamma^5)}{2}\psi Z_\mu \qquad \text{fermion-Z interactions (6)}$$

$$+ \frac{g^2v^2}{4}W^{+\mu}W^-_\mu + \frac{(g^2+g'^2)v^2}{8}Z^\mu Z_\mu \qquad W \text{ and } Z \text{ mass terms (7)}$$

$$+ \frac{1}{2}\partial_\mu H\partial^\mu H + \mu^2 H^2 - \frac{\mu^2 v^2}{4} \qquad \text{Higgs kinetic term, mass and potential (8)}$$

$$+ \lambda v H^3 + \frac{\lambda}{4}H^4 \qquad \text{Higgs self-interactions (9)}$$

$$+ \frac{g^2}{4}(2vH + H^2)W^{+\mu}W^-_\mu \qquad \text{Higgs-W interactions (10)}$$

$$+ \frac{g^2}{8\cos^2\theta_W}(2vH + H^2)Z^\mu Z_\mu \qquad \text{Higgs-Z interactions (11)}$$

$$+ \sum_{fermions} m_f\bar{\psi}\psi \qquad \text{fermion masses (12)}$$

$$+ \sum_{fermions} \frac{m_f}{v}H\bar{\psi}\psi \qquad \text{Higgs-fermion interactions (13)}$$

Table 1.2: Electroweak part of the SM Lagrangian.

- μ and λ are constants appearing in the definition of the Higgs potential. The Higgs doublet field is expanded around the VEV like: $\Phi = \begin{pmatrix} 0 \\ \frac{v+H}{\sqrt{2}} \end{pmatrix}$, where H is the neutral Higgs field and v is its vacuum expectation value.

- The constants g and g' are the original coupling constants of the gauge groups $SU(2)$ and $U(1)$ before SSB. The Weinberg angle is defined by the relationship: $\sin\theta_W = \frac{g'}{\sqrt{g^2+g'^2}}$.

- Line (1) contains interactions among the gauge bosons, with triple and quartic couplings, like γWW and $WWZZ$, among others.

- In line (3), $g\sin\theta_W$ is identified with the electronic charge of the electron e in order to recover QED.

- Lines (4), (5) and (6) show the chiral nature of the weak interaction in the SM. Only left handed fermions couple to the W boson, and for the Z boson, the left and right handed

part of a given fermion couple with different strengths, given by the constants g_v and g_a.

- The Cabibbo-Kobayashi-Maskawa matrix (CKM) elements are visible in line (5), its elements are denoted $V_{q_u q_d}$, mixing the "up" and "down" type quarks when they interact with the W bosons [5].

- For simplicity we are considering the neutrinos to be massless, so neither mass terms nor right handed neutrinos appear in the Lagrangian, and hence no mixing matrix for the lepton sector (this matrix is called Pontecorvo-Maki-Nakagawa-Sakata or PMNS matrix [5]).

The SM contains 21 free parameters that have to be measured experimentally: 3 coupling constants (or 2 plus the Weinberg angle), 12 fermion masses, 4 fermion mixing parameters, the Higgs boson mass and 1 independent gauge bosons mass (leaving outside the mixing parameters of the PMNS matrix). Once these parameters are fixed, the Lagrangian allows to compute amplitudes for scattering processes and decay rates, using perturbation expansions on powers of the coupling constants α (electromagnetic interaction), α_w (weak interaction), and α_s (strong interaction) defined as:

$$
\begin{aligned}
\alpha &= \frac{e^2}{4\pi} \\
\alpha_w &= \frac{g^2}{4\pi} = \frac{e^2}{4\pi \sin \theta_W} \\
\alpha_s &= \frac{g_s^2}{4\pi}
\end{aligned}
\tag{1.2}
$$

The SM has passed all experimental tests with remarkable success, with no serious contradictions between its predictions and the measurements done so far. However, many issues are not addressed by the SM, among which:

- Gravity is not included in the model, as it is much weaker than all others interactions, so it does not manifest in the energy scales typical of high energy experiments. The question remains how to incorporate gravity in a quantum field theory way in the SM.

- Neutrino oscillations have been measured, leading to the conclusion that neutrinos have mass. The appropriate way to incorporate these masses in the SM remains an open question, and why are there so small compared to the other scales of the theory.

- Cosmological observations have shown that more than 90 % of the universe is made of dark matter and dark energy, which are not incorporated in the SM model (see for example recent Planck experiment results [6]).

- The symmetry breaking mechanism is not yet completely understood. Recent observations showed the existence of a Higgs-like particle [7]. However, it remains to be investigated whether it is the scalar Higgs predicted by the theory, or a new particle belonging to a different symmetry breaking scenario.

1.1.3   The Z boson and its properties

After SSB, the Z boson appears in the SM as a mixing of one of the original gauge bosons of the SU(2) group and the gauge boson of the U(1) group (call them W^3 and B, respectively) [4]:

$$
Z_\mu = W_\mu^3 \cos \theta_W + B_\mu \sin \theta_W
\tag{1.3}
$$

The mass of the Z boson is predicted to be:

$$m_Z = \frac{v}{2}\sqrt{g^2 + g'^2} = \frac{m_W}{\cos\theta_W} \tag{1.4}$$

This relationship, together with other relations obtained from the Lagrangian at tree level, allows to compute the Z boson mass as:

$$m_Z = \sqrt{\frac{\pi\alpha}{\sqrt{2}G_F}}\frac{1}{\sin\theta_W \cos\theta_W} \tag{1.5}$$

where G_F is the Fermi constant (introduced comparing the Fermi theory with the low energy limit of the electroweak Lagrangian), and α is the fine structure constant (defined in equation 1.2). Using experimental values for the constants, the equation (1.5) was used to predict the Z boson mass, giving a value of be 92 ± 2 GeV [5]. This prediction was done years before the Z boson discovery at CERN in 1983 by the UA1 and UA2 detectors, which measured the mass to be 91.188 ± 0.02 GeV [8]. The discovery of the Z boson at this mass was considered a great success of the SM. The most recent experimental value for the mass is 91.1876 ± 0.0021 GeV [9].

The Z boson couples to all matter fermions, as shown in the coupling term of line (6) in table 1.2. This vertex conserves the flavor of the fermion, its charge and all its quantum numbers. For this reason, the interactions mediated by the Z boson are called weak neutral interactions or weak neutral currents. The fundamental vertex diagram is shown in figure 1.1.
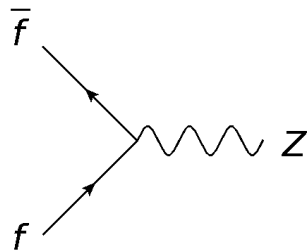
Figure 1.1: Diagram representing the interaction of the boson Z with the fermion f.

The interaction term of the Z boson and a matter fermion f (line (6) in table 1.2) can be written as:

$$
\begin{aligned}
\mathcal{L}_{Z-inter} =& \frac{g}{\cos\theta_W}\bar{\psi}^{(f)}\gamma^\mu \frac{(g_v^{(f)} - g_a^{(f)}\gamma^5)}{2}\psi^{(f)}Z_\mu \\
=& \frac{g}{2\cos\theta_W}\left[(g_v^{(f)} + g_a^{(f)})\bar{\psi}_L^{(f)}\gamma^\mu\psi_L^{(f)} + (g_v^{(f)} - g_a^{(f)})\bar{\psi}_R^{(f)}\gamma^\mu\psi_R^{(f)}\right]Z_\mu
\end{aligned} \tag{1.6}
$$

where $g_v^{(f)}$ and $g_a^{(f)}$ are the vector and axial couplings of the Z boson to the fermion f. This equation shows that the Z boson couples with different strengths to the chiral components (ψ_L and ψ_R) of the fermion. The couplings depend on the flavor of the fermion, and are given by [10]:

$$
\begin{aligned}
g_v^{(f)} =& T^3(f) - 2Q(f)\sin^2\theta_W \\
g_a^{(f)} =& T^3(f)
\end{aligned} \tag{1.7}
$$

where T^3 and $Q(f)$ are the weak isospin and electric charge of the fermion, respectively. The values of the vector and axial couplings of the SM particles are given in table 1.3.

The Z boson decay in pairs particle - antiparticle. The total decay width is 2.4952 ± 0.0023 GeV, which results in short mean lifetime of about $3\cdot 10^{-25}$ s. Experimentally measured branching fraction of the decays are given in table 1.4, that agree with the predicted values. The production of Z bosons is discussed in section 1.3, in the context of hadronic collisions.

Fermion	g_v	g_a
ν_e, ν_μ, ν_τ	$1/2$	$1/2$
e, μ, τ	$-1/2 + 2\sin^2\theta_W$	$-1/2$
u, c, t	$1/2 - 4/3\sin^2\theta_W$	$1/2$
d, s, b	$-1/2 + 2/3\sin^2\theta_W$	$-1/2$

Table 1.3: Vector and axial coupling constants of the Z boson to the matter fermions.

Decay channel	Branching fraction
$Z \to e^+e^-$	(3.363 ± 0.004) %
$Z \to \mu^+\mu^-$	(3.366 ± 0.007) %
$Z \to \tau^+\tau^-$	(3.370 ± 0.008) %
$Z \to \nu^+\nu^-$ (invisible)	(20.00 ± 0.06) %
$Z \to q^+q^-$ (hadrons)	(69.91 ± 0.06) %

Table 1.4: Branching fractions of the Z boson.

1.2 Phenomenology of proton-proton collisions

In the quark model, protons are bound states of two quarks u and one quark d. These quarks are called "valence" quarks. They interact by the interchange of gluons, which at the same time can split forming virtual quark-antiquark pairs, which are called "sea of quarks and gluons". Quarks and gluons are called collectively "partons". The proton structure is probed experimentally through collisions. When two protons collide, different types of processes can occur, that can be classified as:

- Elastic events: the two protons remain intact, except for a small transfer of momentum.

- Inelastic events: one or both protons dissociate into a system of particles. The inelastic events can be:

  - Soft scattering, including diffractive and non diffractive events. In these events, one or two of the protons dissociate into a system of particles with low p_T. The non diffractive events are also called "minimum bias" events, and are characterized by the production of a high number of charged particles.

  - Hard scattering, characterized by high momentum transfer and the production of particles with high p_T.

In figure 1.2 we present the cross-sections for different processes, for the center-of-mass (CM) energies explored by Tevatron and LHC (see section 2.1) [11]. The total proton-proton (pp) cross-section is dominated by the elastic and soft scattering processes. As an example, the Z boson production cross-section at $\sqrt{s} = 7$ TeV is approximately 28 nb, while the total inelastic cross-section is $98 \cdot 10^6$ nb.

The underlying theory for all the scattering processes is QCD. However, the approach and the level of understanding is very different for soft and hard scattering. In hard scattering processes, the quarks and gluons behave as free particles (due to asymptotic freedom), thus the perturbative approach gives accurate predictions. On the other hand, soft processes are dominated by non perturbative QCD effects, which are less understood. Notice that hard processes are usually accompanied by soft interactions (underlying event, soft gluon emissions), so their effect must be included up to some degree of accuracy, in order to produce reliable predictions.
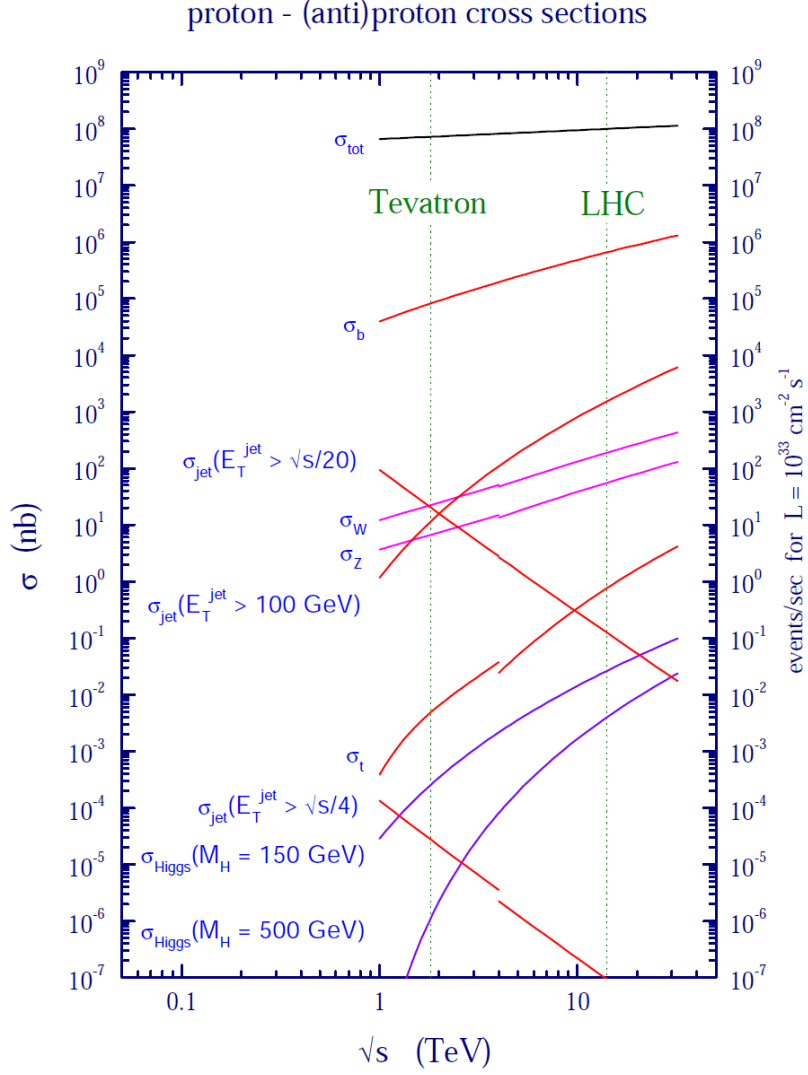
Figure 1.2: SM cross-sections for hadronic collisions, for the range of energies explored by Tevatron and the LHC [11].

1.2.1   Perturbative QCD

The factorization theorem [11][12] allows to compute the cross-section of a hard scattering process in proton-proton collisions, starting from the cross-section of the process at parton level, in the following way:

$$\sigma_{AB->C} = \sum_{a,b} \int_0^1 dx_1 dx_2 \, f_a(x_1, \mu_F) f_b(x_2, \mu_F) \, \hat{\sigma}_{ab->C}(\mu_F, \mu_R) \tag{1.8}$$

where :

- The sum over the indices a and b is a sum over all the partons that can contribute to the process. a runs over the partons of proton A, and b runs over the partons of proton B.

- μ_F is the factorization scale. It can be considered as the scale that separates short and long distance physics, and is usually taken as the mass of the outgoing system of particles.

- μ_R is the renormalization scale, which defines the QCD running coupling and the renormalization.

15

- $f_{a,b}(x, \mu_F)$ are the parton distribution functions (PDF) for the partons a, b, in the proton A, B. It gives the probability of finding a parton with momentum fraction x in the proton. The momentum fraction is defined as:

$$x_{a,b} \equiv \frac{p^z_{a,b}}{p^z_{A,B}} \tag{1.9}$$

where $p^z_{a,b}$ are the longitudinal components of the momentum of the partons a, b (along the collision axis), and $p^z_{A,B}$ the longitudinal components of the total momentum of the protons A, B.

- $\hat{\sigma}_{ab->C}$ is the parton level cross-section for the process $ab-> C$, computed using perturbative QCD up to some level in perturbation theory. It depends on both scales, μ_F and μ_R.

The computation to all orders in perturbation theory is independent of the choice of scales μ_F and μ_R. However, in the absence of a complete set of higher order corrections to $\hat{\sigma}_{ab->C}$, the result is dependent on the choice of scales, introducing theoretical uncertainties in the predicted numerical values. Usually, both scales are chosen equal to a hard scale Q^2 associated with the process, for example the mass of a resonance produced in the interaction [12].

The PDF are solutions to the DGLAP equations, which determine their evolution with the scale μ_R [11]. However, the x dependence of the PDFs have to be obtained by fitting experimental data from deep inelastic and hard scattering experiments. Different sets of PDFs are provided, which use different fit methods and experimental data. In figure 1.3 we show an example, the MSTW PDF set [13], for two different values of the hard scale Q^2.

MSTW 2008 NLO PDFs (68% C.L.)
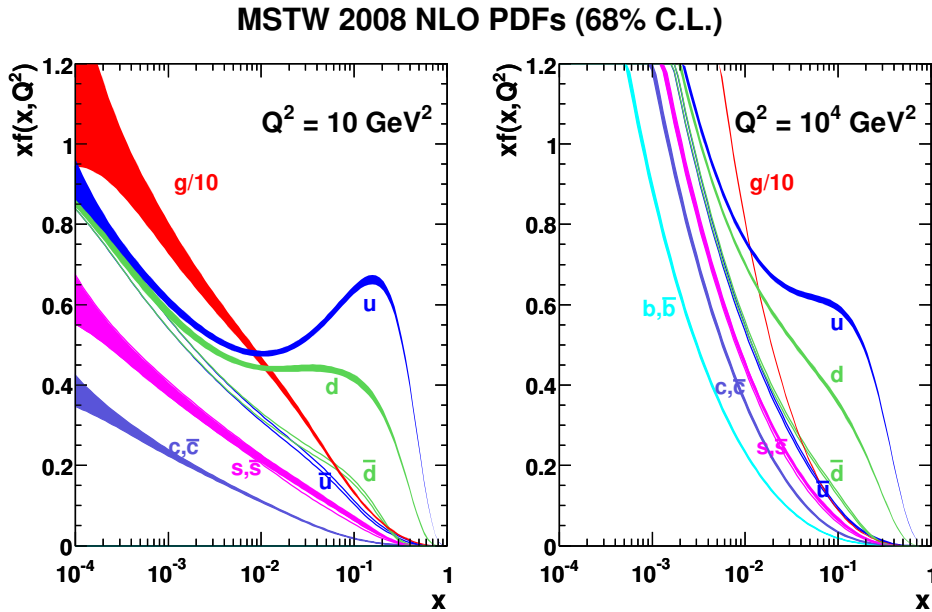
Figure 1.3: MSTW PDF set, for two different values of the Q^2 scale [13].

In principle, the perturbative QCD approach (pQCD) can be used to predict quantities up to some level of precision in the strong coupling constant. However, singularities appear to all orders in the perturbation series, starting from next-to-leading-order (NLO). For example, the amplitude for the process shown in figure 1.4, which involves the production of a vector boson V, has the form [11]:

$$A \sim \alpha_s^2 \frac{t^2 + u^2 + 2m_V^2 \hat{s}}{tu} \tag{1.10}$$

16

where (t, u, s) are the Mandelstam variables of the partons in the diagram, and $\hat{s}$ is the invariant mass squared of the parton system, defined by:

$$\hat{s} \equiv (p_a + p_b)^2 \approx s x_a x_b \tag{1.11}$$
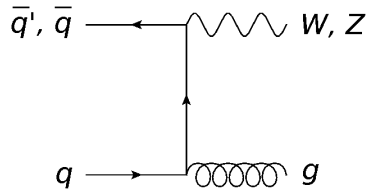
Figure 1.4: Example of NLO diagram in pp collisions, with the production of a vector boson and a gluon.

Here, $s = (p_A + p_B)^2$ is the invariant mass of the proton system, and the proton and parton masses are neglected. This amplitude diverges if the gluons are emitted collinear to one of the quarks or if the gluon is soft ($t \to 0$ or $u \to 0$). This amplitude can be used to compute differential cross-sections, and after some simplifications, it can be shown that [11]:

$$\frac{d\sigma}{dQ^2 \, dy \, dp_T^2} \sim \frac{\alpha_s^2 \log(s/p_T^2)}{p_T^2} \tag{1.12}$$

where a clear divergence is present for $p_\mathrm{T} \to 0$. In order to avoid this divergence, it is necessary to introduce a cutoff below which the prediction is not valid. However, predictions of pQCD are finite, these singularities disappear when the contributions from other diagrams at the same level (NLO) are included in the amplitude.

1.2.2 Resummation schemes

In order to produce more accurate predictions, the perturbative computation should be evaluated at increasing orders in α_s. However, with the increase of order and number of final state particles, the number of Feynman diagrams to evaluate increases enormously, and the loop graphs calculation becomes difficult. On the other hand, higher order effects play an important role in the event structure, for example the emission of multiple gluons affects the shape for differential cross-sections at low p_T.

Contributions at "all orders" in perturbation theory can be included using resummation schemes. In these approaches, the dominant contributions of each order in perturbation theory are added together using an evolution equation. This way, only few diagrams are evaluated at each order. As an example, in the evaluation of the cross-section for the production of vector bosons, two logarithmic terms appear at each order in the perturbative series [11]:

$$\begin{aligned}
L1 &= \alpha_s^n \frac{\log^{2n-1}(1-z)}{1-z} \\
L2 &= \alpha_s^n \log^{2n-1}\left(\frac{Q^2}{p_T^2}\right)
\end{aligned} \tag{1.13}$$

where $z = Q^2/\hat{s} - 1$ and n is the order of the term in the series. L1 diverges near the boundary $Q^2 \to \hat{s}$ and L2 for $p_T \to 0$. The resummation allows to add up all these terms and give a finite prediction near these boundaries. Several techniques are used to resum the contributions. The resummations are done up to some level of accuracy in the logarithmic terms, the state of the art are next-to-next-to-leading logarithms (NNLL), see for example [14].

1.2.3 Parton showers

Another "all orders" scheme is provided by parton showers. Here, multiple parton emissions are added to the hard process, in the form of QCD initial and final state radiation ($q \to qg$, $g \to gg$, $g \to q\bar{q}$). The evolution of the momenta of the emitted partons is controlled by the variation of a scale variable, which gives a sense of time to the shower. This scale increases gradually producing the initial state radiation (ISR) shower, up to the hard process and then decreases producing the final state radiation (FSR) shower [15]. The emission process is related to Sudakov form factors, which give the probability of a given parton to evolve from a higher scale to a lower scale without emitting another parton [11]. In figure 1.5 we show schematically the effect of a parton shower in a hard scattering process. Notice that the parton shower needs to incorporate a mechanism of hadronization.
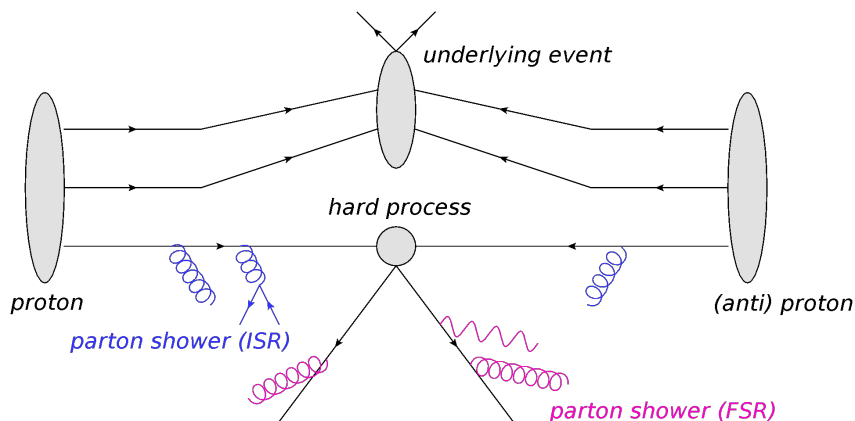
Figure 1.5: Schematic representation of a proton-proton collision, showing the hard process, parton showers and underlying event.

The parton shower incorporates in the calculation the effect of the emission of a large number of soft and collinear partons, and the interference effects between them. However, when the partons are energetic and widely separated, the matrix element calculation (fixed order pQCD) provides a better description. The best description of the process is obtained combining the parton shower calculation with the matrix elements. But a straight addition of the two techniques can lead to double counting, so the merging is done usually restricting the kinematic regions where each calculation is applied [11].

1.3 The Z boson transverse momentum differential cross-section in pp collisions

The Z boson production in pp collisions is an example of hard scattering, where the partons that interact in the hard process have enough momenta to create the Z resonance. The LO and NLO diagrams for Z boson production are shown in figure 1.6, including the quark-antiquak annihilation ($q\bar{q} \to Z$), quark-antiquark annihilation with the emission of a hard gluon ($q\bar{q} \to Zg$) and quark gluon scattering ($qg \to Zq$). In proton-proton collisions, the dominant process is ($qg \to Zq$) due to the high density of gluons in the protons with respect to those of antiquarks [16].

Using the same notation introduced in section 1.2, we can write the momentum 4-vectors of the interacting partons as:
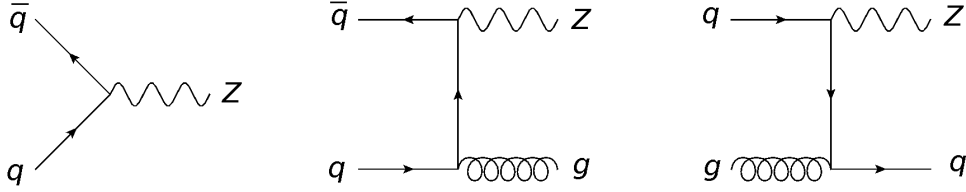
Figure 1.6: LO and NLO diagrams for Z boson production in pp collisions.

$$\underline{p_a} = \sqrt{\frac{s}{2}}(x_a, 0, 0, x_a)$$
$$\underline{p_b} = \sqrt{\frac{s}{2}}(x_b, 0, 0, -x_b)$$

(1.14)

where we have neglected the masses, and assumed that the partons are exactly collinear with the colliding protons. At LO, the Z boson kinematics is determined by the addition of these two vectors. We have then:

$$\hat{s} = s x_a x_b = m_Z^2$$

(1.15)

which allows to estimate the typical momentum fraction of the partons involved in the Z boson production. Assuming $x = x_a = x_b$, we obtain $x = m_Z/\sqrt{s}$. For a center-of-mass energy of $\sqrt{s} = 7$ TeV, we obtain $x \approx 0.014$. Using these value of x together with PDF functions, we can have an idea of the dominating processes in the Z boson production. For example, from figure 1.3, we can see that for the energy scale set by the Z boson mass ($Q^2 \approx m_Z^2$), the most probable process will involve a gluon.

Another interesting relationship, valid at LO, relates the rapidity of the resulting Z boson to the momentum fractions. Using equation 1.14, we can obtain the rapidity of the produced Z boson: $y_Z = 1/2 \log(x_a/x_b)$. Then, using equation 1.15 we obtain:

$$x_a = \frac{m_Z}{\sqrt{s}} e^{y_Z}$$
$$x_b = \frac{m_Z}{\sqrt{s}} e^{-y_Z}$$

(1.16)

When the produced Z boson decays into leptons, it is classified as a "Drell-Yan" process, i.e. the production of lepton pairs in hadron collisions [17]. The Drell-Yan process is one of the standard candles of hadron collisions, which provides information about the QCD structure of the proton, and the dynamics of the hadron interaction in general. The experimental signal is characterized by two hard leptons, that can be easily separated from the huge amount of QCD activity in particle detectors. As electrons and muons are reconstructed with high efficiency and their kinematics measured with high precision, they constitute a precise probe of the hadronic processes.

The transverse momentum of the lepton pair $\mathbf{p_T^Z} = \mathbf{p_T^{(a)}} + \mathbf{p_T^{(b)}}$ is a natural observable of the Drell-Yan process, which probes directly the dynamics of the strong interaction. At leading order, and assuming a head on collision, the Z boson is produced with zero transverse momentum. The emission of additional partons in the initial state in higher order processes allows to produce the Z boson with non zero transverse momentum.

The theoretical computations of the p_T^Z specturm based on pQCD follows the ideas described in section 1.2.1. The matrix elements of the hard process have been evaluated up to NLO, and predictions for the differential spectrum have been obtained [18]. However, this approach fails to describe the properties of the spectrum at low p_T, so resummation techniques an parton

showers are used [11]. In the end, the prediction for low p_T has to be matched with the pQCD prediction, in order to have a full theoretical picture. The differential spectrum is written as:

$$\frac{d\sigma}{dp_T} = \left(\frac{d\sigma}{dp_T}\right)_{\text{(pQCD)}} + \left(\frac{d\sigma}{dp_T}\right)_{\text{(low } p_T)} - \left(\frac{d\sigma}{dp_T}\right)_{\text{(overlap)}} \qquad (1.17)$$

where the last term is needed to remove the "double counting", which arises when the contributions at "all orders" contain some of the effects that have already been accounted for in the pQCD term. Notice that no analytic expression is available for the spectrum, the final shape arises from the contributions entering the different terms of the prediction.

Equation (1.17) shows how the different regimes of the p_T^Z spectrum are sensitive to different aspects of the QCD prediction. For low p_T, the measured spectrum allows to test the validity of the resummation schemes, and tune the parameters of the non-perturbative form factors and parton showers. For high p_T, the spectrum is sensitive to pQCD contributions and the emission of additional hard partons. Globally, the level of agreement between the measurement and the prediction constrains the pQCD - low p_T matching procedure, and the full spectrum can be used to perform fits and improve the understanding of the PDF entering the whole prediction.

Theoretical tools are available that can generate the differential spectrum, which include different approaches for the resummation procedure and the evaluation of higher order matrix elements. Some of them are presented in the context of comparison with the measurement, in chapter 6.

1.4   MC generators

Monte Carlo event generators (MC) are used extensively in experimental and theoretical high energy physics. The production of MC samples involves several steps, that can be summarized as follows:

- Generation: a large number of events are generated based on the probability distributions predicted by the theory. These generated events contain the kinematics of the collision products.

- Simulation: the generated events are interfaced to a simulation of the particle detector, whose final product is a collection of simulated electric signals that represent the detector response.

- Reconstruction: simulated events are given as input to the same algorithms used in the reconstruction of real collision events.

At the end, a data sample is produced with an output format that can be directly compared to real data. The MC samples are used for many purposes, among others:

- Test the predictions of the underlying theory used in the generation, comparing the reconstructed MC events with data.

- Correct measurements for detector effects and extrapolate the result to kinematic regions not accessible by the detector.

- Calibrate the detector energy and momentum measurements, estimate performance parameters and optimize the kinematic selection used to analyze data.

- Measure parameters of theoretical models, through the generation of samples based on different values of the parameters and their comparison with data.

Several generators are available for the simulation of pp collisions, with differences in the way they implement the different features of the QCD processes. In the following paragraphs we describe briefly the generators used in our study.

- PYTHIA is a general purpose generator which implements many different processes, in particular hadron collisions (pp, $p\bar{p}$) and lepton collisions (e^+e^-) [15]. The matrix elements are computed at the LO level. It contains parton showers and hadronization models that have been extensively tested.

- MC@NLO implements the matching between NLO matrix elements for QCD and parton showers [19]. The parton showers are obtained using the HERWIG generator, another general purpose generator [20].

- POWHEG ("Positive Weight Hardest Emission Generator") [21] implements NLO matrix elements in QCD, using a different method to match with the parton showers than MC@NLO. The method is independent of the parton shower implementation, thus the POWHEG output can be interfaced to PYTHIA or HERWIG to generate them.

- ALPGEN is a dedicated generator for hadronic collisions [22], implementing processes with the emission of multiple hard partons (multiparton processes) using tree level diagrams. The parton showers are obtained interfacing it with PYTHIA or HERWIG.

- SHERPA is another general purpose generator [22], with LO matrix elements, parton shower implementation and multiparton events (tree level diagrams).

When processing a given MC sample, one has access to the original kinematics of the process being simulated. This information is called the "truth block" of the MC sample, and any information obtained from it is called "truth level information". In the case of the process $pp \rightarrow Z + X \rightarrow e^+e^- + X$, we can look at the original kinematics of the partons involved in the hard process, the pair electron-positron produced in the decay of the Z boson, and of any other particle involved in the process (FSR and ISR photons, radiated gluons, etc).

There are three reference points to define the electrons used to reconstruct the Z boson kinematics at truth level, namely:

- Born or propagator level: the electrons are taken immediately after the Z boson decay, before any photon radiation.

- Bare level: the electrons are defined as the final state electrons, after the photon radiation.

- Dressed level: the electrons are defined combining the final state electrons with photons found within a cone of radius ΔR.

The bare and dressed levels are experimentally better defined than the Born one, which represent a virtual intermediate state.

Chapter 2

The ATLAS detector and the LHC

This chapter introduces the experimental context of the measurement. First, we describe briefly the LHC and its main operation parameters during the years 2010 to 2012. Then we introduce the ATLAS experiment, describing common notation and definitions frequently used and giving a general summary of the main components of the detector: the inner tracker, the calorimeters, the muon system and the trigger and data acquisition systems. The chapters ends with some remarks about the event reconstruction in ATLAS.

2.1 The Large Hadron Collider (LHC)

The Large Hadron Collider (LHC) [23] is a particle collider currently under operation, located in a ring shaped tunnel of 26.7 km long, and between 45 m and 170 m underground. It was built in the site occupied formerly by the LEP accelerator, located at both sides of the border between France and Switzerland, near Geneva, and is operated by the European Organization for Nuclear Research (CERN). Its construction began in 1998, and culminated in 2008, the first collision took place in November 2009.

The LHC is a synchrotron or cyclic type accelerator [24], meaning that the particles are accelerated in successive turns around a nearly circular path, using radio frequency (RF) cavities to provide the electric field needed for the acceleration, and magnetic fields perpendicular to the trajectory to bend the particle trajectory and keep them in orbit. The magnetic field needs to be increased as the energy of the particles increases, and the maximum magnetic field achievable determines the maximum energy to which the particles can be accelerated. The field provided by the RF cavities also compensate the loss due to synchrotron radiation.

In the LHC, the particles accelerated are protons, so two pipes are needed with opposite bending magnetic fields around them. As the tunnel cross-section (3.7 m of diameter) prevented the installation of two separated proton rings, the two pipes share a common magnet and cooling system, consisting of dipoles with a design field of 8.33 T, which use superconducting coils operating at a temperature of 1.9 K and with a nominal current of 11.5 kA [25]. Quadrupole magnets are used in addition to dipoles. All the magnets are arranged in a complex structure called "lattice", designed to provide the bending and focusing magnetic field needed. In addition to the proton-proton collisions, the LHC physics program includes collisions of heavy ions (Pb), and also heavy ions against protons.

Before entering the LHC rings, the protons are accelerated using the previous existing chain of accelerators, namely: Linac, booster, PS and SPS [25]. Once in the rings, the acceleration continues by means of RF cavities operating at a nominal frequency of 400.8 MHz, with a nominal voltage of 16 MV.

In figure 2.1 we show a schematic view of the LHC ring and its elements [25]. The layout consists of eight bending arcs, the points between two bending arcs are called "insertions" (IR). Four of these insertions are actual interaction points (IP), where separation and recombination

dipoles are used in order to cross one beam with the other, and the collisions occur. Two IR are used for beam injection, one IR for RF accelerating cavities, and another one for beam dump (extraction of the beam from the pipes).
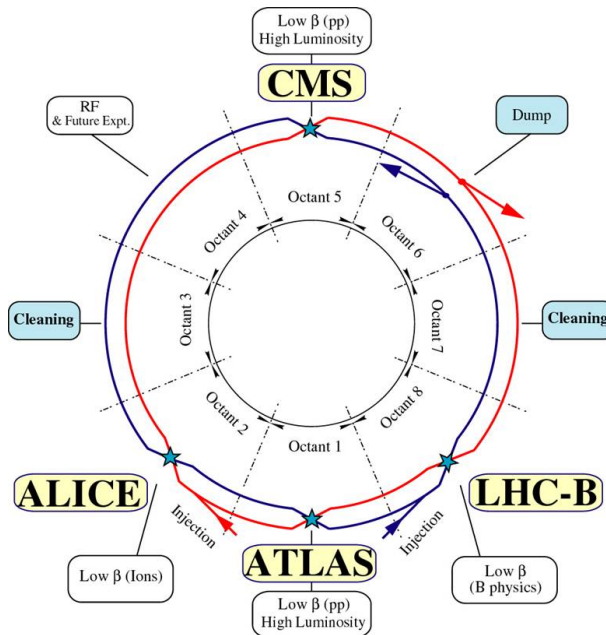
Figure 2.1: Schematic view of the LHC and elements [25].

2.1.1 LHC performance

In accelerator physics, the instantaneous luminosity $\mathcal{L}$, is defined as the interaction rate (R) per unit cross-section (σ), for a given process $A \to B$ [26], so it satisfies the equation:

$$R_{A \to B} = \sigma_{A \to B} \times \mathcal{L} \tag{2.1}$$

The cross-section $\sigma_{A \to B}$ contains the intrinsic probability of the interaction to happen, thus it is determined by the particles involved and the nature of their interaction. This means that the instantaneous luminosity contains the factors that can be controlled experimentally in order to increase the rate of the process, and thus its possible observation. For this reason, it is a figure of merit for a collider. From equation 2.1, we see that the units of the instantaneous luminosity are time$^{-1} \times$ length^{-2}.

In the LHC environment, the instantaneous luminosity is given by [23]:

$$\mathcal{L} = \frac{N_b^2 n_b f_{rev} \gamma_r}{4\pi \epsilon_n \beta_*} F \tag{2.2}$$

where N_b is the number of particles per bunch, n_b the number of bunches per beam, f_{rev} the revolution frequency, γ_r the relativistic gamma factor, ϵ_n the normalized transverse beam emittance, β_* the beta function at the collision point, and F the geometric luminosity reduction factor which depends on the crossing angle at the IP, the transverse beam size and the bunch length.

In order to understand the different factors entering equation 2.2, we have to consider the evolution in time of a bunch of particles as it circulates the accelerator ring. It can be shown that the bunch of particles, as it traverses the magnets, will experience both longitudinal (along the direction of the beam), and transversal oscillations (in the plane perpendicular to the beam). The former are called "synchrotron oscillations", while the latter are called "betatron oscillations".

The normalized emittance (ϵ_n) measures the average spread of the bunch of particles in the transverse plane (constant along the trajectory), while the β_* function describes the wavelength of the betatron oscillations. Assuming that the number of particles in the bunch are distributed following a two dimensional gaussian of standard deviation σ, centered in the origin of the transverse plane (beam line), the following relation holds (up to relativistic kinematic factors) [26]:

$$\sigma^2 \sim \epsilon_n \times \beta_* \tag{2.3}$$

In order to explore as many different physical processes as possible, the LHC needs a high instantaneous luminosity, the design goal being $\mathcal{L} = 10^{34}$ cm^{-2}s^{-1}. In order to reach this, the parameters in equation 2.2 need to be adjusted accordingly, taking into account different performance limitations, coming from different factors, among which the interaction of particles within one bunch, the interactions between different bunches, the mechanical aperture and the maximum energy that can be stored [23]. In table 2.1 we summarize the design values of LHC parameters.

Proton - proton collider	
Nominal energy	7 + 7 TeV
Instantaneous luminosity	10^{34} cm^{-2}s^{-1}
Number of bunches per proton beam	2808
Number of protons per bunch	10^{11}
Circumference	26.659 m
Depth	50 - 175 m
ϵ_n	3.75 μm $\times$ rad
β_*	0.50 m
Dipole field	8.33 T
Injection energy	450 GeV
Bunch spacing	25 ns
Circulating current	0.582 A

Table 2.1: Summary of LHC design parameters.

Using the design numbers of table 2.1, the number of bunch-crossings (BC) per second can be estimated, giving around 40 million bunch-crossings each second.

An informative parameter to characterize the performance of an accelerator is the luminosity integrated over time, $L = \int \mathcal{L}dt$, which measures the amount of particles circulated over time in the accelerator, and hence the number of collisions and data collected. The integrated luminosity (or simply "luminosity") has units of length^{-2}, and is usually expressed in inverse barn units (b^{-1}), with 1b $\equiv 10^{-28}$ m^2.

2.1.2 LHC operation during the period 2010-2012

The LHC started operation in 2010 and since then collision energy, instantaneous luminosity and other operation parameters have been changing according to the progress in the understanding of the machine. During the year 2010, the collisions were done with a center-of-mass energy (c.m.e.) of 7 TeV (3.5 TeV per beam). This condition was kept in 2011, going up to 8 TeV (4 TeV per beam) in 2012. In table 2.2 we present a summary of the LHC configuration during its first 3 years of operation. The integrated luminosity reported corresponds to the total delivered one, which differs from the recorded by the experiments. We only show the performance parameters relevant to the proton - proton collision periods. Figure 2.2 shows the total integrated luminosity

delivered by the LHC to the ATLAS experiment during the period 2010-2012, for proton - proton collisions.

Year	Beam energy (TeV)	Integrated luminosity (fb^{-1})	Maximum instantaneous luminosity ($cm^{-2} s^{-1}$)	Typical number of proton bunches	Bunch spacing (ns)
2010	3.5	0.0481	2.1×10^{32}	200	50
2011	3.5	5.61	3.6×10^{33}	1400	50
2012	4.0	23.3	7.7×10^{33}	1400	50

Table 2.2: Summary of LHC operation during the years 2010 to 2012.
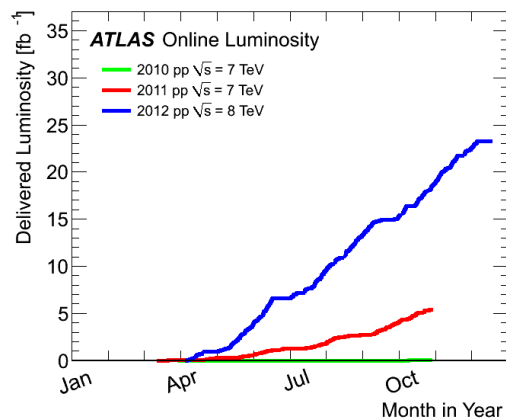
Figure 2.2: Total luminosity delivered by the LHC to the ATLAS experiment, for the period 2010-2012.

There are four experiments installed on the LHC ring, each one surrounding one IP (see figure 2.1), namely:

- ALICE (A Large Ion Collider Experiment)

- ATLAS (A Toroidal LHC Apparatus)

- CMS (Compact Muon Solenoid)

- LHCb (Large Hadron Collider beauty)

ALICE, ATLAS, CMS and LHCb are particle detectors installed in big underground caverns built around the four collision points of the LHC. ATLAS and CMS are general purpose detectors, designed to be sensitive to the broad spectrum of phenomena expected from the collisions. LHCb is designed to study the physics of b hadrons produced in the collisions, and ALICE is optimized to study the heavy ions collisions.

2.2 The ATLAS experiment

The ATLAS experiment is a particle detector installed around one of the LHC IP points (point 1). It is located at the CERN site of Meyrin, in a cavern at 90 m under the surface level. It has a cylindrical shape, 45 m long and 25 m in diameter, and weights about 7000 tonnes. The project involves roughly 3000 scientists and engineers from 175 institutions in 38 countries. It was first proposed in 1994, and its construction was finished in 2008 [27].

ATLAS was designed as a general purpose particle detector, intended to investigate the many different types of phenomena possible in the collision environment of the LHC. The physics program includes:

- Refine the measurement of Standard Model parameters, among them the masses of the W boson and the top quark.

- Measure cross-sections, decaying rates and other observables, important to test and validate the predictions of the Standard Model.

- Search for the the Higgs Boson, and eventually measure its properties (mass, couplings, spin, parity, etc.).

- Perform measurements in the flavor sector of the SM, in particular CP violation.

- Search for dark matter candidates.

- Discover (or rule out) direct evidence of physics beyond the Standard Model (supersymmetry, extra dimensions).

These goals conditioned the design and decisions made about the construction of the ATLAS detector. The basic design criteria includes very good electromagnetic and hadronic calorimetry and high precision muon momentum measurements [28].

The ATLAS detector is a complex system, consisting of several subdetectors, magnets and dedicated electronic systems. It can be divided in several components, according to the function they have in the particle reconstruction and identification, and to which type of particles they are sensitive. These components are described briefly in the following sections, starting from the subdetectors closest to the beam pipe, and moving outwards. Emphasis is put on the inner detector, as it is directly involved in the reconstruction of electrons. The main detector part used in the reconstruction of electrons, the electromagnetic calorimeter, is briefly described here, more details of its construction and performance are given in chapter 3. A schematic view of the ATLAS detector with its parts indicated can be seen in figure 2.3.
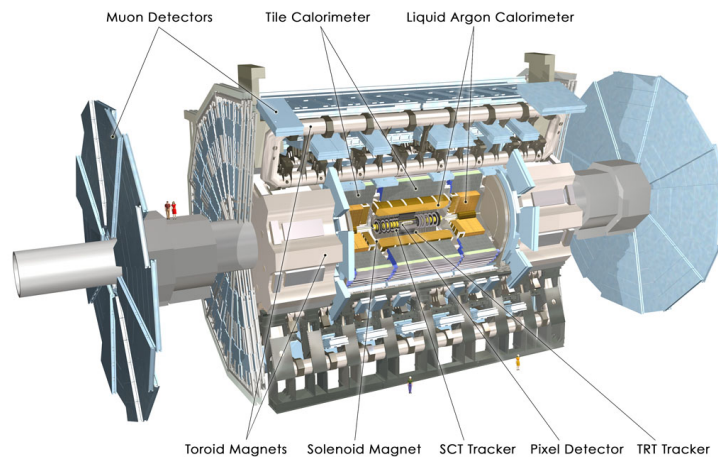
Figure 2.3: Schematic view of the ATLAS detector and its components.

2.2.1 Some definitions and conventions

In this section we introduce conventional terminology and concepts used frequently in the description of the detector and the physics that is explored with it.

Coordinate system

The coordinate system used to describe the particle position in ATLAS and also to describe geometrically the detector, uses the following convention: the beam direction defines the z-axis,

and the x-y plane is the plane transverse to the beam direction. The positive x-axis is defined as pointing from the interaction point to the center of the LHC ring, and the positive y-axis is pointing upwards. A sketch showing the orientation of this coordinate system in relation with the ATLAS detector is shown in figure 2.4 [29]. Using this cartesian coordinate system, the spherical coordinate system (r, θ, ϕ) is defined in the conventional way.
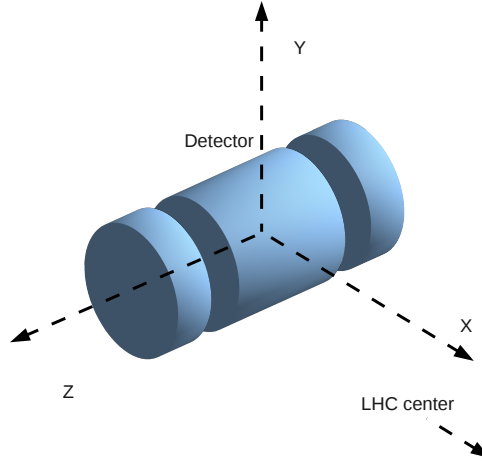
Figure 2.4: Coordinate system.

The x-y plane is called "transverse plane", and all the quantities measured in this plane are called transverse quantities ("T" subindex). For instance, for a particle with mass m and 4-momentum $p = (E, \mathbf{p}) = (E, p_x, p_y, p_z)$, we have the transverse momentum:

$$
\begin{aligned}
\mathbf{p}_\mathrm{T} &\equiv p_x \hat{\mathbf{i}} + p_y \hat{\mathbf{j}} \\
p_\mathrm{T} &\equiv |\mathbf{p}_\mathrm{T}| = \sqrt{p_x^2 + p_y^2} = |\mathbf{p}| \sin\theta
\end{aligned}
\tag{2.4}
$$

The transverse energy E_T is defined as:

$$
E_\mathrm{T} \equiv \sqrt{|\mathbf{p}_\mathrm{T}|^2 + m^2}
\tag{2.5}
$$

So for particles with $m << |p_\mathrm{T}|$ we have $E_\mathrm{T} \sim |\mathbf{p}_\mathrm{T}|$.

Rapidity and pseudorapidity

An important quantity commonly used in particle physics is the rapidity. The rapidity along the z-axis is defined as [9]:

$$
y \equiv \frac{1}{2} \ln\left(\frac{E + p_z}{E - p_z}\right) = \tanh^{-1}\left(\frac{p_z}{E}\right)
\tag{2.6}
$$

The rapidity can be defined along any other axis, but in collider physics its convenience comes when it is defined along the direction of motion of the incident particles, so we will restrict to the z-axis defined one. If we consider a boost in the z direction, to a frame moving with velocity β_{frame}, it can be shown that the rapidity transforms to the new frame in the following way [9][30]:

$$
y \to y' = y - \tanh^{-1}(\beta_{frame})
\tag{2.7}
$$

If we call $\tanh^{-1}(\beta_{frame})$ the rapidity of the moving frame, equation 2.7 shows that under boosts the rapidity is additive, so it transforms in an analogue way to the velocity in classical

mechanics. This transformation law implies that rapidity differences are invariant, and the shape of rapidity distributions dN/dy as well (N is number of particles produced).

Another important property of rapidity is that in hadron collisions the rapidity distribution of the collision products is approximately flat around the value $y = 0$ [30][31], that is, for particles with low p_Z compared to E.

Consider next a particle with a small mass compared to its momentum, and centered in the origin of coordinates. Then we have $E \sim |\mathbf{p}|$ and $p_z = |\mathbf{p}|\cos(\theta)$, so:

$$y \sim \frac{1}{2} \ln \left(\frac{1 + \cos(\theta)}{1 - \cos(\theta)} \right) = -\ln \left[\tan \left(\frac{\theta}{2} \right) \right] \equiv \eta \tag{2.8}$$

The last quantity is called pseudorapidity (η). Notice that unlike the rapidity, it depends only on the polar angle θ. In figure 2.5 the geometrical relationship between the θ angle and the pseudorapidity η is shown. We can see that the "central region" of the detector ($\theta \sim 90°$) corresponds to low η regions, and the "forward regions" ($\theta \sim 0°$ or $\theta \sim 180°$) correspond to $|\eta| \to \infty$ (region close to the beam).
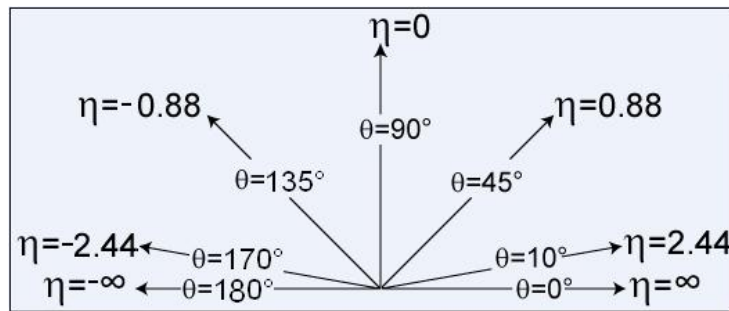
Figure 2.5: Relation between the polar angle θ and the pseudorapidity η, where the z-axis is taken in the horizontal direction.

The pseudorapidity η is preferred over the polar angle θ due to the reason mentioned above: the pseudorapidity distribution is approximately constant around the central region, so the number of particles produced is expected to be uniform in η. This makes it a more natural variable to be used in the description of the detector and physics phenomena.

The uppercase "R" is used to denote distance in the (η, ϕ) space, i.e. $\Delta R = \sqrt{\Delta \eta^2 + \Delta \phi^2}$.

Definition of acceptance

The acceptance of a subdetector is defined as the spatial coverage of the detector. In the case of ATLAS, the detector is hermetic in the azimuthal direction, thus limitations in acceptance come from cracks or regions given as ranges of the polar angle, or equivalently of pseudorapidity.

Definition of granularity

Modern electronic detectors are divided in many cells (sensors or readout channels), each one responding with an individual electric signal that indicate the passage of a particle or group of particles through it. As the position of each cell is known, it is possible to extract geometrical information from the collection of signals. The term "granularity" is used to refer to the density of individual cells in a given subdetector. So for a given detector volume, higher granularity means higher number of channels and thus higher spatial resolution in that given volume.

"Barrel" and "end-cap" regions

The different subdetectors are divided in regions, one of them covering the central region (typically $|\eta| < 1.5$) called "barrel" with cylindrical shape, and two complementary sections located

in the ends of the central cylinder or barrel, called "end-caps" ($|\eta| > 1.5$).

Missing transverse energy

In the collisions, the original transverse momentum of the proton-proton system is almost zero (negligible compared to the longitudinal momentum), so conservation of momentum implies that after the collision, the sum of all transverse momenta of the produced particles must be zero. However, not all the particles are visible to the detector, so in a given event, if we call missing transverse energy, E_T^{miss}, the undetected transverse momentum in the event, we have:

$$E_T^{miss} = \left| \sum \mathbf{p_T^{reco}} \right| \qquad (2.9)$$

where the vectorial sum is done over all the reconstructed particles in the event.

2.2.2 Inner detector

The inner detector (ID) is the layer of detectors nearest to the beam axis. It measures the tracks left by charged particles, revealing information about the momentum, charge and type of particle. It is designed to have a very good spatial precision ($\sim \mu$m), and is composed of three parts: the pixel detector (PD), the semiconductor tracker (SCT) and the transition radiation tracker (TRT). The layout of the ID is shown in figure 2.6.
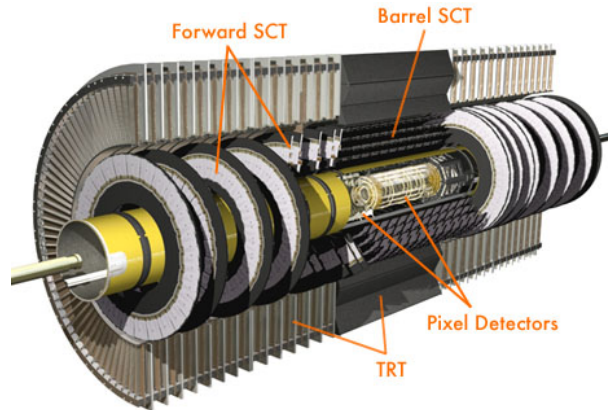
Figure 2.6: Schematic view of the inner detector of ATLAS.

The pixel detector

The pixel detector and the semiconductor tracker use solid state technology to detect the passage of charged particles. They are made of several p-n junctions with reversely biased polarization, that detect the passage of charged particles through the formation of additional electron-hole pairs [32]. As several junctions can be installed next to each other, with a very small size, a spatial resolution of the order of few μm can be achieved (see table 2.3).

The pixel detector is made of 1744 silicon pixel sensors, each one containing 46080 individual channels or "pixels", of 50 μm x 400 μm each. They are arranged in three cylindrical layers in the "barrel" region, the first layer located at a radius of 51 mm from the beam axis, and in the end-cap region, there are 3 disks on each side, thus providing 3 precision measurements or "hits" in the full acceptance. The total number of readout channels is around 80 millions [33]. The high granularity is required in order to have the spatial resolution needed to reconstruct the high number of tracks going out of the IP in the collisions.

The pixel detector is fundamental in the reconstruction of vertices and tracks of charged particles, and in the identification of short lived particles (reconstruction of secondary decay

vertex). The first layer of the pixel detector is called b-layer, as it plays an important role in the identification of short lived b-hadrons.

The semiconductor tracker

The semiconductor tracker is composed of silicon microstrip detectors, which have electrodes segmented in the form of strips or pads [32]. Each silicon microstrip contains 768 readout strips. It has high granularity, although not as high as the pixel detector, with a number of channels of 6.3 millions [29], and a spatial resolution coarser than the pixel detector, although still on the μm scale (see table 2.3). It is divided in 8 layers covering both the barrel and the end-cap region, which provide 4 precision measurements per track. This contributes to the measurement of momentum, impact parameter and vertex position.

The transition radiation tracker

The transition radiation tracker consists of straw drift tubes (ionization detectors), filled with a gas mixture containing xenon. It detects the passage of charged particles through the ionization of the gas, and estimates the position where they passed by measuring the time the ionization electrons take to reach the electrodes [32]. In addition, when charged particles go trough the interface gas - straw tube, they produce transition radiation photons, which in turn ionize more atoms and increase the intensity of the signal. The transition radiation effect is inversely proportional to the mass of the particle, thus measuring the amount of transition radiation allows to discriminate between particles leaving hits in the TRT, typically electrons and pions.

The TRT is made of several layers of straw tubes, giving approximately 30 hits per track. The TRT is not segmented in the longitudinal z directions, it provides information only in the (R-ϕ) plane, with a resolution of 130 μm. The total number of TRT readout channels is approximately 351,000. [29].

Magnet system of the ID

The ID is surrounded by a solenoid magnet which provides a field of 2 T, called central solenoid (CS). It is made of superconducting coils, designed to be as thin as possible to reduce the material in front of the calorimeters. It operates with a nominal current of 7.73 kA and it has to be cooled down to a temperature of 2.5 K [28]. The CS shares a common vacuum / cryogenics vessel (known as cryostat) with the electromagnetic calorimeter.

Track reconstruction in the ID

The trajectory of charged particles (tracks) is reconstructed from the signals produced by the ID ("hits"). The first step is to associate spatial coordinates to every hit, this is done by using the knowledge of the position of every channel (detector conditions). Once the information is in the form of spatial points, algorithms are implemented to identify and fit tracks from the spatial points. In general these algorithms start by looking at track patterns in the pixel and the first layer of SCT, and then fits are performed including all the SCT. At these stage, quality cuts are applied, for example, maximum number of "holes" (sensors crossed by the track which have no signal associated). The selected tracks are extended to include TRT information, and new fits are performed including all levels of the ID. After the track candidates have been identified, dedicated algorithms run to reconstruct primary and secondary vertices [27].

The track finding strategy and track fitting procedure have different implementations, which take into account the material traversed by the particles. In particular, to take into account the electron bremsstrahlung, two tools are available, the dynamic noise adjustment (DNA) and gaussian sum filters (GSF).

The magnetic field present in the ID allows to measure the momentum and the sign of the charged particles going through it, using the curvature of the trajectory. This trajectory has a helix shape, with axis parallel to the z axis, and can be parametrized using the "perigee" parameters [34]:

- z_0: z coordinate of the point of the trajectory closer to the z axis (this point is called "perigee" of the trajectory). z_0 is also called longitudinal impact parameter.

- d_0: distance of the perigee to the z axis. This value is also called the transverse impact parameter.

- ϕ_0: azimuth angle of the perigee.

- θ_t: polar angle of the track.

- q/p_T: charge divided by the magnitude of the transverse momentum of the track.

The track fitting allows to measure these 5 parameters, using the ID hits and the known magnitude of the magnetic field. The precision that can be obtained is affected by the multiple scattering of particles in the ID (for low p_T), and by the intrinsic resolution of the detector for high p_T (granularity). The resolution for the track parameter "X" can be written as a function of p_T in the following way [27]:

$$\sigma_X(p_T) = c_X \oplus d_X/p_T \qquad (2.10)$$

where the numbers c_X and d_X are independent of p_T, and describe the intrinsic resolution and the multiple scattering effects respectively. The operation "$\oplus$" is defined as:

$$a \oplus b \equiv \sqrt{a^2 + b^2} \qquad (2.11)$$

The constants c_X and d_X are functions of pseudorapidity. Notice that the relative resolution for the parameter q/p_T is given by:

$$\sigma_{q/p_T}^{rel} = \frac{1}{q/p_T}\sigma_{q/p_T} = \frac{1}{q}\sqrt{c_{q/p_T}^2 p_T^2 + d_{q/p_T}^2} \qquad (2.12)$$

which increases with p_T as expected (for high p_T, the track has less curvature, so it is more difficult to measure the p_T).

The parameters that define the resolution have been estimated using simulated events and a precise modeling of the detector response [27]. As an example, in figure 2.7 we show the resolution obtained for the transverse impact parameter and q/p_T for charged pions and muons respectively, as functions of η and for different values of p_T. We can see that the precision of the transverse impact parameter improves with momentum, while the precision on q/p_T decreases.

The reconstruction of tracks is affected by the material traversed by the particles in the ID. In figure 2.8a we show the amount of material traversed by particles in the ID, as a function of η. The distance is measured in units of radiation length X_0, that will be defined in chapter 3. The reconstruction of pion tracks is affected by hadronic interactions, while the reconstruction of electrons is affected by bremsstrahlung. This can be seen in figure 2.8b, where we compare the reconstruction efficiency for muons, pions and electrons of $p_T = 5$ GeV [27].

2.2.3 Electromagnetic calorimeter

The electromagnetic calorimeter (ECAL) measures the energy of particles that interact electromagnetically (electrons, positrons and photons). Its working principle is the production of an electromagnetic shower, which is the product of consecutive bremsstrahlung and pair production processes, that occur in the "absorbing" material (lead). The large volume of electrons
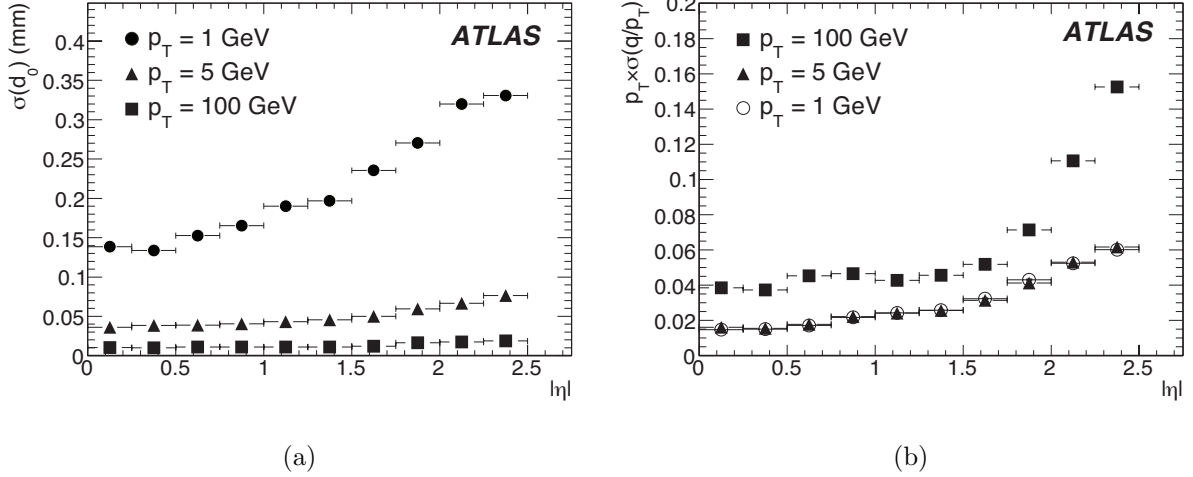
(a)   (b)

Figure 2.7: Examples of expected resolution for track parameters measurement in the ID. a) Transverse impact parameter for charged pions, b) q/p_T for muons (relative resolution) [27].

(a)   (b)
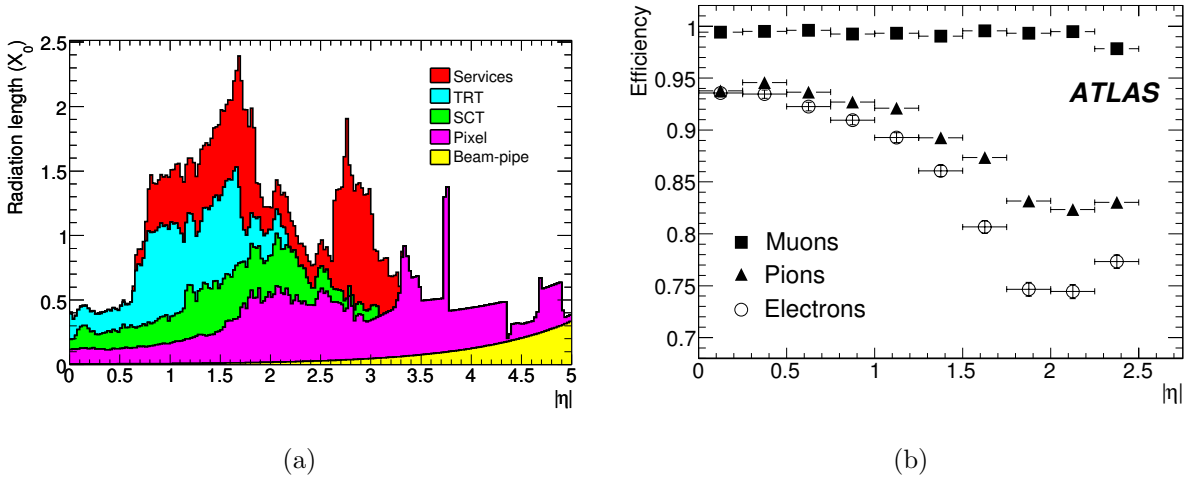
Figure 2.8: Effect of the ID material in the efficiency of track reconstruction. a) Amount of material traversed by a particle in the ID, given in units of radiation length X_0. (b) Track reconstruction efficiency for muons, pions and electrons with $p_T = 5$ GeV [27].

produced in the shower ionize the "active" or "sampling" material (liquid argon) thus producing electric signals that are collected by copper electrodes. The calorimeter depth guarantees that the shower is entirely contained on it. The electrodes of the electromagnetic calorimeter are accordion shaped, providing a full uniform azimuthal coverage [29].

The ECAL is divided in the barrel part (EMB), and the end-cap part (EMEC). The cells in the ECAL are designed to be projective in η, meaning that they follow radial lines of constant η and ϕ coordinates. They provide separate energy deposits that allow a better energy measurement and provide particle identification based on shower shape. The readout is also split in the radial direction, in three layers known as "samplings". Each sampling has a different (η, ϕ) granularity and thickness. In the central region (barrel and part of the end-caps) another layer of cells, known as "presampler" is installed, used to have an additional energy measurement that allows to correct for the energy loss in the material traversed by the particles upstream to the ECAL.

The characteristics of the ECAL and its performances in terms of electron energy measurement, reconstruction and identification are detailed in chapter 3. The granularity of the barrel middle layer is shown in table 2.3.

2.2.4 Hadronic calorimeter

Similarly to the electromagnetic calorimeter, the hadronic calorimeter (HCAL) measures the energy of particles that interact via the strong interaction (mesons and baryons), by the production of hadronic showers. The formation of hadronic shower is based on several processes, among them strong decays, weak decays and electromagnetic showers. As in the case of the electromagnetic calorimeter, the measurement is done via the interaction of the charged particles produced, i.e. scintillation (excitation of atoms and emission of light) and ionization. The shower is entirely contained on the calorimeter volume.

The HCAL uses two different technologies: tile scintillators in the barrel and liquid argon (similar to the ECAL) in the end-cap regions. In the barrel part, the absorbing material is iron, and the energy deposited is detected from the light produced in plastic scintillation tiles (active material), which is directed to optical fibers and converted in electric signals by photomultipliers.

The HCAL has a coarser granularity than the ECAL, but enough to satisfy the physics requirements for jet reconstruction and missing transverse energy measurements. It is subdivided in the barrel part (HB), the extended barrel part (HEB), the end-caps (HEC), and the forward calorimeter (FCAL). All the parts of the two calorimeter which have as active material liquid argon are known collectively as "liquid argon calorimeter" (LAr). The granularity of the barrel is shown in table 2.3.

In figure 2.9 we show the spatial organization and coverage of the different parts of the ATLAS two calorimeters.

| (a)   (b) |
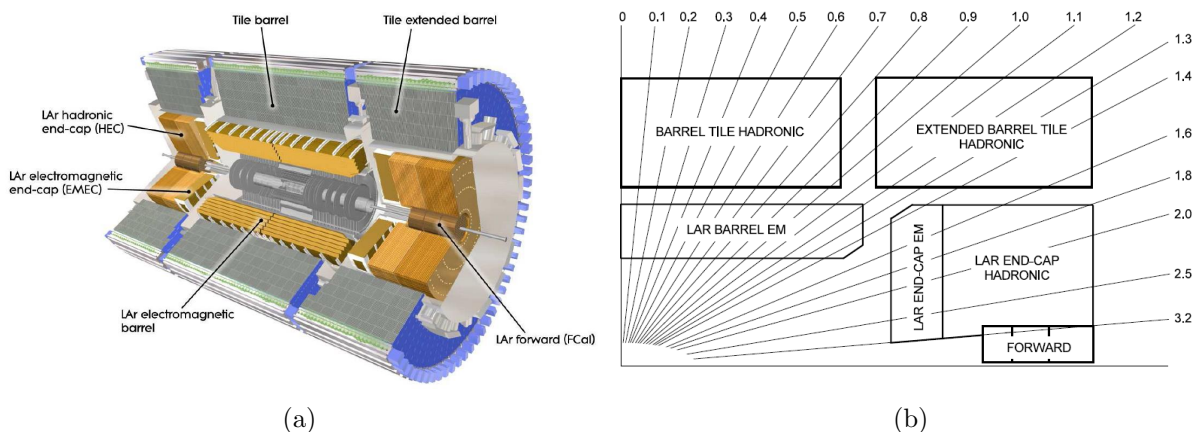
Figure 2.9: (a) Spatial organization of the ATLAS calorimeters. (b) Coverage in pseudorapidity of the different parts of the calorimeters.

2.2.5 Muon spectrometer

The muon spectrometer makes additional measurements of the tracks left by muons. It is a big arrangement of ionization detectors and magnets, designed to provide the tracking resolution to match the ID measurement and allow the identification of muons. It is is composed of the following parts:

- Precision detectors: monitored drift tubes (MDT) and cathode strip chambers (CSC), both ionization gaseous detectors, designed to provide a precise measurement of the η coordinate of the hits left by muons. The MDT are proportional drift chambers and the CSC are multiwire proportional chambers [32]. The MDT and the CSC are grouped together in three cylindrical layers at different separations from the interaction region. They are arranged in a geometry such that most of the particles traverse the three layers, thus providing three precise position measurements.

- Trigger chambers: resistive plate chambers (RPC) and thin gap chambers (TGC), fast response gaseous ionization detectors, designed to provide trigger information (fast signal indicating hits) and also to measure the ϕ coordinate of the muon tracks, complementing the measurements made by the MDT and CSC. They are located also in layers, next to the precision chambers.

- The magnet system, composed of a barrel toroid and two end-cap toroids. They provide a field of variable intensity of up to 4 T, that bends the track of charged particles traversing the chambers.

In figure 2.10 we present the layout of the different muon chambers in ATLAS. In figure 2.11 a schematic view of the toroid magnets is shown, together with the solenoid. The spatial resolution of the MS is given in table 2.3.
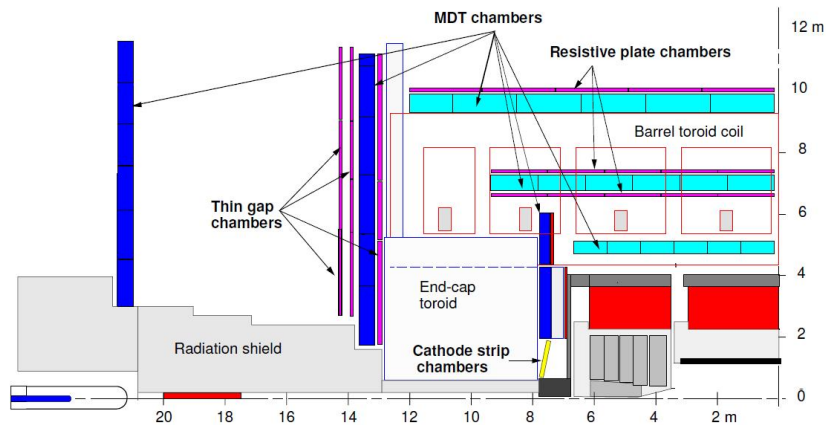
Figure 2.10: Schematic view of the ATLAS muon spectrometer different parts.
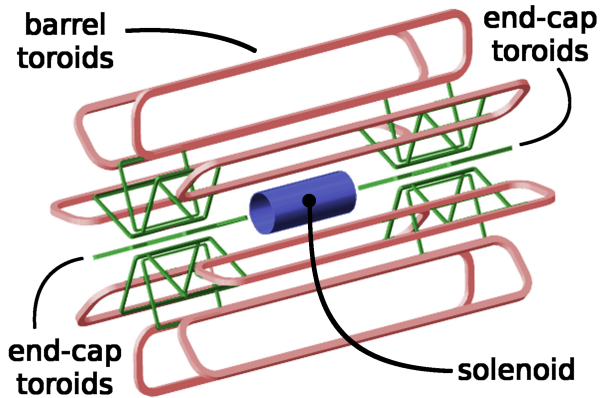
Figure 2.11: Schematic view of the ATLAS magnets.

In table 2.3 we present a summary of the detector characteristics, listing the spatial coverage, number of readout channels and intrinsic resolution in the spatial measurements (roughly the size of the individual channels). In the case of the calorimeters, the typical cell size is given (barrel part for both ECAL and HCAL, and middle sampling for ECAL). The granularity of the calorimeters is more complex, it will be detailed for the electromagnetic part in chapter 3.

2.2.6 Trigger system

In the LHC, bunches of protons collide every 50 ns (setup during the first run period, 2010-2012), i.e. with a frequency of 20 MHz (notice that these values are different from the design

Subdetector	Spatial coverage	Number of channels	Spatial resolution
Pixel detector	$|\eta| < 2.5$	$\sim 80.4 \times 10^6$	10 μm (R, ϕ), 115 μm (z)
SCT	$|\eta| < 2.5$	$\sim 6.3 \times 10^6$	17 μm (R, ϕ), 580 μm (z)
TRT	$|\eta| < 2.0$	~ 351000	130 μm (R, ϕ)
ECAL	$|\eta| < 3.2$	~ 190000	0.025×0.025 ($\Delta\eta \times \Delta\phi$)
HCAL	$|\eta| < 4.9$	~ 18000	0.1×0.1 ($\Delta\eta \times \Delta\phi$)
Muon system	$|\eta| < 2.7$	~ 1000000	100 μm (η, ϕ)

Table 2.3: Summary of ATLAS detector characteristics. Typical values are shown for the calorimeters (barrel region, and second sampling in the case of the ECAL).

parameters shown in table 2.1). The total theoretical cross-section in pp collisions is of the order of 100 mb, so with an instantaneous luminosity of 10^{33}cm^{-2}s^{-1} the expected rate of interactions is 10^8 events per second. The ATLAS trigger system performs the difficult task of selecting interesting events, reducing the event rate to approximately 300 events per second, which are stored for offline analysis. The ATLAS trigger system is structured in three levels, that work in parallel to the readout system (ROS), performing online analysis of signals in order to select events. A schematic view of the trigger system is shown in figure 2.12.
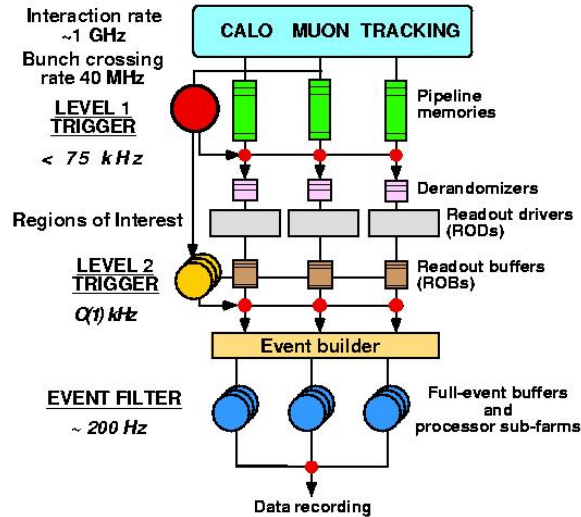
Figure 2.12: Schematic view of the ATLAS trigger system.

The level 1 trigger system (LVL1) processes electronic signals collected in a subset of ATLAS subdetectors (calorimeters and muon spectrometer) with lower granularity and performs event selection based on the recognition of basic physics signatures in the energy deposits. The LVL1 is implemented using custom made electronics, and has a maximum latency of 2.5 μs. The LVL1 provides to the next trigger level the geometrical positions of detected signals, called regions of interest (ROI). The events selected by the LVL1 are read out from the front end electronics, into the readout drivers (ROD) and then into the readout buffers (ROB), which are the starting point of the data acquisition system (DAQ). The calorimeter part of the LVL1 is explained in section 4.1.1.

Events passing LVL1 selection are then processed by the trigger level 2 (LVL2), which has access to all the subdetectors with full granularity. It does online reconstruction of events (online meaning that the data processing is done in real time, in parallel to the data taking), reconstructing and identifying physics objects (electrons, photons, jets), based on the data

retrieved from the ROI. The LVL2 is software based, and has a latency of 10 ms.

The last trigger level (Event Filter) uses full detector information together with the latest available calibration and alignment parameters to reconstruct and identify objects. The EF performs the final selection of events that are recorded, with a latency of a few seconds.

The last two stages of trigger are called High level trigger (HLT). These last two stages use algorithms similar to the ones used by the offline reconstruction (described in section 2.3), but with changes and simplifications due to the limitations on the processing time.

2.3   Generalities on event reconstruction in ATLAS

An interesting event in ATLAS consists of a hard interaction between a parton from one proton in one of the beams, with a parton from a proton in the other beam. This is accompanied by the interaction among the other partons (known as underlying event), and the interactions between the other protons in the bunchs (these extra interactions are known as "pile-up"). The product of the collision is a high number of particles, that have to be identified and their properties measured as precisely as possible in order to understand the physics of the event.

In this section we describe briefly the process of offline event reconstruction in ATLAS, offline meaning that the processing is done on events that has been selected and stored by the trigger and DAQ systems. The event reconstruction begins with the processing of all the electrical signals stored during the event. Here, algorithms are applied in order to associate hits together and produce the following objects:

- Tracks left by charged particles in the ID. This process was explained in section 2.2.2.

- Electromagnetic (EM) clusters, built from signals left in the ECAL. The reconstruction of electromagnetic clusters is described in chapter 3.

- Hadronic clusters, built from signals left in the HCAL.

- Muon tracks, built from hits found in the muon spectrometer.

This process is called reconstruction. Next, the offline algorithms need to combine these objects according to their properties in order to understand which kind of particle or set of particles originate them. This process is called "identification". The identification is applied to particles that are stable within the detector volume, or within a fraction of it. The identification of stable objects is summarized in the following paragraphs.

Electrons   An electron candidate is an EM cluster matched to a track in the ID. Electron identification is described in chapter 3.

Photons   A photon candidate is an EM cluster without a matching track ("unconverted photon"), or an EM cluster with matching track, when the track does not cover the whole ID ("converted photon", i.e. photon that produced a e^+e^- pair within the ID volume). It is important to notice that the photons are not absorbed by the silicon detectors, nor they ionize the gas in the TRT, because at the high energies typical of the photons produced in the collisions the photon cross-section for photoelectric effect or Compton scattering is negligible, thus only pair production is observed.

Jets   Jets are defined as groups of particles possessing a large transverse energy, and contained within a conical region of radius R between 0.4 and 0.7. Jets are originated from the fragmentation of partons, so they are composed of stable hadrons (pions, protons, neutrons) and the decay products of unstable ones (electrons, photons, etc). Jets are identified by HCAL clusters matched to EM clusters and tracks.

Muons Tracks in the ID matched to tracks in the muon spectrometer. As the energy losses by bremsstrahlung are inversely proportional to the mass of the moving particle, the muons leave a very small fraction of their energy in the calorimeters.

Neutrinos The neutrinos leave no trace in the detector, so they are identified looking for missing transverse energy (E_T^{miss}).

τ leptons and b, c jets τ leptons and the quarks b and c have lifetimes that allow them to travel some measurable distance within the ID, so they can be identified using secondary vertex information combined with other signatures (the quarks hadronize to form b and c mesons).

In addition, unstable particles are identified by their decay products. An example of this is will be given in chapter 5, where Z bosons are identified when they decay into electron and positron. Figure 2.13 shows a transverse plane cut of the ATLAS detector, showing the different detector layers and the interaction of different kinds of particles with them, illustrating the reconstruction and identification.
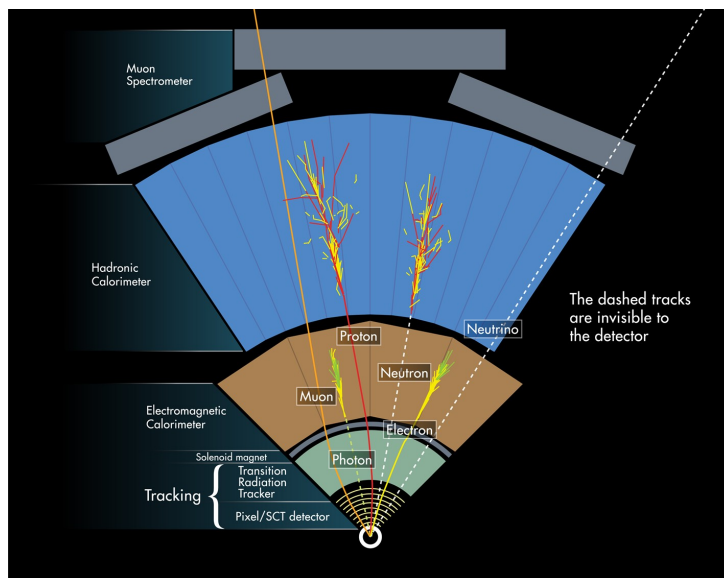
Figure 2.13: Transverse cut of the ATLAS detector, showing the different layers and the interaction of different kinds of particles with them.

2.3.1 Data formats and streams

The ATLAS raw data for events selected by the trigger system is stored for offline analysis. In the last stage of the trigger (EF), the events are sorted according to the trigger criteria they have passed. This sorting is called "streaming" and the different output channels are called "streams". For example, events that have triggered due to activity in the ECAL, with the subsequent online reconstruction of an electron or photon by the HLT, are stored in a different stream than those events which have triggered due to activity in the muon spectrometer. The following streams are defined:

- Egamma stream: events with important activity in the ECAL.

- Muon stream: events with important activity in the muon spectrometer.

- JetTauEtMiss etream: Events with important activity in the HCAL, or detected E_T^{miss}.

- CosmicCalo: events that are triggered when there are no protons at the IP (empty bunch-crossings).

The events can be stored in more than one stream, but the streams are defined in order to avoid too much overlap. In addition, other special streams are defined, called "Calibration" (containing important information for calibration purposes) and "Express", which contains selected events and information useful for detector monitoring [28].

The streamed data are stored as raw bytes, which are then processed in several stages. Each step of processing produces a new data format, with different levels of information:

- Byte-stream: raw data in form of bytes collected in the different streams.

- RDO (Raw Data Object): C++ object representation of the byte stream information.

- ESD (Event Summary Data): contains all details of the reconstruction algorithms output.

- AOD (Analysis Object Data): contains a summary of the reconstructed events, with enough information to perform physics analysis.

- DPD (Derived Physics Data): data derived from some of the formats above, with some event selection and less information per event. A particular example is the D3PD, derived from the AOD, which uses a format directly accessible with the ROOT software (ROOT ntuple) [35].

Chapter 3

The ATLAS electromagnetic calorimeter and electron performances

In this chapter we review the physics and performance of the ATLAS electromagnetic calorimeter. We begin with a revision of the physics of electromagnetic calorimeters, including the interaction of electrons and photons with matter and the electromagnetic showers. Then we describe in detail the ATLAS electromagnetic calorimeter, its construction and its performance, starting from the readout up to the reconstruction and identification of electrons. The chapter ends with a brief explanation of the calorimeter in-situ energy calibration and the efficiency measurements done using collision data.

3.1   Interaction of electrons and photons with matter

Electrons are detected through electromagnetic interactions when they traverse a given medium. These interactions make the electrons lose some part of their energy, the main processes involved are ionization and excitation of the atoms of the material, and bremsstrahlung. The energy loss due to ionization and excitation is described by the following equation [32]:

$$
\begin{aligned}
\frac{dE}{dx} = & -4\pi N_A r_e^2 m_e c^2 \rho_m \frac{Z_m}{A_m} \frac{1}{\beta^2} \left[\ln\left(\frac{\gamma m_e c^2 \beta \sqrt{\gamma-1}}{\sqrt{2} I_m} \right) + \frac{1}{2}(1-\beta^2) \right. \\
& \left. - \frac{2\gamma-1}{2\gamma^2} \ln(2) + \frac{1}{16}\left(\frac{\gamma-1}{\gamma}\right)^2 \right]
\end{aligned}
\tag{3.1}
$$

Equation (3.1) gives the rate of energy loss when the electrons traverse the distance dx. This loss depends on the absorbing material through the following parameters: Z_m and A_m, atomic number and weight number, mean excitation energy I_m, and the density ρ_m. Other constants involved are the Avogadro number (N_A), the classical electron radius (r_e), the electron mass (m_e), and the speed of light in vacuum (c). The β and γ factors are defined as $\beta = \frac{v}{c}$ and $\gamma = \frac{1}{\sqrt{1-\beta^2}}$, where v is the velocity of the electron.

Equation (3.1) is a corrected version of the Bethe equation [32], which takes into account the smallness of the electron mass and other effects. In order to gain insight about the energy dependence of the loss, we evaluate it using lead as material, and apply the following considerations:

- Use the approximation $I \approx 16 Z^{0.9}$ (eV) [32] to evaluate the ionization potential.

- Assume that we deal with ultrarelativistic electrons, as is the case in the ATLAS experiment, so we have $\beta \sim 1$ and $\gamma >> 1$.

By doing so, after simplifying and neglecting small terms, we obtain the following approximation for the relative rate of energy loss:

$$\frac{1}{E}\frac{dE}{dx} \approx -(18.90 + 1.40 \ln E)\frac{1}{E} \times 10^{-3} \tag{3.2}$$

where the energy should be given in GeV, and the resulting relative rate is in cm^{-1}. This equation shows that for energetic electrons, the relative energy loss due to ionization and excitation is low, of the order of 10^{-3}, and decreases with energy, as the negative power of E prevails over the logarithmic rise. In figure 3.1 we show the relative loss for lead, obtained from the complete expression (3.1) without simplification (absolute value). The trend observed in the plot proves what can be seen from the simplified expression (3.2). The ionization energy loss for positrons can be described with an equation slightly different to (3.1), which have the same approximate behavior shown before. In what follows, we refer to electrons and positrons both as "electrons", as it is commonly done in high energy physics.
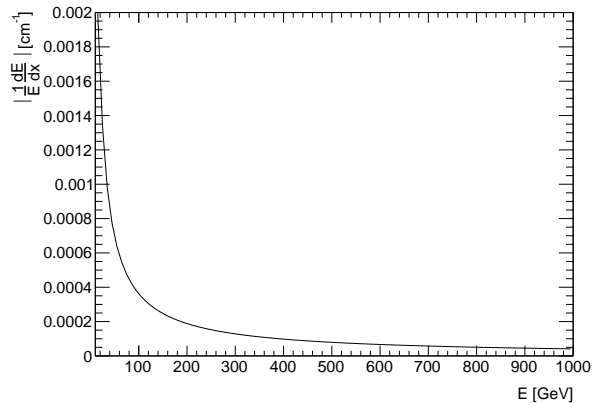
Figure 3.1: Relative energy loss by ionization and excitation, for ultrarelativistic electrons traversing lead.

The main energy loss for relativistic electrons when traversing matter comes from bremsstrahlung, i.e. electrons are decelerated in the electric field of the atomic nuclei and emit photons. This energy loss can be described approximately by the following equation [32]:

$$\frac{dE}{dx} \approx -4\alpha N_A \rho_m \frac{Z_m^2}{A_m} r_e^2 E \ln\left(\frac{183}{Z_m^{1/3}}\right) \tag{3.3}$$

where α is the fine structure constant ($\alpha = e^2/(4\pi\epsilon_0\hbar c)$). Notice the linear dependence on energy, as opposed to the weak logarithmic dependence of the ionization and excitation loss. The bremsstrahlung loss is inversely proportional to the square of the mass of the incident particle, in equation (3.3) this dependence is hidden in the constant r_e.

In order to compare with the ionization and excitation loss, we perform the same exercise, taking lead as material. We obtain:

$$\frac{1}{E}\frac{dE}{dx} \approx -1.94 \ cm^{-1} \tag{3.4}$$

So the electrons will lose approximately half their original energy per unit length traversed of the material. Equation (3.3) can be written as:

$$\frac{dE}{dx} = -\frac{E}{X_0}\rho_m \tag{3.5}$$

which defines the "radiation length" X_0 [g/cm^2], characteristic of the material, which following equation (3.3) can be approximated by:

$$X_0 \approx \frac{A_m}{4\alpha N_A Z_m^2 r_e^2 \ln(183/Z^{1/3})} \tag{3.6}$$

Equations (3.2) shows that the energy losses due to ionization and excitation grow as $\ln(E)$, while in equation (3.3) we can see that the energy loss due to bremsstrahlung grows linearly with energy. The energy such that the two losses are equal is called the critical energy, and is denoted by E_c. Beyond this energy, bremsstrahlung losses dominate. The critical energy for electrons in solids can be approximated by [32]:

$$E_c = \frac{610}{Z + 1.24}[\text{MeV}] \tag{3.7}$$

For example, for lead, $E_c \approx 7.32$ MeV.

We turn our attention now to photons. They are detected via their electromagnetic interaction in the medium, this interaction ends with the production of charged particles (electrons), which are subsequently detected. The interactions of photons are different from the ionization process or charged particles, because photons can be completely absorbed (as in the photoelectric effect or pair production), or only scattered (Compton effect). Photon beams are attenuated in matter according to a exponential law [32]:

$$I = I_0 e^{-\mu x} \tag{3.8}$$

where the attenuation coefficient μ is proportional to the total interaction cross-section. The interaction cross-section depends on the energy of the photons. However, for energies above 1 GeV, the cross-section for pair production in the field of the atomic nuclei dominates, and have the following energy independent value:

$$\sigma_{pair} = 4\alpha r_e^2 Z_m^2 \left[\frac{7}{9}\ln\left(\frac{183}{Z_m^{1/3}}\right) - \frac{1}{54} \right] \tag{3.9}$$

If we evaluate this expression for lead, we obtain $\sigma_{pair} = 0.448 \cdot 10^{-22}$ cm^2/atom $= 44.8$ b/atom. In figure 3.2 we show the total experimental and theoretical cross-section of photons interacting with lead [9].

Using the approximation (3.6), equation (3.9) can be written as:

$$\sigma_{pair} \approx \frac{1}{X_0}\frac{7A_m}{9N_A} \tag{3.10}$$

So, for a given material, the attenuation of a photon beam by means of pair production is inversely proportional to X_0, in analogy to the energy loss of electrons by bremsstrahlung.

The energy from which pair production dominates depends on the material. In figure 3.3 the energy ranges for photoelectric effect, Compton scattering and pair production are shown as a function of the atomic number of the absorbing material [32]. We can see that for energies above ~ 100 MeV, pair production dominates for most materials.
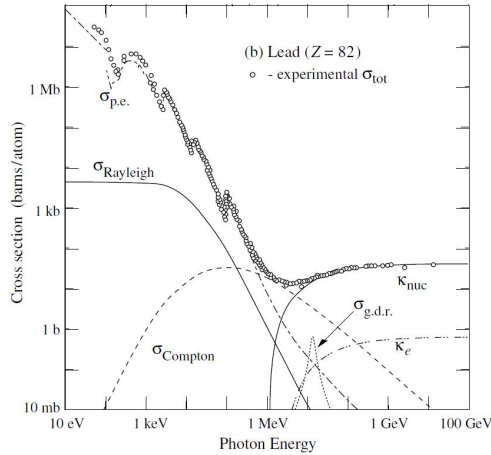
Figure 3.2: Photon interaction cross-section as a function of energy in lead, showing the contributions of different processes: $\sigma_{p.e.}$ = Atomic photo-electric effect; $\sigma_{Rayleigh}$ = Rayleigh scattering (atom neither ionized nor excited); $\sigma_{Compton}$ = (Compton scattering); κ_{nuc} = Pair production, nuclear field; κ_e = Pair production, electron field; $\sigma_{g.d.r}$ = Photonuclear absorption (nuclear absorption, usually followed by emission of a neutron or other particle) [9]. Notice the dominance of pair production for $E > 1$ GeV.
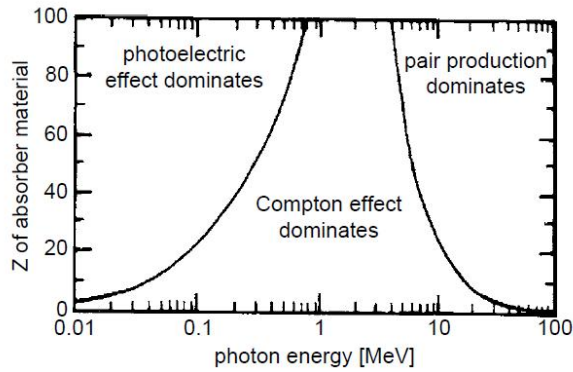

Figure 3.3: Energy ranges in which pair production, Compton scattering and photoelectric effect dominate, as a function of the photon energy and the absorber atomic number Z [32].

3.1.1 Electromagnetic shower

As was discussed earlier, electrons and photons with energies above ~ 100 MeV interact mainly by bremsstrahlung and pair production, respectively. When high energetic photons or electrons enter a given media, a physics phenomenon called "electromagnetic shower" takes place. It consists of the succession of several bremsstrahlung and pair production processes, that originate a shower or cascade of electrons and photons. This process is the principle of detection of particles and energy measurement in electromagnetic calorimeters.

A simple model of electromagnetic showers can be made in order to understand its main characteristics. Assume that in one radiation length each electron undergoes bremsstrahlung, resulting in an electron and a photon each with half energy of the original electron. Similarly, in a radiation length, a photon undergoes pair production, the resulting electron and positron having each one half the energy of the original photon. This process continues until the produced electrons and photons have energies under the critical one (E_c), so electrons start losing energy by ionization and excitation, and photons by Compton scattering or photoelectric effect. Figure 3.4 shows a schematic view of the process in the case that it starts from an electron.

If we call E_0 the initial energy of the particle entering the absorbing material, and we measure the distance in units of radiation length, after the layer defined by $x = tX_0$, the particles in the shower will have the energy:
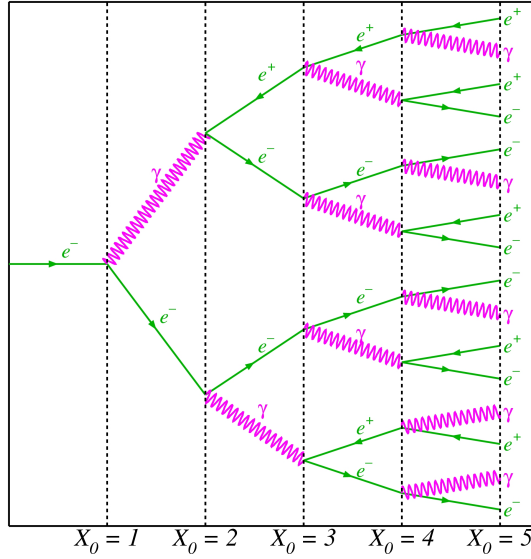
Figure 3.4: Schematic of an electromagnetic shower starting with an electron.

$$E(n) = E_0 \, 2^{-t} \tag{3.11}$$

The shower maximum (maximum of particles) occurs when $E(t_{max}) = E_c$, so

$$t_{max} = \frac{1}{\ln 2} \ln\left(\frac{E_0}{E_c}\right) \tag{3.12}$$

and the number of particles in the maximum is:

$$N(t_{max}) = 2^{-t_{max}} = \frac{E_0}{E_c} \tag{3.13}$$

Equations (3.12) and (3.13) show that the position of the shower maximum increases as the logarithm of the initial energy, and the number of particles in the shower maximum is proportional to the initial energy. In practice, the development of electromagnetic showers is more complicated. Figure 3.5 shows the energy deposited per unit distance (longitudinal development of the shower), when electrons of different energies enter a block of copper. The curves were obtained using simulations [36].

In order to use the electromagnetic shower as a particle detection method, an electronic signal needs to be obtained from it. In practice this is done in two ways. In homogeneous calorimeters, the soft particles produced in the shower will end up exciting atoms of the material, and this excitation is detected using the scintillation light or other methods. In contrast, in sampling calorimeters, a second type of material is inserted in the way of the shower, and the detection is done through the ionization and excitation of the atoms of this new material.

3.2 Performance of the ATLAS ECAL

As was mentioned earlier, the ATLAS electromagnetic calorimeter is a sampling calorimeter, which uses liquid argon as active material, and lead as absorbing material. The liquid argon was chosen due to its radiation hardness and fast response. The layout of absorbing, sampling material and electrodes in the accordion geometry is shown schematically in figure 3.6. This layout allows for a full uniform azimuthal coverage without cracks. The calorimeter thickness is larger than 22 X_0 in the barrel and 24 X_0 in the end-caps [29].
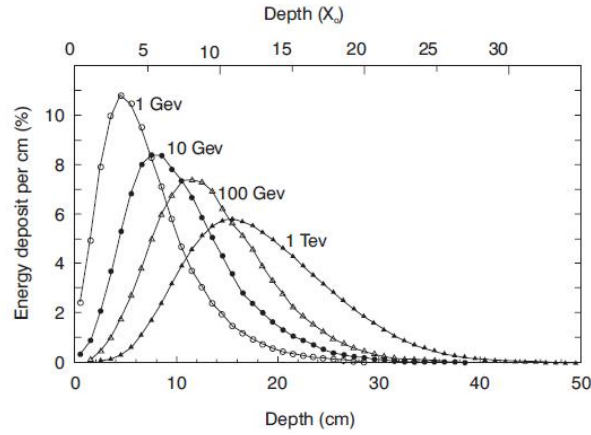
Figure 3.5: Longitudinal development of an electromagnetic shower started by electrons of different energies traversing a block of copper [36].
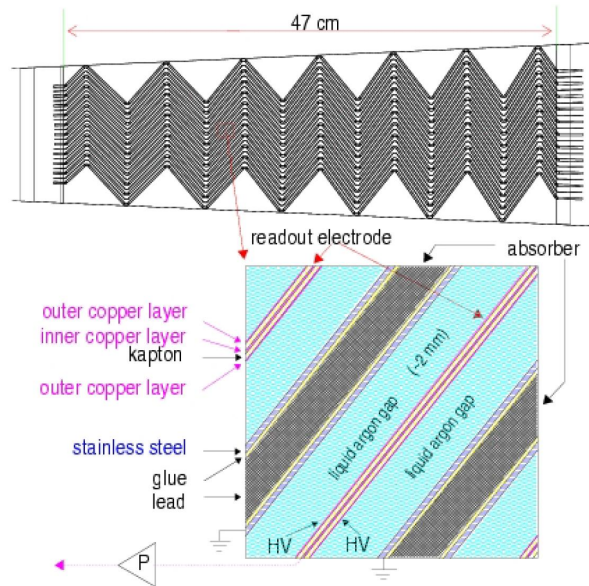
Figure 3.6: Schematic view of the ATLAS electromagnetic calorimeter geometry. The accordion geometry arrangement of the lead, liquid argon and electrodes in layers is shown in detail.

The ECAL granularity varies according to the sampling (layer of cells) and the region of the calorimeter (barrel or end-caps). In figure 3.7 we show a scheme of the cell arrangement and size in the barrel part of the calorimeter. In table 3.1 the cell granularity in each part of the calorimeter is summarized, along with the pseudorapidity coverage [29].

Electrons and photons entering the calorimeter start the development of a shower, as explained in section 3.1. The calorimeter is designed to contain all the shower in its volume, in order to measure accurately the energy of the original particle. The shower spans across many cells of the calorimeter, the collection of cells containing signals from a shower is called "cluster".

The reconstruction (i.e., measurement of energy and position) of an electromagnetic cluster is performed in several stages. First, the signals collected in the cells are processed by the readout system (ROS) of the calorimeter, and stored for further offline analysis if the event is selected by the trigger system. The "raw" data stored is then processed offline by reconstruction algorithms, which perform calibration and correction of the energy values, search for fixed-size clusters using "sliding window" methods, and compute final energy and position for the cluster. This process is explained in the following sections.

Figure 3.7: Granularity of a barrel sector of the electromagnetic calorimeter. The size of the cells and the thickness is shown for the three samplings.

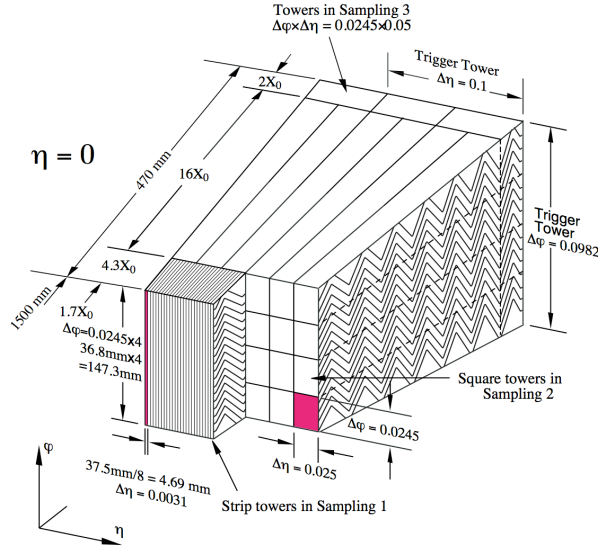|	Subdetector	Spatial coverage	Granularity ($\Delta\eta \times \Delta\phi$)
	Presampler	$|\eta| < 1.52$	0.025×0.1
Barrel	Sampling 1	$|\eta| < 1.475$	0.003×0.1
(EMB)	Sampling 2	$|\eta| < 1.475$	0.025×0.025
	Sampling 3	$|\eta| < 1.475$	0.05×0.025
	Presampler	$1.5 < |\eta| < 1.8$	0.025×0.1
Endcap	Sampling 1	$1.375 < |\eta| < 3.2$	$0.025 - 0.1 \times 0.1$
(EMEC)	Sampling 2	$1.375 < |\eta| < 3.2$	$0.025 - 0.1 \times 0.1$
	Sampling 3	$1.5 < |\eta| < 2.5$	0.05×0.025

Table 3.1: Detailed granularity and pseudorapidity coverage of the ATLAS ECAL.

3.2.1 ECAL readout system

The LAr calorimeter (ECAL, HEC, and FCAL) has an uniform readout architecture, whose block diagram is shown in figure 3.8 [37]. The electric signals produced in the cells are processed by electronic boards called "front end boards" (FEB), which are mounted directly on the detector cryostat. Each of the 1524 FEBs processes the signal from up to 128 channels. The original triangular-shaped pulse produced in the electrodes is first amplified by a preamplifier array. The output of the preamplifier is then shaped and amplified again, splitting it into three gain scales (1-10-100). The signal is then sampled and stored during the LVL1 latency (up to 25 ns). When a positive LVL1 decision arrives, the signal is digitized in a 12 bits analog to digital converter (ADC), and the data sent via an optical link to the readout drivers electronic boards (ROD) [38].

The RODs are installed in a radiation free environment next to the detector cavern. Each of the 192 RODs receives the digitized raw data from 8 FEBs. The main task of the RODs is the digital filtering of the cell pulse and the online calculation of the energy, time and quality of the signal. Usually 5 samples are received per signal pulse, and an Optimal Filtering algorithm is used to extract cell energies, time, and quality information. The energy is computed as a weighted sum of the samples s_i:
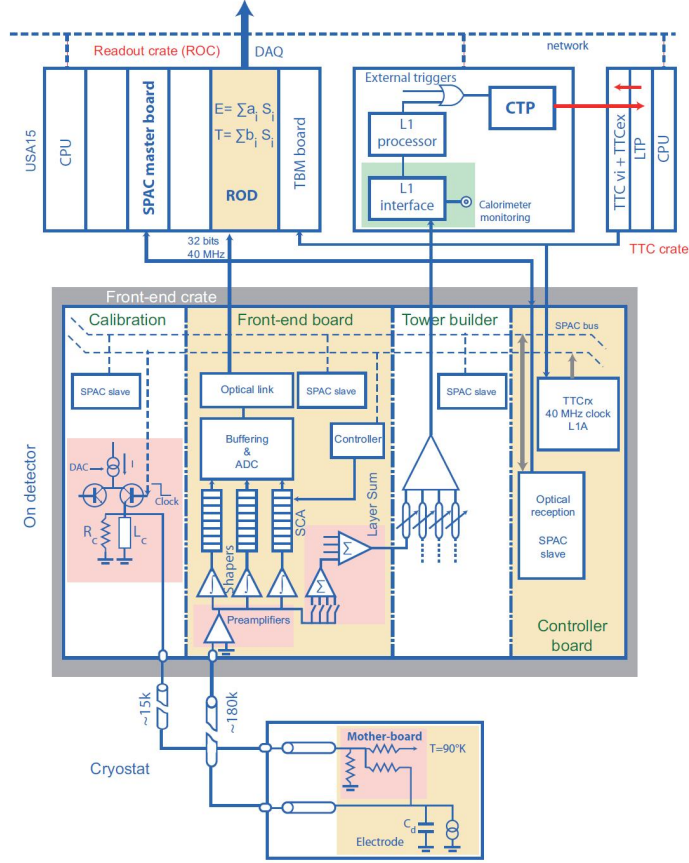
Figure 3.8: Block diagram of the LAr readout system [37].

$$E = k \sum_{i=1}^{N} [a_i(s_i - ped)] \tag{3.14}$$

where a_i are the optimal filtering weights, which are estimated in an optimization procedure that reduces the noise contribution to a minimum, and "ped" is a pedestal value. The factor k converts the ADC count values into MeV, and is determined experimentally for each cell, using calibration studies [38].

The information of the cell pulse is further processed by transition modules, and then sent through another optical link to the software based Data Acquisition System (DAQ). There, the signals are read out by the HLT algorithms if needed. If the event is selected by the trigger system, all the detector data is stored, including all the cells signals from the ECAL.

3.2.2 EM cluster reconstruction

The information stored for every event is processed offline by the ATLAS software. The "sliding window" algorithm is used in order to reconstruct clusters in the EM calorimeter. This algorithm works as follows [39]:

- The cell energies are added together across the calorimeter layers, to form a grid of longitudinal "towers". The size of the towers is (0.025×0.025) in $(\Delta\eta, \Delta\phi)$.

- A window of (5×5) towers ("sliding window") is moved across the elements of the tower grid. If the total transverse energy of the window is above 3 GeV, a "precluster" or "seed" is defined.

- The precluster center is computed, doing an energy weighted average of the η and ϕ coordinates of the cells inside a window of (3×3) towers. This window is defined around the tower at the center of the sliding window.

- Then a cluster is formed around the seed. This is done adding first all cells in the middle sampling within a window of (3×7) around the precluster center.

- Next, a new cluster center is computed using the new added cells (middle sampling). This new center is used as reference to add cells from the first and third sampling.

- Another center is computed using the cells from the first sampling, and used as reference to add cells from the presampler.

The cluster size has been optimized according to the particle type that is being hypothesized and the cluster location. The cluster should be large enough to contain most of the energy deposited, but not too large in order to avoid the inclusion of noise. In the case of electrons, for the middle layer the size is (3×7) in the barrel and (5×5) in the end-caps. The larger size in the barrel in the ϕ direction is needed because the magnetic field of the ID bends the electron trajectory increasing the bremsstrahlung and the shower size in ϕ. In the end-caps, the effect of the magnetic field is smaller, so the size in the ϕ direction is the same than in the η direction (more cells are included in the end-caps because the cells have a smaller physical size). Notice that as the magnetic field does not affect the photon trajectory, the size of the cluster for unconverted photons is (3×5) in the barrel, and (5×5) in the end-caps. The size of the window used to include cells from the presampling, first sampling, and third sampling layers is approximately the same than the one used in the middle layer [39].

Once the cluster has been reconstructed (i.e., the cells within the clusters have been identified), the position and energy are recalculated. This is explained in the following sections.

Position measurement

The first step in the recalculation is the computation of energy weighted cluster positions for each calorimeter layer. At this stage, two corrections derived from MC studies are done [27]:

- For each layer, the η position is corrected for the bias due to the finite size of the cells. This correction depends on the energy of the cluster and the η position.

- For the middle sampling, the ϕ coordinate is also corrected, to take into account effects due to the non uniformity of the accordion structure.

The corrected positions in the first two layers are combined to obtain the final cluster position. In figure 3.9 the expected precision for the position measurement of clusters is shown. These plots were obtained using simulation studies [27]. Figure 3.9a shows the expected precision of the η coordinate, for a photon of 100 GeV, and figure 3.9b the expected precision in the measurement of the ϕ coordinate for electrons and photons of 100 GeV. Both plots are shown as a function of the cluster pseudorapidity. The precisions, for this value of energy, are $\sigma_\eta \approx 0.03\%$ (first calorimeter layer) and $\sigma_\phi \approx 0.1\%$.

Energy measurement

The energy of the cluster is computed adding together the energy of all the cells that belong to it. This is done adding the cells in each layer, and then combining the layers using the following expression:

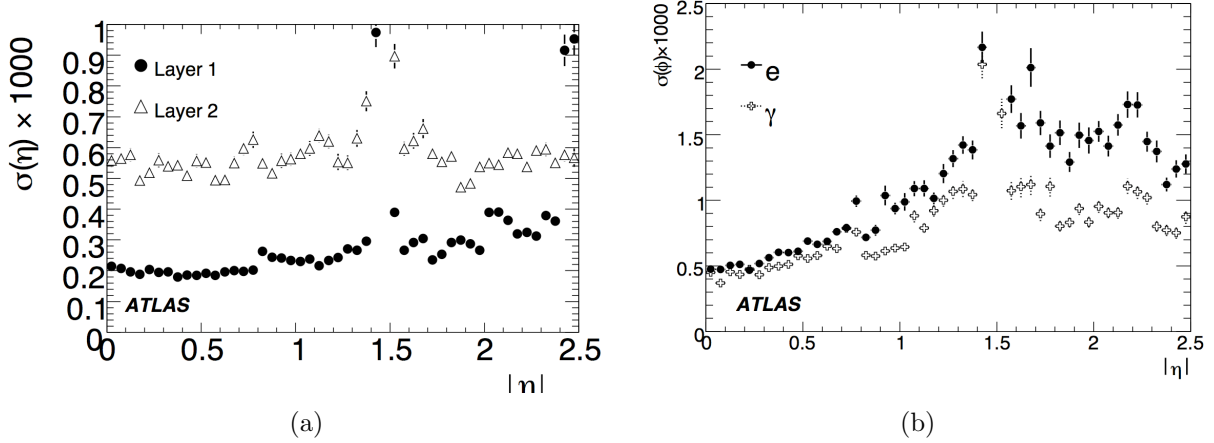$$E_{reco} = A(B + w_{ps}E_{ps} + E_1 + E_2 + w_3E_3) \tag{3.15}$$

Figure 3.9: Expected precision of the cluster position measurement, for (a) the η coordinate and (b) the ϕ coordinate, expressed in relative units, as a function of the η coordinate [27].

where E_{ps} and $E_{1..3}$ are the energies measured in the presampler and the layers of the calorimeter. The factors A, B, w_{ps} and w_3 are called longitudinal weights [27], and they are adjusted in order to correct for the energy losses due to the material before the ECAL, the leakage in the third layer of the ECAL, and at the same time optimize the linearity and resolution of the calorimeter response.

The longitudinal weights have been computed using MC simulation studies, separately for electrons and photons, and as functions of η. In figure 3.10 we show a comparison of the corrected and uncorrected energy for an electron of 100 GeV, as a function of η. In the plot the average energy loss is also shown [27].
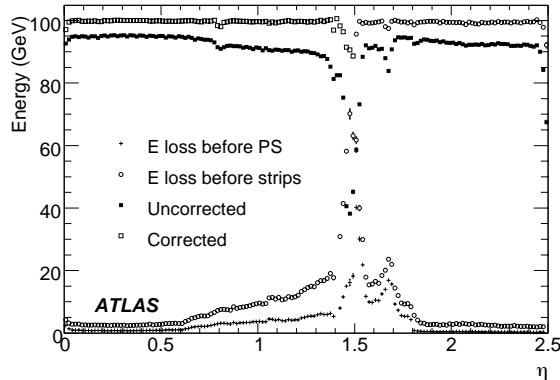
Figure 3.10: Reconstructed energy for a 100 GeV electron before and after the MC based calibration correction. The energy loss before reaching the ECAL is also shown [27].

A final correction is done, which compensates the variations in the active material traversed by a particle as a function of ϕ. This correction is called "cluster energy modulation correction", and represents a small effect (maximum of 0.5 %).

Linearity and resolution

In a sampling calorimeter, the electronic signal collected is proportional to the energy deposited in the sampling material, which in turn is proportional to the energy of the particle that started the shower. This means that the individual cell responses are intrinsically linear with respect to the energy of the incoming particle. However, the linearity is degraded by several instrumental

effects, among them saturation of the electronic response, shower leakage, and recombination of electrons and ions in the active material [36].

The energy resolution is also affected by many instrumental issues. In the case of sampling calorimeters, the resolution can be written as the sum of three uncorrelated terms, that summarize the most important effects:

$$\sigma = \sigma_{sampling} \oplus \sigma_{noise} \oplus \sigma_{constant} \tag{3.16}$$

where:

- $\sigma_{sampling}$ takes into account the random fluctuation in the number of particles that produce the calorimeter signal, for a shower of a given energy. This number follows Poisson statistics, so if N is the number of particles, the corresponding standard deviation is given by $\sqrt{N}$. As N is proportional to the energy of the incoming particle, we have $\sigma_{sampling} \propto \sqrt{E}$.

- σ_{noise} accounts for the electronic noise in the detector, originated in the capacitive effects of the electrodes and the collection of electric charges in the absence of shower [36]. It is independent of the energy of the showering particle.

- $\sigma_{constant}$ arises from other sources, like calibration and readout electronics, the amount of material before and in the calorimeter, and the energy reconstruction scheme [40]. The relative contribution of these effects to the resolution is independent of energy, thus $\sigma_{constant}/E = \text{constant}$.

Adding the three terms together, taking into account their dependence on the energy we obtain:

$$\frac{\sigma(E)}{E} = \frac{a}{\sqrt{E}} \oplus \frac{b}{E} \oplus c \tag{3.17}$$

The constants a, b and c then describe the sampling, noise and constant term in the calorimeter resolution, respectively. This equation shows the most important characteristic of calorimeters: the relative resolution improves with energy, contrary to the behavior of the momentum resolution in the trackers.

The linearity and resolution of the ATLAS ECAL has been measured using test beams [37][41]. The result of a test done on a barrel calorimeter module is shown in figure 3.11.

Following the results of the test beam [41], the relative resolution can be written as:

$$\frac{\sigma(E)}{E} \approx \frac{0.25}{E} \oplus \frac{0.101}{\sqrt{E}} \oplus 0.0017 \tag{3.18}$$

where the energy should be given in GeV. The noise term dominates for low energies (few GeV) and for high energies the resolution is determined by the constant term. According to equation (3.18), the energy of an electron of 30 GeV is measured with a precision of 2 %.

3.2.3 Electron reconstruction and identification

The electron reconstruction starts with EM clusters reconstructed in the ECAL, which are then associated to reconstructed tracks of charged particles in the ID. This matching is done extrapolating tracks from their last measurement point to the middle layer of the ECAL. The position in (η, ϕ) of the track extrapolation is compared to the position of the EM precluster (see section 3.2.2), and the track is matched to the cluster if $\Delta\eta < 0.05$ and $\Delta\phi < 0.1$ or $\Delta\phi < 0.05$ (0.1 is used to account for bremsstrahlung losses). If several tracks are matched, the one with the minimum distance in the (η, ϕ) plane to the center of the precluster is chosen. The four momentum of the electron candidate is built using the energy measured in the cluster (as explained in section 3.2.2), and the η and ϕ of the track at the vertex [42].
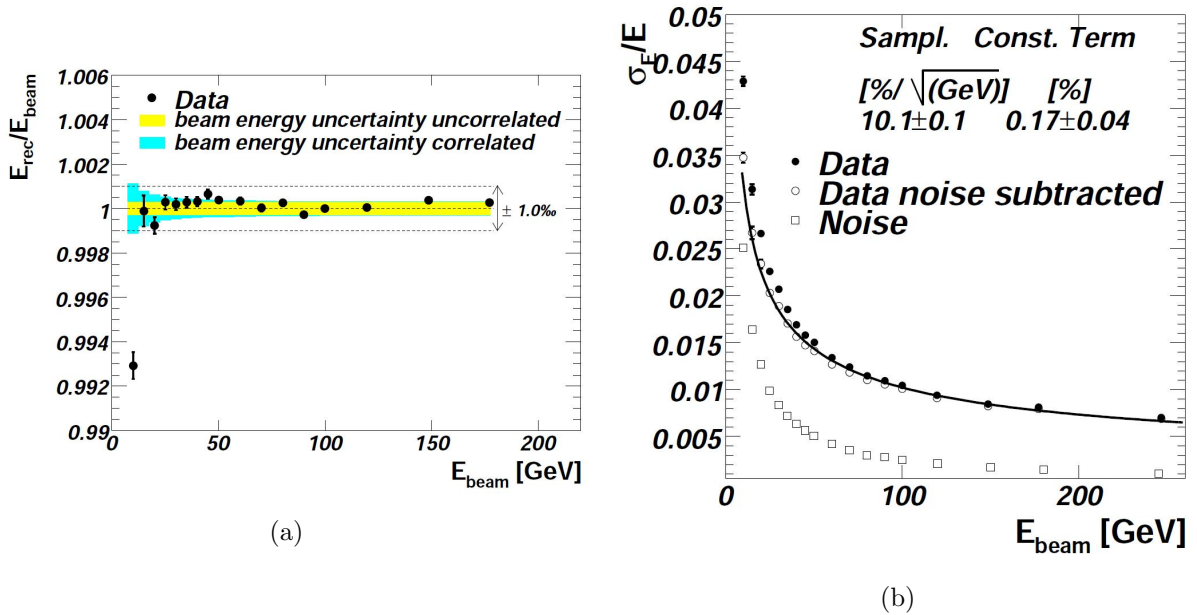
Figure 3.11: Linearity (a) and resolution (b) of a module of the ECAL, measured in a test beam [41].

The procedure described above is valid for "central electrons", meaning clusters in the region defined by $|\eta| < 2.5$, where track information is available. Outside this region, electrons are reconstructed using only cluster information. They are called "forward electrons".

Once the electron candidate has been reconstructed, several identification variables are defined which use track and cluster information, and allow to assign a quality to the object. This is done in order to reject undesired objects like non-isolated electrons, electrons from photon conversions, and jets faking electrons.

A cut optimization procedure has been done in order to select cut values for these variables that guarantee the highest possible selection efficiency for a given jet rejection. The procedure was done in kinematic regions defined with 10 bins in cluster η and 11 bins of cluster E_T. Three reference sets of cuts have been defined in order to facilitate the selection in the central region, with increasing background rejection power. These sets of cuts are labeled loose, medium and tight, and are described in the following paragraphs (values of the cuts are given if it is constant across all η and E_T regions, for the complete set of cuts see [43]).

Loose identification The loose identification is done on electrons inside the region defined by $|\eta_{cluster}| < 2.47$. It is based on cuts done in hadronic leakage variables and shower shape variables defined in the middle layer of the ECAL. This set of cuts provides excellent identification efficiency, but low background rejection. The following variables are used:

- Hadronic leakage:

  - $R_{had1} = \frac{E_T^{had1}}{E_T^{cluster}}$: fraction of the cluster transverse energy deposited in the first layer of the hadronic calorimeter.

  - $R_{had} = \frac{E_T^{had}}{E_T^{cluster}}$: fraction of the cluster transverse energy deposited in the hadronic calorimeter.

- Shower shape:

  - $R_\eta = \frac{E_{3\times7}}{E_{7\times7}}$: fraction of energy deposited in a region of 3×7 cells in (η, ϕ) cell space of the middle layer of the ECAL, with respect to the energy deposited in the region 7×7 centered at the cluster position.

50

- $w_{\eta 2} = \sqrt{\frac{\sum (E_i \eta_i^2)}{\sum E_i} - \frac{\sum (E_i \eta_i)}{\sum E_i}}$: lateral shower width. The sums are done over the cells contained in a window of 3×5 of the middle layer.

Medium identification   The medium identification includes all the cuts of the loose identification, plus additional cuts using variables of the first ECAL layer (strips), track quality in the ID and track cluster-matching. The medium cuts increase the jet rejection by a factor of 3-4 with respect to the loose cuts, while reducing the identification efficiency by near 10 %. The following variables are defined:

- Variables using information from the strip layer (rejection of photons from pion decays):

  - $w_{stot} = \sqrt{\frac{\sum [E_i (i - i_{max})^2]}{\sum E_i}}$: shower width, the index i runs over cells in a region corresponding typically to 20 strips centered in the cluster, and i_{max} is the index of the cell with the maximum energy.

  - $E_{ratio} = \frac{E_{max} - E_{min}}{E_{max} + E_{min}}$: energy difference between the cell with maximum energy and the cell with minimum energy in the cluster, divided by the sum of these energies.

- Track variables:

  - $n_{pixel} \geq 1$: minimum number of hits in the pixel detector.
  - $n_{si} \geq 7$: minimum number of hits in the pixel and SCT detectors.
  - $|d_0| < 5$mm : transverse impact parameter cut.

- Track cluster matching:

  - $\Delta \eta_1 = |\eta_1 - \eta_{track}| < 0.01$: difference between the η position of the cluster in the first layer and the extrapolated track.

Tight identification   The tight identification uses all the medium cuts, but requires more stringent cuts in the track - cluster matching and the track quality, and adds information of the TRT and the comparison between the reconstructed energy and momentum.

- Track variables: $|d_0| < 1$mm.

- Track cluster matching:

  - $|\Delta \eta_1| < 0.005$.
  - $\Delta \phi_2 = |\phi_2 - \phi_{track}| < 0.02$: maximum difference between the ϕ position of the cluster in the middle layer and the extrapolated track.
  - $E/|\mathbf{p}|$: ratio of the cluster reconstructed energy and the track reconstructed momentum. As the electron mass is negligeable compared to the typical energy scales involved, this quantity is close to unity.

- TRT information:

  - n_{TRT} : number of hits on the TRT.
  - $f_{HT} = \frac{n_{TRT}^{high}}{n_{TRT}}$: ratio of the number of high threshold hits in the TRT (transition radiation hits) to the total number of hits in the TRT.

- Reject photon conversions:

  - $n_b \geq 1$: minimum number of hits in the b layer (first layer of ID).

In figure 3.12 we show examples of distributions for some of the identification variables. These distributions have been obtained using simulations, and the simulated objects are classified according to their true nature in the MC simulation: isolated electrons (from Z or W decays), background electrons (from photon conversions or Dalitz decays), non isolated electrons (originating from decays of b or c mesons), and fake electrons (hadrons). In the figure, we can see how the distributions allow to separate the different nature of the objects, with a certain efficiency depending on the cut values [43].

3.2.4 Efficiency measurements

Only a fraction of the electrons produced in the collisions is reconstructed and identified, due to the limitations of the instruments and the high amount of background present in the pp collisions. The fraction of electrons seen as final objects is called efficiency, and can be written as the product of several factors:

$$C = \epsilon_{event} \cdot \epsilon_{reco} \cdot \epsilon_{ID} \cdot \epsilon_{trig} \cdot \epsilon_{isol} \tag{3.19}$$

where ϵ_{event} is the efficiency of selection of the event due to preselection cuts, like vertex requirements and other cleaning cuts; ϵ_{reco} is the reconstruction efficiency of the electron, meaning the fraction of clusters that are found and matched to tracks, accounting also for other kinematic and geometrical cuts done on the reconstructed object, ϵ_{ID} is the efficiency of the identification cuts, ϵ_{trig} the trigger efficiency and ϵ_{isol} the efficiency of isolation cuts, if applied. In equation (3.19), every efficiency is computed with respect to the one immediately before, for example, the ϵ_{ID} is defined with respect to electrons that have been reconstructed, ϵ_{trig} is defined with respect to electrons that have been identified, and so on.

The factors entering equation (3.19) depend on the values of the cuts done, and on kinematic variables like E_T and η of the electron candidate. The efficiencies can be estimated using MC simulations, however they can be measured more accurately using a data driven method, called "tag and probe". This method is based on the selection in data of a clean and unbiased sample of electrons, called probes, that can be used to evaluate the efficiency of the different cuts. In order to select this sample, tight requirements are done on other objects of the event, called tags, that are related to the probes by means of a decay or other process. For example, consider the $Z \rightarrow ee$ process. In order to use this process for tag and probe, one electron is required to pass tight ID cuts, the other one to have opposite charge to the first one (looser selection), and the invariant mass of the pair to be close to the Z resonance peak. This way, the event is "tagged" by the tight selected electron and the requirement on the invariant mass, and the loose selected electrons can be used as probes, just by applying a given cut on them and evaluating the fraction of times the cut is passed.

The electron efficiencies have been measured using 2010 and 2011 data. In figure 3.13 we show some of the results of the measurements performed with 2010 data, obtained with the $Z \rightarrow ee$ process. The figures also show the result of the same procedure applied on MC samples. The difference observed between data and MC prediction is due to mis-modeling of the detector in the simulation, in particular shower shapes and hits in the TRT. These differences are corrected using scale factors, that are computed comparing the distributions measured in data with the distributions measured in MC [42].

3.2.5 In-situ calibration of the ECAL

The calibration of the energy in the ECAL is done in three steps:

- The electronic calibration which assigns an energy value to the signals collected in cells, as discussed in section 3.2.1.
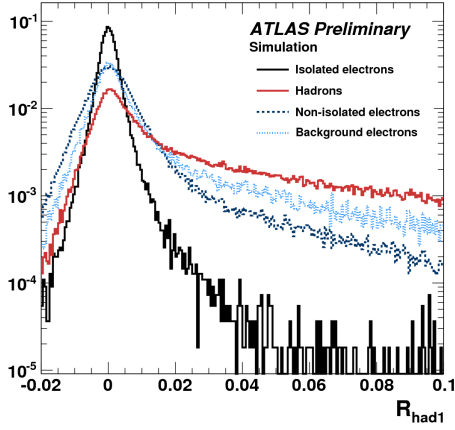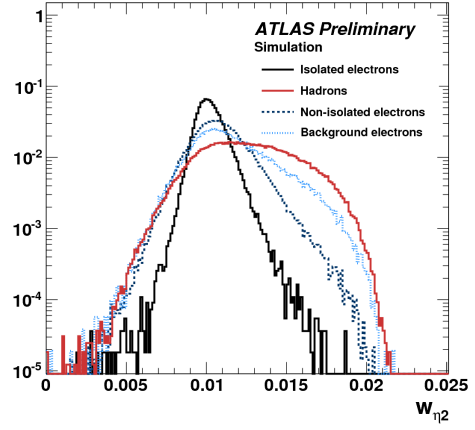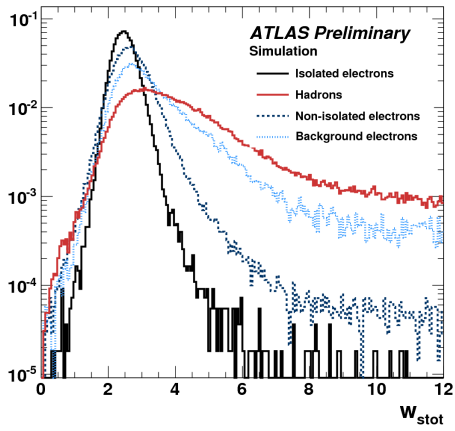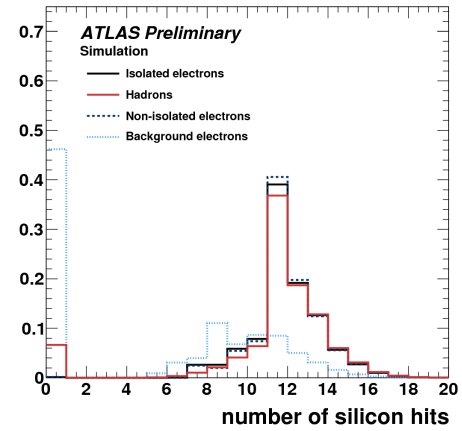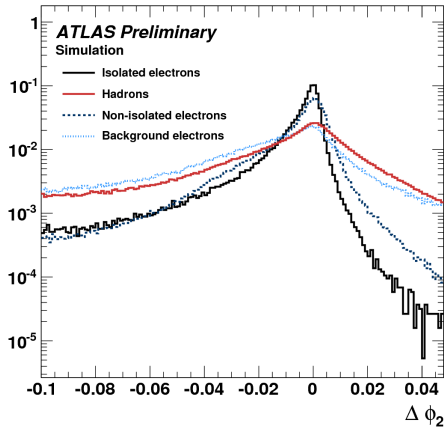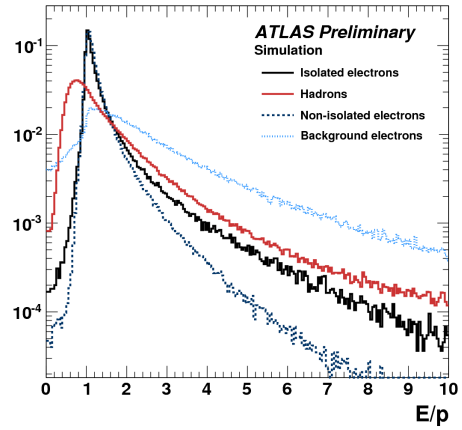
Figure 3.12: Examples of variables used in the electron identification. a) and b) show variables used in the loose selection, hadronic leakage and shower lateral width; c) and d) variables used for the medium selection, shower width and number of silicon hits in the ID; and e) and f) variables used in the tight identification, difference in the ϕ coordinate of the cluster in the middle layer and the extrapolated track, and the ratio of the cluster energy to the momentum of the track. The distributions were obtained using simulations [43].
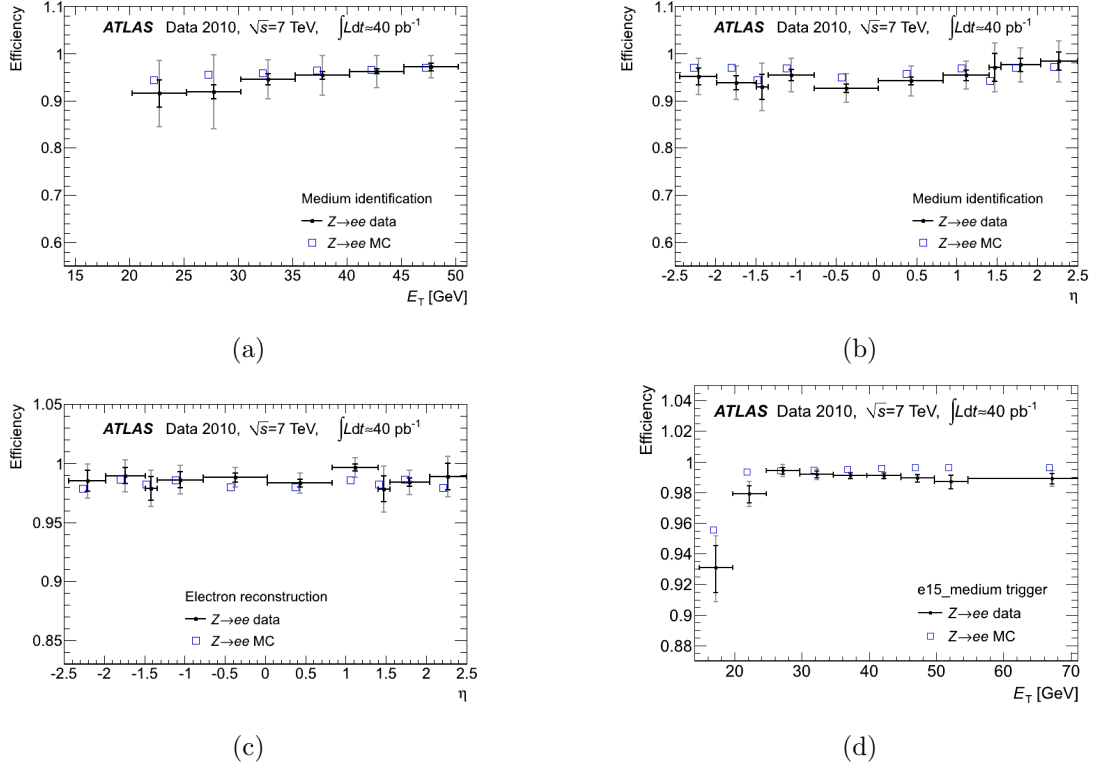
Figure 3.13: Electron efficiencies measured in 2010 data, using tag and probe methods and the process $Z \rightarrow ee$. a) and b) Efficiency of the medium ID cut, as a function of the E_{T} and η of the electron; c) reconstruction efficiency as a function of η; d) efficiency of the trigger e_15_medium with respect to tight identified electrons. The efficiencies are reported for data and MC. The data points show statistical (inner bars) and total errors (outer bars) [42].

- The MC based calibration of the cluster, where the energies of the cells are added, and corrections are done in order to compensate effects like the leakage and the amount of material, as discussed in section 3.2.2.

- The "in-situ" calibration, that makes use of collision data and well known processes like $Z \rightarrow ee$ and $J/\psi \rightarrow ee$, to measure the energy scales as a function of η, intercalibrate the calorimeter layers and measure the resolution.

The in-situ calibration using the $Z \rightarrow ee$ process is done selecting in data a clean sample of $Z \rightarrow ee$ events, then comparing the invariant mass distribution of the electron pair to the theoretical expected distribution centered in the well measured Z boson mass. Then correction factors for the electron energy scale are computed using an unbinned log-likelihood fit. The correction factors relate the measured energy (E_{meas}) to the corrected energy E_{true} via the equation:

$$E_{meas} = E_{true}(1 + \alpha) \tag{3.20}$$

where α is the parameter measuring the additional correction. These parameters have been measured in 2010, doing fits binned in 58 η regions, the results are shown in figure 3.14.

To complement this study, $J\psi \rightarrow ee$ events are used to measure the scale correction for lower energy electrons, and to measure the linearity. Also, a complementary calibration is done using the ratio $E/|\mathbf{p}|$. The uncertainty on the correction factors gives the uncertainty associated to the electron energy scale. The sources of uncertainty are, among others, the additional material in front of the ECAL (1 % to 2 %), the presampler energy scale (up to 1.4 %) and the background estimation (0.1 % to 1.2 %) [42].
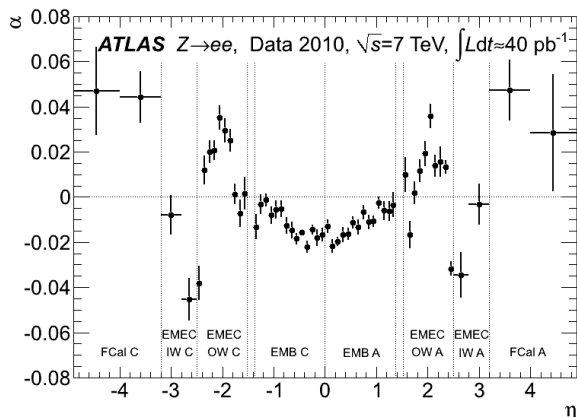
Figure 3.14: Electron energy scale correction factors measured using 2010 collision data [42].

The resolution measurement is done using fits on the dielectron mass distribution of data and MC predictions. The fits are done using a Breit-Wigner distribution convolved with a Crystal Ball function, and allow to measure the gaussian component of the resolution, both for data and MC. This allows to measure the constant term of the resolution function, as explained in [42]. In figure 3.15, we show an example of fit done in the region defined by $|\eta| < 1.47$. The data and MC predictions are shown, together with the fit results.
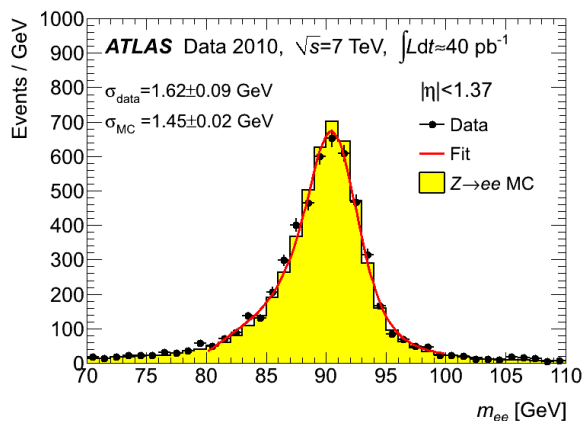
Figure 3.15: Example of fit for the resolution measurement, using the region defined by $|\eta| < 1.47$. The data, MC prediction and the fit results are shown [42].

The observed differences in the energy resolution in data and MC predictions are used to compute resolution corrections. The resolution corrections are used to generate perturbations (smearing) on the electron energy in the MC samples, in order to match the resolution observed in data.

Notice that a complete in-situ calibration and resolution measurement has been done using 2011 data, using the template method, explained in [44].

Chapter 4

Validation of the bunch-crossing identification of the L1Calo at very high transverse energies

The ATLAS experiment is expected to be sensitive to a broad spectrum of energies, ranging from a few GeV up to several TeV. For instance, many physics searches like the Z' and W' resonances and other exotic particles involve very energetic leptons and jets as signatures, and the calorimeters should be able to detect and measure these final states correctly. This fact represents a challenge to the detector electronics, in particular the trigger system, which should respond correctly to electrical signals covering several orders of magnitude.

An important function of the LVL1 is the association of electronic signals in the detector with the appropriate LHC bunch-crossing (here, we use bunch-crossing (BC) to refer to intervals of 25 ns, dictated by the LHC clock, which can contain an actual crossing of protons, or not). This is a very important step, given that the readout of the detector by the HLT is done only for the BC selected by the LVL1, so potential failures in the identification could lead to the loss of interesting events. On the other hand, the signals deposited in the subdetectors extend over several BC, making this task difficult.

In this chapter, we review a method used to validate the bunch-crossing identification (BCID) in the calorimeter part of the LVL1 (L1Calo). The method is based on the measurement of the response of the L1Calo to physics signals of typical energies, and the use of this measurement to determine energy validity ranges and efficiency of the BCID. The method is applied and used to validate 2011 ATLAS data. In addition, we study the L1Calo response to high energetic pulses.

The chapter begins with a description of the main elements of the level 1 calorimeter trigger system, with emphasis on the bunch-crossing identification algorithms and its setup for 2011. We present the validation method and the results for 2011 data in the following section, and then show the new observations based on the analysis of high energy deposits in the trigger towers, and analyze the impact of these new observations on the validation method. Finally, the conclusions of the study are presented.

4.1   Introduction

4.1.1   The Level 1 Calorimeter Trigger System

In this section, we give the details of the L1Calo architecture, needed to introduce the BCID and the validation method. In figure 4.1 the architecture of the L1Calo system is shown [28].

The L1Calo receives signals from the electromagnetic and hadronic calorimeters, and reduces the granularity by adding the analog signals coming from cells inside projective regions called trigger towers (TT). This is done in order to have less channels to process ($\sim$ 7200 towers instead
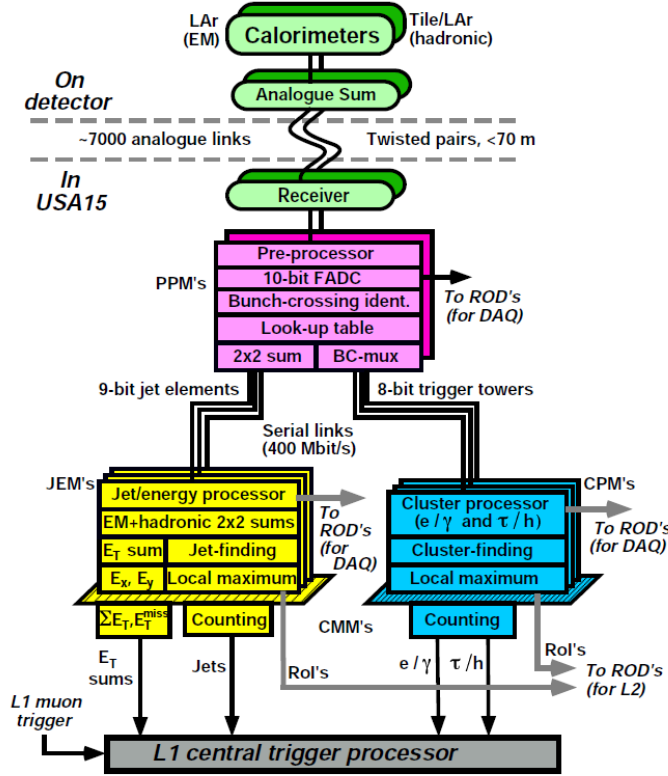
Figure 4.1: Level 1 calorimeter trigger architecture [28].

of $\sim$ 200000 cells), so the LVL1 decision can be made as fast as possible. The size of the TT is $(\Delta\eta, \Delta\phi) = (0.1, 0.1)$ for $|\eta| < 2.5$ and larger for higher $|\eta|$. Notice that the size of the TT is larger than the size of the towers used in the EM cluster reconstruction (section 3.2.2). The number of readout cells added inside a trigger tower ranges from a few (for example 3 in the hadronic end-cap), to 60 (electromagnetic barrel). In figure 4.2 we show the cell composition of a trigger tower in the electromagnetic barrel [37], and in table 4.1 we summarize the TT distribution in the ECAL.
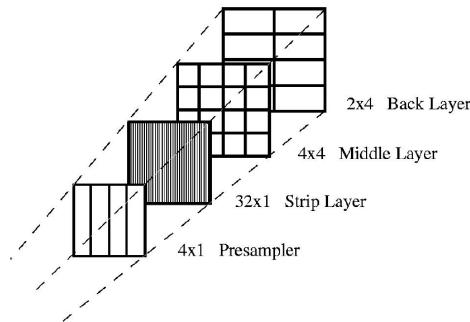
Figure 4.2: Granularity of an electromagnetic barrel trigger tower.

The processing of signals in the L1Calo is done in parallel to the ROS. In the electromagnetic towers, the analog sums are performed first by group of 4 cells, then by calorimeter layer, and then the layer signals belonging to a trigger tower are added in the Tower Builder Boards (TBB), which are visible in figure 3.8. There, corrections are done for gain, shape and timing of the different signals added. Conversion to transverse energy is done using η-dependent gain factors. The output of the TBB is a signal with a peaking time of 35 ns, and normalized at 2.5 V for

Region	η limits	Number of towers	Size of tower ($\Delta\eta \times \Delta\phi$)	Number of cells per tower
Barrel	$|\eta| < 1.4$	1792	0.1×0.1	60
End-cap outer wheel	$1.5 < |\eta| < 2.5$	1280	0.1×0.1	60
End-cap inner wheel	$2.5 < |\eta| < 3.2$	256	0.2×0.2	8

Table 4.1: Summary of TT distribution in the ECAL.

$E_T = 256$ GeV [45]. After the analog processing, the TT signals are sent to receivers located in the ATLAS service cavern, where they get additional shaping and energy calibration.

The next steps of processing in the L1Calo are done in electronic boards called preprocessors modules (PPM). The TT signals are digitized using 10 bits with a frequency of 40 MHz, and a pedestal is added. These samples are then processed and an energy value for the pulse is determined with the help of a look up table (LUT) and assigned to a given bunch-crossing (BC). After this point, the processing is done separately in the jet/energy processor modules (JEM) and cluster processor modules (CPM). The CPM identify e, γ and τ candidates with E_T above a given threshold, while the JEM search for jets candidates and compute missing and total transverse energy sums. The output of the CPM and JEM is sent to the level 1 central trigger processor (CTP), which decides whether to keep or not the event. When an interesting physics signature is found by the CTP, the information from all the ATLAS subdetectors belonging to the corresponding event is moved to the ROS, where it remains available for further processing by the HLT [28].

4.1.2   Bunch-crossing identification in the L1Calo

As explained in the previous section, the CTP receives signals from the L1Calo, together with the muon trigger signals, for every BC, and based on this information takes the decision to keep or not the event. The bunch-crossing identification (BCID) is the process done in the PPM, which allows to send downstream to the CTP the TT signals for the correct time slice. It is important that all the pulses are assigned to the right BC, so the CTP can have all the potential interesting signals for every BC and can take an appropriate decision. If the TT signals are assigned to a wrong BC, the CTP could miss information, it could not trigger and potential interesting events would be lost.

Ideally, the BCID should associate a single digitized energy value to a broad TT pulse and send it to the CTP in a time slice corresponding to the peak of the pulse. As the peaking time of the TT pulse is known, the identification of the peak sample allows to identify correctly the BC that originated the pulse. Therefore the main problem is the identification of this peak sample. The bunch-crossings that are not identified as the central one are assigned a zero energy value. [46].

The L1Calo is designed to respond linearly for transverse energies up to ~ 256 GeV; from this value on digital saturation in the PPM occurs (this is unlike the readout chain, which is designed to be linear on the full energy range) [46]. In figure 4.3 two digitized pulses are shown, one of them non-saturated and the other one saturated, together with the desired output of the LUT (notice that the sampling frequency is 40 MHz, so the separation in time of the samples is the same as a BC, i.e. 25 ns). As can be seen from the figure, the central sample is not easily identified when there is saturation.
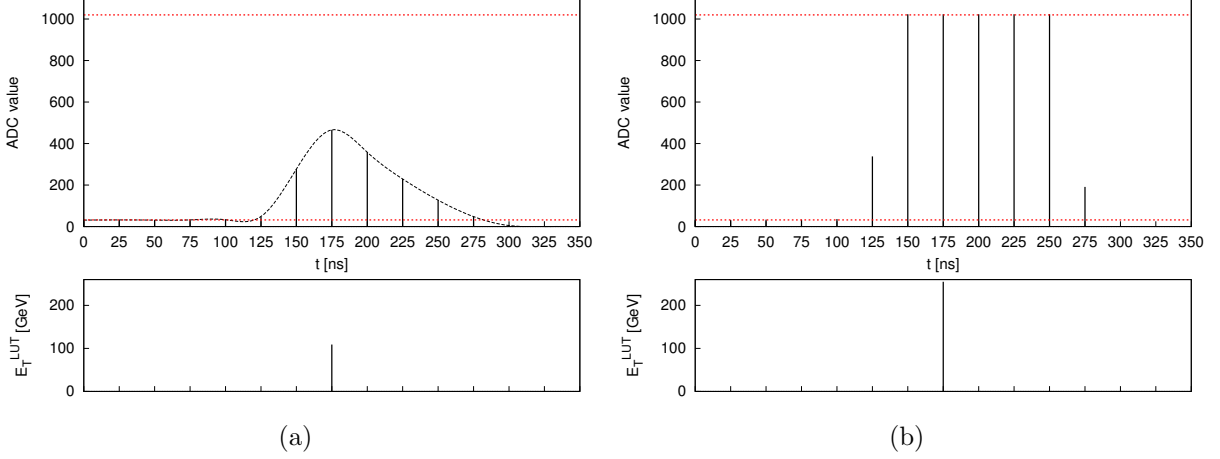
Figure 4.3: Example of digitized trigger tower pulses, as seen in a calibration run (15 samples are available). The pedestal value (~ 32) and the saturation value (1020) are shown in dashed lines. Below the pulses, the desired output of the LUT is shown in the form of a single digitized value located in the peak sample. a) Non-saturated pulse (a smooth line is drawn connecting the samples), b) saturated pulse.

4.1.3   Notation

We introduce the notation that is used in the following sections, in the description of the BCID algorithms and the explanation of the method used. For a given pulse in a given TT, we define:

- n : number of the right bunch-crossing (or peak sample).

- $ADC(i)$: output value of the ADC converter of the PPM, for the sample described by the discrete index "i".

- X : number of the bunch-crossing (or sample) selected by the BCID as the central sample.

- E_T^{LUT} : output transverse energy of the look up table.

- s : for saturated pulses, the first saturated sample.

Using this notation, the desired situation is: $X = n$.

4.1.4   BCID algorithms

Two BCID methods are implemented in the PPM, one designed to work for normal sized pulses, and the other designed to work for saturated pulses. We describe briefly this two algorithms in the following paragraphs.

BCID for non-saturated pulses: the "FIR" algorithm

In this algorithm, five consecutive samples are kept in a pipeline, processed by a finite response digital filter (FIR), and then a subsequent peak finder searches for the peak sample of the pulse [46]. The following weighted sum is computed

$$S_m = \sum_{i=-2}^{2} [b_i ADC(m+i)] \tag{4.1}$$

where m is the central sample of the pulse. $\{b_i\}$ is a set of filter coefficients designed to maximize the signal/noise ratio (they can differ from one TT to another, and are adjusted using calibration

tests). The next clock cycle, the samples are shifted in the pipeline, and the sum is computed again, but this time centered around the sample $m + 1$. Three consecutive sums are compared, and a given bunch-crossing X is selected if:

$$S_X > S_{X-1} \quad \text{and} \quad S_X \geq S_{X+1} \tag{4.2}$$

The sum S_X is used as input to the LUT, which performs pedestal subtraction, noise suppression and computes the energy of the pulse in GeV encoded in 8 bits (E_T^{LUT}). The value is sent to the CTP in accordance to the selected BC, X.

BCID for saturated pulses: the "threshold" algorithm

The BCID algorithm for saturated pulses is based on comparisons of the leading edge of the pulses with two predefined thresholds: HT for high threshold, and LT for low threshold. Let s be the first saturated sample in a given pulse, so $s - 1$ and $s - 2$ are the samples one and two BC before, respectively, then the algorithm will select the BC "X" according to the following comparison:

- If $ADC(s - 1) > HT$ and $ADC(s - 2) > LT$ then $X = s$

- else $X = s + 1$

The thresholds can be adjusted from one tower to another to adapt the behavior of the algorithm. When a saturated signal is detected, an energy value of 255 GeV will be assigned to the pulse by the LUT and sent to the CTP. The L1Calo configuration guarantees that if there are saturated energies in some tower for a given event, the event will be automatically accepted by the LVL1.

It should be pointed out that even though the actual energy of the saturated pulse is not kept, it could be computed offline by adding the individual readout energies of the cells inside the TT.

4.1.5 2011 BCID setup and the need for validation

In the original ATLAS BCID setup, the FIR algorithm was active only for unsaturated pulses, and beyond saturation energies the control was given to the threshold algorithm. This setup assumed that the threshold algorithm could work for an energy range extending from ~ 250 GeV to the maximum expected energy (~ 3 TeV), and that the transition between saturation and non-saturation would be smooth. Calibration and simulation studies were made, and the thresholds in the towers were adjusted in order to maximize the validity range of the saturated BCID.

This setup was used during the first data-taking periods of 2010. Later, it was realized that a setup with the two algorithms working in parallel provided a better BCID performance. When the two algorithms give different answers, the earlier BC is selected, due to the configuration of the LVL1 electronics that does not allow to trigger in two consecutive BC. This setup, together with the values of the thresholds adjusted as before, was used for the remaining periods of 2010 data-taking.

For 2011 data-taking, the thresholds of the saturated BCID were readjusted in order to improve its predictability, following the 2010 validation results [47]. It was shown that, provided that the two algorithms run in parallel, this would not mean a degradation in the performance. The values of the low and high thresholds were fixed for all towers at 5 and 1020 ADC counts, respectively. With this setup, for saturated pulses the threshold algorithm always identifies the BC next to the first saturated one, that is $X = s + 1$.

However, this setup assumes that there is enough overlap of the two BCID algorithms, and that the threshold algorithm works up to the highest expected energies. This has to be checked in

order to guarantee the correct performance of the L1Calo. If we call $E_T^{FIR}(MAX)$ the maximum transverse energy such that the FIR algorithm identifies the correct BC, $E_T^{THR}(MIN)$ and $E_T^{THR}(MAX)$ the transverse energies defining the working range of the threshold algorithm, the validation of the BCID can be done checking the two following conditions (notice that we use the η coordinate of the TT to compute the energy in the second condition):

$$E_T^{FIR}(MAX) - E_T^{THR}(MIN) > 0 \text{ GeV} \tag{4.3}$$

$$E^{THR}(MAX) = E_T^{THR}(MAX) \cosh(\eta) > 3500 \text{ GeV} \tag{4.4}$$

Therefore, in order to validate the BCID setup, we need to estimate the energy limits entering equations (4.3) and (4.4). This estimation should be done using physics data, instead of calibration data, for the following reasons:

- The calibration pulses in the TT have shapes that are different from the shapes in physics runs, especially in the leading edges. Although the difference is small for low energies, for high saturated energies it can lead to a different behavior of the algorithm with respect to the observed one in calibration.

- As the saturated BCID is based on the comparison of ADC samples with threshold values, the outcome is very sensitive to variations in timing and calibration of the L1Calo that can alter the position in time and the value of the samples, during physics data-taking.

- For the same reason stated above, the electronic noise can affect the performance of the saturated BCID.

- The calibration boards do not allow to probe very high transverse energies in the outer parts of the calorimeter (end-caps).

In addition, this should be done for separate regions of the calorimeter (because of differences in pulse shapes), and repeated if there are changes in the trigger system configuration. In what follows we concentrate on the electromagnetic part of the L1Calo, and only for the barrel and end-cap regions. This is justified by the following points:

- The electromagnetic barrel and end-cap have homogeneous electronic design.

- The jets leave an important fraction of their energy in the electromagnetic calorimeter, so validating the BCID in the electromagnetic part is enough.

- The towers in the forward calorimeter (FCAL) do not receive energies high enough to reach 256 GeV of transverse energy (with 3.5 TeV beams), so saturation is not expected.

4.2   Validation of 2011 data

The validation method consists of the measurement, using physics data, of the energy limits of equations (4.3) and (4.4), for the trigger towers in the barrel and end-cap part of the ECAL. This can be done looking at the behavior of the BCID algorithms with the 2011 setup. For increasing energy, this behavior can be described as follows:

1. The FIR algorithm starts identifying the right bunch-crossing ($X = n$). Then, starting from some energy on, it identifies the sample right after the correct one ($X = n+1$). This happens when the sum (4.1) centered around $n + 1$ is bigger or equal to the sum centered around n. This allows us to define $E_T^{FIR}(MAX)$ as:

$$E_T^{FIR}(MAX) : \text{minimum transverse energy such that } S_{n+1} \geq S_n \tag{4.5}$$

2. The threshold algorithm starts by identifying as the right bunch-crossing one sample after the correct one ($X = n+1$), then when the sample $n-1$ reaches saturation level, it starts to get the right one ($X = n$), and then as energy increases at some point the sample $n-2$ saturates and the algorithm identifies one BC before the correct one ($X = n-1$). Then, we can define the energy bounds for the threshold algorithm as:

$$E_T^{THR}(MIN) : \text{minimum transverse energy such that } n-1 \text{ saturates} \qquad (4.6)$$

$$E_T^{THR}(MAX) : \text{minimum transverse energy such that } n-2 \text{ saturates} \qquad (4.7)$$

Figure 4.4 shows the algorithms behavior and the energy limits definitions.

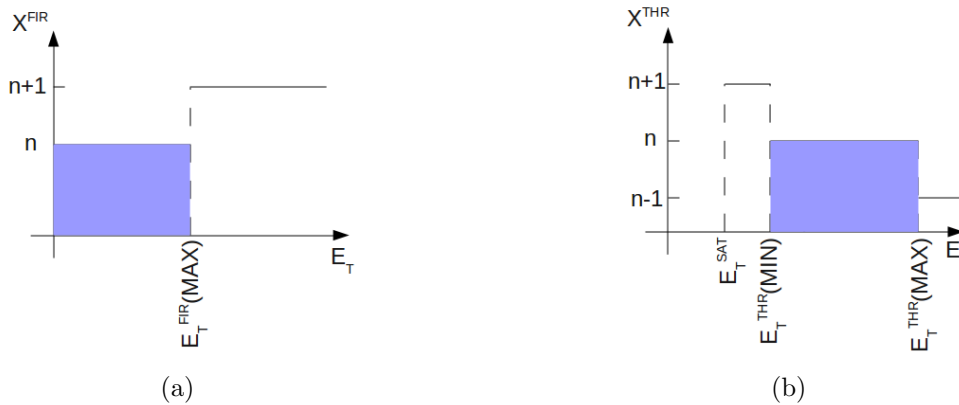
<div align="center">(a)   (b)</div>

Figure 4.4: Behavior of the BCID algorithms as a function of the trigger tower pulse energy. X is the bunch-crossing identified by the algorithm, and n is the correct one. The shaded energy regions correspond to the working ranges of the algorithms. a) FIR algorithm, b) threshold algorithm.

If the validation condition (4.3) is not satisfied, that is, if there is not enough overlap between the working ranges of the algorithms, then from the considerations above it is clear than we will have $X = n+1$, and the LUT energy value corresponding to the given tower will be sent to the CTP one BC after the correct one. This implies a possibility of losing the event if it was not triggered correctly by another TT. On the other hand, if there is enough overlap, when the FIR algorithm starts failing (giving $X = n+1$), the threshold algorithm already gives $X = n$, and then due to the L1Calo configuration, the earlier BC will be taken (the correct one).

Concerning the second validation condition (4.4), when the threshold algorithm fails for very high energies and gives as output $X = n-1$, the LUT saturated signal is sent too early to the CTP, the event is triggered before time and all the detector information corresponding to the correct BC is lost. This is why it is very important to assess the performance of the threshold algorithm up to energies as high as possible.

4.2.1 LVL1 intermediate information and calibration

In order to measure the energy limits, we need to access LVL1 information stored in events selected by the trigger, i.e., information related to the LVL1 processing and decision. In figure 4.5 we show a scheme of the signal flow from the subdetectors up to the HLT and DAQ. As shown in the figure, for events passing the LVL1 selection, intermediate information is stored in the final data, together with raw detector data. Reading these intermediate information allows to collect information about the pulses received by the TT and processed by the PPM.

The electronic calibration of the liquid argon calorimeter is done by special boards that inject pulses of known amplitude into the ROS, allowing to determine the energy scale of the readout (see section 3.2.1). This system can also be used to calibrate the L1Calo and check the
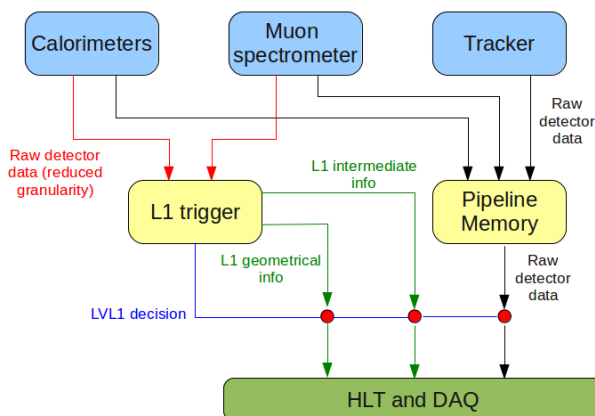
Figure 4.5: Scheme of the information flow in the LVL1. Notice that intermediate LVL1 information is kept for LVL1 selected events.

TT response. In this section, we describe the output of a calibration run taken during April 2011, which consisted in an energy scan of the LAr calorimeter, probing energies in the TT that go from ~ 18 GeV to ~ 2700 GeV in the barrel. In figure 4.6, we show trigger tower maps with the energy response (E_T^{LUT}) to two calibration inputs. We see that there are no towers giving a blank response, so no serious hardware malfunctions specific to saturated regime are present (in 2010 there was a problematic TBB that was replaced). The irregularities observed in the response are characteristic of the calibration runs, and are not normally observed in the physics runs (they could be due to non-nominal high voltages present in the readout cells during calibration). Notice that many towers in the barrel region in figure 4.6b show saturation (red area around the center limited by $|\eta| \approx 0.5$).

(a)   (b)
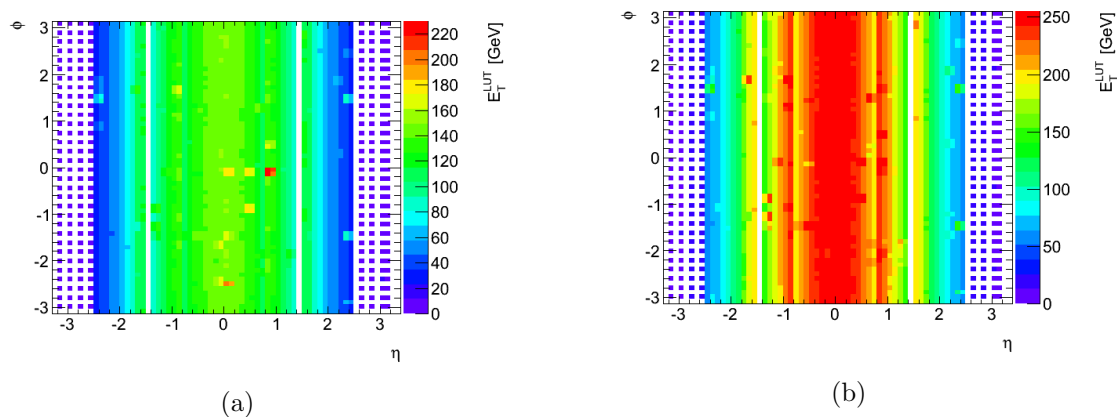
Figure 4.6: Trigger tower maps showing the trigger tower response to two calibration inputs. In the maps, each square with coordinates (η, ϕ) represents a trigger tower with those coordinates, and the color scale gives the LUT energy (E_T^{LUT}). The input current in b) is larger than in a). No serious hardware malfunctions are observed. Saturation is already observed in the barrel region in b).

Using the same calibration run, we can look at the ADC pulses samples behavior as energy increases. In figure 4.7 we show the ADC values of the central sample and its neighbors, for a barrel trigger tower with coordinates $(\eta, \phi) = (0.05, 1.23)$, as a function of transverse readout energy. There is a clear linear response of all the samples before they reach saturation, except

63

for $n - 2$. This linearity is the basis of the method presented in the next section.

4.2.2   Description of the method

The energy limits (equations (4.5), (4.6) and (4.7)) can be estimated if the linear dependence of the ADC samples with the transverse energy is known. In the previous section, we saw that the evolution of the ADC samples with respect to energy is linear (in calibration), so fits can be done to quantify the corresponding slopes. We perform these fits using non-saturated pulses taken from physics data, assuming that the same behavior observed in calibration can be extended to physics data.

The first step of the method consists on selecting TT pulses. This is done in the following way:

1. Take a sample physics run, belonging to a given period of stable L1Calo configuration (for more details on the ATLAS physics runs in 2011 see appendix B).

2. Look at the intermediate LVL1 information stored in the run file (normally this is accessible in the ESD, see section 2.3.1), loop on the events and select and store TT pulses using the following criteria:

   (a) Reject events with explicit problems in the liquid argon.

   (b) Reject saturated pulses.

   (c) Select good quality pulses (avoid noisy pulses). Here, we use the LAr quality factor [48]. This factor works as a "χ^2" value for the cell pulses (it is obtained by comparing the cell pulse with a reference shape), therefore high values mean bad shaped pulses. It is encoded in 16 bits, so it has a maximum value of 65535. For every tower pulse, we keep as quality factor the worse (largest) value among those of the cells inside the tower. Then, we impose the condition: "tower pulse quality" < 12000.

3. For the selected pulses, we store the following information:

   (a) The transverse energy of the pulses (the output of the LUT for the electromagnetic part of the tower).

   (b) The ADC values of the samples (5 samples are available).

   (c) The coordinates of the tower the pulse belongs to.

The collection of pulses is done reading some physics data stream (JetTauEtmiss or Egamma), and the empty bunches stream "CosmicCalo" (see section 2.3.1). Once the pulses have been collected, we proceed to analyze every TT separately. This involves the following steps:

1. Use the pulses collected from the CosmicCalo stream to measure the pedestal p. We perform a gaussian fit on the distribution of the ADC values of the central sample. The mean of this fit is used as the pedestal value, and the standard deviation of the fit (σ_p) is used as an estimation of the electronic noise.

2. Use the pulses collected from the physics stream, and the pedestal computed above, to measure the following coefficients:

   • k_i: slope obtained from the linear fit of the graph $ADC(n+i) - p$ vs. $ADC(n) - p$. i can take the values $-2, -1, 1, 2$.

   • k_E: slope obtained from the linear fit of the graph E_T^{LUT} vs. $ADC(n) - p$.
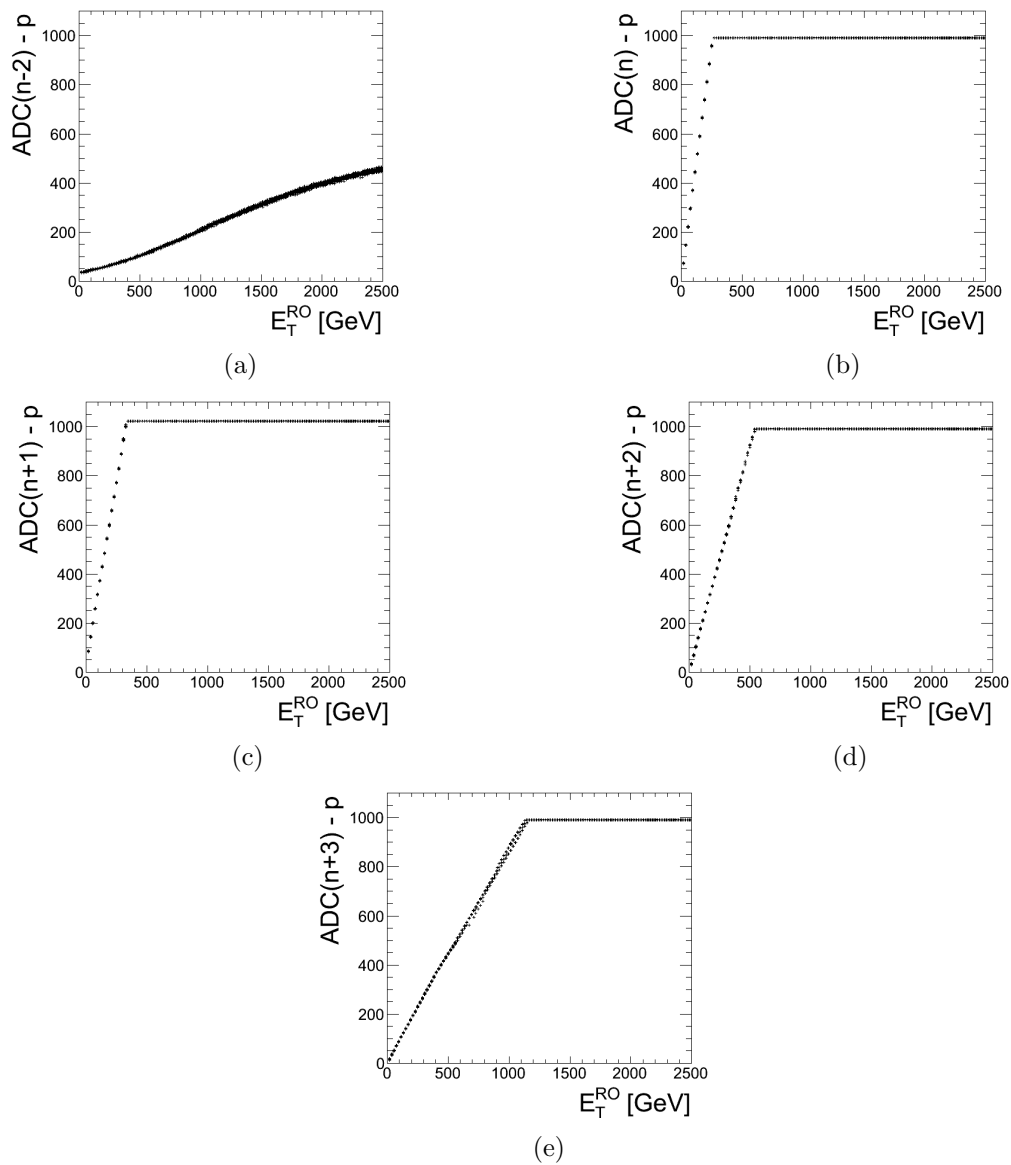
(a)

(b)

(c)

(d)

(e)

Figure 4.7: ADC samples (pedestal subtracted) vs. transverse energy as observed for a barrel trigger tower with coordinates $(\eta, \phi) = (0.05, 1.23)$, during a calibration run. The x axis of the plots is the calorimeter readout transverse energy. A clear linear behavior is observed before digital saturation, except for sample $n - 2$.

3. Parametrize the ADC values as a function of transverse energy, as follows:

$$ADC(n + i) \approx \frac{k_i}{k_E} E_T + p \tag{4.8}$$

The maximum estimated ADC value is limited to the saturation value (1020).

4. Compute $E_T^{FIR}(MAX)$ for this tower. We use the estimated ADC samples (4.8) to evaluate S_n and S_{n+1} (definition (4.1)). This is done iteratively starting from small energies until the condition (4.5) is satisfied.

5. Use the coefficients k_i to compute $E_T^{THR}(MIN)$ and $E_T^{THR}(MAX)$ in the following way (based on conditions (4.6) and (4.7)):

$$E_T^{THR}(MIN) = \frac{k_E}{k_{-1}} [1020 - p + 5\sigma_p] \tag{4.9}$$

$$E_T^{THR}(MAX) = \frac{k_E}{2[k_{-2} + 3\sigma_{k_{-2}}]} [1020 - p - 5\sigma_p] \tag{4.10}$$

In equations (4.9) and (4.10), we have introduced variations around the pedestal to make the computation more conservative. The computation of $E_T^{THR}(MAX)$ is affected by the nonlinearity observed in calibration (see figure 4.7). Therefore a safety factor of two is used in the denominator to double the slope, so the result of this computation is a conservative estimate.

6. Check the validity conditions (4.3) and (4.4), giving a safety range of 10 GeV to the overlap.

7. If the two conditions above are satisfied, the BCID in this tower is validated. If one of them is not satisfied, we can immediately know up to which energies it can be validated, by looking at the energy limits.

Step 4 requires the FIR coefficients to be known ((4.1)), which are obtained from the ATLAS database. In addition, this step requires the computation of S_{n+1}, which implies knowing the evolution of sample $n + 3$ (or the coefficient k_3). As the sample $n + 3$ is not kept in physics data, the coefficient can not be measured in the same way as the others. In order to have an estimate, we look at the correlation plot of k_3 vs. k_2, for towers inside a given region (barrel, end-cap inner wheel and end-cap outer wheel), and measured using calibration pulses (from the same calibration run described in section 4.2.1). The resulting plot for the barrel towers is shown in figure 4.8. Using these plots, we parametrize k_3 as a function of k_2, giving enough margin (for example, red line in figure 4.8) and extend this parametrization to data. This assumption is valid because the correlated behavior of the samples $n + 3$ and $n + 2$ is expected to be similar in data and calibration.

4.2.3 Results

The procedure described in section 4.2.2 was applied to a run belonging to each period of stable conditions of the L1Calo. These periods were defined following reference [49]. As the L1Calo calibration and timing conditions are kept constant during these periods, the results obtained for every sample run can be extended for the rest of the period it belongs to.

As an example, we show in figure 4.9 the detailed results for the run 189483. There, we can see that both validity conditions are fulfilled for all the towers in this run. Detailed results for the other runs are shown in appendix D.

As a matter of illustration, in figure 4.10 we show the values of the coefficient k_2 measured in calibration and in the physics run 189483. Clearly, the values in the two maps are not the
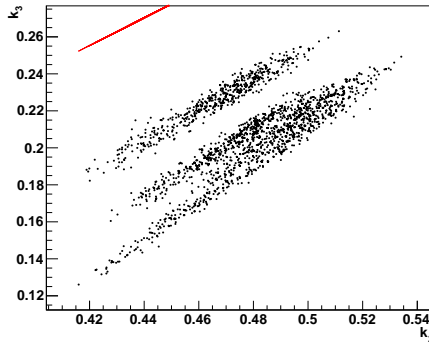
Figure 4.8: Example of correlation plot for the coefficients k_3 and k_2, as measured for barrel towers, using calibration pulses. The red line shows the parametrization used in data.

same. This is a manifestation of the difference between the TT pulse shapes in calibration and physics signals.

The results for all sample runs show that for all periods the overlap validation condition (4.3) is satisfied by all the towers. Thus the possible problems arise only from the non fulfillment of the second validation condition (4.4), i.e., the BC could be identified too early.

In order to present the results in a summarized manner, we group the towers in the following three pseudorapidity regions:

- Barrel: $|\eta| < 1.4$

- End-cap outer wheel: $1.5 < |\eta| < 2.5$

- End-cap inner wheel: $2.5 < |\eta| < 3.2$

We define the following variables (valid inside each region):

- Variable "$E^{100\%}$": maximum energy up to which all the trigger towers are validated (satisfy the second validation condition).

- Variable "efficiency" (eff): percentage of trigger towers that stay validated up to the maximum energy of 3.5 TeV (non transverse energy).

We show the results for all periods in table 4.2. The definitions in terms of the run interval, and the run used for the analysis are also shown. When there is missing information about some trigger towers in a given region (not enough data to perform the analysis), the $E^{100\%}$ can not be computed. In those cases we report the number of trigger towers with missing information (for example, "9 mt" means 9 towers with missing information).

For period D7-E, the combination of three physics runs was done to increase the number of pulses collected.

The hardware problems present during periods E to H, i.e, the failure of some Front End Boards (FEB) of the liquid argon calorimeter, do not affect our computations. The trigger towers containing cells affected by the failure continue to receive signals from cells processed by another FEB. This way, the failure is seen only as a reduction in the number of pulses collected for the towers. In figure 4.11 we show the number of pulses collected for the run 183081 (period G4), together with the coefficient k_E. There, we can see that the number of pulses collected falls down for the affected region, however this number is still high enough to perform the study.
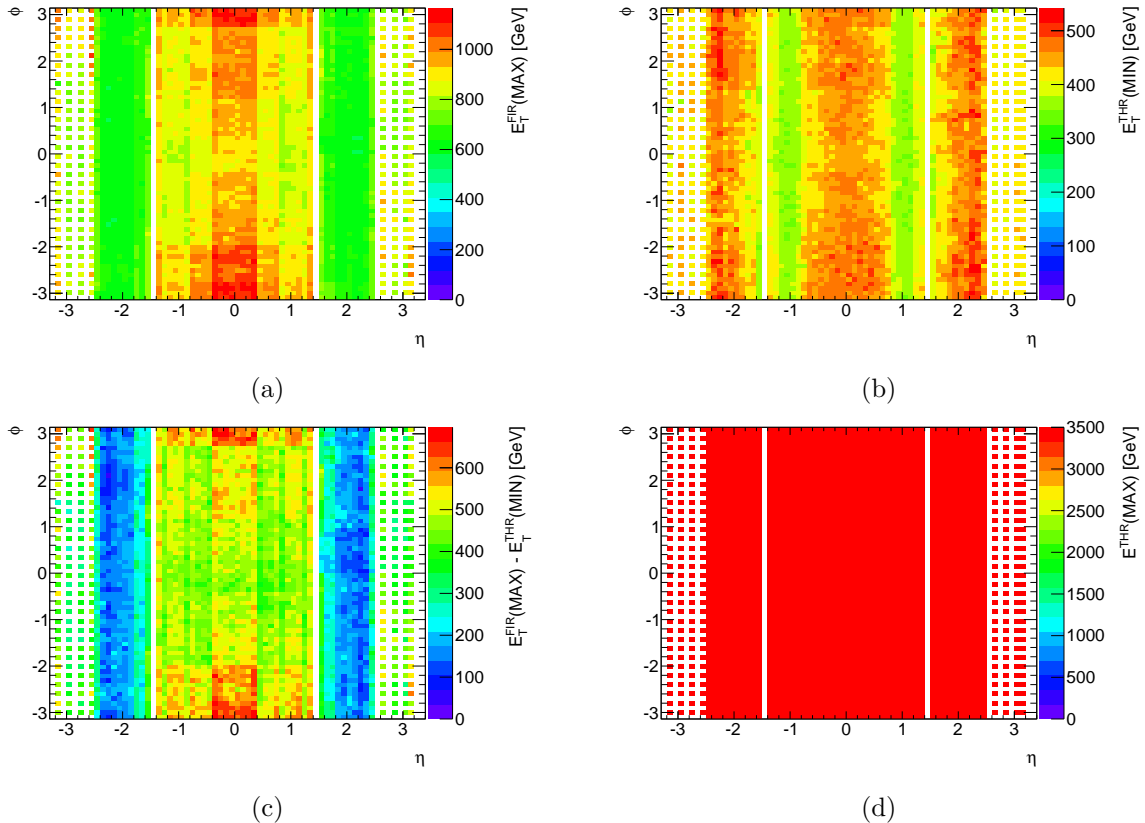
Figure 4.9: Detailed results for run 189483. Maps with values for every trigger tower are shown. For this run, the two validation conditions are fulfilled, so the BCID in all the trigger towers is validated. a) Maximum transverse energy of the FIR algorithm, b) minimum transverse energy of the threshold algorithm, c) overlap of the two algorithms, d) maximum energy of the threshold algorithm (all values in this map are greater or equal to 3.5 TeV).

4.3 High energy pulses in 2011 data

In addition to the validation method presented in the previous sections, we have performed a study which was made possible thanks to the large amount of data collected in 2011. We collected trigger tower pulses whose transverse energies were above a threshold of 200 GeV from a sample of 2011 physics data (around 40 % of the total). This allows to investigate the linearity of the ADC sample values with respect to energy, for saturated pulses and above. This linearity had been observed only in calibration runs (figure 4.7), and in physics runs but only for energies far below saturation levels. By doing this, we can test and validate the fitting procedure presented in section 4.2.2, basis of the validation method.

4.3.1 Collection and selection of pulses

We analyzed ESD for several 2011 runs, adding up to a luminosity of $\sim 2.1\,\mathrm{fb}^{-1}$. The events kept pass standard calorimeter data quality requirements. We selected pulses with the cut $E_T^{RO} > 200$ GeV, where E_T^{RO} is the readout energy of the pulse (the sum of all the readout energies of the cells belonging to the tower). Notice the difference with the selection of pulses explained in section 4.2.2, where saturated pulses were rejected. Doing this selection, we get a sample of 427124 pulses. We further refine the selection using the following criteria:

1. We demand "tower quality factor" < 65535 (see section 4.2.2). This is used to reduce the noise bursts, keeping a maximum of the saturated pulses that are useful for the study.

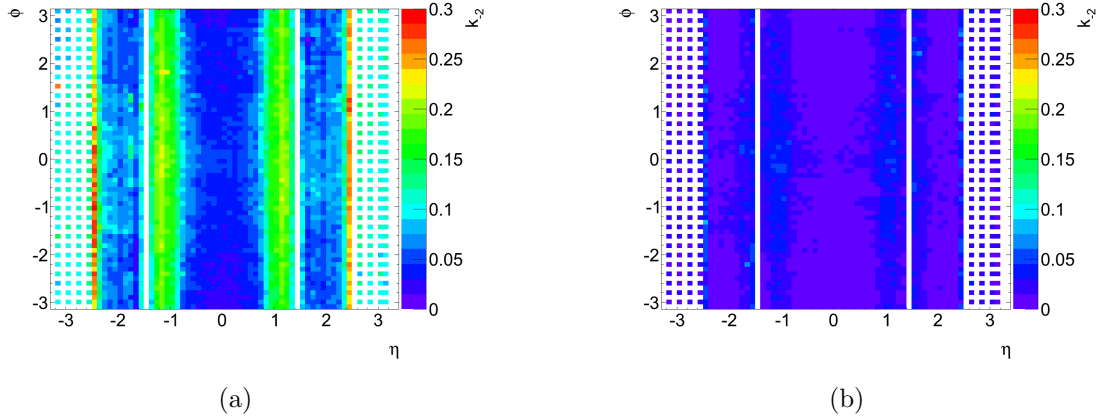Figure 4.10: The coefficient k_2 measured in calibration (a), and physics run 189483 (b). The values are clearly different, consequence of the differences in pulse shapes between physics and calibration.

Data period interval	Run interval	Sample run	Barrel $\|\eta\| < 1.4$		End-cap outer wheel $1.5 < \|\eta\| < 2.5$		End-cap inner wheel $2.5 < \|\eta\| < 3.2$	
			$E^{100\%}$ [GeV]	eff [%]	$E^{100\%}$ [GeV]	eff [%]	$E^{100\%}$ [GeV]	eff [%]
B-C	177986-178264	178044	2827	99.2	(4 mt)	99.7	3500	100
D1-D6	179710-180448	179710	3500	100	2721	99.9	3500	100
D7-E	180481-180776	180481,636,710	3500	100	3500	100	(9 mt)	96.5
F-H	182013-184169	183081	(1 mt)	99.4	2054	99.3	3500	100
I1-I2	185353-185856	185649	3494	99.9	3500	100	3500	100
I3-I4	185976-186275	186217	3500	100	3500	100	3500	100
I4-J1	186361-186533	186533	3384	99.9	3500	100	3500	100
J1-K3	186669-187501	187014	3500	100	3500	100	3500	100
K3-K6	187543-187815	187763	3299	99.9	3500	100	3500	100
L1-L6	188902-190046	189483	3500	100	3500	100	3500	100
L6-M4	190116-190975	190300	3500	100	3500	100	3500	100
M4-M10	191135-191933	191517	3500	100	3500	100	3500	100

Table 4.2: Results for all the periods of 2011 data-taking. The results are given in terms of the variable $E^{100\%}$ (maximum energy up to which the BCID is validated in all the towers), and "eff" (percentage of towers that stay validated up to 3.5 TeV). Notice that the energies are full energies, no transverse ones. When there is missing information to do the analysis for some towers, the $E^{100\%}$ can not be computed. In these cases, the number of missing towers (mt) is shown instead.

2. Pulses whose ADC samples have relative values inconsistent with the expected shape are eliminated. In detail, we require the pulses to satisfy the conditions:

$$\begin{aligned} ADC(n-1) &\geq ADC(n-2) \\ ADC(n) &\geq ADC(n-1) \\ ADC(n) &\geq ADC(n+1) \\ ADC(n+1) &\geq ADC(n+2) \end{aligned} \tag{4.11}$$

3. We require the pulses to have ADC values above a minimum level, characteristic of the electronic noise. In order to choose a reasonable minimum value, we looked at non-saturated good quality pulses already used in the previous low energy analysis (run 190300). In figure 4.12 we show the distribution of $ADC(n-2)$ and $ADC(n+2)$ for good quality pulses satisfying $E_T^{RO} > 200$ GeV. We choose as minimum values 3 and 5 standard deviations above the pedestal, respectively, i.e we demand:

$$\begin{aligned} ADC(n-2) &\geq p + 3\sigma_p \\ ADC(n+2) &\geq p + 5\sigma_p \end{aligned} \tag{4.12}$$
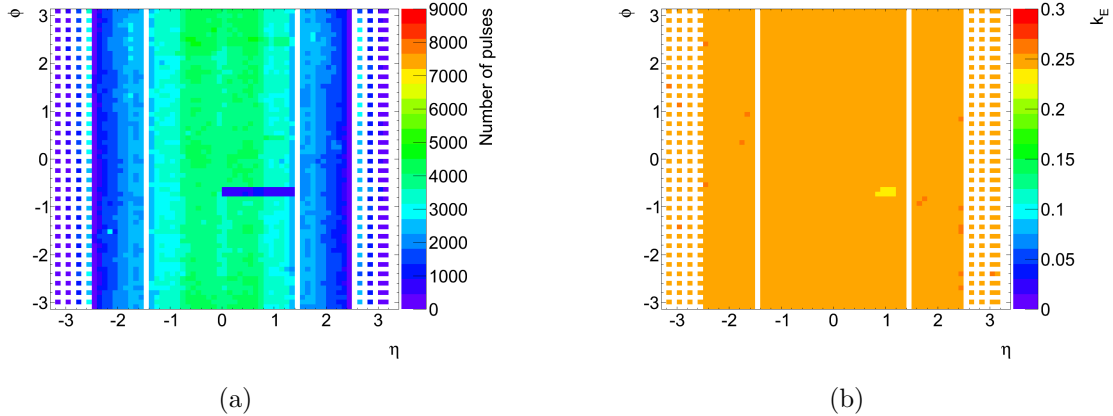
(a)   (b)

Figure 4.11: Number of pulses collected (a) and the k_E coefficient (b) for run 183081. The liquid argon hole region is visible, the number of pulses collected in the affected towers is much less than that of the neighboring unaffected towers. This does not affect the computations, as shown by the values obtained from the fits for the k_E coefficient.

In equation (4.12), we use the pedestal and the standard deviation corresponding to the tower and the period the pulse comes from. The vertical lines shown in figure 4.12 are tower averaged values, shown for illustrative purpose only.

(a)   (b)
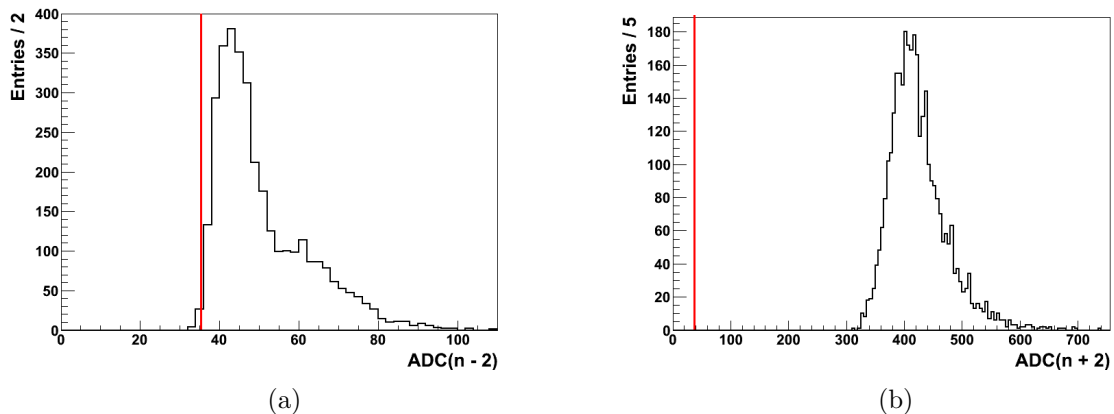
Figure 4.12: Distribution of (a) ADC(n - 2) and (b) ADC(n + 2) for good quality pulses with readout energies above 200 GeV, from run 190300. In red, the values chosen as noise threshold (tower averaged), 3 and 5 standard deviation above the pedestal value, respectively.

In table 4.3 we show the number of pulses kept after each selection cut was applied. We end up with 274476 pulses, distributed in the towers as shown in figure 4.13a. The energy spectrum of the pulses and their distribution according to the number of saturated samples are shown in figures 4.13b and 4.13c, respectively. 31 % of the total of pulses collected are saturated.

Events with high energy pulses in the TT represent only 0.2 % of the total of events analyzed. For this reason, in order to have a reasonable amount of events we need to combine the data for all the runs. Moreover, we combine towers having the same η coordinate, reducing the granularity to η rings. As the pulses have different shapes from one tower to another, and the L1Calo configuration changes according to the periods (as defined in table 4.2), we need to compensate for these differences before adding up pulses. We chose as reference period L1-L6 (run 189483), and the tower with $\phi = -2.6$ inside each η ring. The main plots we are interested in are the plots of ADC values as functions of readout energy, so we correct the readout energy values in a plot of ADC(n + i) in the following manner:

70

	Number of pulses
Original	427124
Passing (1) (Quality)	282667
Passing (2) (Basic shape)	282644
Passing (3) (Above noise level)	274476

Table 4.3: Number of pulses in the sample, after each of the selection criteria is applied.

(a)

(b)

(c)
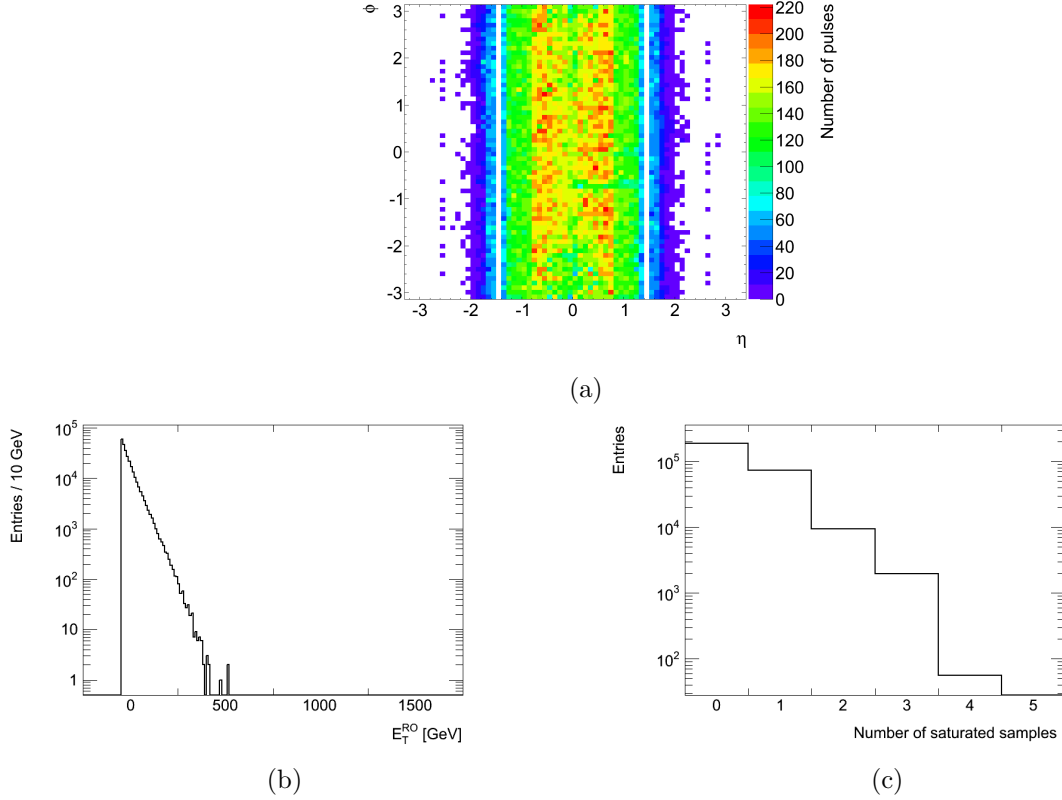
Figure 4.13: a) Distribution of the number of high energy pulses collected in the trigger towers; b) energy spectrum of the pulses; c) distribution of the pulses according to the number of saturated samples.

$$E_T^{RO}(corr) = E_T^{RO} \frac{k_{i\,E}}{k_{i\,E}^{ref}} \tag{4.13}$$

where $k_{i\,E} = k_i/k_E$ and $k_{i\,E}^{ref} = k_i^{ref}/k_E^{ref}$. In these definitions, the coefficients without label are those corresponding to the tower and the period the pulse belongs to, and the coefficients labeled "ref" are those of the tower of reference in the period L1-L6. By doing this, we scale the graphs $ADC(n+i) - p$ vs E_T^{RO} of a given tower to make it compatible with that of the reference tower in the η ring and in the reference period (the factors used to do the transformation are the slopes in the low energy region).

4.3.2 Validation using high energy pulses

The selection explained in the previous section provides enough statistics to draw conclusions only for the region defined by $|\eta| \leq 1.85$ (barrel and part of the end-cap outer wheel). In figure 4.14, we show as an example the behavior of the ADC samples with respect to the readout energy, for the TT η ring defined by $\eta = -0.05$. On top of the measured points, we show the straight lines with the slope $k_{i\,E}^{ref}$, i.e. the slope obtained from the fit in the low energy

region, for the reference tower and the reference period (notice that a factor of 2 is used in the plot of $n-2$).

In figure 4.14, the x coordinate (transverse energy) of the points was shifted according to the transformation given in equation (4.13). The response of the towers in physics looks similar to what was observed in calibration (figure 4.7). The samples n (figure 4.14c), $n+1$ (figure 4.14d and $n+2$ (figure 4.14e) have a linear behavior up to saturation, and the slope is the expected one from the measurement at low energy. This validates the fitting procedure done on these three samples, at low energy. The other two samples are treated using specific procedures, explained in the following paragraphs.

Behavior of $n-2$

The plot for the sample $n-2$ shows a large spread, without a clear linear behavior (figure 4.14a). In order to check the compatibility with the low energy study, we perform fits on the plots $ADC(n-2)$ vs. energy, and obtain values for the coefficients $k_{-2\,E}$, for every η region.

In figure 4.15a we show an example plot of $n-2$ for the region with $\eta = -0.05$. On the same plot, we show straight lines with slopes corresponding to the new fit, the low energy fit and twice the low energy fit. In figure 4.15b, the values of the new fits for each η region are shown, compared to the old coefficients (already including the safety factor of 2). We can see that the new slopes are smaller than twice the old ones.

Behavior of $n-1$

For the sample $n-1$, we observe a non linearity near the point of saturation (figure 4.14b). In order to estimate new $k_{-1\,E}$ coefficients, we draw a straight lines passing below the non-saturated points in the plots of ADC(n - 1), and take the slope of this line as the new coefficient. In figure 4.16a we show an example of this procedure for the region $\eta = -0.05$, and in figure 4.16b the comparison of the new and old coefficients for the η rings. We can see that the new slopes are smaller than the original ones.

Energy limits for high energy pulses

We recompute energy limits for the reference period L1-L6, using the updated values for the coefficients $k_{-1,E}$ and $k_{-2,E}$, together with low energy values for the other coefficients.

We compute $E^{THR}(MAX)$ using equation (4.10) without the factor of 2 in the denominator, and $E_T^{THR}(MIN)$, for each η region, and then convert back to tower granularity using the inverse of equation (4.13). To compute $E_T^{FIR}(MAX)$, we convert back to tower granularity the new coefficients $k_{-2\,E}$ and $k_{-1\,E}$, and use them together with values of the other coefficients obtained with the low energy fits, to obtain a new estimate per tower. In figure 4.17 we show the results of these computations. As we are trying to go beyond the threshold of 3.5 TeV, we modify the second validation condition using this time 4 TeV. We can see that all the examined towers fulfill the validation conditions.

As we have chosen as reference period L1-L6 (run 189483), we should compare the results shown in figure 4.17 with the validation results for this period done previously (figure 4.9). As can be seen from the TT maps, the distribution of $E_T^{FIR}(MAX)$ is unaffected. The values of $E_T^{THR}(MIN)$ change by a maximum of 80 GeV, but the overlap condition is still satisfied with enough margin. The new $E^{THR}(MAX)$ estimations are bigger than the old values, because the observed slopes are smaller. Thus the BCID validation obtained using high energy pulses gives results compatible with the validation at low energies.
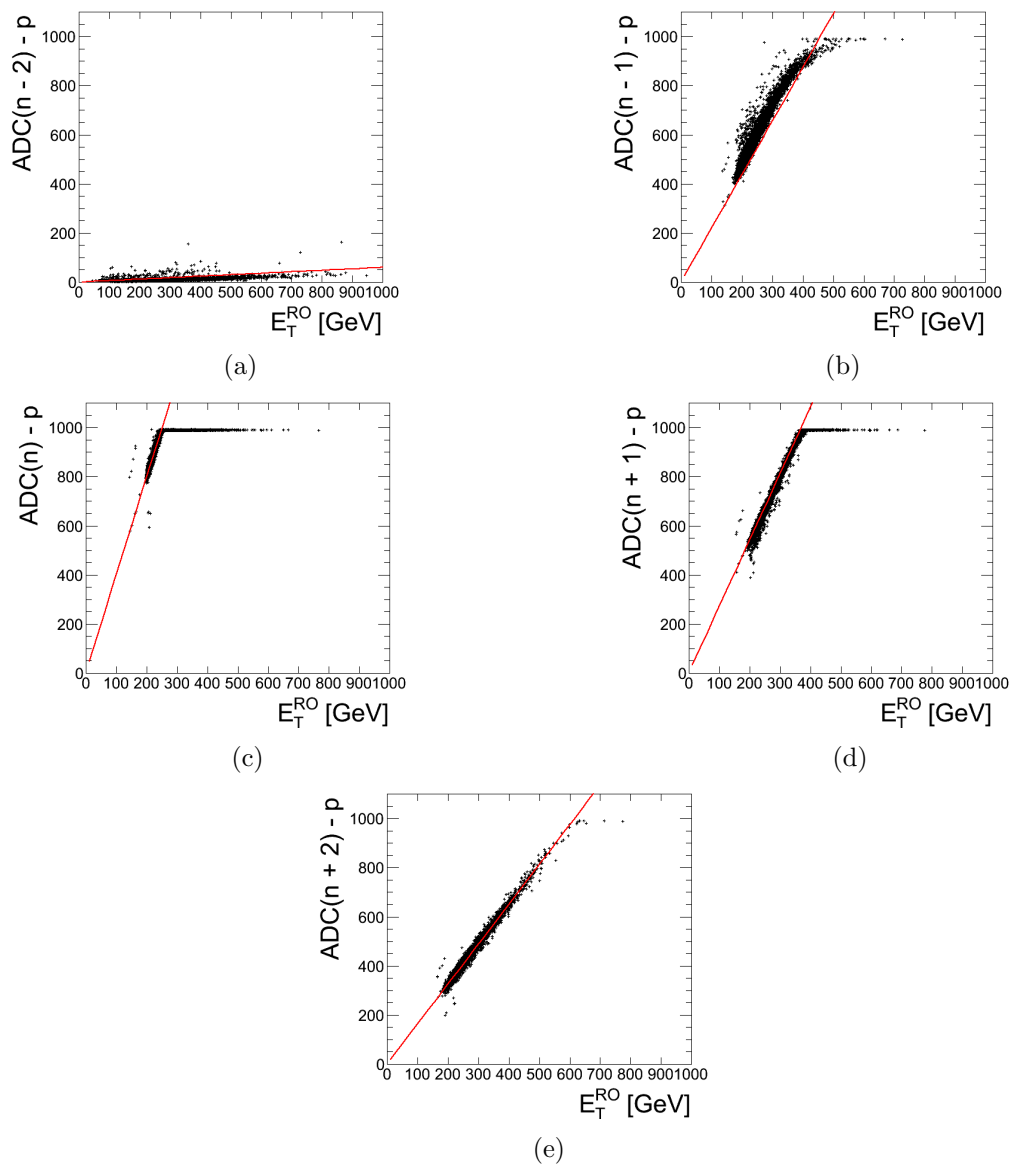
Figure 4.14: ADC samples vs. transverse energy as observed in the trigger tower region defined by $\eta = -0.05$ (barrel), in physics runs, using high energy pulses. The x axis of the plots is the calorimeter readout transverse energy. Straight lines with slopes measured using low energy pulses are shown in red. A linear behavior following the measured slope is observed before digital saturation, for the samples n (c), $n+1$ (d) and $n+2$ (e). The cases of $n-2$ (a) and $n-1$ (b) are discussed in the text.

(a)

(b)
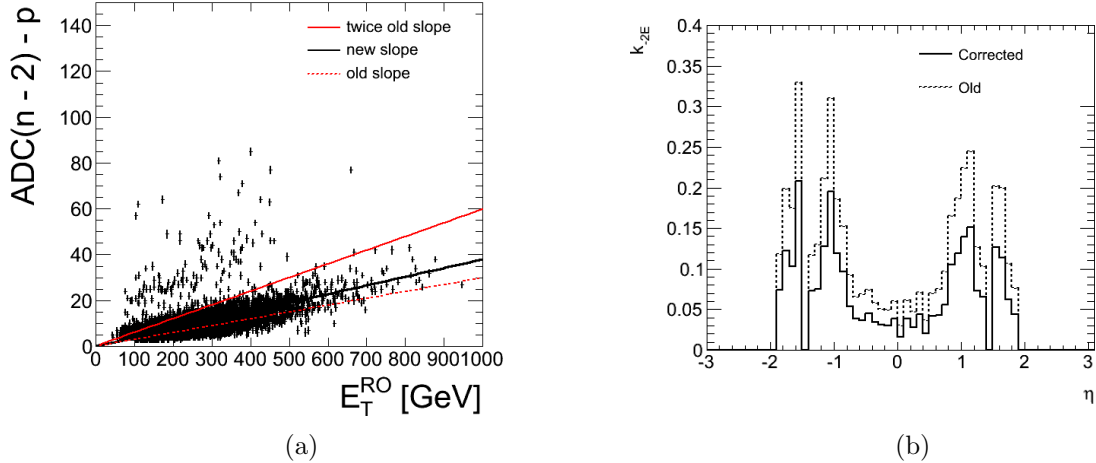
Figure 4.15: a) Plots ADC(n - 2) vs readout transverse energy for the region defined by $\eta = -0.05$. The results of the new fit and straight lines with slopes measured at low energy are shown (the measured slope and twice the slope). b) Comparison of the new slopes with the old ones, for each η ring.

(a)

(b)
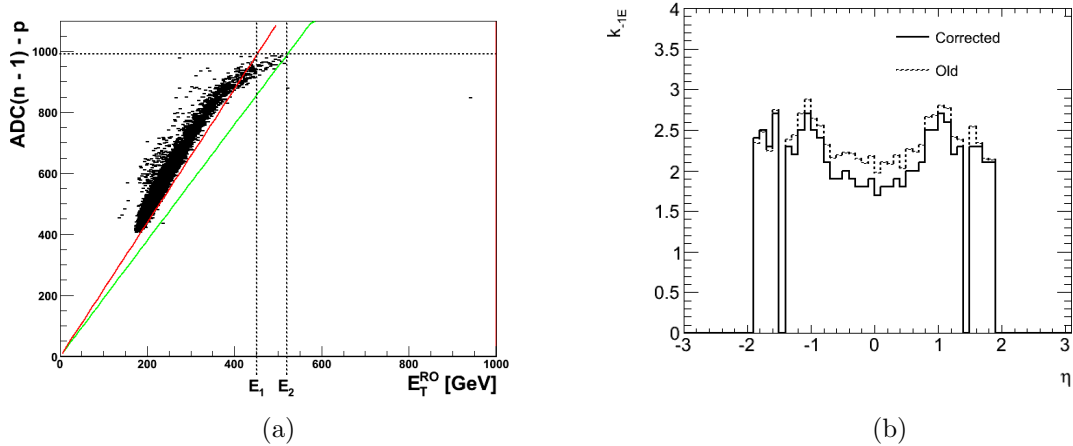
Figure 4.16: a) Estimation of new $k_{-1,E}$ coefficient, using a straight line passing below the points. A straight line with the original slope is shown in red. The old and new values for $E_T^{THR}(MIN)$ are indicated as E_1 and E_2, respectively. b) Comparison of the new slopes with the old ones, for each η ring.

4.4 Conclusions of the BCID validation study

The BCID validation method presented in this chapter allows to assess the performance of the calorimeter part of the LVL1 trigger for high energy objects, in particular when the energy is enough to saturate the trigger chain. The application of the method to all 2011 data-taking periods shows that the BCID performance is excellent, with only some potential problems due to mistrigger at very high energies. The BCID is certified valid for 99 % of towers up to 3.5 TeV for most of the 2011 periods. In addition, the analysis of high energy deposits in the trigger towers shows that the method based on only low energy measurements is reliable.

The method has the advantage of being based on the analysis of physics data, so its results can be readily used in the estimation of trigger BCID efficiencies for the physics analysis in ATLAS. However, when the trigger configuration is changed, it has to be repeated in order to cope with possible differences in the TT responses.

The accuracy of the method could be improved with the much higher statistics available by 2012. The collection and analysis of more pulses, specially the high energetic and saturated ones, would improve the understanding of the TT electronic response. This is becoming very

(a) (b)

(c) (d)
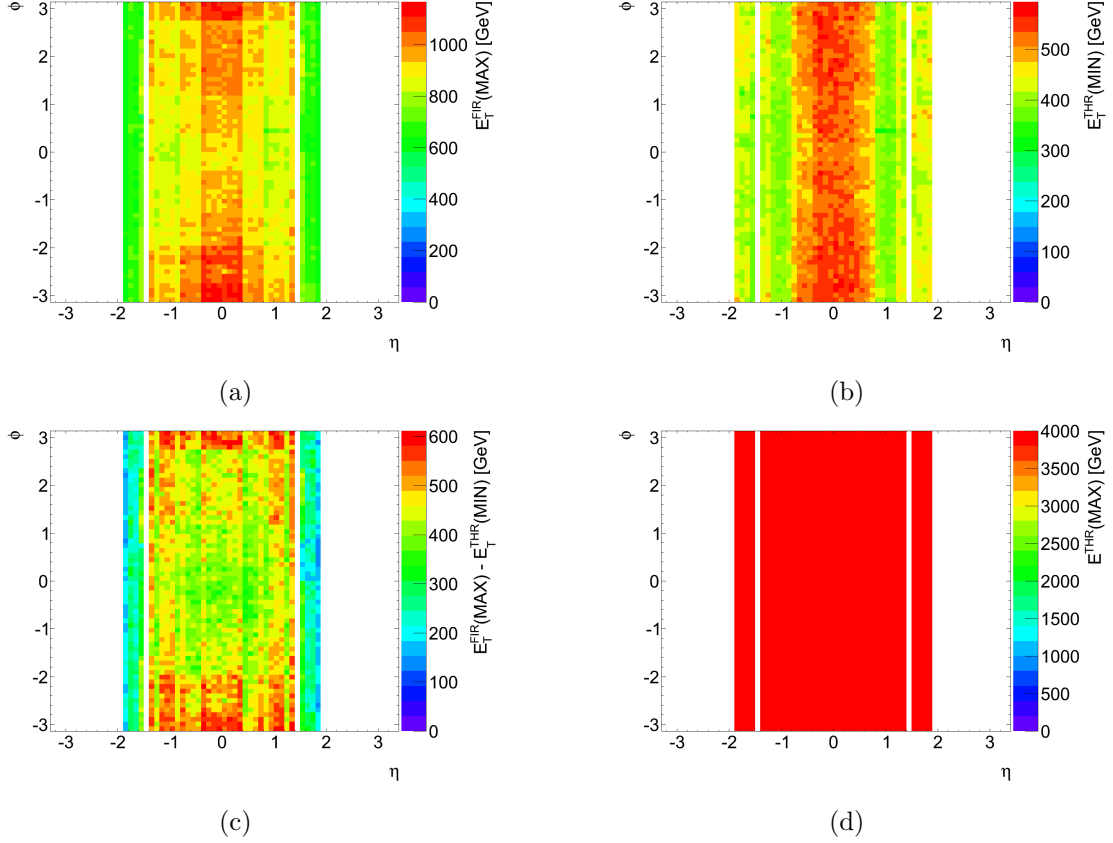
Figure 4.17: Results using new values of the coefficients. All data was normalized to period L1-L6 (run 189483). The two validation conditions are fulfilled. a) Maximum transverse energy of the FIR algorithm, b) minimum transverse energy of the threshold algorithm, c) overlap of the two algorithms, d) maximum energy of the threshold algorithm (all values in this map are greater or equal to 4 TeV).

pertinent, given the plans to increase the beam energy of the LHC, which will require the trigger system to respond properly to energies of up to 6.5 TeV.

The results presented here are to be taken into account by future performance studies of the BCID, for example changes in the BCID algorithms, and the electronic setup of the PPM. Also, it could serve as basis for future validation methods designed to test future setups of the L1Calo, needed to cope with the challenging environment of collisions at 13 TeV.

Chapter 5

Measurement of the Z boson differential cross-section in transverse momentum in the electron-positron channel in ATLAS

In this chapter we present the measurement of the Z boson transverse momentum distribution using ATLAS proton-proton collision data, taken during the 2011 LHC run at a center-of-mass energy of $\sqrt{s} = 7$ TeV. As was mentioned in section 1.3, the Z boson is produced in hadron colliders through Drell-Yan processes, and it is accompanied by the emission of one or more partons, which allows the Z boson to be produced with non-zero transverse momentum.

The Z boson transverse momentum distribution is an important observable that can be used to constrain theoretical models based on QCD fixed order perturbative predictions and resummation schemes. In addition, the comparison of the measured spectrum with MC generators predictions can be used to tune parton shower parameters. The MC tuning can in turn improve substantially the precision of other measurement which rely on them, like the W mass measurement.

The Z boson is reconstructed using its decay products. We concentrate on the clean signature provided by the decay mode electron-positron: $Z \rightarrow e^+ e^-$, thus the Z reconstruction depends on the electron reconstruction performance of the detector (throughout this chapter, we refer to the pair electron-positron as the electron pair). In order to avoid uncertainties due to the luminosity measurement and detector inefficiencies, we perform a normalized measurement in the fiducial region:

$$\frac{1}{\sigma^{\text{fid}}} \frac{\mathrm{d}\sigma^{\text{fid}}}{\mathrm{d}p_{\text{T}}^Z} \tag{5.1}$$

where σ^{fid} is the measured cross-section of the process $pp \rightarrow Z + X$ (X represents the hadronic products and the underlying event), multiplied by the branching ratio of $Z \rightarrow ee$. The "fiducial region" is defined as the explored region of the phase space. The fiducial region is restricted using kinematic requirements, in order to avoid regions where the detector is known to be inefficient, and at the same time reduce the background, thus reducing the sources of uncertainty. In addition, three regions of Z boson rapidity bins are defined, and the measurement is repeated inside each region, in order to probe different values of the parton momentum fraction (see section 1.3).

Throughout this chapter we use the notation p_{T}^Z to denote the transverse momentum of the Z boson reconstructed from the electron pair, and y^Z its rapidity. We use $\mathbf{U}$ to denote the measured normalized p_{T}^Z distribution, and the content of its N bins are denoted by U_i, with

$i = 1..N$ (in general, we use boldface characters to denote histograms, and normal characters with sub indexes to denote the content of the bins). Notice that the measurement includes a small interference effect from the production of photons (via the process $pp \rightarrow \gamma + X \rightarrow e^+ e^- + X$) which is taken into account as part of the signal (we use the notation Z boson to refer to both, Z and γ).

The chapter begins with details of the data and MC samples used, the selection of events and the different corrections applied. Then we describe the different stages of the measurement, including the estimation of background, the unfolding procedure and the uncertainty estimation. Next, we give the results of the measurement, for the inclusive analysis and for the three regions of rapidity. Finally, we compare the result with the muon channel measurement done using the same dataset, describe the method used for the combination of channels and present the combined results.

5.1 Event selection

5.1.1 Data and MC samples

The analysis was performed using data collected in 2011, when the LHC delivered proton-proton collisions at $\sqrt{s} = 7$ TeV with an integrated luminosity of $5.5 \, \text{fb}^{-1}$. Only data taken during stable beam conditions, and with fully operating magnet system, tracking and calorimeter as defined by the ATLAS data quality group are considered. The luminosity of the data sample taking into account these requirements is $4.64 \, \text{fb}^{-1}$.

The input files used for the analysis are D3PD produced after several steps of data processing (see section 2.3.1). In order to reduce the processing time and ease the handling of data files, skimmed D3PD were used, meaning that only selected events were looked at. The skimming was done by selecting events having at least two leptons (electrons or muons) with p_T higher than 10 GeV, electrons passing medium identification criteria (see section 3.2.3), and muons loose criteria [50].

In order to model the properties of signal and background processes, we use fully simulated Monte Carlo (MC) samples. The detector is simulated using the GEANT4 program [51], and the simulated response to the MC events is given as input to the same reconstruction chain used for real data. The Monte Carlo samples used in the analysis are shown in table 5.1. The theoretical cross-section values for the electroweak samples ($Z \rightarrow ll$, $W \rightarrow l\nu$ and diboson) are taken from [52], the uncertainties arising from the choice of PDF, factorization and renormalization scale dependence and the size of the NLO and NNLO corrections. For the $t\bar{t}$ sample, the cross-section value is taken from [53].

The baseline MC sample used to model the signal process ($Z \rightarrow ee$) and the detector response is the PowhegPythia sample (dataset 108303). It was produced with the Powheg generator [21], which provides next-to-leading-order matrix element implementation of the hard process, and use the PDF set CT10 NLO PDF [54]. Parton showering is provided by Pythia6 [15] with the AMBT1 tune [55]. The effect of final state radiation is simulated with Photos [56]. The other signal samples (Pythia, Mc@nlo and Sherpa) are used as auxiliary samples, to estimate uncertainties and other effects.

5.1.2 Selection steps

The selection of events is done applying "cuts" on the event variables, following the recommendations of the ATLAS performance and physics groups [57]. The values and variables used as cuts are optimized to have the highest signal to background ratio and according to the involved subdetectors acceptance. They are applied in sequence, i.e., one given cut is applied to events passing the one immediately before. In the following paragraphs we describe each one of the steps of the selection.

Process	Generator	Dataset ID	Number of events	$\sigma \times BR \times \epsilon_{filter}$ [nb]	$\delta\sigma$ [%]
		Signal samples			
$Z \to ee$	PowhegPythia	108303	$\sim 20 \cdot 10^6$	1.006	5
$Z \to ee$	Pythia	106046	$\sim 10 \cdot 10^6$	0.99	5
$Z \to ee$	Mc@nlo	106087+129913	$\sim 10 \cdot 10^6$	0.99	5
$Z \to ee$	Sherpa	147770	$\sim 10 \cdot 10^6$	1.070	5
		Background samples			
$W \to e\nu$	Pythia	106043	$\sim 40 \cdot 10^6$	10.46	5
$W \to \tau\nu$	Pythia	107054	$\sim 10^6$	10.46	5
$Z \to \tau\tau$	Pythia	106052	$\sim 10^6$	0.99	5
$t\bar{t}$	Mc@nlo	105200	$\sim 15 \cdot 10^6$	0.08	7
WW	Herwig	105985	$\sim 2.5 \cdot 10^6$	0.0175	7
ZZ	Herwig	105986	$\sim 0.25 \cdot 10^6$	0.00128	7
WZ	Herwig	105987	$\sim 10^6$	0.00574	7

Table 5.1: MC samples used in the analysis.

Trigger

We use a trigger requiring the online reconstruction and identification of two electrons passing the lowest p_T threshold available (12 GeV). The identification is required to pass the "medium" selection (see section 3.2.3). The trigger definitions change according to the LHC collision parameters and ATLAS configuration. The details of the triggers used are given in appendix B.

LAr Error cleaning

The LAr error flag is used to remove events where there were known hardware failures in the LAr calorimeter, for example failures of FEB or voltage drops in the calorimeter electrodes. This information is stored as a variable that can be read offline.

Vertex cleaning

We require that the primary vertex has at least 3 tracks associated. The primary vertex is defined as the vertex with the largest total p_T (scalar sum of the p_T of the associated tracks). This requirement is done in order to select collision events (reject events without real reconstructed primary vertices, for example from cosmic rays).

Electron selection

For each event passing the cleaning explained above, we look at the electron objects stored for the event (containing offline reconstructed variables), and demand the following requirements:

- Ask the objects to be reconstructed in areas of the calorimeter without local hardware problems.

- Ask the objects to pass the electron reconstruction algorithm for the central region (this is done to remove photon background).

- Ask the objects to pass the medium identification. As explained in section 3.2.3, this requirement removes undesired objects like electrons coming from semi-leptonic decays, photon conversions, and fakes.

- The electron should pass the kinematic requirement $p_T > 20$ GeV. This is done to work in a kinematic region where the electron performance of the detector has been well tested, having a large background rejection in the ID and an accurate measurement of the energy. In addition, the cut is far above the trigger threshold, avoiding trigger efficiency problems.

- The electrons are required to pass the acceptance requirement: $|\eta_{cl}| < 2.47$, and ($|\eta_{cl}| < 1.37$ or $|\eta_{cl}| > 1.52$). This is done in order to work in the central region of the ECAL which has well known performances, and to avoid the "crack" between the barrel and end-cap parts of the ECAL ($1.37 \leq |\eta_{cl}| \leq 1.52$), where the electron reconstruction is known to be less efficient (see for example figure 3.10).

Final event selection

Once "good" electrons have been selected, we demand the event to have exactly two such electrons (in order to avoid background with more electrons in the final state, like ZZ production), ask the two electrons to have opposite charges, and to have an invariant mass close to the Z mass peak (window 66 GeV $< m_{ee} <$ 116 GeV). The Z boson is reconstructed using the selected electron pair.

The selection requirement are summarized in table 5.2.

Trigger	`EF_2e12_medium` for data periods D to J
	`EF_2e12T_medium` for data period K
	`EF_2e12Tvh_medium` for data periods L to M
Event cleaning	No LAr error
	The primary vertex has ≥ 3 tracks
Electron selection	Object quality
	Medium Identification
	$p_T > 20$ GeV
	$|\eta_{cl}| < 2.47$ and ($|\eta_{cl}| < 1.37$ or $|\eta_{cl}| > 1.52$)
$Z \to ee$ candidate selection	Exactly two electrons
	Electrons oppositely charged
	66 GeV $< m_{ee} <$ 116 GeV

Table 5.2: Summary of selection requirements.

The results of the selection applied to 2011 data are given in table 5.3 in terms of number of events passing each step of the selection. A total of 1.2 million events were selected in data. The absolute efficiencies are computed with respect to the initial number of events (before skimming), and the relative efficiencies with respect to the previous cut in the selection chain.

5.1.3 Corrections on data and MC

The MC samples used in the analysis include a full simulation of the detector and the collisions according to the 2011 LHC and ATLAS setup. The simulation is tuned to reproduce the detector response as close as possible to reality. However, there are physical and detector effects that either were not simulated correctly, or that were measured more accurately after the production of the MC samples was done. In order to correct these effects and obtain the best possible agreement between data and MC, some corrections are done, that are explained in the following sections.

Cut name	Number of events	ϵ_{abs} [%]	ϵ_{rel} [%]
Original	385322059	-	-
Skim	88598631	22.99	-
GRL	80613168	20.92	90.99
LAr error flag	80372226	20.86	99.70
Vertex	80333880	20.85	99.95
Trigger	3070944	0.80	3.82
Exactly two "good" electrons	1327362	0.34	43.24
(including acceptance, p_T cut and identification)			
Charge	1301351	0.34	98.01
Invariant mass	1228863	0.32	94.43

Table 5.3: Number of events in 2011 data passing the selection. The absolute efficiencies (computed with respect to the original number of events) and the relative ones (computed with respect to the number of events passing the cut immediately before) are given.

Pile-up reweighting

The MC samples used in 2011 were generated with four different pile-up conditions, in order to match the evolution of the pile-up in the real collisions [58]. However, the amount of events simulated with a given amount of pile-up in a sample does not match necessarily the proportion of events in data with this same condition. To correct for this effect, pile-up weights are applied to all MC samples. In figure 5.1 we show the distribution of the μ variable (defined as the average number of interactions per bunch-crossing), as observed in data and compare it with raw MC and pile-up reweighted MC. Applying the weights improves the χ^2/ndof between data and MC distributions from $\sim$200 to $\sim$25. The weights were obtained using the official tool [59], and are applied on an event-by-event basis.
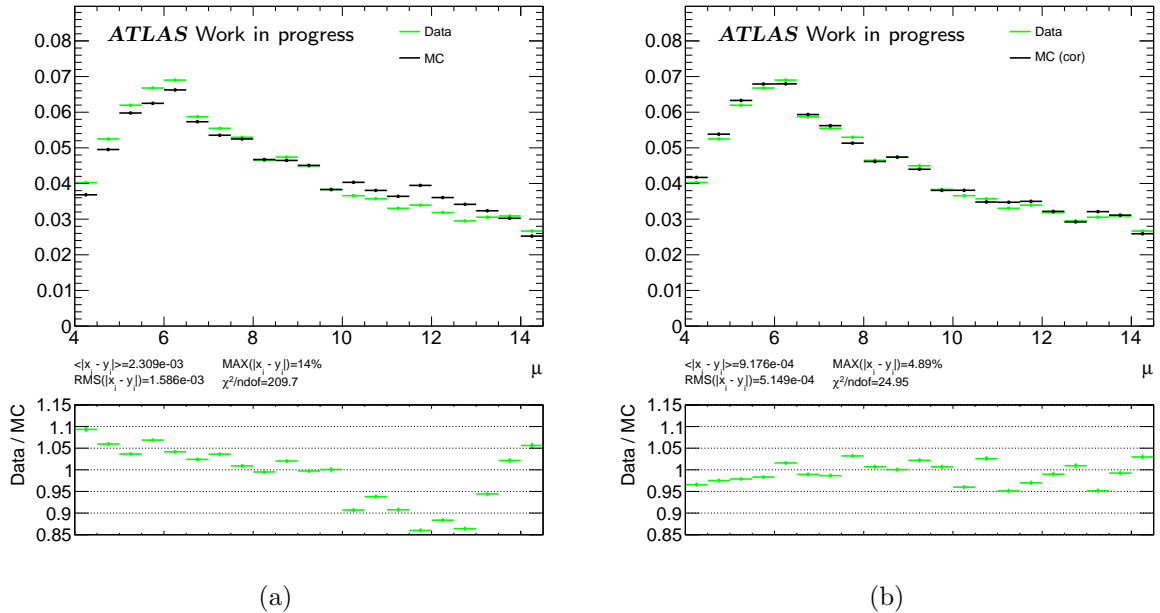

Figure 5.1: Pile-up distributions observed in data (average number of interactions per bunch-crossing), compared to the distribution in the MC signal sample. (a) Without correcting the MC, (b) applying the pile-up weights.

Z vertex position

The distribution of the z coordinate of the primary vertex (z_{vtx}) differs in data and the MC samples. Similarly for the case of the pile-up, weights are applied to the MC events in order to correct for this effect. In figure 5.2 we show the effect of this reweighting, comparing the original and corrected distributions in MC with data. We can see how after the reweighting the distributions in data and MC agree within 1 % for the central bins ($|z_{vtx}| < 100$ mm). The weights were obtained using the tool documented in [57].
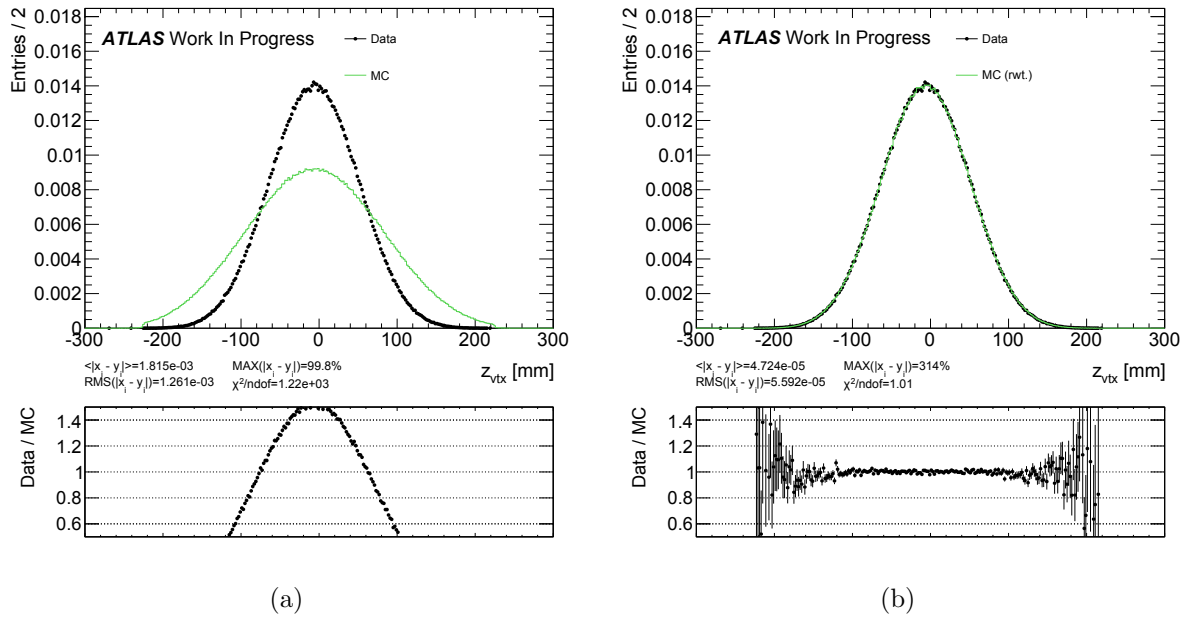

(a)   (b)

Figure 5.2: Distribution of the z coordinate of the primary vertex for data and signal MC. (a) Original MC, (b) reweighted MC.

Boson p_T distribution reweighting

Looking at the p_T^Z shapes predicted by the MC samples produced for 2011 analysis, it was noticed that their description was not in agreement with the observed distribution in data. On the other hand, the description made by the MC PYTHIA sample produced for 2010 analysis (with generation and simulation adjusted for 2010 collisions), was in better agreement with data, both in 2010 and in 2011. The MC PYTHIA samples produced for 2010 analysis were done using the AMBT1 tune [60][55], while the 2011 ones were done using the AUET2B tune [61][62][63].

In order to have the best possible description in MC, we perform a reweighting of all the MC signal samples to the p_T^Z shape of PYTHIA obtained with the 2010 simulation (from now on, we call this shape the "PYTHIA-MC10 shape"). The reweighting is done in the following way:

- We plot truth distributions for each sample at truth level (using Born leptons), defined in the fiducial region of the measurement (section 5.2). The distributions are defined with a finer binning than the one used in the measurement (defined in section 5.2.1), in order to keep the fine structure of the distribution.

- We compute weights comparing the truth distributions of each MC signal sample with the PYTHIA-MC10 shape.

- The computed weights are used on an event-by-event basis to reweight all the distributions of the MC samples.

Figure 5.3 shows an example of the reweighting procedure. We show the original shapes for the MC samples PYTHIA and POWHEGPYTHIA before and after reweighting, and data. The distributions are taken at detector level. The original distributions show a disagreement with respect to data of ~ 20 % in the first 3 bins, which is reduced to ~ 4 % with the reweighting to the PYTHIA-MC10 shape.
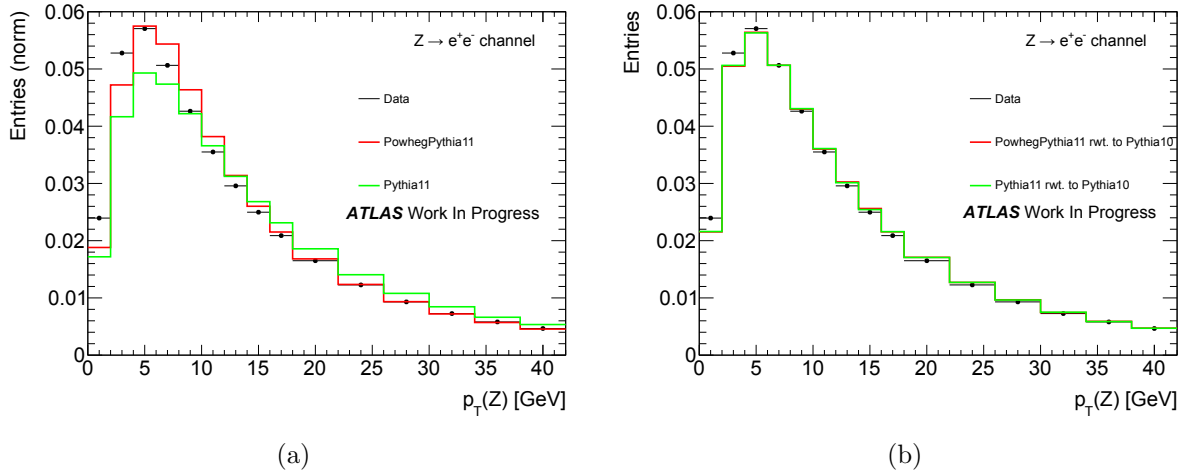

Figure 5.3: Comparison of p_T^Z shapes at detector level, for data and the MC signal samples used in the analysis (POWHEGPYTHIA and PYTHIA). The plots show normalized number of entries. (a) The MC original distributions, (b) the distributions reweighted to the PYTHIA-MC10 shape.

The three corrections explained above are considered independent, thus the weights obtained for each one are multiplied and applied on an event-by-event basis. Notice that the effect of the p_T^Z shape modeling in MC is investigated as a source of systematic uncertainty (section 5.3.5).

Energy scale and resolution

Correction factors are applied to data in order to correct for remaining mis-calibration of the electron energy (as described in section 3.2.5). The official tool [64] is used in order to get the η dependent scale factors. In figure 5.4a we show the output of the tool (E_{cor}/E_{raw}) as a function of the η coordinate of the cluster. The correction are of the order of 2 % in the acceptance region of the measurement.

The energy resolution is corrected in MC by smearing the electron energy, that is, changing the reconstructed energy value in order to compensate for the difference in the resolution modeling of the detector simulation with respect to the resolution measured in real data (see section 3.2.5). The same official tool used for the energy rescaling is used [64]. In figure 5.4b we show the amount of smearing (standard deviation of the gaussian distribution used to generate the energy correction), as a function of the η coordinate of the calorimeter cluster. The smearing goes up to 3 % of the electron energy.

In figure 5.5 we show the combined effect of the two corrections (energy scale and resolution). After the corrections are applied, the Z line shape in data and MC agree within 5 % (the uncorrected distributions disagree up to 23 % in the range 80 - 100 GeV).

Efficiencies

The MC samples are weighted to correct for differences in the modeling of electron reconstruction, identification and trigger efficiencies with respect to data. These efficiencies are measured in data using tag and probe methods, as explained in section 3.2.4. Using these efficiency measurements, "scale factors" (SF) for a given selection cut C are defined as the ratio between the efficiency of the cut measured in data and the efficiency of the cut measured in MC:
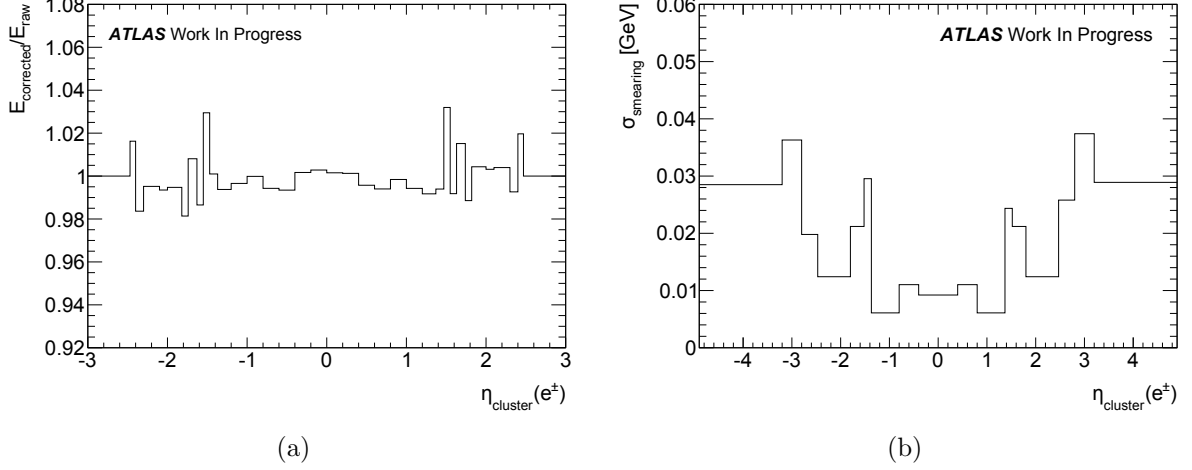
Figure 5.4: Energy scale correction factors used to correc data (a), and amount of smearing used to correct MC (b), as a function of the η coordinate of the electromagnetic cluster. The energy scale correction is of the order of 1 % to 2 %, while the additional smearing goes up to 3 %.

$$\mathrm{SF}_{(C)} = \frac{\epsilon_{(C)}^{\mathrm{data}}}{\epsilon_{(C)}^{\mathrm{MC}}} \tag{5.2}$$

In figure 5.6 we show the values of the electron scale factors for reconstruction, identification and trigger as functions of the electron p_T and the η coordinate of the cluster. The trigger scale factors shown correspond to a single electron trigger, which requires the online reconstruction of an electron with p_T larger than 12 GeV and passing medium identification criteria. The scale factors were obtained using the tool provided by the ATLAS performance group [65].

Notice that the trigger SF shown in figure 5.6 are for a single electron trigger, while in the selection we require the event to pass a trigger with two electrons (section 5.1.2). In order to compute the SF of the dielectron trigger, we use the equation:

$$\begin{aligned}
\mathrm{SF}_{(diel-trig)} &= \frac{\epsilon_{(diel-trig)}^{\mathrm{data}}}{\epsilon_{(diel-trig)}^{\mathrm{MC}}} \\
&= \frac{1 - [1 - \mathrm{SF}_{(el-trig)}(\mathrm{e}_1) \cdot \epsilon_{(el-trig)}^{\mathrm{MC}}(\mathrm{e}_1)] \cdot [1 - \mathrm{SF}_{(el-trig)}(\mathrm{e}_2) \cdot \epsilon_{(el-trig)}^{\mathrm{MC}}(\mathrm{e}_2)]}{1 - [1 - \epsilon_{(el-trig)}^{\mathrm{MC}}(\mathrm{e}_1)] \cdot [1 - \epsilon_{(el-trig)}^{\mathrm{MC}}(\mathrm{e}_2)]}
\end{aligned} \tag{5.3}$$

where $\mathrm{SF}_{(el-trig)}(\mathrm{e}_i)$ and $\epsilon_{(el-trig)}^{\mathrm{MC}}(\mathrm{e}_i))$ are the SF and MC efficiency for the single electron trigger, respectively, both evaluated on the coordinates of electron i. The total efficiency weight is computed as follows:

$$\mathrm{w}_{eff} = \mathrm{SF}_{(reco)}(\mathrm{e}_1) \cdot \mathrm{SF}_{(reco)}(\mathrm{e}_2) \cdot \mathrm{SF}_{(ID)}(\mathrm{e}_1) \cdot \mathrm{SF}_{(ID)}(\mathrm{e}_2) \cdot \mathrm{SF}_{(diel-trig)} \tag{5.4}$$

Here, $\mathrm{SF}_{(C)}(\mathrm{e}_x)$ is the scale factor of type C for the electron x. This weight is used on an event-by-event basis in order to correct the MC. In figure 5.7 we show the effect of this reweighting, comparing the p_T^Z distribution at reconstruction level in signal MC with and without the efficiency weights. The effect of the weights is small on the p_T^Z shape, < 0.2 % for the reconstruction scale factors, $< 1\%$ for the identification scale factors and < 0.05 % for the trigger scale factors.
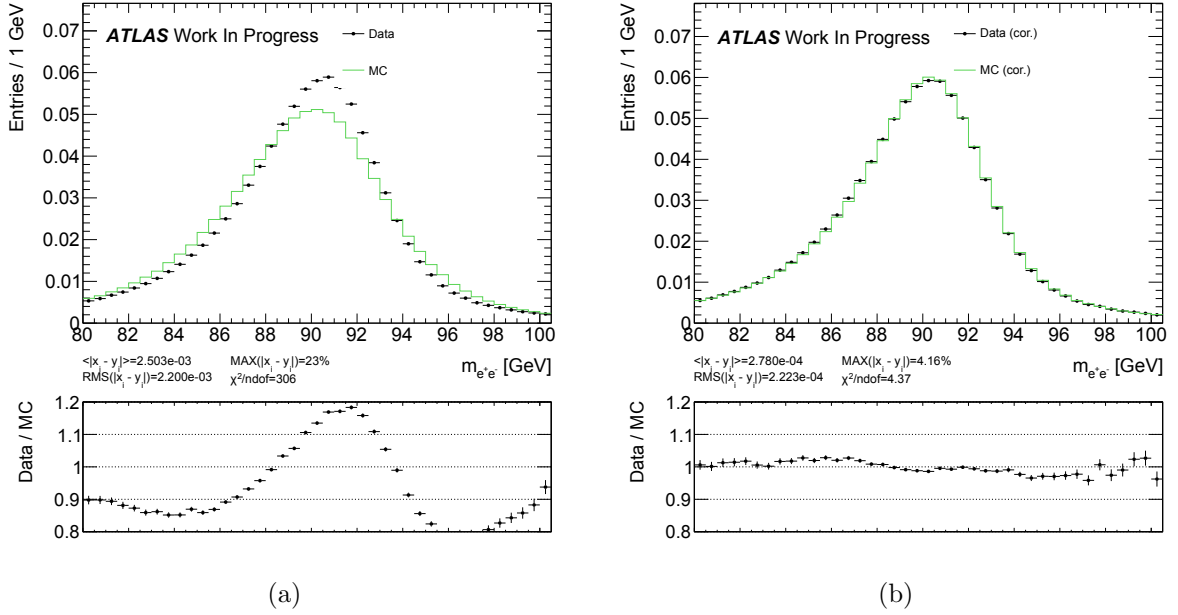
Figure 5.5: Comparison of the Z boson line shape for data and signal MC (PYTHIA sample). Both distributions are normalized to unity. (a) Comparison without applying the scale and resolution corrections. (b) Comparison with the corrections applied. The corrected distributions agree within 5 %, while the uncorrected ones show a disagreement up to 23 %.

5.2 Cross-section measurement

The measurement of the normalized cross-section is performed in the fiducial region defined by the following requirements:

- Acceptance: $|\eta(e)| < 2.4$.

- Transverse momentum of electrons: $p_T(e) > 20$ GeV.

- Invariant mass window: 66 GeV $< m_{ee} < 116$ GeV.

Notice that the definition of the fiducial region is similar to the the event selection (table 5.2), except for the requirement $|\eta| < 2.4$, which is defined in order to have a common phase space with the muon channel measurement. This difference means that a small acceptance correction have to be applied to the electron channel measurement, in order to be combined with the muon channel measurement (see section 5.6).

The measurement proceeds as follows:

- The selected events are used to define the raw distribution of events in bins of p_T^Z. The binning used in the measurement is defined later in section 5.2.1.

- The background that is not eliminated by the event selection is estimated and subtracted from the raw p_T^Z distribution.

- The resulting distribution is corrected to compensate the detector effects (bin migrations due to resolution, and inefficiencies), and extrapolate the measurement to the correct fiducial region. This is called unfolding.

- Finally, the resulting unfolded distribution is used to estimate the normalized spectrum. For this, each bin content is divided by its width, and the integral of the distribution is computed and used to normalize the spectrum.
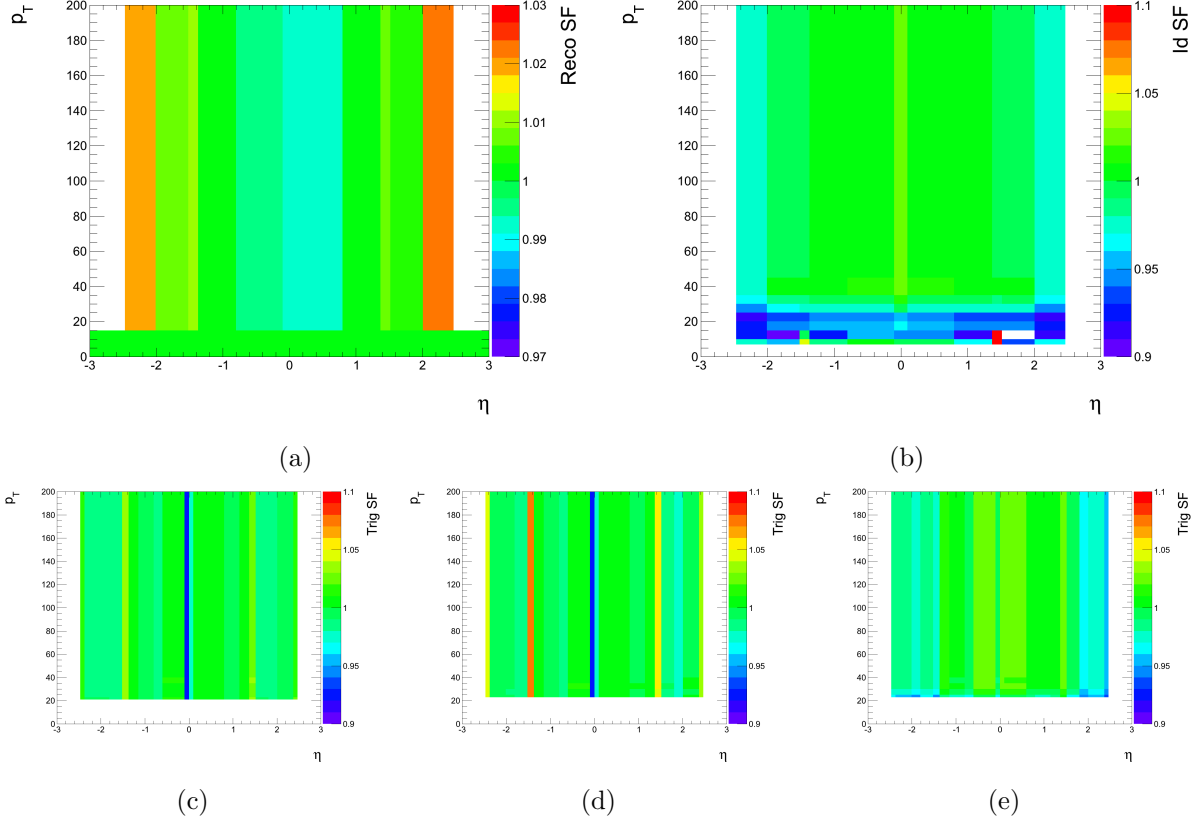
Figure 5.6: Scale factors for electrons, defined as the ratio of the efficiencies measured in data and the efficiencies measured in MC. The scale factors are given as functions of the η coordinate of the electromagnetic cluster and its p_T. (a) Reconstruction scale factor, (b) identification scale factor, (c) (d) and (e) trigger scale factor for different data-taking periods.

The unfolding, explained later in section 5.2.4, is done assuming that the "true" level is the Z boson propagator level, before any QED final state radiation (see section 1.4). This allows to perform the combination with the muon channel result (section 5.6). However, we give correction factors that allow to convert the result to bare and dressed kinematics. These factors are defined as:

$$k_i^{bare} = \frac{U_i^{bare}}{U_i^{Born}}, \quad k_i^{dressed} = \frac{U_i^{dressed}}{U_i^{Born}} \tag{5.5}$$

where the normalized distributions U^{bare}, $U^{dressed}$ and U^{Born} are computed from MC at truth level, in the fiducial region.

In the following sections we describe the binning, background estimation and unfolding procedure.

5.2.1 Binning

The binning is chosen to balance statistical and systematic uncertainties while taking into account the typical experimental resolution. The chosen binning is 2 GeV steps from 0 GeV to 18 GeV, then 4 GeV steps from 18 GeV to 54 GeV, then bins of increasing size, 6 GeV, 10 GeV, 20 GeV, 50 GeV, 100 GeV, 500 GeV. The last bin ends at 800 GeV. This gives a total of 26 bins.

In addition to this, we have to consider the bin purity, defined as the fraction of reconstructed events in a given p_T^Z bin, that were originally in that bin at truth level, divided by the total number of events in the bin at reconstruction level:
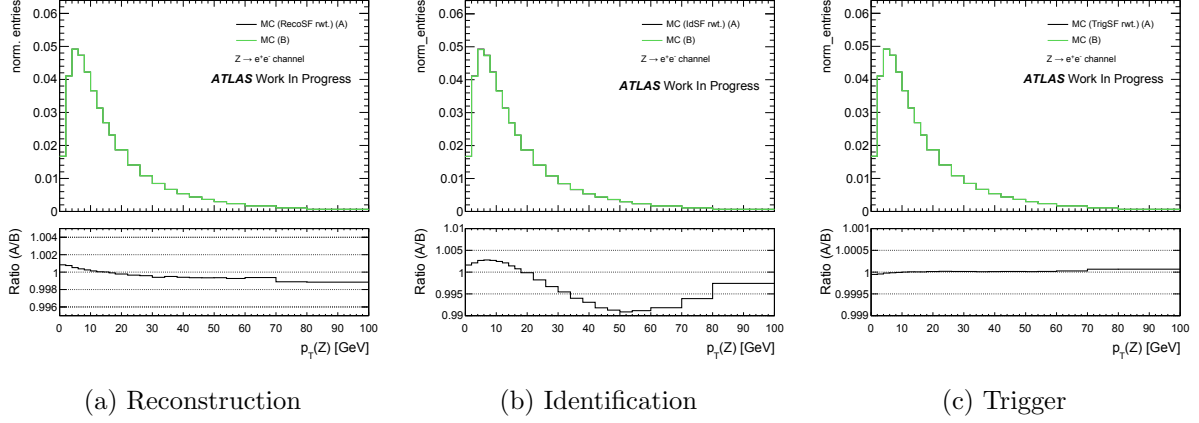
(a) Reconstruction   (b) Identification   (c) Trigger

Figure 5.7: Effect of each one of the efficiency weights in the p_T^Z distribution. Each time, only one type of weight is applied.

$$P_i = \frac{N^{MC}(\text{truth bin} = i\ \&\ \text{reco bin} = i)}{N^{MC}(\text{reco bin} = 1)} \tag{5.6}$$

The bin purity, estimated using the baseline MC signal sample, is shown in figure 5.8. We can see that the purity is above 50 % for all bins. The jumps in the plots of purity are due to the changes in the bin size.
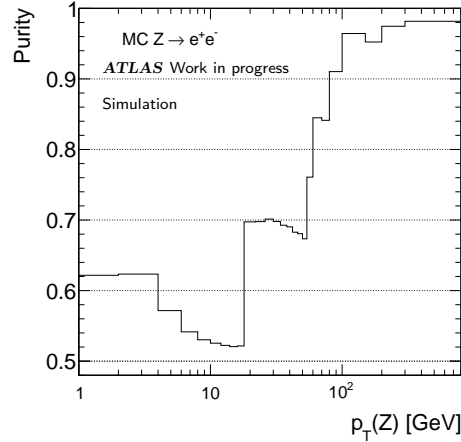
Figure 5.8: Purity of the p_T^Z bins. The purity is larger than 50 % for all bins.

5.2.2   Background estimation

Due to the clear signature of the $Z \rightarrow ee$ events, the selection cuts explained in section 5.1.2 remove almost all background. However, a small fraction of background remains, composed of:

- Events with the Drell-Yan production of W bosons, decaying into electron and neutrino: $W \rightarrow e\nu$.

- Events with the production of top quark pairs, where one or two of the W bosons produced in the decay of the top quarks decay into electron and neutrino.

- Electrons coming from the decay of τ leptons produced via the processes $Z \rightarrow \tau\tau$ and $W \rightarrow \tau\nu$.

86

- Diboson events, where more than one weak boson is produced in the proton collision, and their decay products contain leptons (WW, WZ, ZZ).

- Events containing hadronic activity, with non-isolated electrons produced in secondary decays, or jets misidentified as leptons.

The first 4 categories are grouped under the name "electroweak background". The hadronic activity background is called "QCD background". The estimation of these two types of background is explained in the next sections.

Electroweak background

The electroweak background is estimated using the MC samples mentioned in table 5.1. Cuts identical to those applied to data are applied to these samples. The number of selected events and the resulting background distributions are rescaled to data luminosity using the following factor:

$$\alpha = \frac{L_{data}}{L_{MC}} = \frac{L_{data}}{N_{MC}/\sigma_{MC}} \tag{5.7}$$

where L_{data} is the data integrated luminosity, N_{MC} the number of events in the MC sample and σ_{MC} the theoretical cross-section of the MC sample (table 5.1). This way, we normalize the MC distributions and number of events to their expectation given by the luminosity of the data.

QCD background

The cross-section of the process entering the QCD background is huge in hadron colliders. In order to estimate this background using MC samples, we need a luminosity comparable to data, so the number of events needed is prohibitively large. In addition, the number of different processes involved is large, which leads to theoretical uncertainties. For these reasons, we use data driven methods to estimate this type of background.

The QCD background is estimated doing fits on data distributions, using a composite model of signal and background shapes which gives as output the fraction of QCD events. This method is called "template fit". The distributions used for the fits are electron isolation variables, defined as the sum of cell energies in a cone of radius ΔR (in (η, ϕ) space) around the electromagnetic cluster, excluding a grid of $\Delta\eta \times \Delta\phi = 5 \times 7$ cells in the center of the cone (using middle layer granularity) [66] (notice that the isolation variables are not used in the nominal $Z \to ee$ event selection). The isolation variables are denoted "$E_T ConeX$", where X represents the size of the cone ($\Delta R = X/100$). In the fits, we use relative isolation i.e. we divide the isolation by the transverse energy of the cluster: $E_T ConeX/E_T$. In addition, we separate the isolation distributions in two: for every event, we take the minimum isolated electron (the one with the largest value of isolation variable) and build minimum isolation distributions ($E_T ConeX(min)/E_T$), and the maximum isolated electron (the one with smallest value of the isolation variable) to build maximum isolation distributions ($E_T ConeX(max)/E_T$).

The QCD background estimation procedure can be summarized as follows:

- Run a different selection on data to obtain a sample enriched in QCD background events. This is done by reversing the medium electron identification requirement. The sample obtained this way, called "control sample" is used to obtain the shapes of QCD background distributions, called "QCD templates".

- Run the standard selection on signal and EW background MC samples to build signal distributions. These distributions are called "signal templates".

- Perform fits on data distributions (with events selected using the standard cuts), using shapes composed of QCD and signal templates, with a relative normalization parameter. The fits are done on isolation variables, using cones of several sizes and performing the fits in different ranges. These fits allow to estimate the fraction of QCD background events present in the original data sample.

In the next section we detail the steps mentioned above, and explain the corrections done on the templates before the fitting procedure is performed.

QCD control sample

The control sample is built using 2011 collision data, with the selection cuts summarized in table 5.4. We use inclusive D3PD's instead of skimmed ones, in order to have background events available for the selection. The trigger requirement is modified in order to require loose electromagnetic clusters (instead of online reconstructed electrons), and the electron identification is inverted, asking the electrons to pass the loose identification but not the medium one (see section 3.2.3). This cut inversion allows to select mostly background and fake electrons. The opposite charge requirement is removed, keeping all events and dividing the selected sample in two, according to the relative charge of the two electrons in the event, opposite sign (OS) and same sign (SS) samples.

Trigger	`EF_2g20_loose`
Event cleaning	The primary vertex has ≥ 3 tracks No LAr error
Electron selection	Object quality Identification: Loose and not Medium $p_T > 20$ GeV $\|\eta\| < 2.47$ and ($\|\eta\| < 1.37$ or $\|\eta\| > 1.52$)
Event selection	Exactly two electrons 66 GeV $< m_{ee} < 116$ GeV

Table 5.4: Summary of the selection applied to select the QCD control sample from data, used to estimate the QCD background. Notice that no requirement is done on the charge of the electrons.

The selection done this way gives a sample enriched in multijet events, but some signal contamination ($Z \to ee$ events) is present. In order to have an estimate of this contamination, we perform the same special selection (table 5.4) on MC samples (signal and EW background) and scale the output according to data luminosity (equation (5.7)). The distributions obtained this way are subtracted from the QCD templates. For comparison, original invariant mass distributions for the QCD sample (both OS and SS parts) are shown in figure 5.9, together with the result when the signal contamination is removed. The signal contamination is visible in the distributions before the subtraction, as a small peak around the Z mass.

Signal templates

The signal templates are taken from the baseline signal sample and MC EW background samples (see table 5.1), with objects selected at reconstruction level, using the standard selection (see table 5.2). The EW background distributions are added to the signal one, normalizing them according to the relative luminosity of each sample (this is done in order to separate the EW contributions from the QCD background when performing the fits). All the corrections are applied on the MC samples (see section 5.1.3).
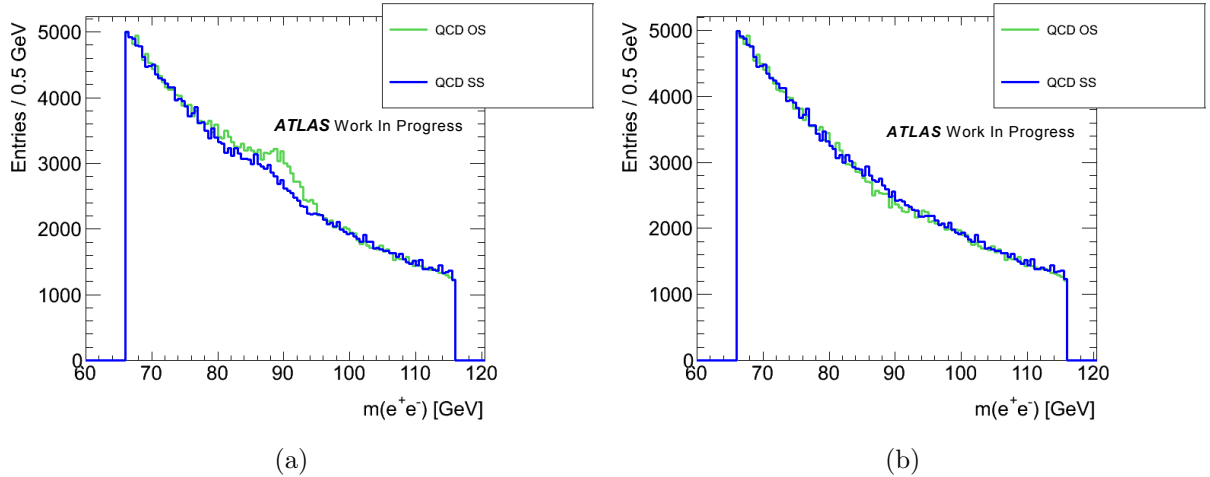
Figure 5.9: Invariant mass distribution of the QCD samples (OS and SS), original (a) and after signal removal (b).

Before using the signal template on the fits, we perform a small shift correction on the distributions. In figure 5.10, we show the $E_T Cone30/E_T$ distribution for data and signal MC, obtained using a selection asking tight identification criteria for electrons instead of medium. A shift of the MC distribution with respect to data, for both selections, can be seen. As the shift is also visible in the distributions with tight selection, it is clear that it is not due to the presence of background in data.
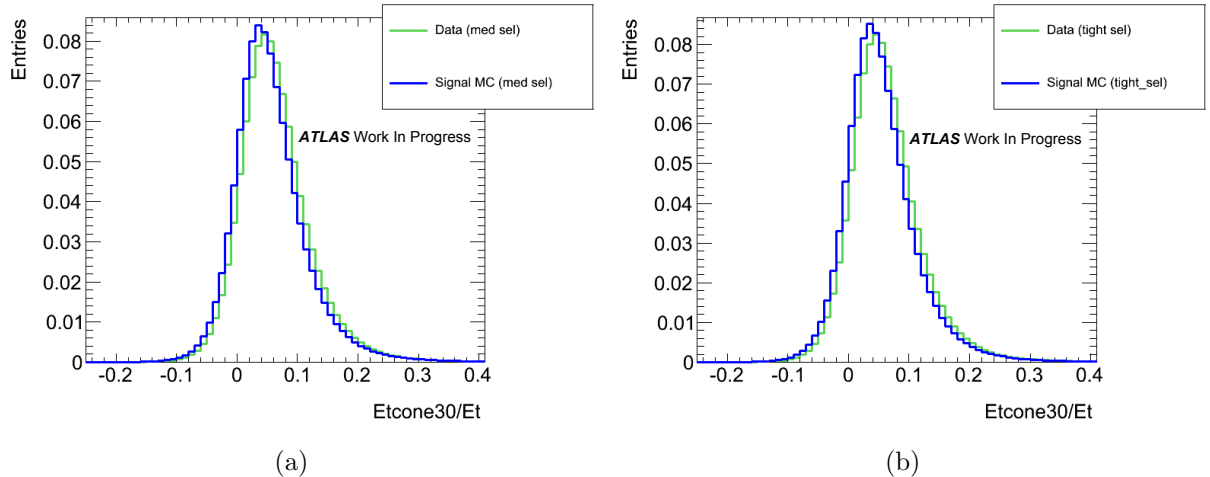

Figure 5.10: Normalized distributions of the relative isolation variable $E_T Cone30/E_T$ for data and signal MC. (a) The distributions for the standard selection, (b) the distributions for the tight selection. The mis-modeling of the distribution in MC is visible for both selections as a shift of the distribution.

In order to investigate the possible origin of these disagreement, we look at the values of the shifts (mean$_{data}$ - mean$_{MC}$), obtained using the tight selection, as a function of the effective cone area defined as: $(\Delta R)^2 \times \pi - 35 \times 0.025 \times 0.025$ (this represents the area of a circle in the (η, ϕ) plane, without the area taken by the EM cluster), and separating the points for different ranges of the number of reconstructed vertices in the event. These plots are shown in figure 5.11, both for maximum and minimum isolation variables (in these cases we show isolation variables, not relative isolations). We see that the size of the shifts increases both with the cone size and the number of vertices, this indicates that the problem arises from mis-modeling of the pile-up and underlying event in MC.

The signal templates are corrected for this problem in the following manner: we compute
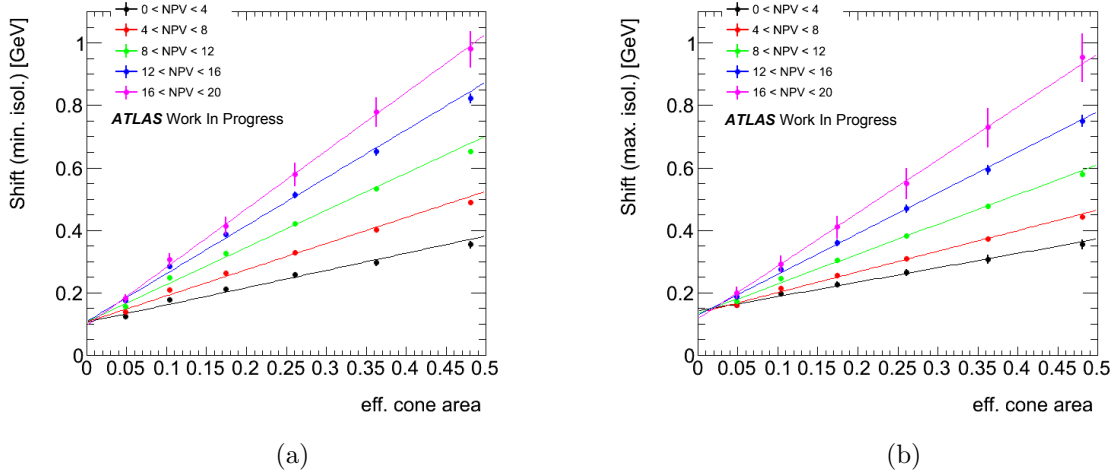
Figure 5.11: Shifts observed in the isolation distributions, computed as the difference of the means in data and MC, as a function of the effective area of the cone, for different numbers of reconstructed vertices. The events are selected requiring "tight" identification. a) Shift values for minimum isolation, b) shift values for maximum isolation.

a shift using the relative isolation distributions with the tight selection (mean$_{data}$ - mean$_{MC}$), for every cone size, then we use these values to shift the nominal distributions (signal and EW background) along the x axis (the shifts are computed independently of the number of vertices). An example of this correction is shown in figure 5.12, where the MC signal distributions are compared to data before and after performing the shift correction. We can see that the signal template approaches the data distribution once the correction is applied, reaching an agreement within 11 %, while the uncorrected ones show a disagreement up to 37 %.

Fits to data distributions

The fits are done using relative isolation variables of the most isolated electron in the $Z \to ee$ event, because the QCD fraction is more visible in the distribution of the most isolated electron than in the distribution of the less isolated one, as can be seen in figure 5.13, where the difference between the signal template and the data distribution indicates the presence of QCD events.

We fit the data using a function of the form:

$$D(x) = q \cdot B(x) + (1 - q) \cdot S(x) \tag{5.8}$$

where $B(x)$ is a normalized distribution obtained from the control sample template (with signal contamination subtracted), and $S(x)$ the normalized distribution obtained from the signal template (corrected using the shift, as explained above). The only free parameter in the fit is q, which gives the fraction of QCD events in the fitted region. In principle, we perform the fits in the range of the relative isolation variable $T = (-0.25, 1.5)$ which covers all the events. However, as the QCD fraction is very small, we change the fitting range in order to test the stability of the fit and estimate the uncertainty.

If the fit is done in a subrange of T, the output fraction needs to be adjusted to the whole range. Suppose we perform the fit in a subrange of T, called R. Notice that the distributions $B(x)$ and $S(x)$ are obtained normalizing the original histograms $h_{QCD}(x)$ and $h_{SIG}(x)$, obtained from the control sample and signal template, respectively:

$$B(x) = \frac{h_{QCD}(x)}{\int_R h_{QCD}(x)dx} = \frac{h_{QCD}(x)}{I_{QCD}(R)} \tag{5.9}$$
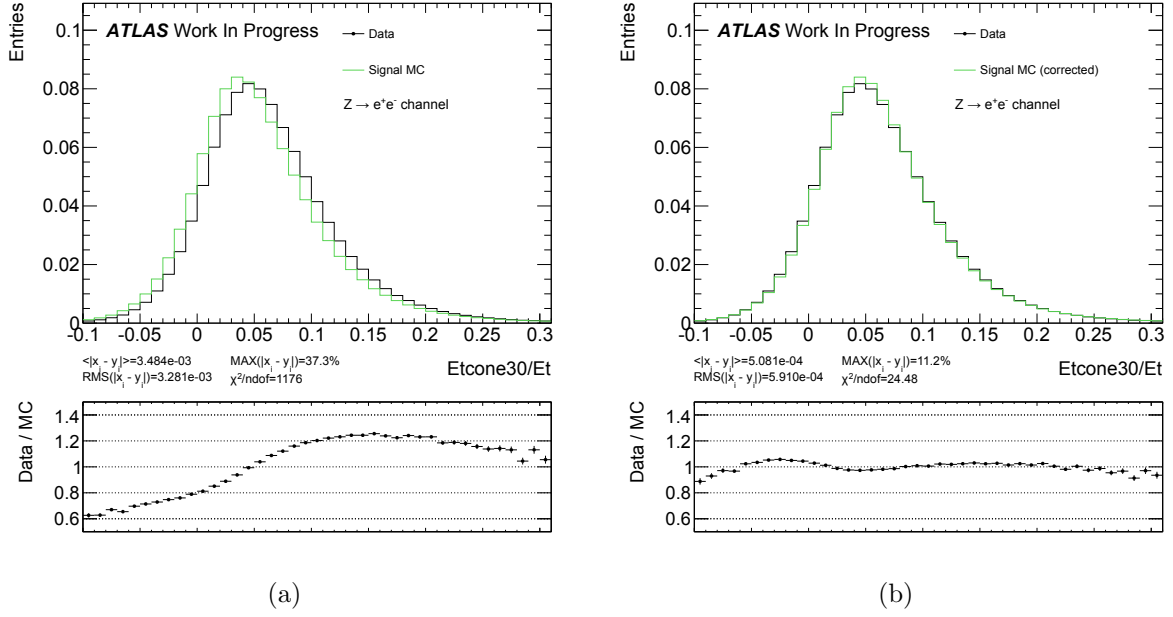
Figure 5.12: Isolation variable distributions comparison for data and MC. (a) Before the shift correction, (b) after the shift correction. After the correction, the isolation distributions agree within 11 %, while the uncorrected ones show a disagreement up to 37 %. In these plots, all distributions are normalized to unity.

$$S(x) = \frac{h_{SIG}(x)}{\int_R h_{SIG}(x)dx} = \frac{h_{SIG}(x)}{I_{SIG}(R)} \tag{5.10}$$

where $I_{QCD}(R)$ and $I_{SIG}(R)$ are the integrals of the original QCD and signal templates over the reduced range R, respectively. Once the fit has been done, the fraction q gives the number of QCD events in the range R with respect to the total number of events in the same range. The number of QCD and signal events in the extended range T, for this value of q, can be computed as:

$$N_T^{QCD} = q \int_T B(x)dx = q\frac{\int_T h_{QCD}(x)dx}{I_{QCD}(R)} = q\frac{I_{QCD}(T)}{I_{QCD}(R)} \tag{5.11}$$

$$N_T^{SIG} = (1-q) \int_T S(x)dx = (1-q)\frac{\int_T h_{SIG}(x)dx}{I_{SIG}(R)} = (1-q)\frac{I_{SIG}(T)}{I_{SIG}(R)} \tag{5.12}$$

where $I_{QCD}(T)$ and $I_{SIG}(T)$ are the integrals over the range T. Then, the QCD fraction in the range T is given by:

$$q_T = \frac{N_T^{QCD}}{N_T^{QCD} + N_T^{SIG}} = \frac{q\frac{I_{QCD}(T)}{I_{QCD}(R)}}{q\frac{I_{QCD}(T)}{I_{QCD}(R)} + (1-q)\frac{I_{SIG}(T)}{I_{SIG}(R)}} \tag{5.13}$$

The fits are done using the relative isolation variables $E_T ConeX/E_T$, for $X = 20, 25, 30, 35, 40$ and using the opposite sign (OS) and same sign (SS) QCD template alternatively (giving a total of 10 possible configurations for the fit). In figure 5.14 we show examples of the fits where the data distribution, the total and the QCD templates are visible.

In figure 5.15 the resulting QCD fractions, for the different configurations and fit ranges, are shown. The result stabilizes around 0.001 for increasing lower bound of the fit range. The final value for the fraction is taken as the average value of results, with the errors covering the span of results. The resulting estimate is:
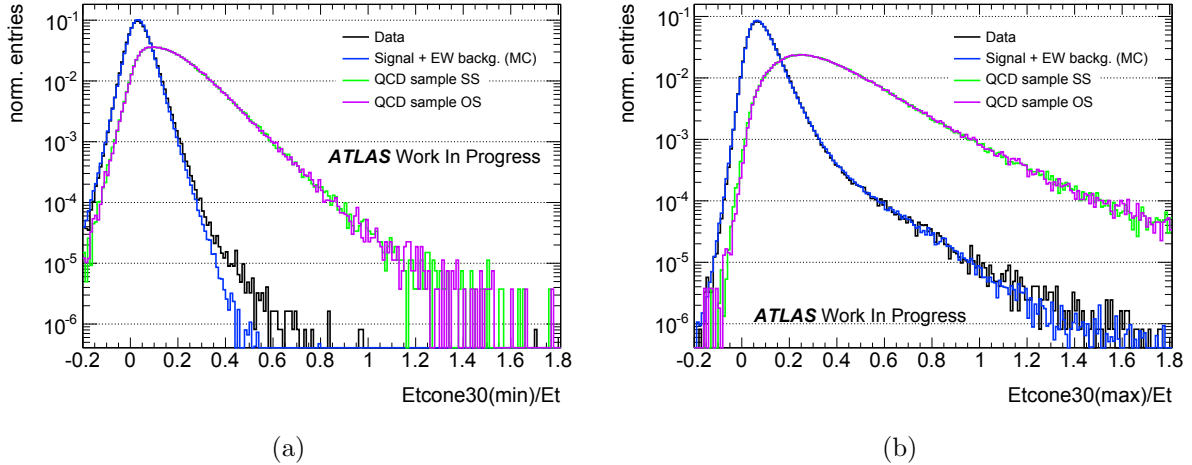
Figure 5.13: Comparison of the relative isolation variable distributions ($E_T Cone30/E_T$) for data, MC signal and QCD templates. The signal templates are already shifted as explained above. (a) The distributions for the most isolated electrons (minimum value of the isolation variable), (b) the distributions for the less isolated electrons (maximum value of the isolation variable). The QCD events are visible in (a) as the small difference between the signal template and the data distribution.

$$q_T = 0.0014^{+0.0010}_{-0.0005} \qquad\qquad (5.14)$$

The resulting fraction q_T is used to normalize the QCD templates of the OS sample, such that their integral is equal to $0.0014 \times 1228863 = 1720$ events. These normalized histograms are used as QCD background distributions, in particular to estimate the p_T^Z dependence of the QCD background. The variation of the background obtained using the SS sample instead of the OS one is taken as a source of systematic uncertainty.

5.2.3   Data / prediction comparisons

In this section, we compare the signal and background predictions with the observed distributions in data. We use the MC POWHEGPYTHIA sample as baseline to model the signal distributions (see table 5.1), normalized to data luminosity using equation (5.7). In table 5.5 the number of expected events for signal and each type of background are shown. The agreement between the observed number of events and the expected one is at the 0.25 % level. The total background amounts to 0.50 % of the expected events, the dominant ones are the $t\bar{t}$ (0.11 % of total expected events) and the QCD background (0.14 %).

In figure 5.16 we show plots of kinematic distributions for electrons in the selected $Z \to ee$ events, including the signal expectation and the final determination of background. The variables for MC events are taken at reconstruction level, with all corrections explained in section 5.1.3 applied. The plots are shown in linear and logarithmic scale, in order to appreciate the agreement in shape (linear scale) and the background composition as well (logarithmic scale). Below the plots we show the ratio between the data and the total expectation, in order to appreciate the level of agreement. The error bars show only statistical uncertainties. The agreement is within 5 %, except for the $\phi(e)$ distribution, which shows a 10 % disagreement around $\phi \approx -0.7$. The origin of this disagreement is a mis-modeling in the MC samples of a failure in the LAr calorimeter. This is explored in section 5.3.4.

In figure 5.17 we show plots for the Z boson variables, showing similarly the distributions in linear and logarithmic scale, and the ratios. Notice that for the p_T^Z distribution the expected number of events falls outside the 10 % band of agreement with data, due to the MC mis-modeling of the distribution.
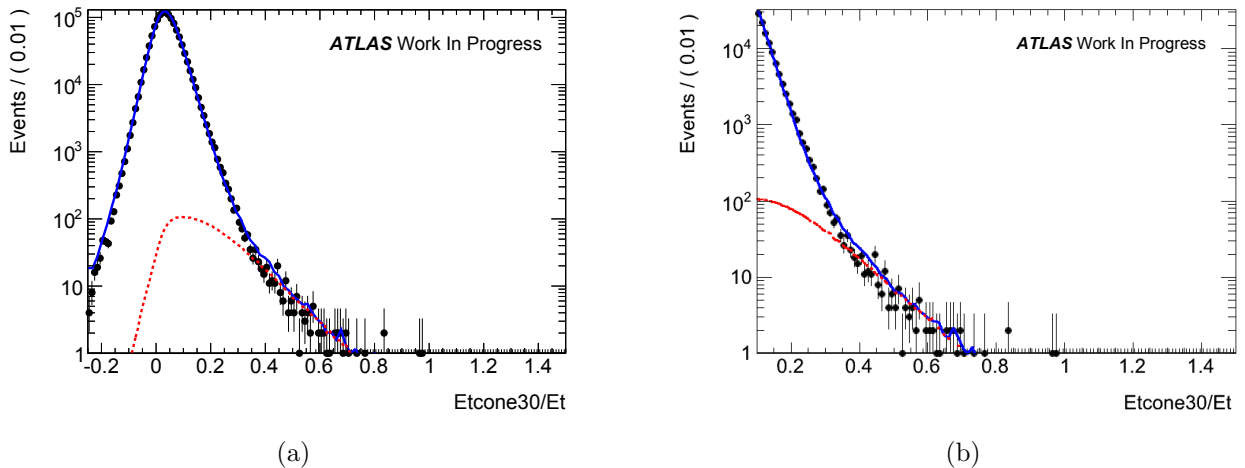
(a)　　　　　　　　　　　　　　　　(b)

Figure 5.14: Example of template fits for the estimation of the QCD background. The fits shown are performed using the variable $E_T Cone30/E_T$ and the OS QCD template. The black points represent the data distribution, the blue line the fit result, and the red dashed line the QCD component of the fit. The fit is shown in two different ranges: a) complete range (-0.25, 1.5), b) reduced range (0.1, 1.5).

Finally, in figure 5.18 we show the invariant mass distributions for data and expected signal and background, in linear and logarithmic scale. The spectrum is well modelled (within 5 %), around the Z mass peak.

5.2.4　Unfolding

The measurement of the p_T^Z distribution is affected by the limited resolution of the detector, which causes events with some true value of the p_T^Z variable to fall in a different bin of the reconstructed histogram (bin migrations), and by detector inefficiencies, which means that some events are not reconstructed. The procedure to correct these undesired effects and obtain an estimation of the "true" distribution is called unfolding (also called deconvolution or unsmearing). Notice that for the measurements of inclusive cross-sections, normally a single correction factor, usually estimated from MC, is enough; however the measurement of a differential distribution relies directly on the precision on the variable of interest, thus bin migrations can become a problem if the bin sizes are smaller or comparable to the resolution.

The unfolding can be formulated as follows. Suppose we want to measure a "true" histogram, with M bins with values: $\mathbf{y} = \{y_1, y_2, ..., y_M\}$. In order to estimate this histogram, we measure an histogram with N bins and content: $\mathbf{x} = \{x_1, x_2, ..., x_N\}$. If the measured variables have expectation values given by: $E(x_i) = \nu_i$, then we can write [67]:

$$\nu_i = \sum_{j=1}^{M} R_{ij} y_j \qquad (5.15)$$

The $N \times M$ matrix R_{ij} gives the probability of observing an event in the bin i if the true value was in bin j. This matrix is called "response matrix". The matrix depends on the detector properties and the modeling of the physics involved. In order to unfold, we need to estimate the distribution $\mathbf{y}$, starting from the measured values $\mathbf{x}$.

In principle, the unfolding can be done using the measured values $\mathbf{x}$ as estimates of the expectation values ν, and then invert equation (5.15) to compute $\mathbf{y}$. However, the result obtained this way is highly unstable and dependent on the statistical fluctuations of $\mathbf{x}$, so this method is not used in practice [67].
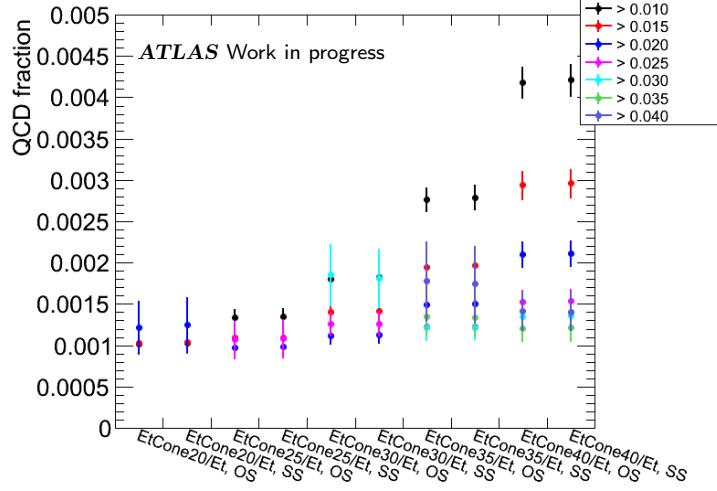
Figure 5.15: Comparison of all the fit results, for all the isolation variables and for the two QCD templates, shown for several values of the minimum limit used for the fit. For a given variable and QCD template, the fit result stabilizes for high enough value of the lower limit.

Iterative bayesian unfolding

The measurement we present here is done using iterative bayesian unfolding. This method relies on iterative applications of the Bayes theorem in order to estimate the true histogram, starting from the original content of the bins, a prior assumption of the true distribution and a response matrix. Using this method, the estimation of true values $\mathbf{y}$ for the iteration $k+1$ is given by [68]:

$$\hat{y_i}^{(k+1)} = \sum_{j=1}^{N} S_{ij}^{(k)} x_j \tag{5.16}$$

where $\mathbf{x}$ are the observed values and $S_{ij}^{(k)}$ is the "smearing matrix" obtained after iteration k, given by:

$$S_{ij}^{(k)} = \frac{1}{\epsilon_j} P(y_i|x_j)^{(k)} = \frac{P(x_j|y_i)P^{(k)}(y_i)}{\epsilon_j \sum_{l=1}^{M} \left[P(x_j|y_l)P^{(k)}(y_l) \right]} \tag{5.17}$$

In (5.17) we recognize the Bayes theorem: if we observe the "effect" x_j, the probability that is has been produced by the "cause" y_i, $P(y_i|x_j)$, is proportional to the probability of the cause y_i, $P(y_i)$, times the probability of the cause y_i to produce the effect x_j, $P(x_j|y_i)$. In this equation we have the following elements:

- $P(x_j|y_i)$ is the normalized response matrix, which has to be obtained from MC simulation. The element (i,j) can be computed dividing the number of events with truth values in the bin i and reconstructed in bin j, divided by the total of events generated in bin i:

$$P(x_j|y_i) = \frac{N^{MC}(\text{truth bin} = \text{i \& reco. bin} = \text{j})}{N^{MC}(\text{truth bin} = \text{i})} \tag{5.18}$$

- The factors ϵ_j represent the efficiency correction. They are estimated from MC using:

$$\epsilon_j = \sum_{l=1}^{N} P(x_l|y_j) = \frac{N^{MC}(\text{total reco. with truth bin} = \text{i})}{N^{MC}(\text{truth bin} = \text{i})} \tag{5.19}$$

94

Figure 5.16: Distribution of electron kinematic variables, including the final background estimation, for the selected events. The plots are shown in linear (left column) and logarithmic scale (right column), and show only statistical errors. (a) Electron p_T, (b) Electron η and (c) electron ϕ angle.
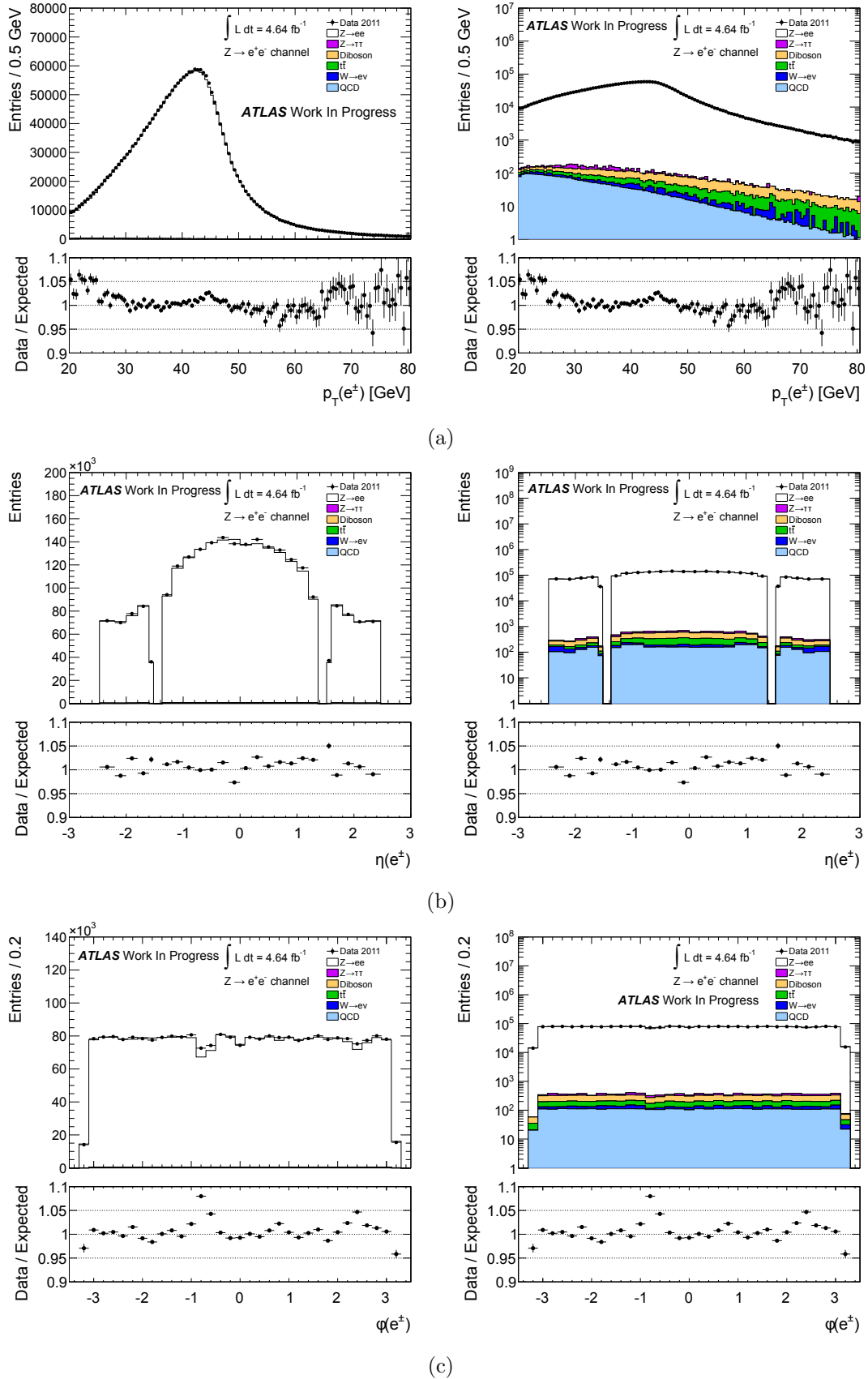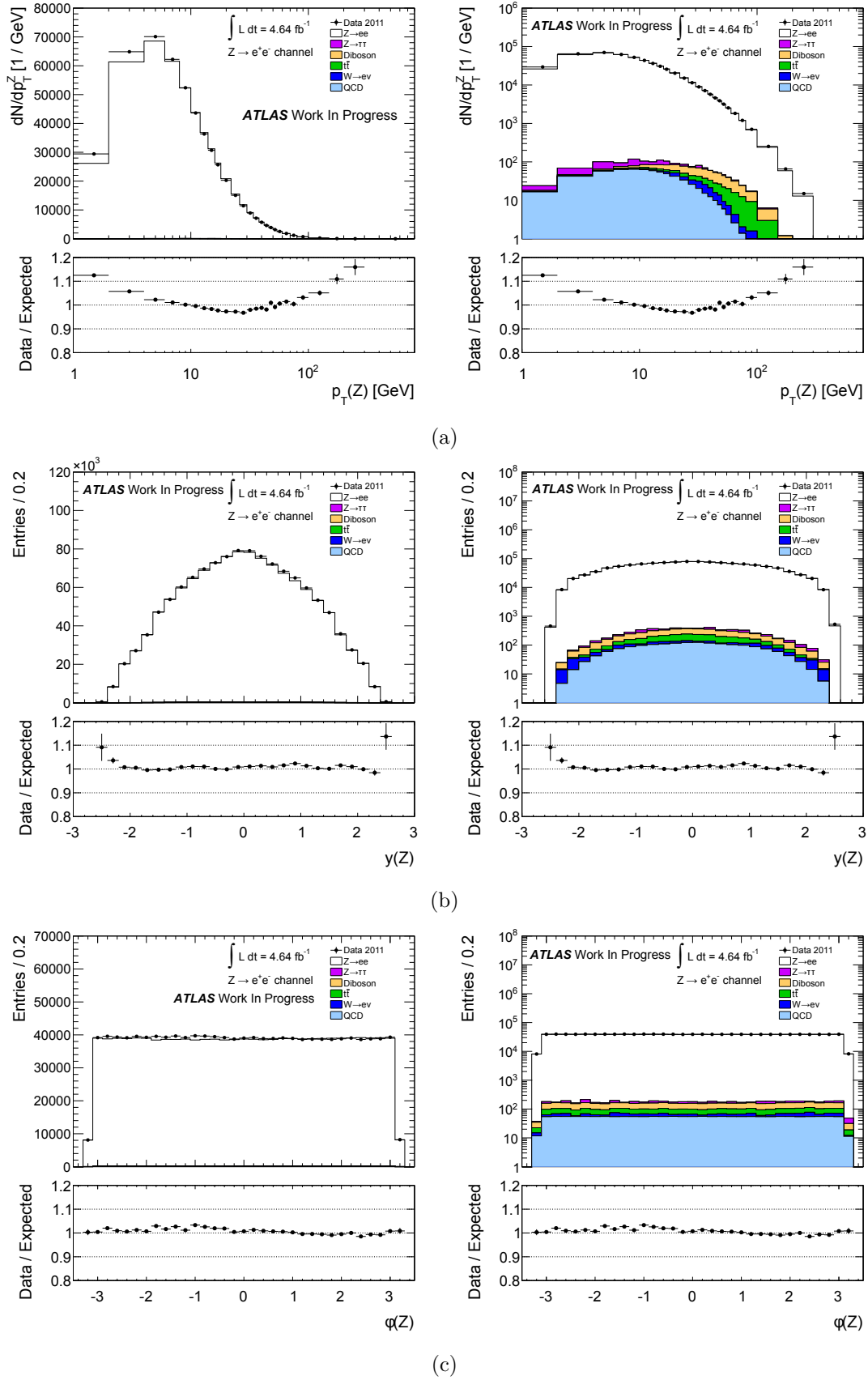
Figure 5.17: Distribution of Z boson kinematic variables, including the final background estimation, for the selected events. The plots are shown in linear (left column) and logarithmic scale (right column), and show only statistical errors. (a) Z boson p_T, (b) Z boson rapidity and (c) Z boson ϕ angle.

Process	Number of events
Signal ($Z \rightarrow ee$)	1219707.9
$W \rightarrow l\nu$	385.2
$W \rightarrow \tau\nu$	97.2
$Z \rightarrow \tau\tau$	625.3
$t\bar{t}$	1398.8
WW	317.8
ZZ	642.3
WZ	922.6
QCD	1720.4
Total background	6109.5
Total expected	1225817.3
Data (observed)	1228863

Table 5.5: Number of events in data and expected signal and backgrounds. The electroweak background is estimated using MC samples and the QCD background using a data driven method.

- The distribution $P^{(k)}(y_i)$ is the prior assumption on the true distribution. For the first iteration $P^{(0)}(y_i)$ can be assumed to be an uniform distribution, or taken from a truth distribution of a MC sample. This distribution is updated after each iteration in the following way:

$$P^{(k)}(y_i) = \frac{\hat{y}_i^{(k)}}{\hat{N}_{true}^{(k)}} = \frac{\hat{y}_i^{(k)}}{\sum_{l=1}^{M}[\hat{y}_l^{(k)}]} \tag{5.20}$$

Notice that every estimation of the true distribution $\mathbf{y}$ is used as prior for the next iteration in equation (5.17). It as been shown using MC studies that, after each iteration, the distribution $\hat{\mathbf{y}}^{(k)}$ lies between the true distribution $\mathbf{y}$ and the prior assumption of the iteration $\hat{\mathbf{y}}^{(k-1)}$, so each iteration gets closer to the true distribution. After some number of iterations, the result converges to the true distribution, independently of the initial assumption $P^{(0)}(y_i)$ [68][69].

The bayesian iterative unfolding has the advantage that it does not contain a matrix inversion procedure, so it produces stable results. In this work, we use the RooUnfold implementation, discussed in [70][71]. Given a measured distribution, the algorithm performs the unfolding in three steps:

- Correct the data for possible "fakes", i.e., events that are reconstructed but are not present at truth level (this happens when the measurement is done in a limited phase space, so there are events that at reconstruction level pass the fiducial cuts, but not at truth level). This correction is done using correction factors for each bin, computed in the following way:

$$\epsilon_i^{fakes} = \frac{N^{MC}(\text{total truth with reco bin = i})}{N^{MC}(\text{reco bin = i})} \tag{5.21}$$

The factors are computed using a MC sample.

- The data distribution corrected for fakes, is given as input to the iterative bayesian algorithm. The initial prior $P^{(0)}(\mathbf{y})$ is obtained from the MC truth distribution, and the response matrix is computed from the MC sample as well.

- After some number of iterations, the resulting corrected distribution is multiplied by efficiency factors in order to correct for the "miss" events (events that pass the fiducial cuts at
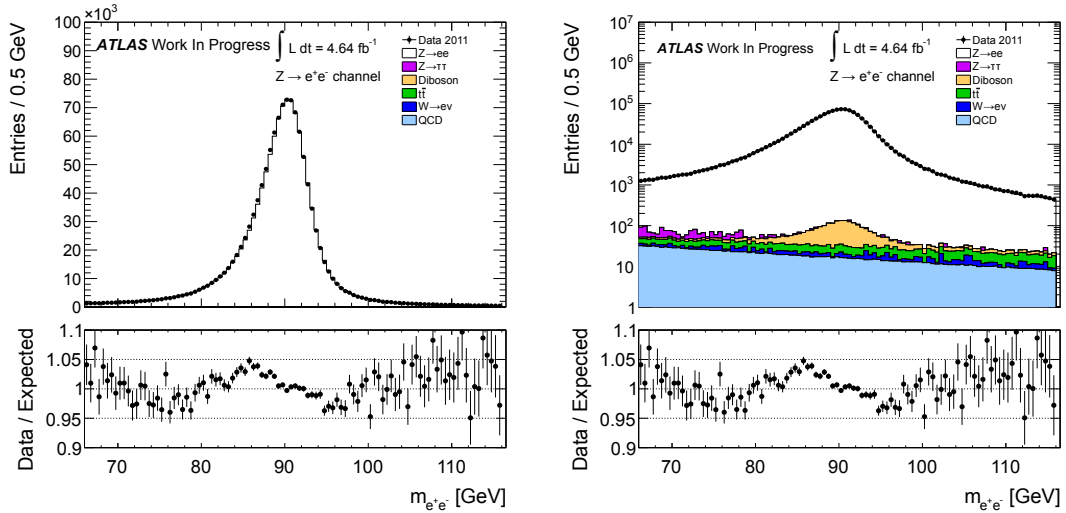
Figure 5.18: Distribution of electron pair invariant mass, including the final background estimation, for the selected events. The error bars include only statistical uncertainties. The plot is shown in linear scale (a) and logarithmic scale (b).

truth level, but are lost at reconstruction events due to the detector inefficiencies). These are the factors shown in (5.19), and are computed also from the MC sample.

In figure 5.19, a schematic of the unfolding process is shown. Notice that the information from the MC samples enters in several stages of the process (fakes correction - matrix response - efficiency correction). The RooUnfold implementation allows to define an object from a MC sample, which contains all the needed information to perform the unfolding. We refer to this object as the "response object" from now on.
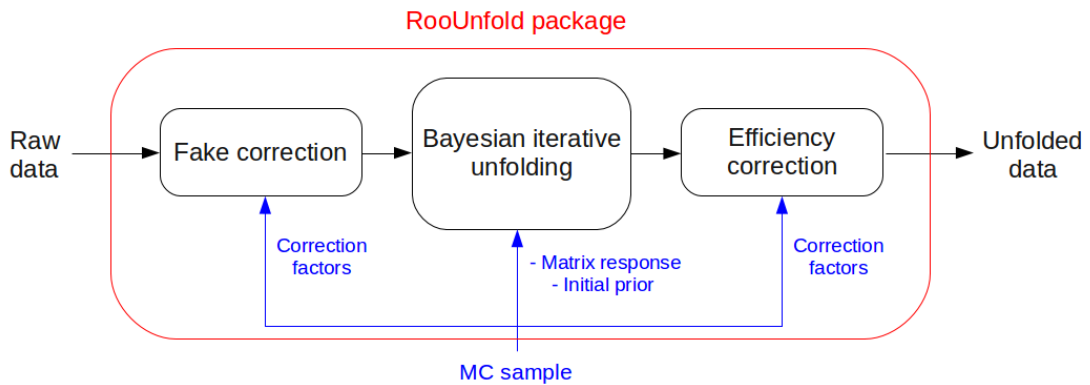
Figure 5.19: Schematic showing the unfolding process.

The nominal MC sample used to define the response object is the POWHEGPYTHIA sample 108303 (see table 5.1), reweighted to the PYTHIAMC10 shape, as described in section 5.1.3. In figure 5.20 we show the matrix response constructed from this sample, without normalization (showing number of events). The bin migrations are visible, specially for low p_T bins. Notice that the "truth" level is defined from electrons at Born level, i.e., before any QED radiation.
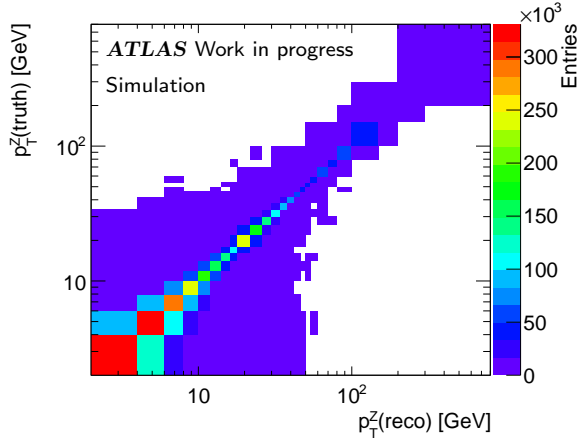
Figure 5.20: Response matrix obtained using the POWHEGPYTHIA MC sample. Notice the non-zero off-diagonal elements (bin migrations).

Bin-by-bin unfolding and closure test

A simple unfolding method called "bin-by-bin method" consists in computing correction factors for each bin, using a MC sample, and use them to correct the measured data:

$$\hat{y}_i = x_i \frac{N^{MC}(\text{truth bin} = i)}{N^{MC}(\text{reco bin} = i)} \tag{5.22}$$

This method corrects for efficiencies and bin migrations, but introduces a bias toward the truth distribution of the MC sample used to compute the correction factors.

In order to compare the performance of the bayesian method with the bin-by-bin one, we unfold pseudo data obtained from MC samples, using both methods. The response object for the bayesian method, and the correction factors for the bin-by-bin method, are obtained using the POWHEGPYTHIA sample (108303s of table 5.1), reweighted to the PYTHIA-MC10 shape. We use as pseudo data the same sample, but without the p_T^Z reweighting, thus keeping the original p_T^Z shape, which differs largely from the PYTHIA-MC10 description, as shown in figure 5.3. The unfolded distribution is compared in both cases to the truth distribution of the POWHEGPYTHIAsample. The results of the comparisons are shown in figure 5.21.

As can be seen in figure 5.21, the corrected distribution obtained using the bayesian method agrees with the truth level one up to differences of 1 %, much better compared to the bin-by-bin method, which produces discrepancies of the order of 2 % to 4 % in the first 3 - 4 bins. This indicates that the bayesian method introduces less bias toward the distribution used to fill the response than the bin-by-bin method, and allows to estimate the underlying true distribution, which in the case of MC pseudo data is represented by the truth distribution.

Convergence and number of iterations

The result of the bayesian unfolding method should converge after some number of iterations to the underlying true distribution, each iteration lessening the dependence on the initial assumed shape. However, with each iteration, the initial statistical uncertainty of the observed events propagates to the estimation, and with each iteration the uncertainty on the estimation and the correlations across bins increase [70]. For this reason, an optimal number of iterations needs to be determined, such that it provides reasonable independence on the initial prior, without increasing the statistical uncertainties beyond acceptable levels.

To determine the optimal number of iterations, pseudo data from MC samples with different p_T^Z shapes are unfolded and the result compared with their truth distributions, using a similar procedure as the one explained in section 5.2.4, but this time varying the number of iterations.
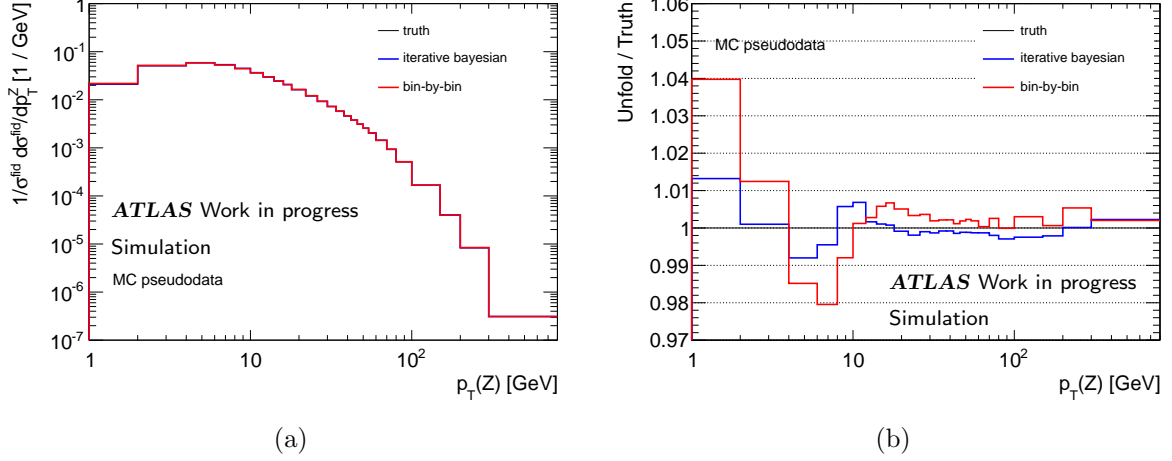
Figure 5.21: Comparison of unfolded normalized distributions, with the truth level one, for the two unfolding methods. The pseudo data (reconstruction level) is from POWHEGPYTHIA (without p_T^Z reweighting), and the corrections factors and response matrix are taken from the baseline sample. (a) Comparison of unfolded spectra, (b) ratios of the unfolded spectra to the truth. The agreement obtained with iterative bayesian unfolding stays within 1%, giving thus a better correction than the bin-by-bin. The test was done using electron channel samples.

The pseudo data samples are obtained from the PYTHIA signal sample, one sample with the original p_T^Z spectrum (PYTHIA-MC11 shape, as in section 5.2.4), and the other reweighted to the ResBos p_T^Z shape (see section 6.2.1). The response object is defined using the PYTHIA sample reweighted to the PYTHIA-MC10 shape. The unfolding is done using 1 to 10 iterations, and the result is compared with the corresponding truth distribution. In figure 5.22 we show an example of the behavior of corrected bin values compared with truth values (bin 1 to bin 8, the bins that are not shown behave in a similar way than bin 8), and a global comparison of the result with the truth distribution, using the sum of squared residuals, given by: $\sum_{i=1}^{26}(U_i^{unfolded} - U_i^{truth})^2$.

Figure 5.22 shows that all bins converge to the truth distributions after 3 or 4 iterations. We chose as convention 3 iterations, and use this number for all the results presented in this chapter.

5.2.5 Summary of selected events

In table 5.6, we show a summary of the events in each p_T^Z bin after each stage of the analysis: original number of observed events, the number of events after background subtraction and the unfolded number of events.

5.3 Uncertainties

Uncertainties on the measurement arise from limited statistics in the simulation as well as in the data samples, from experimental sources (experimental systematics), and from the unfolding method and other theoretical sources (theoretical systematics). In the following sections we describe the estimation of each type of uncertainty.

5.3.1 Statistical uncertainties

The propagation of statistical uncertainties to the final results is affected by the unfolding method in a non trivial way. In particular, it introduces bin-to-bin correlations, which have to be accounted for in view of the combination with the muon channel measurement (see section 5.6). We adopt the following strategy: do fluctuations of the different inputs, repeat the unfolding
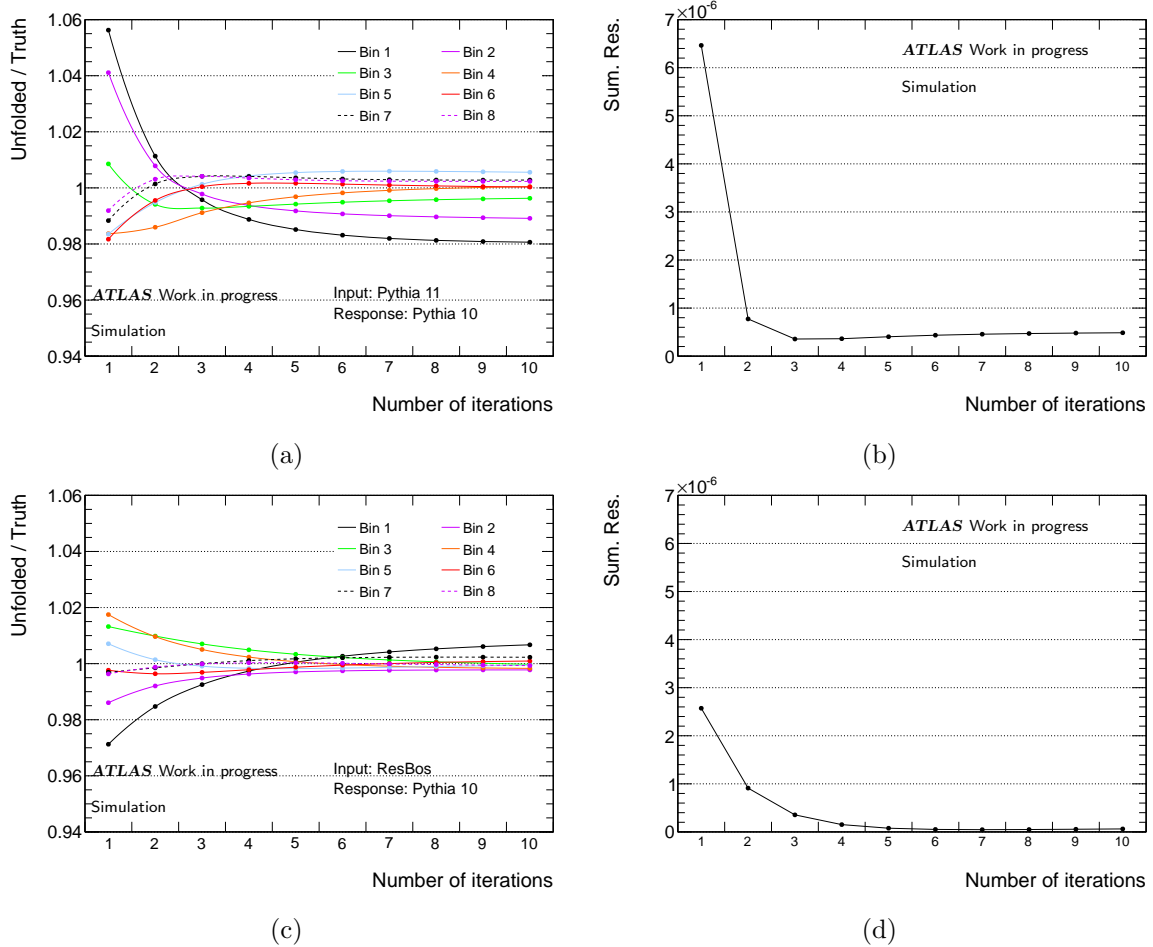
Figure 5.22: Behavior of the unfolded distributions for MC pseudo data, compared to the truth distribution, for different number of iterations. a) and b) show the behavior of the first 8 bins, and the values of the sum of squared residuals, as a function of the number of iterations, for pseudo data with PYTHIA-MC11 p_T^Z shape. c) and d) show the equivalent information, this time using pseudo data with ResBos p_T^Z shape. Each time the unfolded result is compared to the corresponding truth distribution.

procedure, and estimate the errors from the spread of the results. There are two sources: the limited statistics of data, and the limited statistics of the MC sample used to define the response object. The statistical errors introduced by the background estimation are negligible compared to the systematic errors of the same estimations, and are thus neglected.

Statistical uncertainty from data

The statistical uncertainties due to data are propagated in the following way:

- Generate Poisson fluctuations of the measured raw distribution, considering the bins as independent variables. This means, we build varied histograms doing:

$$x_i^{(k)} = x_i + \delta x_i^{(k)} = \text{Poisson}(x_i) \tag{5.23}$$

where x_i is the original number of observed events in the bin i, and $\text{Poisson}(x_i)$ is a random integer taken from a Poisson distribution with mean x_i. We generate a number M of varied histograms, so k goes from 1 to M.

- For every variation k, the analysis is repeated, i.e., the background is subtracted, the distribution is unfolded using the baseline response object, and the result is normalized. We obtain this way the unfolded histogram with bin content: $U_i^{(k)}$.

101

| Bin | Number of events | | |
limits (GeV)	Observed	Backg. corrected	Unfolded
0 - 2	58856	58808.1	121872.6
2 - 4	129727	129588.8	252210.3
4 - 6	140216	140015.4	250767.3
6 - 8	124444	124255.5	212016.3
8 - 10	104752	104515.6	176043.3
10 - 12	87249	87041.1	146179.6
12 - 14	72689	72489.8	121741.6
14 - 16	61383	61160.9	102722.2
16 - 18	51325	51117.6	87188.5
18 - 22	81098	80734.9	138466.3
22 - 26	60315	59970.0	104060.8
26 - 30	45735	45430.2	79634.3
30 - 34	35708	35385.2	62961.5
34 - 38	28530	28250.3	50587.8
38 - 42	22882	22642.5	40721.8
42 - 46	18465	18245.7	32849.6
46 - 50	15567	15359.2	28123.3
50 - 54	12683	12497.9	22795.0
54 - 60	15203	14964.5	27560.9
60 - 70	18268	17931.8	32893.4
70 - 80	12003	11756.5	21543.6
80 - 100	14075	13730.2	24530.7
100 - 150	12623	12309.4	20977.4
150 - 200	3269	3209.4	5228.3
200 - 300	1498	1473.2	2360.3
300 - 800	298	292.8	424.7

Table 5.6: Summary of events in each p_T^Z bin, for each stage of the analysis: observed number of events, number of events after background subtraction, and number of events after the unfolding correction.

- The resulting set of histograms is used to estimate the covariance matrix of the bins. The element (i, j) of the covariance matrix C is estimated computing the average of the product of variations around the nominal unfolded result ($U_\mathrm{i}^\mathrm{nom}$), for the bins i and j, this average is given by:

$$C_{ij}^{stat} = \frac{1}{M} \sum_{k=1}^{M} \left[(U_i^{(k)} - U_i^{nom})(U_j^{(k)} - U_j^{nom}) \right] \qquad (5.24)$$

The statistical covariance matrix is needed for the combination with the muon channel measurement (section 5.6), which is affected by the correlations across the bins. In order to report the results we need the statistical error for every bin, which is computed from the covariance matrix using its diagonal elements. The relative error assigned to the bin i is given by:

$$\delta_i^{stat}(\%) = \frac{\sqrt{C_{ii}^{stat}}}{U_i^{nom}} \times 100 \qquad (5.25)$$

In figure 5.23 we show the statistical covariance matrix and the relative statistical errors. The error has an average value of 0.55 % for p_T^Z below 6 GeV, and 1 % over the whole range.

Statistical uncertainty from the simulated samples

The effect of the limited statistics of the MC sample used to define the response object is estimated doing Poisson fluctuations of this object, then repeating the unfolding for each varied
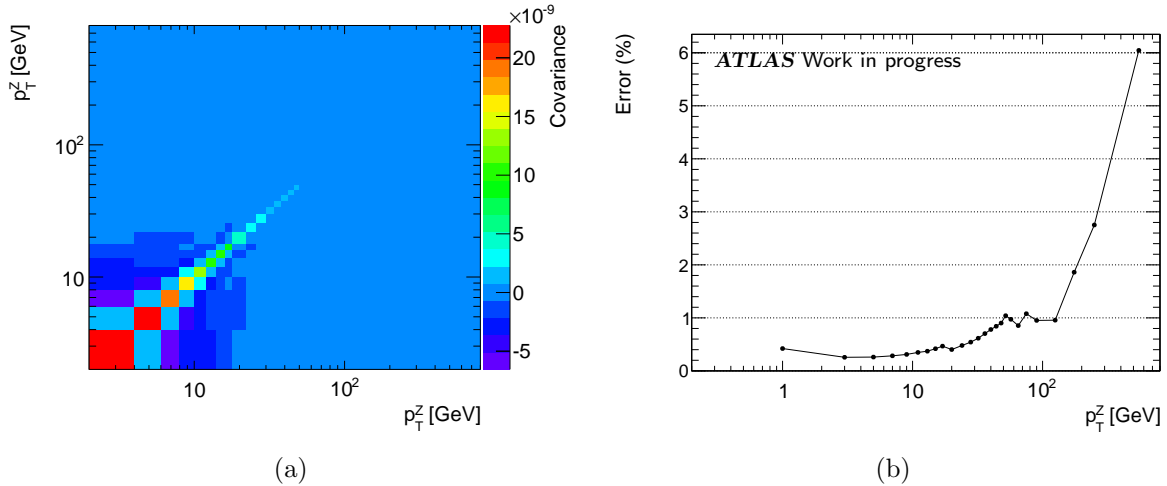
Figure 5.23: (a) Covariance matrix of the statistical errors from data. (b) Relative errors obtained from the diagonal elements of the covariance matrix.

response object (using the same input data), and estimating a covariance matrix using equation (5.24). However, as pointed out in section 5.2.4, the MC signal sample enters the unfolding calculation in three different stages of the process. For this reason, the fluctuations are done separately in three steps:

- Varying every element of the response matrix (2-dimensional object, with reconstruction values in the x axis and truth values in the y axis). The total reconstructed and total truth level distributions of the response object are left untouched.

- Varying only the histogram containing "missed" events. The varied missed distribution is added to the y axis projection of the response matrix to obtain a varied truth distribution.

- Varying the distribution of "fakes" events. The varied fakes distribution is added to the x axis projection of the response matrix to obtain a varied reconstructed distribution.

Every variation is done assuming that the bin contents (both for the 1-d objects and the 2-d objects) are independent variables distributed according to Poisson statistics. This way, we obtain three different covariance matrices, one for each type of source. The total covariance matrix due to the MC statistics is obtained adding these three covariance matrices.

The statistical errors assigned to each bin are obtained using equation (5.25). In figure 5.24 we show the relative errors obtained from each one of the three sources. The error due to the fakes variation is sub-dominant, of the order of 0.05 % for p_{T}^Z below 60 GeV. The errors due to the matrix response variations and miss events variations are of the order of 0.2 % and 0.1 % for p_{T}^Z below 60 GeV, respectively.

5.3.2 General strategy for the estimation of systematic uncertainties

For each source of uncertainty, we introduce a change in the analysis chain, and repeat the analysis steps leaving all the other parameters and the rest of the method untouched. Using the notation U_i^{nom} to refer to the content of the bin i of the nominal result (normalized cross-section), and $U_i^{(S)}$ the corresponding changed result coming from the systematic source S, the systematic uncertainty due to the source S on the bin i is computed as:

$$\delta U_i^{(S)} = U_i^{(S)} - U_i^{nom} \tag{5.26}$$

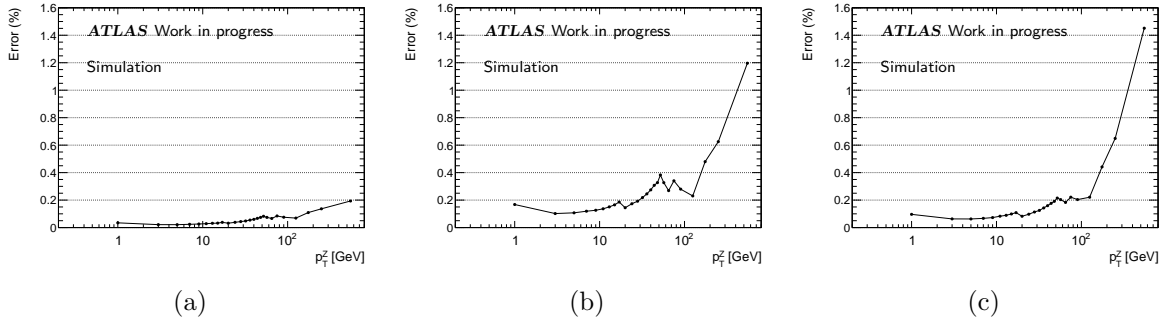The relative uncertainty in percentage is defined as:

Figure 5.24: Statistical uncertainties on the result, due to each component of statistical uncertainties associated to the MC sample. (a) Uncertainties from the "fake" events correction, (b) uncertainties from the matrix response, (c) uncertainties from the "missed" events correction.

$$\delta U_i^{(S)}(\%) = \frac{U_i^{(S)} - U_i^{nom}}{U_i^{nom}} \times 100 \tag{5.27}$$

For the uncertainty sources that have two directions ("up" and "down"), we take as estimation the direction that produces the maximum variation, in absolute value, preserving the sign of one of the directions, for example "up":

$$\delta U_i^{(\pm S)} = \max(|U_i^{(+S)} - U_i^{nom}|, |U_i^{(-S)} - U_i^{nom}|) \times \mathrm{sign}(U_i^{(+S)} - U_i^{nom}) \tag{5.28}$$

Most of the systematic sources are propagated to the final result through their effect on the response object defined from the MC sample, that is, the systematic variation is introduced in the signal MC sample, a new response object is defined from it, and the unfolding is repeated to obtain the varied unfolded distribution, to be compared with the nominal result (equation (5.26)).

5.3.3 Background estimation

In this section we describe the propagation of uncertainties due to the background estimation.

Electroweak background

The electroweak background estimation is affected by two sources of uncertainty: the theoretical cross-sections and the data luminosity, the two of them entering the computation of the normalization of every type of background (see equation (5.7)).

The effect of the cross-section uncertainty is estimated in the following way: the cross-sections are varied within the errors shown in table 5.1, one time adding all the backgrounds with normalization obtained with increased values of the cross-sections, and one time with decreased values. These varied backgrounds are subtracted to the raw data, and the analysis is repeated in order to propagate the effect.

In a similar way, the data luminosity entering the computation of the normalization is changed within $\pm 1.8\%$ of its central value [72], producing varied backgrounds with respect to luminosity. These varied backgrounds are subtracted to the raw data, and the analysis is repeated.

The total uncertainty on the final result arising from the electroweak background estimation is < 0.1 % for the whole p_{T}^Z spectrum.

QCD background

For the QCD background uncertainty estimation, two sources of uncertainty are considered, one coming from the QCD fraction fit (reflecting the different configurations used for the fit), and the other from the assumed QCD background shape.

To quantify the first effect, the fraction of QCD events is allowed to change according to the equation (5.14), and the effect is propagated to the final measurement as described previously. The second effect is quantified changing the assumed QCD shape for the p_T^Z distribution (using SS distribution instead of OS distribution), and the effect propagated.

The final uncertainty due to the QCD background estimation stays below 0.1 % for the whole p_T^Z spectrum.

5.3.4 Electron performances

In this section we describe the systematic errors arising from the electron performances of the detector.

Energy scale and resolution

The in situ calibration method described in section 3.2.5 provides the energy scale uncertainties to be propagated to the measurement. The energy scale uncertainties are obtained from the official tool described in [64], which provides independent variations in the energy scale according to three different kinds of systematic sources [42]:

- Z lineshape scale uncertainties (including statistics, the fit method, the choice of generator).

- Presampler scale uncertainty, arising from the sensitivity of the calibration procedure to the independent energy scale of the presampler.

- Material uncertainty, due to the imperfect knowledge of the material in front of the ECAL.

These scale variations are applied independently to the electron energy in the MC signal sample, and then propagated to the final measurement through the unfolding.

Similarly, the energy resolution is varied using the tool [64], and the effect is applied on the signal MC and propagated to the measurement. The energy scale systematic are below 0.26 % (Z lineshape), 0.45 % (presampler) and 0.17 % (material) for p_T^Z up to 100 GeV, while the resolution systematic gives values below 0.5 % for the same p_T^Z range.

The energy scale and resolution uncertainties fluctuate across the bins, due to the limited MC statistics. As these uncertainties are dominating, we use the following smoothing procedure:

- Repeat the unfolding using the signal PYTHIA sample instead of the baseline (POWHEG-PYTHIA), both for standard scale corrections and varied scales.

- Compute averages for the central and varied distributions:

$$\bar{\mathbf{U}}^{nom} = \mathbf{U}_{\text{PYTHIA}}^{nom} + \mathbf{U}_{\text{POWHEGPYTHIA}}^{nom} \qquad (5.29)$$

$$\bar{\mathbf{U}}^{(S)} = \mathbf{U}_{\text{PYTHIA}}^{(S)} + \mathbf{U}_{\text{POWHEGPYTHIA}}^{(S)} \qquad (5.30)$$

here, the symbol "+" means weighted bin-by-bin average, taking into account the associated statistical errors coming from the MC samples (computed using the method explained in section 5.3.1).

- Compare the average varied distribution with the average nominal to estimate the uncertainty:

$$\delta\mathbf{U}^{(S)} = \bar{\mathbf{U}}^{(S)} - \bar{\mathbf{U}}^{nom} \tag{5.31}$$

- If the resulting distribution is not smooth enough, we perform "rebinning", i.e., we reduce the number of bins of the histograms combining the content of adjacent bins, of the distributions $\bar{\mathbf{U}}^{(S)}$ and $\bar{\mathbf{U}}^{nom}$ before comparing them.

In figure 5.25 we show examples of the result of the smoothing procedure, applied to the energy scale uncertainty (Z lineshape and presampler).

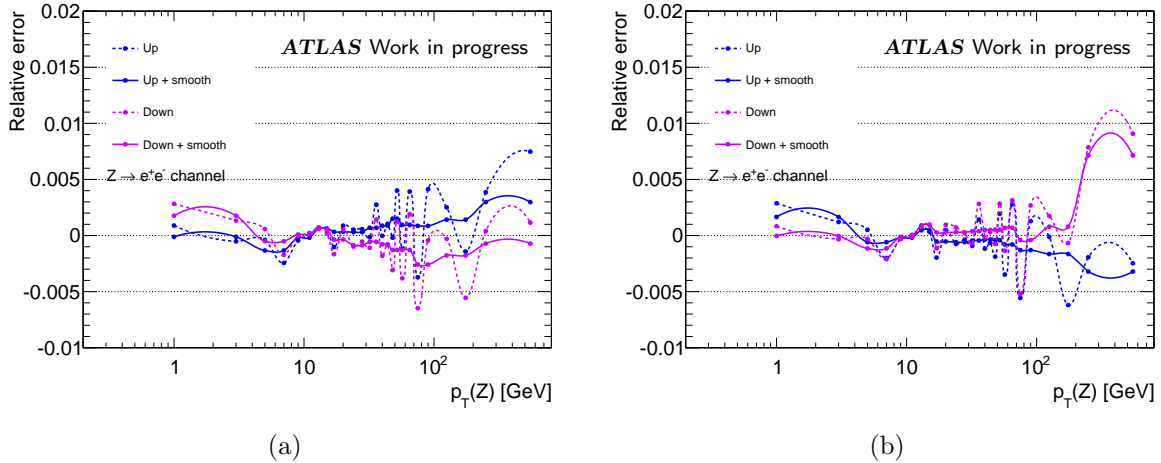(a)   (b)

Figure 5.25: Examples of results of the smoothing procedure, applied to the energy scale systematic errors. The original estimations are shown in dashed lines, and the smoothed estimations in solid lines. (a) Z lineshape scale uncertainy, (b) presampler scale uncertainy.

Reconstruction, identification and trigger efficiencies

To evaluate the efficiency uncertainties, we change the corresponding scale factors according to the uncertainties provided by the official tool [65]. These uncertainties come directly from the tag and probe methods used in the efficiency measurements (see section 3.2.4). The "varied" scale factors are applied to the MC sample instead of the standard ones, as explained in section 5.1.3, and the changed MC sample is used to propagate the effect to the final measurement.

The scale factors have a non-negligible effect on the overall normalization of the p_{T}^{Z} spectrum. However, as we measure a normalized spectrum, the effect of the scale factors cancel out, leaving only a small effect which depends on p_{T}^{Z}. The reconstruction and identification uncertainties affect the final result by less than 0.1 % for most of the spectrum (for $p_T < 100$ GeV), and the trigger efficiency by less than 0.01 %.

Charge mis-identification

To check the impact of charge mis-identification in the ID, the analysis was repeated relaxing the opposite sign requirement (see table 5.2). This leads to an increase of 1.8 % in the number of candidates in data (1250861 events selected). The efficiency of selection in the MC sample increases by 2 %. The analysis is repeated using the new data distribution, and the response object defined using the MC sample with the changed selection. The relative difference between this result and the baseline one is shown in figure 5.26. The systematic error is 0.3 % on average. In order to reduce the oscillations introduced by this systematic across the p_{T} spectrum, we combine adjacent bins together.
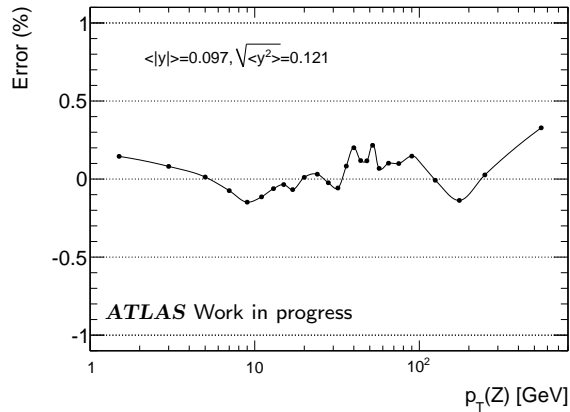
Figure 5.26: Charge mis-identification systematic uncertainty. The baseline result is compared to a measurement done relaxing the opposite sign requirement. The figure shows the average uncertainty across the p_T^Z bins ($< |y| >$) and the root mean squared of the points ($\sqrt{< y^2 >}$).

GEANT4 detector description

Detailed studies done on the MC simulation used in 2011 showed that some physical effects were not modeled with enough accuracy, in particular the electron multiple scattering, bremsstrahlung and the photon conversion (pair production), affecting the energy calibration. A new version of the GEANT4 detector simulation was produced addressing these issues, and new MC samples were produced using this new version.

In order to assess the impact of the GEANT4 improvement in the result, the analysis is repeated using a signal MC sample obtained with the fixed simulation. In addition, updated energy scale correction factors and smearing corrections are applied. The changed result is compared to the baseline in figure 5.27, where we show the relative difference between the varied result and the baseline one. The differences observed are due to residual mis-modeling of the material in front of the ECAL, and stay within 1 % for p_T^Z below 100 GeV, reaching 4 % in the last p_T^Z bin.
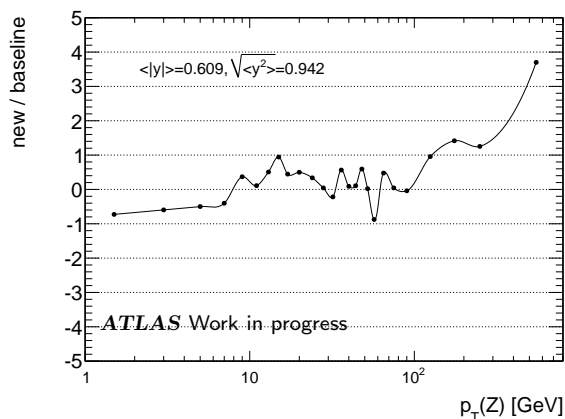
Figure 5.27: Comparison of the result obtained with the GEANT4 fixed MC sample, with the baseline one. The figure shows the average uncertainty across the p_T^Z bins ($< |y| >$) and the root mean squared of the points ($\sqrt{< y^2 >}$).

The differences observed in this comparison are taken as an additional systematic uncertainty. In order to reduce the oscillations across the bins, we combine adjacent bins together. Notice that the result based on the original MC sample is kept, due to the fact that complete systematics are not available for the new sample, and in addition the residual mis-modeling of the detector geometry needs to be assessed.

LAr hole and MC simulation

During the 2011 data taking period in ATLAS, there were some hardware failures that affected the electromagnetic part of the liquid argon calorimeter. The failure that had the most important effect were 6 disabled front-end boards (FEB), covering the area defined by $0 < \eta < 1.475$ and $-0.791 < \phi < -0.595$ in the second and third layer of the calorimeter, resulting in ~ 2 % of LAr coverage affected (known as "LAr hole"). This happened during the data periods E-H (approximately 17 % of 2011 luminosity). This failure was taken into account in the MC simulations [73].

However, the LAr hole was simulated in MC beyond its real duration. This can be seen in figure 5.16c which shows the ϕ distribution of the electrons: in the hole region data are above the expected number of events by ~ 10 %. In order to investigate the possible impact of this mis-modeling we performed a test, consisting on removing from the MC signal sample the events belonging to the period where the LAr hole was wrongly simulated (MC run Number = 186169), removing the corresponding events in data (data periods represented by the eliminated MC period, i.e. periods I to K), and repeating the analysis with these changes.

Figure 5.28a shows the distribution of the ϕ angle of the electrons, after removing the mentioned events. The data vs. expectation agreement improves, the 10 % point seen before disappears (the LAr hole is still visible, but now it is well modeled). In figure 5.28b we compare the measured distribution after these changes with the baseline result. The plot shows that the measurement is stable within the uncertainties, and no trend is observed, proving that the problem in the MC simulation can be safely ignored. This is not taken as a source of systematic uncertainty.
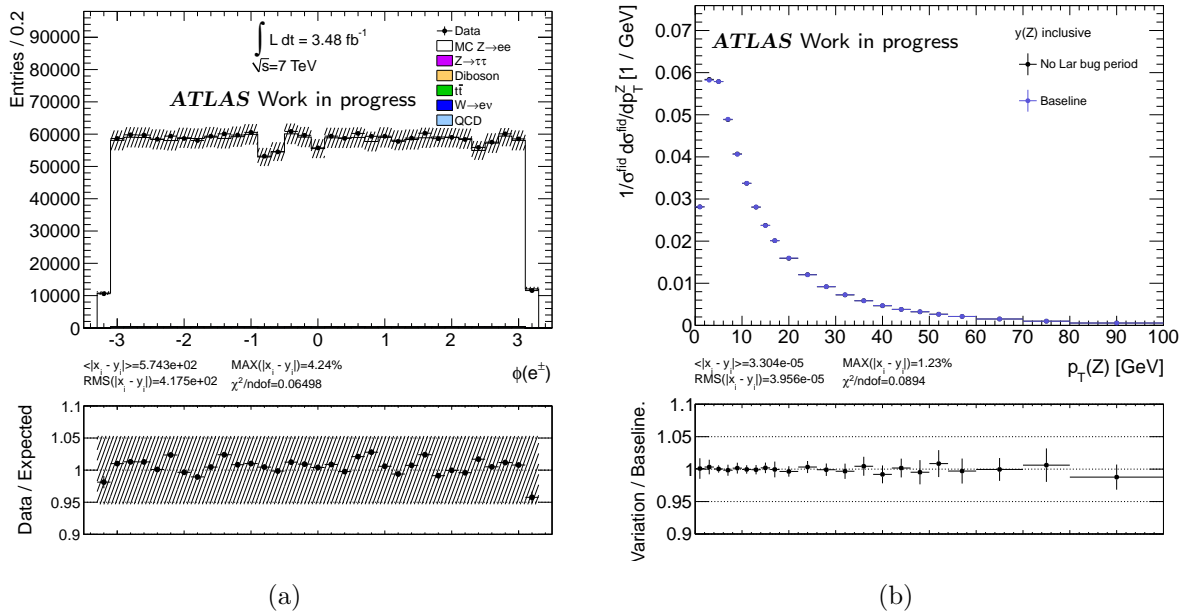
Figure 5.28: (a) ϕ distribution of electrons after the removal in data of events from period I to K, and the removal in MC of events with the wrong LAr hole simulation. (b) Comparison of the result obtained after the removal of events, with the nominal result (distributions and ratio). The result is stable within the uncertainties.

5.3.5   Theoretical uncertainties

In this section we describe the estimation of uncertainties due to the theoretical description, which enter the measurement via the response object used in the unfolding and the definition of the final state electrons.

p_T^Z shape modeling

We consider the bias coming from the description done by the MC baseline sample of the p_T^Z distribution. In order to assess this systematic, we define a new response object using the baseline sample, but reweighting the p_T^Z shape to a different distribution, and repeat the analysis with this sample. In principle, the p_T^Z reweighting can be done to any shape, however, in order to avoid overestimating this systematic, we choose to reweight the distribution to the p_T^Z shape given by data. Figure 5.29 illustrates the reweighting process, where we show a comparison of different p_T^Z shapes, including the data interpolation done using splines [35], and the result of the reweighting to data.
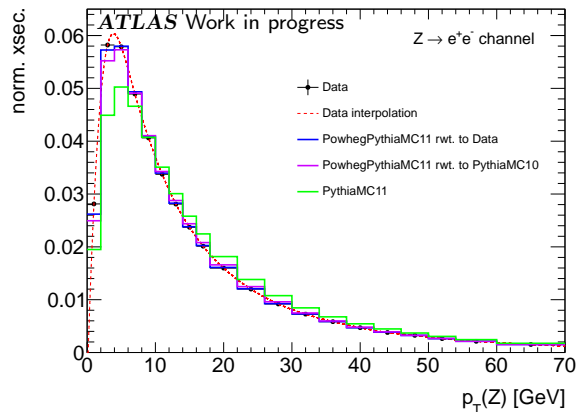
(a)

Figure 5.29: Comparison of different p_T^Z shapes used in the estimation of the p_T^Z modeling unfolding systematic, including MC baseline, unfolded data, and MC reweighted to data.

The final estimation of this systematic is illustrated in figure 5.30. In figure 5.30a we show the comparison of the varied unfolded distribution, obtained using the reweighted sample, with the baseline result (relative difference). We notice the fluctuations due to the limited statistics. In order to smooth this systematic across the p_T^Z spectrum, we adopt the following strategy: this systematic is common to the electron and muon channels (see section 5.6), so the estimations done for each channel can be combined in order to increase statistics. The procedure is similar to what is explained in section 5.3.4, instead of using a different MC sample we use the muon channel results. Further smoothing is obtained with rebinning, and the final estimation is shown in figure 5.30b. The uncertainty has an average value of 0.18 % across the p_T^Z spectrum.

Accuracy of the hard process matrix element

Here, we estimate the systematic error due to the description of the hard process in the MC generator. It is estimated building the response matrix from MC samples which implement different calculations of the Z production matrix element. The MC samples are reweighted to the same p_T^Z shape, in order to disentangle the p_T^Z modeling effects (evaluated as explained in the previous section) from the present effect.

In principle this uncertainty can be estimated comparing the result obtained from any two different MC generators. As our baseline is the POWHEG generator, we take as variation the MC@NLO generator (see table 5.1), in order to use two different NLO generators. However, this direct comparison results in many fluctuations, due to the limited statistics of the MC samples. In order to increase the statistics and improve the estimation, we combine the estimations with muon channel results, in a similar to what is done with the p_T^Z systematic. The result of this comparison is shown in figure 5.31 (relative differences with respect to baseline result). The error bars used in the plots are computed using the method explained in section 5.3.1.
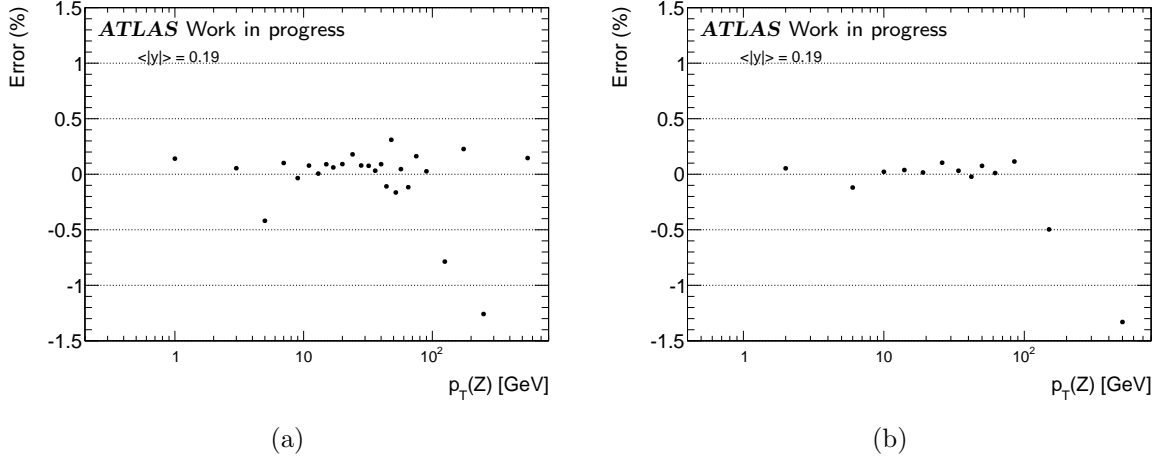
Figure 5.30: Unfolding systematic error associated to the modeling of the p_T^Z shape in MC. (a) Relative difference of the varied sample with respect to the baseline one; (b) relative differences combining electron and muon channel estimations, and rebinning histograms (dividing the number of bins by 2).
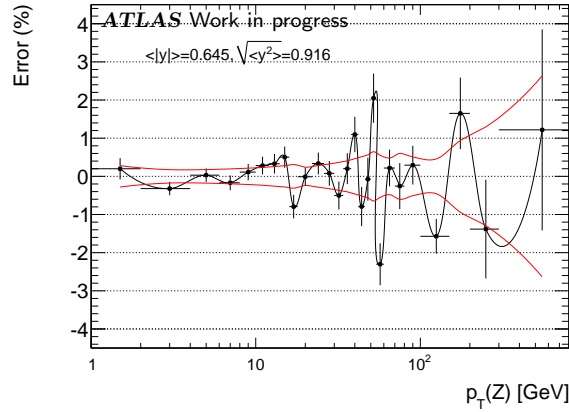

Figure 5.31: Comparison of baseline result with result using MC@NLO, where a previous average has been done with the results of the muon channel in order to reduce fluctuations (we show the relative difference with respect to the baseline result). The red lines show the size of the errors on the ratio.

The plot of figure 5.31 does not not show a clear trend, and many points are compatible with zero, within the error bars. In order to be conservative and at the same time avoid the statistical fluctuations, we take as estimation, for each bin, the maximum value between the size of the error bar associated to the bin, and the value of the shift itself. In order to smooth remaining fluctuation, adjacent bins are combined. The final estimation has an average of 0.65 % across the spectrum.

PDF uncertainties

The uncertainty associated with the PDF choice is assessed in a similar way than other uncertainties: the baseline MC sample is reweighted to other PDF sets, the unfolding is repeated with the new response matrix obtained from this MC, and the results are compared to the nominal one. The PDF reweighting is done using the LHAPDF interface [74]. Two effects are considered:

- Internal variations of the original PDF set of the baseline sample (CT10 [54]). There is a total of 26 parameters that can be varied. In order to add up all the variations we follow the recommendation given in reference [11]. The resulting relative uncertainty (relative difference with respect to baseline) is shown in figure 5.32a.

- Comparison of result obtained using the central values of the CT10 PDF set with the result obtained using the central values of the MSTW 2008 NLO PDF [13]. The relative differences are shown in figure 5.32b.
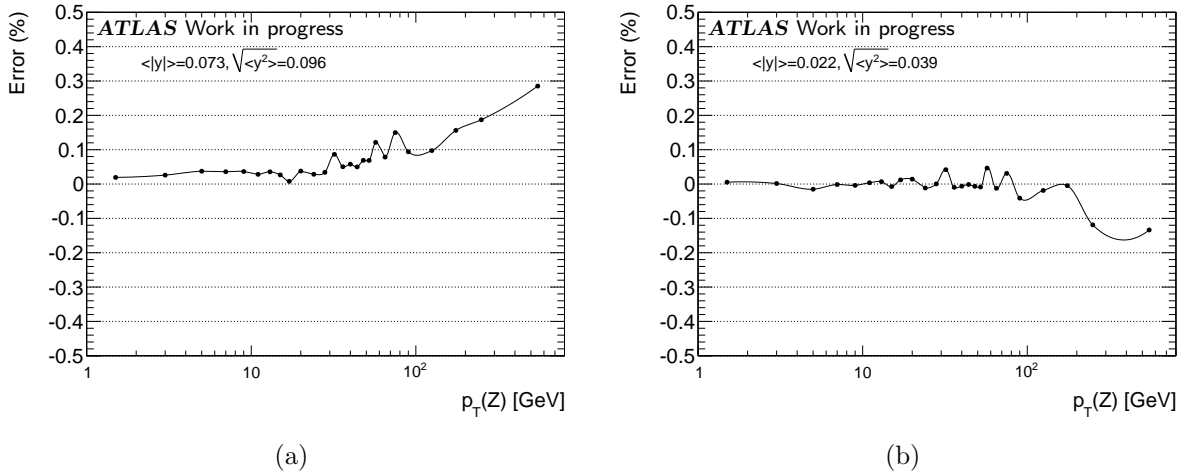

(a)

(b)

Figure 5.32: PDF uncertainty, in percentage of the bin content. a) Internal variations of the PDF set CT10. b) Comparison of the central values of CT10 and MSTW2008.

The two effects are considered as independent uncertainties in the measurement, and are assumed equal for the two channels. Figure 5.32 show that the uncertainty is small, below 0.10 % for $p_T < 100$ GeV.

FSR model

The uncertainty induced by the accuracy of the theoretical description of QED final state radiation (FSR) is obtained in the following way. We compare the FSR correction factors, defined in section 5.2 (k_i^{bare} and $k_i^{dressed}$ in equation (5.5)) predicted by PHOTOS (baseline sample) with the factors predicted by SHERPA, which offer a different implementation of the FSR process. The correction factors and their respective ratios are shown in figure 5.33.

The electron reconstruction implicitly collects a significant fraction of collinearly radiated photons (they are included in the electromagnetic cluster), so reconstructed electrons are closer in kinematics to dressed electrons than to bare. For this reason, the comparison of $k_{dressed}$ factors (figure 5.33b) is appropriate as estimation of this uncertainty in the case of electrons. A value of 0.2 % is assumed across all the spectrum (RMS of the points in the ratio plot).

5.4   Results

The results of the measurement are summarized in table 5.7. The normalized differential cross-section values per bin are reported in the table, together with the FSR correction factors (defined in section 5.2) and the relative statistical, systematic and total uncertainties, in percent of the bin content. The cross-section is measured with an average uncertainty of 0.96 % up to $p_T^Z = 60$ GeV, and with an average uncertainty of 1.48 % over the entire p_T^Z range. Notice that the uncertainty in the last bin is dominated by statistics. The cross-section values given in the table are defined at Born level. The normalized cross-section is shown in figure 5.34, for the whole p_T^Z range in logarithmic scale, and for $p_T^Z < 80$ GeV in linear scale.

In table 5.8 we present the detailed relative uncertainties for every bin. The dominant systematics are the energy scale, the GEANT4 detector description and the unfolding matrix element, with average values over the whole range of 0.42 %, 0.46 % and 0.53 % respectively.
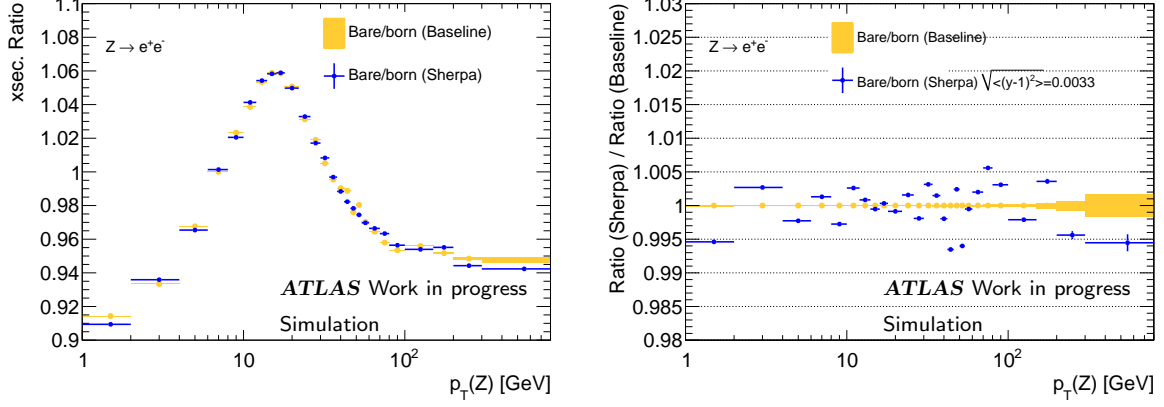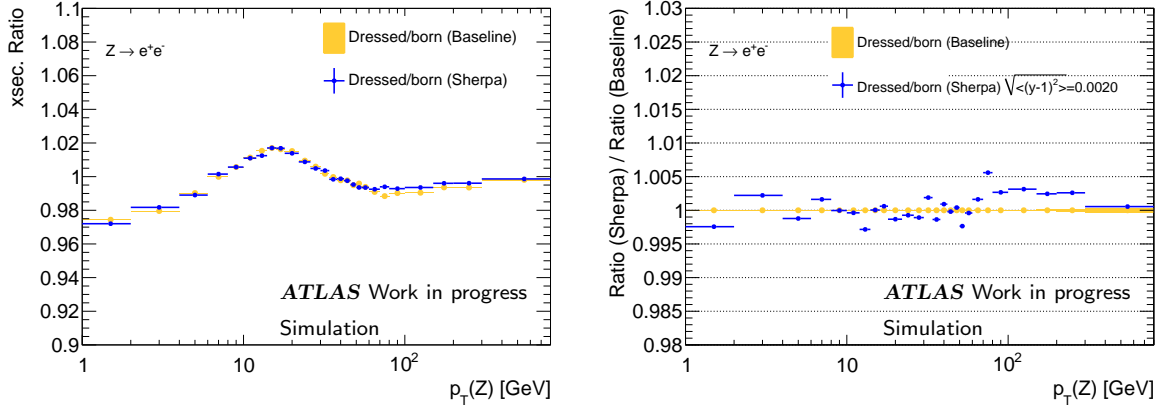
Figure 5.33: Comparison between FSR correction factors, as predicted by PHOTOS and SHERPA. a) k_{bare} factors (left) and their ratio (right); b) $k_{dressed}$ factors (left) and their ratios (right). Next to the legend of the plots the RMS of the points computed around one is given ($\sqrt{<(y-1)^2>}$).

Figure 5.35 shows the evolution of the uncertainties across the p_T^Z spectrum. Figure 5.35a shows all the uncertainties, and figure 5.35b the splitting of the uncertainties that are common with the muon channel measurement (see section 5.6).

Bin limits (GeV)	$\frac{1}{\sigma^{\text{fid}}}\frac{\mathrm{d}\sigma^{\text{fid}}}{\mathrm{d}p_T^Z}$ (1/GeV)	k_{bare}	$k_{dressed}$	Uncertainty (%) Stat.	Sys.	Tot.
0 - 2	0.0281271	0.920	0.976	0.42	1.02	1.10
2 - 4	0.0582079	0.937	0.979	0.26	1.00	1.04
4 - 6	0.0578749	0.970	0.990	0.26	0.62	0.67
6 - 8	0.0489315	1.002	1.000	0.28	0.62	0.68
8 - 10	0.0406292	1.025	1.007	0.31	0.51	0.60
10 - 12	0.0337370	1.039	1.012	0.35	0.51	0.62
12 - 14	0.0280969	1.054	1.016	0.37	0.89	0.96
14 - 16	0.0237074	1.059	1.018	0.42	0.89	0.98
16 - 18	0.0201223	1.059	1.017	0.47	0.75	0.89
18 - 22	0.0159784	1.050	1.016	0.40	0.74	0.85
22 - 26	0.0120082	1.030	1.010	0.48	0.50	0.69
26 - 30	0.0091894	1.019	1.006	0.54	0.51	0.74
30 - 34	0.0072655	1.005	1.002	0.62	0.52	0.81
34 - 38	0.0058376	0.996	1.000	0.70	0.53	0.88
38 - 42	0.0046991	0.990	0.998	0.78	0.61	0.99
42 - 46	0.0037907	0.990	0.998	0.84	0.63	1.05
46 - 50	0.0032453	0.977	0.996	0.90	1.12	1.44
50 - 54	0.0026304	0.981	0.996	1.04	1.14	1.55
54 - 60	0.0021203	0.972	0.994	0.97	1.43	1.73
60 - 70	0.0015183	0.965	0.991	0.85	1.42	1.65
70 - 80	0.0009944	0.959	0.989	1.08	0.85	1.37
80 - 100	0.0005661	0.956	0.991	0.95	0.81	1.25
100 - 150	0.0001937	0.958	0.991	0.96	1.68	1.94
150 - 200	0.0000483	0.957	0.994	1.86	1.79	2.58
200 - 300	0.0000109	0.953	0.994	2.75	3.36	4.34
300 - 800	0.0000004	0.956	0.998	6.05	3.77	7.12

Table 5.7: Summary of results. The uncertainties are given in percent of the bin content.

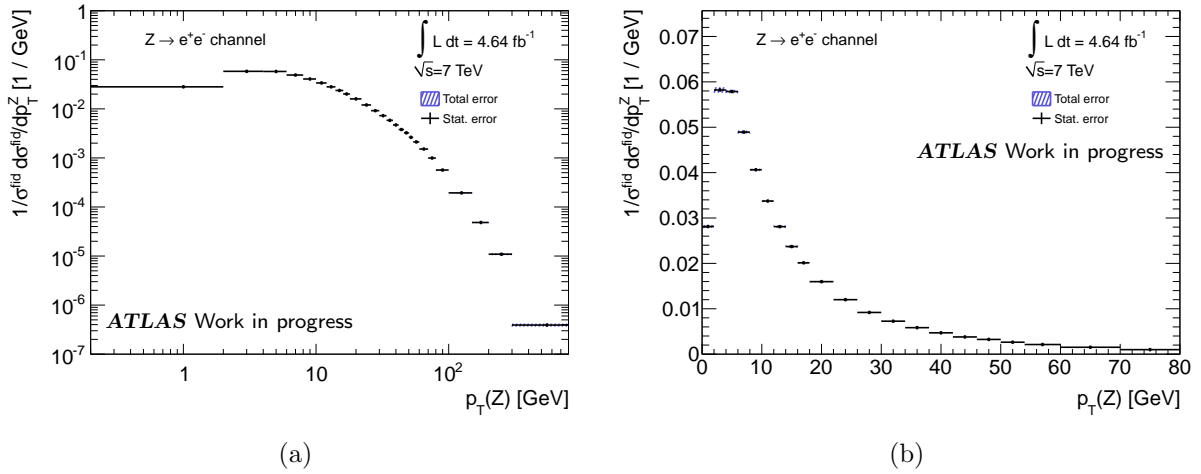
Figure 5.34: Measured normalized differential cross-section. (a) Full p_T^Z range, logarithmic scale; (b) low p_T^Z range.

Bin										Uncertainty (%)												
	Data	EW backg.		QCD backg.		E. scale.			E.	Scale factors			Cha.	G4	FSR	PDF		Unfolding		MC	Total	Total
limits (GeV)	Stat.	Xsec.	Lumi.	Frac.	Shape	Scale	Mat.	Pres.	Resol.	Reco.	Id.	Trig.	Id.	Fix		CT10	Ext.	p_T^Z	Mat.	stat.	sys.	
0 - 2	0.42	0.02	0.01	0.07	0.00	0.18	0.45	0.17	0.50	0.00	0.01	0.01	0.10	0.64	0.20	0.02	0.01	0.05	0.15	0.20	1.02	1.10
2 - 4	0.26	0.02	0.01	0.06	0.00	0.18	0.45	0.17	0.50	0.00	0.02	0.00	0.10	0.64	0.20	0.03	0.00	0.05	0.15	0.12	1.00	1.04
4 - 6	0.26	0.02	0.00	0.04	0.00	0.13	0.23	0.11	0.04	0.01	0.03	0.00	0.03	0.45	0.20	0.04	0.02	0.11	0.13	0.13	0.62	0.67
6 - 8	0.28	0.02	0.00	0.03	0.00	0.13	0.23	0.11	0.04	0.01	0.03	0.00	0.03	0.45	0.20	0.04	0.00	0.11	0.13	0.14	0.62	0.68
8 - 10	0.31	0.02	0.00	0.01	0.00	0.02	0.06	0.02	0.27	0.01	0.03	0.00	0.13	0.25	0.20	0.04	0.00	0.03	0.19	0.15	0.51	0.60
10 - 12	0.35	0.02	0.00	0.01	0.00	0.02	0.06	0.02	0.27	0.01	0.02	0.00	0.13	0.25	0.20	0.03	0.00	0.03	0.19	0.16	0.51	0.62
12 - 14	0.37	0.01	0.00	0.02	0.00	0.06	0.15	0.09	0.08	0.00	0.02	0.00	0.05	0.71	0.20	0.04	0.01	0.04	0.41	0.18	0.89	0.96
14 - 16	0.42	0.01	0.00	0.03	0.00	0.06	0.15	0.09	0.08	0.00	0.01	0.00	0.05	0.71	0.20	0.03	0.01	0.04	0.41	0.20	0.89	0.98
16 - 18	0.47	0.01	0.00	0.04	0.00	0.04	0.16	0.05	0.17	0.00	0.01	0.00	0.03	0.47	0.20	0.01	0.01	0.01	0.45	0.22	0.75	0.89
18 - 22	0.40	0.01	0.00	0.05	0.00	0.04	0.16	0.05	0.17	0.00	0.00	0.00	0.03	0.47	0.20	0.04	0.01	0.01	0.45	0.17	0.74	0.85
22 - 26	0.48	0.00	0.00	0.06	0.01	0.09	0.20	0.06	0.05	0.01	0.01	0.00	0.01	0.21	0.20	0.03	0.01	0.10	0.22	0.20	0.50	0.69
26 - 30	0.54	0.01	0.00	0.07	0.00	0.09	0.20	0.06	0.05	0.01	0.02	0.00	0.01	0.21	0.20	0.03	0.00	0.10	0.22	0.23	0.51	0.74
30 - 34	0.62	0.02	0.01	0.07	0.01	0.07	0.20	0.04	0.11	0.01	0.04	0.00	0.01	0.13	0.20	0.09	0.04	0.03	0.27	0.26	0.52	0.81
34 - 38	0.70	0.03	0.01	0.06	0.00	0.07	0.20	0.04	0.11	0.01	0.06	0.00	0.01	0.13	0.20	0.05	0.01	0.03	0.27	0.29	0.53	0.88
38 - 42	0.78	0.03	0.01	0.06	0.01	0.09	0.21	0.05	0.00	0.01	0.08	0.01	0.01	0.10	0.20	0.06	0.01	0.03	0.34	0.32	0.61	0.99
42 - 46	0.84	0.04	0.01	0.06	0.00	0.09	0.21	0.05	0.00	0.01	0.10	0.01	0.16	0.10	0.20	0.05	0.00	0.03	0.34	0.36	0.63	1.05
46 - 50	0.90	0.06	0.02	0.04	0.00	0.15	0.30	0.05	0.01	0.01	0.13	0.01	0.16	0.34	0.20	0.07	0.01	0.07	0.88	0.39	1.12	1.44
50 - 54	1.04	0.07	0.02	0.04	0.01	0.15	0.30	0.05	0.01	0.01	0.14	0.01	0.16	0.34	0.20	0.07	0.01	0.07	0.88	0.45	1.14	1.55
54 - 60	0.97	0.07	0.02	0.02	0.00	0.13	0.31	0.08	0.05	0.01	0.16	0.01	0.08	0.31	0.20	0.12	0.05	0.01	1.26	0.39	1.43	1.73
60 - 70	0.85	0.10	0.03	0.00	0.00	0.13	0.31	0.08	0.05	0.02	0.19	0.02	0.08	0.31	0.20	0.08	0.01	0.01	1.26	0.33	1.42	1.65
70 - 80	1.08	0.11	0.03	0.02	0.00	0.26	0.39	0.13	0.02	0.02	0.15	0.02	0.12	0.01	0.20	0.15	0.03	0.11	0.43	0.41	0.85	1.37
80 - 100	0.95	0.15	0.04	0.03	0.00	0.26	0.39	0.13	0.02	0.02	0.08	0.01	0.12	0.01	0.20	0.09	0.04	0.11	0.43	0.35	0.81	1.25
100 - 150	0.96	0.15	0.04	0.05	0.00	0.18	0.63	0.16	0.02	0.03	0.04	0.01	0.03	1.05	0.20	0.10	0.02	0.50	0.92	0.33	1.68	1.94
150 - 200	1.86	0.11	0.03	0.07	0.01	0.18	0.63	0.16	0.02	0.04	0.17	0.01	0.03	1.05	0.20	0.16	0.00	0.50	0.92	0.66	1.79	2.58
200 - 300	2.75	0.09	0.02	0.08	0.00	0.30	2.14	0.71	0.19	0.06	0.24	0.02	0.04	1.34	0.20	0.19	0.12	1.27	1.29	0.91	3.36	4.34
300 - 800	6.05	0.10	0.03	0.08	0.00	0.30	2.14	0.71	0.19	0.11	0.37	0.02	0.04	1.34	0.20	0.29	0.13	1.27	1.29	1.89	3.77	7.12
Avg.	0.96	0.05	0.01	0.04	0.00	0.13	0.42	0.13	0.12	0.02	0.08	0.01	0.07	0.46	0.20	0.07	0.02	0.18	0.53	0.36	1.09	1.48
Avg. (< 60)	0.55	0.03	0.01	0.04	0.00	0.09	0.22	0.07	0.13	0.01	0.05	0.00	0.08	0.36	0.20	0.05	0.01	0.05	0.39	0.24	0.77	0.96

Table 5.8: Detailed uncertainties, given in percent with respect to the bin content. The last two rows show the average errors, for the whole p_T^Z range and for $p_T^Z < 60$ GeV.
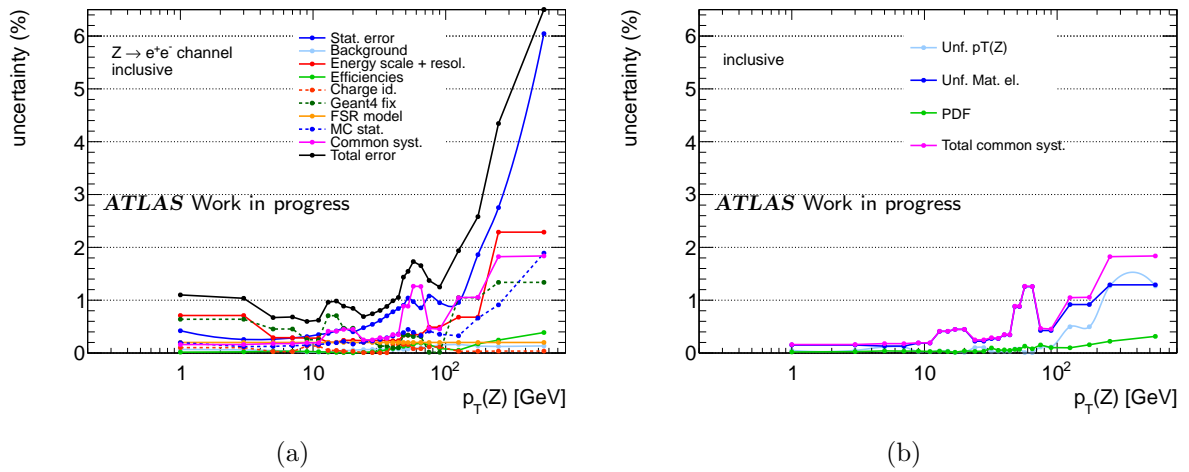
114

Figure 5.35: Summary of uncertainties, given in percent of the central value of the bin, as a function of p_T^Z. (a) Uncertainties for the electron channel measurement, (b) splitting of the uncertainties that are common with the muon channel measurement.

5.5 Measurement in Z boson rapidity bins

In order to take advantage of the large data statistics collected in 2011, we perform the measurement of the normalized differential cross-section in three regions of Z boson rapidity defined by: $0.0 \le |y^Z| < 1.0$, $1.0 \le |y^Z| < 2.0$ and $2.0 \le |y^Z| < 2.4$. This binning was chosen in order to probe events with different values of momentum fraction of the hard scattering partons (see section 1.3).

The measurement is repeated in each of the rapidity regions independently, as the bin migrations across rapidity bins are negligible (independent response objects are defined for the unfolding). Figure 5.36 shows the purity of the rapidity bins, which is $\sim 99\%$ in the first 2 bins, and $\sim 98\%$ in the last bin.
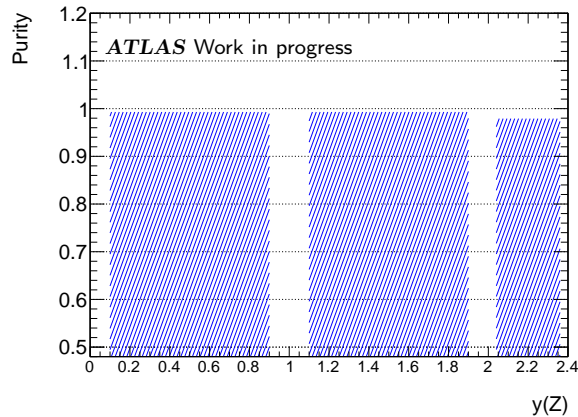

Figure 5.36: Purity of rapidity bins. The purity is $> 98\%$ for all bins.

The number of selected events in data for each rapidity bin, together with the percentage with respect to the total number of selected events, is shown in table 5.9.

Bin	Number of events	% of total
Total	1228863	
$0.0 \le |y^Z| < 1.0$	723554	58.9
$1.0 \le |y^Z| < 2.0$	446796	36.4
$2.0 \le |y^Z| < 2.4$	57531	4.7

Table 5.9: Number of selected events in each Z boson rapidity bin.

The number of QCD background events in the Z rapidity regions is estimated using the same fraction q_T (equation (5.14)), but scaling it according to the fraction of events falling in every rapidity region with respect to the total in the QCD control sample, using the original template histograms, that is:

$$q(y_i) = q_T \frac{N_{orig}^{QCD}(y_i)}{N_{orig}^{QCD}} \tag{5.32}$$

here, $q(y_i)$ is the fraction of QCD events in the Z boson rapidity bin i, with respect to the total number of data events in that rapidity bin, $N_{orig}^{QCD}(y_i)$ is the original number of events in the QCD sample in the rapidity bin i, and N_{orig}^{QCD} the original number of events in the QCD sample.

The estimation of uncertainties follows the same procedure used for the inclusive measurement, comparing distributions defined inside each rapidity bin. In table 5.10 we present a summary of the results, including the cross-section values and the total relative uncertainty.

The cross-section is measured with an average error of 1.74 %, 2.50 % and 8.35 % for the first, second and third y^Z bin, respectively. Detailed errors for each y^Z bin are given in appendix A.

Figure 5.37 shows the spectra measured in the y^Z bins and the inclusive one, for low p_T and full p_T range. The broadening of the spectrum observed in the last y^Z bin will be discussed in section 6.2.1.
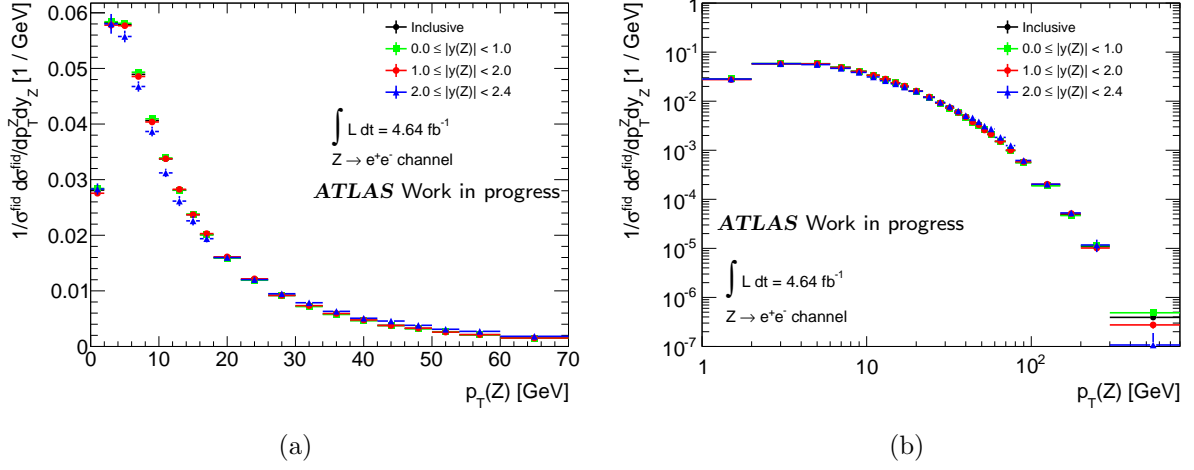

(a)   (b)

Figure 5.37: Measured p_T^Z spectra in rapidity bins, and the inclusive one. (a) low p_T^Z region, (b) full spectrum.

Table 5.10 rotated 90°.

Bin limits (GeV)	0.0 ≤ $|y^Z|$ < 1.0		1.0 ≤ $|y^Z|$ < 2.0		2.0 ≤ $|y^Z|$ < 2.4	
	$\frac{1}{\sigma^{\mathrm{fid}}}\frac{\mathrm{d}\sigma^{\mathrm{fid}}}{\mathrm{d}p_T^Z}$ (1/GeV)	Tot. Unc. (%)	$\frac{1}{\sigma^{\mathrm{fid}}}\frac{\mathrm{d}\sigma^{\mathrm{fid}}}{\mathrm{d}p_T^Z}$ (1/GeV)	Tot. Unc. (%)	$\frac{1}{\sigma^{\mathrm{fid}}}\frac{\mathrm{d}\sigma^{\mathrm{fid}}}{\mathrm{d}p_T^Z}$ (1/GeV)	Tot. Unc. (%)
0 - 2	0.0284156	1.13	0.0275569	1.41	0.0283146	3.57
2 - 4	0.0584021	1.03	0.0577837	1.28	0.0580207	3.06
4 - 6	0.0581184	0.79	0.0576814	0.69	0.0557437	1.88
6 - 8	0.0493239	0.81	0.0485502	0.73	0.0467494	1.99
8 - 10	0.0409429	0.64	0.0403704	0.88	0.0386565	2.25
10 - 12	0.0339007	0.67	0.0337654	0.91	0.0312127	2.41
12 - 14	0.0281324	0.92	0.0282658	1.19	0.0261412	3.46
14 - 16	0.0238150	0.95	0.0236985	1.23	0.0225890	3.63
16 - 18	0.0200645	0.95	0.0202933	1.44	0.0193835	3.43
18 - 22	0.0158968	0.88	0.0161145	1.40	0.0159937	2.77
22 - 26	0.0119128	1.10	0.0121642	1.03	0.0120211	3.93
26 - 30	0.0091695	1.15	0.0091842	1.10	0.0094849	4.18
30 - 34	0.0071724	1.00	0.0073385	1.33	0.0078661	3.91
34 - 38	0.0057538	1.08	0.0059200	1.46	0.0063157	4.20
38 - 42	0.0046346	1.30	0.0047656	1.65	0.0050773	4.57
42 - 46	0.0037489	1.41	0.0037808	1.82	0.0045749	4.72
46 - 50	0.0031802	1.73	0.0032931	2.05	0.0038055	5.18
50 - 54	0.0026330	1.82	0.0025868	2.27	0.0030948	5.68
54 - 60	0.0020790	1.84	0.0021256	1.96	0.0027181	7.94
60 - 70	0.0014977	1.77	0.0015200	1.87	0.0018278	7.82
70 - 80	0.0009728	1.64	0.0010030	2.45	0.0012439	7.04
80 - 100	0.0005538	1.48	0.0005818	2.25	0.0006191	6.97
100 - 150	0.0001879	1.89	0.0002029	2.78	0.0002035	7.03
150 - 200	0.0000467	2.86	0.0000512	4.04	0.0000527	11.34
200 - 300	0.0000113	5.82	0.0000102	9.75	0.0000117	28.45
300 - 800	0.0000005	8.54	0.0000003	15.90	0.0000001	75.59

Table 5.10: Summary of results for the cross-section measurement in bins of y^Z. The total errors are given in percentage of the bin content.

118

5.6   Combination with muon channel

In parallel to the measurement in the $Z \to e^+e^-$ channel, a measurement was done in the $Z \to \mu^+\mu^-$ channel, using the same data set. The experimental part of the measurement and the experimental systematics uncertainties differ naturally from those of the electron channel, however, the unfolding method used is exactly the same, and it is based on a similar MC sample. For this reason, the theoretical systematics are assumed to be common to the two channels. The experimental aspects of the measurement in the muon channel are described in [75].

5.6.1   Channel comparison

In figure 5.38 the comparison of the measurement in the two channels is presented, inclusive and for the y^Z rapidity bins. The error bars include total experimental errors, (statistical and experimental systematics). We can see that the agreement between the two distributions is reasonable, with a $\chi^2/ndof$ value of 1.05 in the range $p_T^Z < 100$ GeV, for the rapidity inclusive measurement.

Even though agreement between the channels is acceptable, we observe some trend in the first rapidity bin. This trend can be explained by the fact that some experimental uncertainties are fully correlated between bins, introducing tilts in the unfolded distribution that can change the slope of the $ee - \mu\mu$ comparison. In figure 5.39 we show two examples of these uncertainties: the passive material contribution to the energy scale in the e^+e^- channel and the isolation efficiency in the $\mu^+\mu^-$ channel [75] (we show relative differences between the varied distributions and the baseline). The scale uncertainty induce a positive variation of up to 0.5 % below p_T^Z=10 GeV, which is compensated by a negative variation of near 0.2 % in the rest of the spectrum ("down" curve in the plot). Similarly, the isolation efficiency scale factor for the muon channel introduce positive deviations of up to 0.3 % low p_T^Z, and 0.4 % in the negative direction at high p_T^Z.
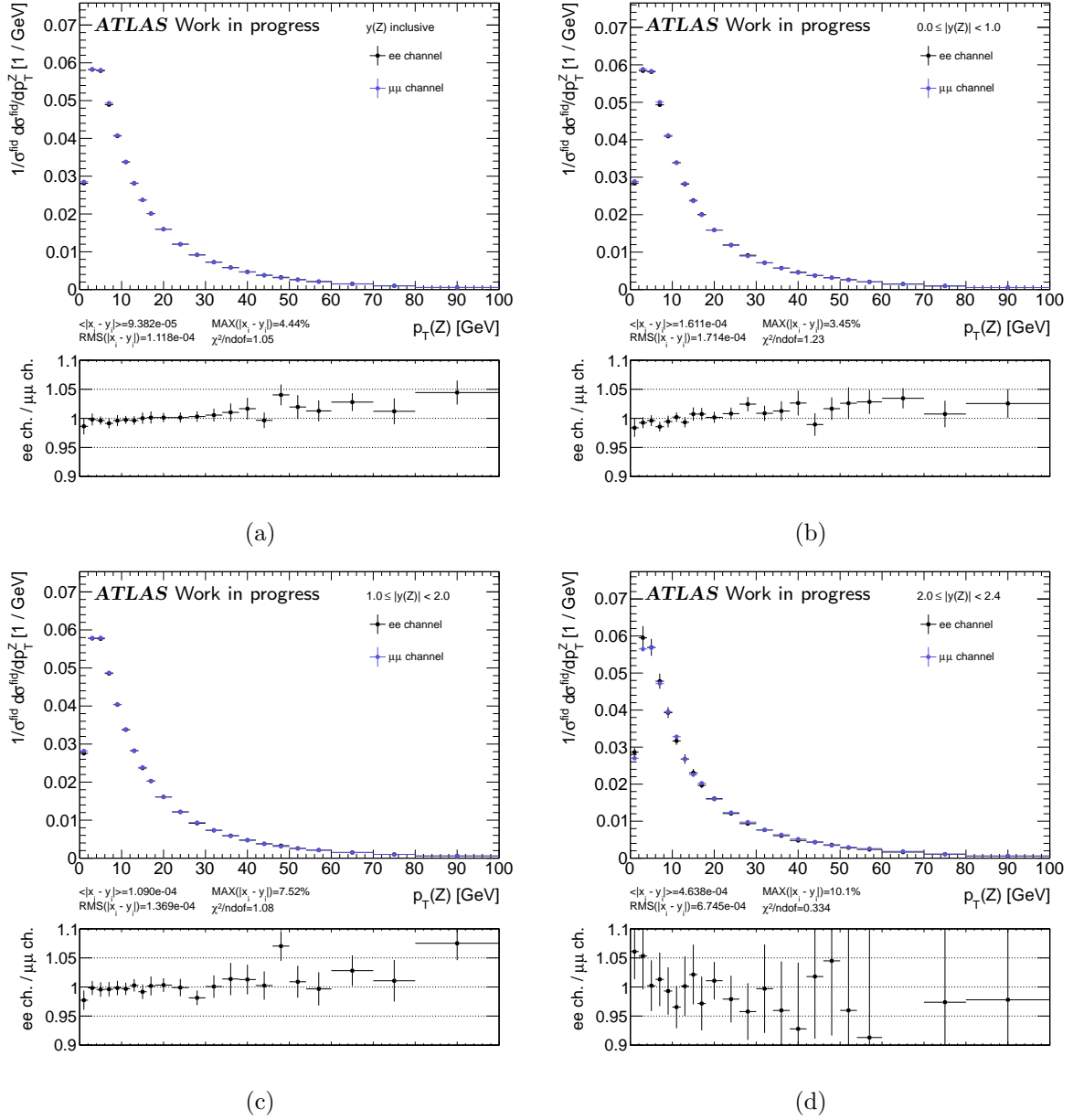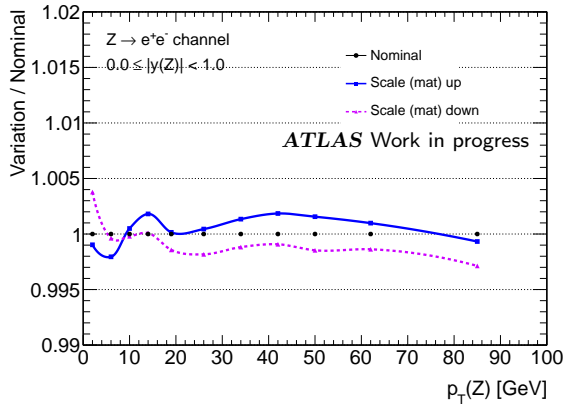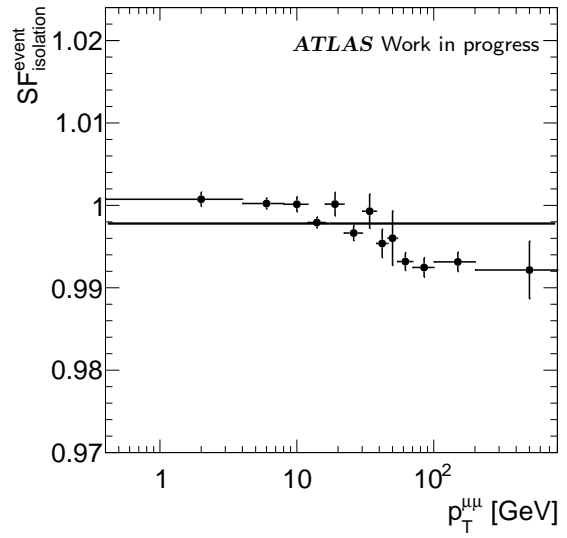
(a)

(b)

(c)

(d)

Figure 5.38: Comparison of measurements in the muon and electron channel, for $p_T^Z < 100$ GeV. (a) Inclusive in rapidity, (b) $0.0 \leq |y^Z| < 1.0$, (c) $1.0 \leq |y^Z| < 2.0$, (d) $2.0 \leq |y^Z| < 2.4$. The error bars include total experimental errors (statistical uncertainties and experimental systematics).

Figure 5.39: Example of two experimental uncertainties that show correlation across the bins, and can change the agreement between the electron and muon channel measurements. (a) Energy scale systematic due to the passive material modeling in the electron channel, (b) isolation scale factors in the muon channel. Notice the p_T^Z dependence of both effects.

121

5.6.2 Combination method

The normalized cross-section for the two channels are combined at the Born level, where the lepton distribution are universal. The combination method is based on the estimation of best linear unbiased estimators ("BLUE"), which is done via a least squares method [76][67]. The χ^2 to be minimized is defined as:

$$\chi^2 = (\mathbf{X} - \bar{\mathbf{X}})^{\mathbf{T}} \mathbf{C}^{-1} (\mathbf{X} - \bar{\mathbf{X}}) \tag{5.33}$$

where X is the joint histogram of measured N-bin distributions in the electron and muon channels, i.e the $2N$-sized vector $\mathbf{X} = \{U_1^e, ..., U_n^e; U_1^\mu, ..., U_n^\mu\}$, $\bar{\mathbf{X}}$ is a $2N$-sized vector containing twice the underlying "true" distribution, to be determined: $\bar{\mathbf{X}} = \{U_1^{comb}, ..., U_n^{comb}; U_1^{comb}, ..., U_n^{comb}\}$, and $\mathbf{C}$ is the $2N \times 2N$ joint covariance matrix, defined as:

$$\mathbf{C} = \begin{pmatrix} \mathbf{C^e} & \mathbf{C^{e\mu}} \\ \mathbf{C^{e\mu}} & \mathbf{C^\mu} \end{pmatrix} \tag{5.34}$$

The $N \times N$ covariance matrices $\mathbf{C^e}$ and $\mathbf{C^\mu}$ are derived from the uncertainties that are independent between the channels, and $\mathbf{C^{e\mu}}$ contains the sources of uncertainty that are correlated across the channels.

The minimization of χ^2 in equation (5.33) gives as a result the combined distribution $\mathbf{U^{comb}}$ and the combined covariance matrix. The minimization is performed using the minimization program MINUIT [77].
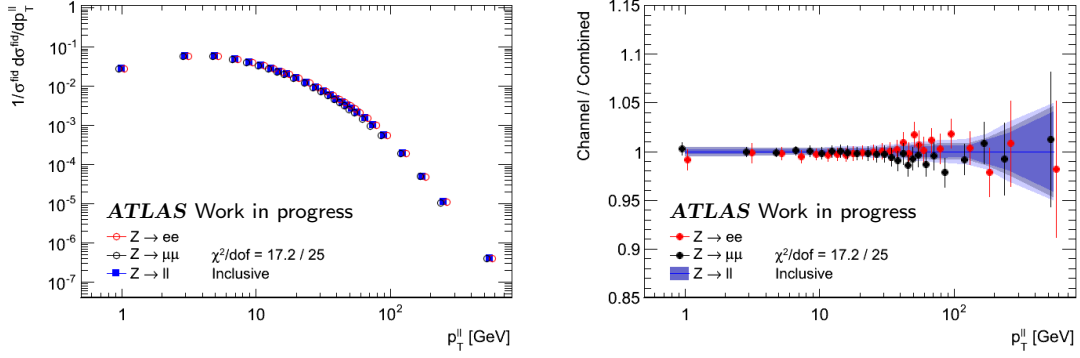
5.6.3 Combined results

The combined results are given in table 5.11. Notice the reduction of the uncertainties after the combination, in comparison with the uncertainties for the individual electron channel. The new uncertainties are, on average across the spectrum, 0.96 %, 1.26 %, 1.62 % and 4.54 % for the inclusive and first, second and third y^Z bins, respectively.
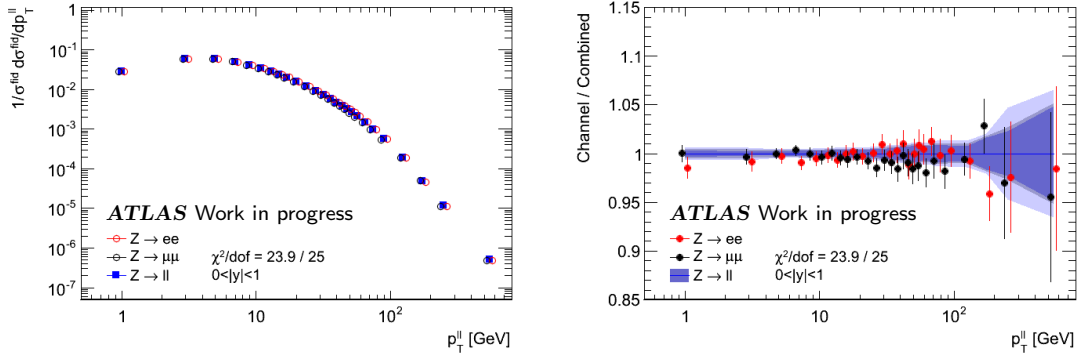
The combined result is compared to the individual channel result in figure 5.40, where the value of the minimized χ^2 for the combination are given.
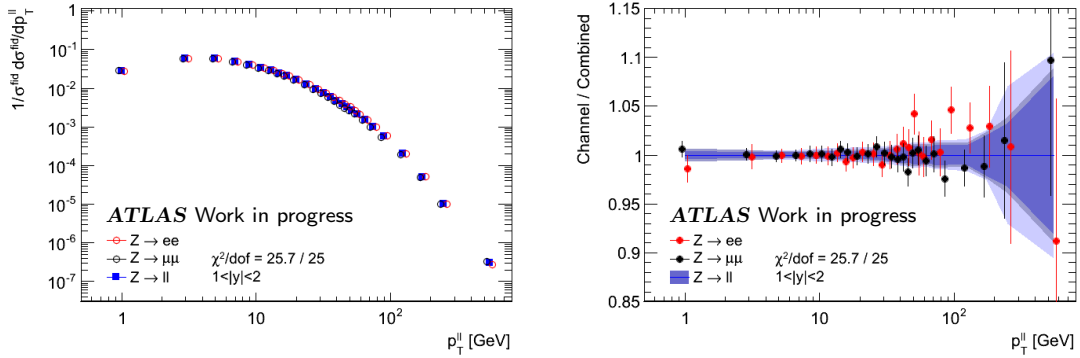
Table 5.11: The combined measured normalized cross-section $\frac{1}{\sigma^{\text{fid}}}\frac{d\sigma^{\text{fid}}}{dp_T}$ in bins of p_T^Z. The cross-sections at Born level are given as well as the relative total error.

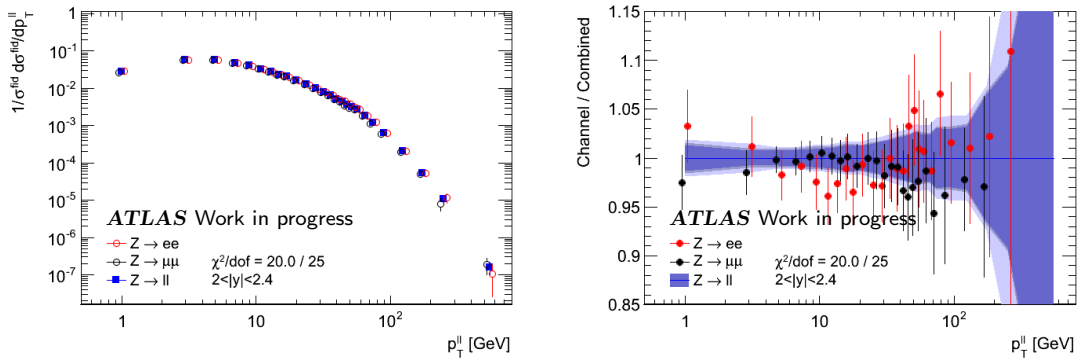| Bin limits (GeV) | Inclusive | | Combination $Z \to e^+e^-$ and $Z \to \mu^+\mu^-$ channels | | | | | |
| | $\frac{1}{\sigma^{\text{fid}}}\frac{d\sigma^{\text{fid}}}{dp_T^Z}$ (1/GeV) | Tot. Unc. (%) | $0.0 \le |y^Z| < 1.0$ | | $1.0 \le |y^Z| < 2.0$ | | $2.0 \le |y^Z| < 2.4$ | |
			$\frac{1}{\sigma^{\text{fid}}}\frac{d\sigma^{\text{fid}}}{dp_T^Z}$ (1/GeV)	Tot. Unc. (%)	$\frac{1}{\sigma^{\text{fid}}}\frac{d\sigma^{\text{fid}}}{dp_T^Z}$ (1/GeV)	Tot. Unc. (%)	$\frac{1}{\sigma^{\text{fid}}}\frac{d\sigma^{\text{fid}}}{dp_T^Z}$ (1/GeV)	Tot. Unc. (%)
0 - 2	0.0283400	0.53	0.0288300	0.71	0.0279400	0.70	0.0274200	1.92
2 - 4	0.0582300	0.44	0.0588800	0.65	0.0578800	0.55	0.0573500	1.47
4 - 6	0.0579400	0.37	0.0582700	0.43	0.0577200	0.45	0.0567300	1.09
6 - 8	0.0491500	0.37	0.0498000	0.45	0.0486100	0.52	0.0471600	1.18
8 - 10	0.0407000	0.39	0.0411500	0.52	0.0403700	0.64	0.0396300	1.30
10 - 12	0.0337900	0.40	0.0339500	0.55	0.0338000	0.67	0.0324800	1.37
12 - 14	0.0281500	0.51	0.0283100	0.58	0.0282100	0.69	0.0268500	1.48
14 - 16	0.0237600	0.53	0.0238100	0.60	0.0238600	0.72	0.0228400	1.66
16 - 18	0.0201200	0.53	0.0200300	0.64	0.0203500	0.76	0.0200900	1.76
18 - 22	0.0159600	0.51	0.0159400	0.61	0.0160600	0.74	0.0161100	1.64
22 - 26	0.0119900	0.49	0.0119000	0.68	0.0121500	0.80	0.0123600	1.97
26 - 30	0.0091630	0.53	0.0090830	0.73	0.0092750	0.86	0.0097650	2.17
30 - 34	0.0072460	0.57	0.0071780	0.81	0.0073400	0.94	0.0078710	2.34
34 - 38	0.0058100	0.63	0.0057370	0.86	0.0058840	0.99	0.0063830	2.59
38 - 42	0.0046460	0.69	0.0045870	0.96	0.0047090	1.07	0.0051440	2.80
42 - 46	0.0037860	0.74	0.0037930	1.02	0.0037530	1.17	0.0044300	2.98
46 - 50	0.0031800	0.89	0.0031810	1.09	0.0031600	1.22	0.0036280	3.15
50 - 54	0.0026030	0.95	0.0026120	1.17	0.0025820	1.32	0.0030670	3.46
54 - 60	0.0021090	1.01	0.0020700	1.13	0.0021300	1.25	0.0027000	3.36
60 - 70	0.0014950	1.02	0.0014790	1.12	0.0014970	1.28	0.0018520	3.33
70 - 80	0.0009879	0.99	0.0009748	1.32	0.0010000	1.50	0.0011670	4.18
80 - 100	0.0005543	0.97	0.0005521	1.31	0.0005562	1.52	0.0006096	4.33
100 - 150	0.0001918	1.27	0.0001893	1.36	0.0001974	1.61	0.0002014	4.38
150 - 200	0.0000491	1.69	0.0000487	2.06	0.0000498	2.55	0.0000516	7.33
200 - 300	0.0000107	2.93	0.0000116	4.74	0.0000101	7.05	0.0000106	18.12
300 - 800	0.0000004	4.97	0.0000005	6.55	0.0000003	10.54	0.0000002	36.81

(a) y^Z inclusive

(b) $0.0 \leq |y^Z| < 1.0$

(c) $1.0 \leq |y^Z| < 2.0$

(d) $2.0 \leq |y^Z| < 2.4$

Figure 5.40: Comparison of the combined result and the individual channels, for the inclusive measurement and the rapidity bins. The left column show the distributions, and the right column the ratios of the channels to the combined distribution. (a) rapidity inclusive measurement, (b) $0.0 <\leq |y^Z| < 1.0$, (c) $1.0 \leq |y^Z| < 2.0$ and (d) $2.0 \leq |y^Z| < 2.4$.

124

Chapter 6

Interpretation of the measurement

As was mentioned in chapter 1, the p_T^Z represents a very clear observable that gives important information on QCD dynamics and the structure of the proton. The result that was presented in chapter 5 has a precision that makes it very valuable to test pQCD theoretical predictions, tune parameters of parton showers and resummation schemes, and perform PDF fits. In this chapter we present comparisons of the p_T^Z measurement with different models, discuss the observed level of agreement and show preliminary results of parameter tuning based on it. The data used for the comparisons is the result of the combination of channels described in section 5.6, which has less uncertainty and then more discriminating power than the individual channels.

The chapter begins with a review of previous measurements of the p_T^Z spectrum. Then comparisons with some theoretical predictions and MC generators are presented. The chapter ends with preliminary MC parton shower tuning results based on the p_T^Z and ϕ^* measurements, which show the compatibility of these two observables.

6.1 Previous measurements

The p_T^Z normalized spectrum in $p\bar{p}$ collisions was measured by the D0 collaboration, using an integrated luminosity of 0.98 fb^{-1} in the electron decay channel [1]. The spectrum was measured up to 260 GeV, and the precision obtained on the measurement was of the order of 3 % below 150 GeV, and up to 80 % for higher p_T^Z bins, where the statistical uncertainty dominates. The measurement was found to be in good agreement with resummed predictions made using ResBos (see section 6.2.1), tuned to previous Tevatron measurements [78]. In the other hand, fixed order QCD predictions at NNLO [79] were found to underestimate the data, up to about 25 %. In figure 6.1 we show the measured p_T^Z spectrum, and the comparison of data with the theoretical predictions.

Two recent measurements of the p_T^Z spectrum were done using LHC pp data collected in 2010, by both ATLAS and CMS collaborations [2][3]. Both analysis used approximately 36 pb^{-1} of data luminosity. The ATLAS measurement was done up to 350 GeV, with a precision from 3 % to 10 % below 180 GeV. The CMS measurement was done up to 600 GeV, obtaining a precision that goes from 4 % to 16 % below 180 GeV. Both measurements are dominated by statistical errors above 50 GeV. The measurements were found to be described within the uncertainties across the whole p_T^Z spectrum by the resummed predictions of ResBos (tuned to Tevatron results). Comparisons to pQCD computations underestimate the data by an amount of up to 10 %, with a noticeable improvement when going from NLO to NNLO in the strong coupling constant (FEWZ predictions, see section 6.2.2). In figure 6.2, the ATLAS p_T^Z measurement and the corresponding comparison with predictions are shown (the measurement is reported at Born level).

The present p_T^Z measurement has a typical precision of 1 % below 100 GeV, and up to 5 % in the last bins, exploring values of p_T^Z up to 800 GeV. Comparing the precision and the reach in
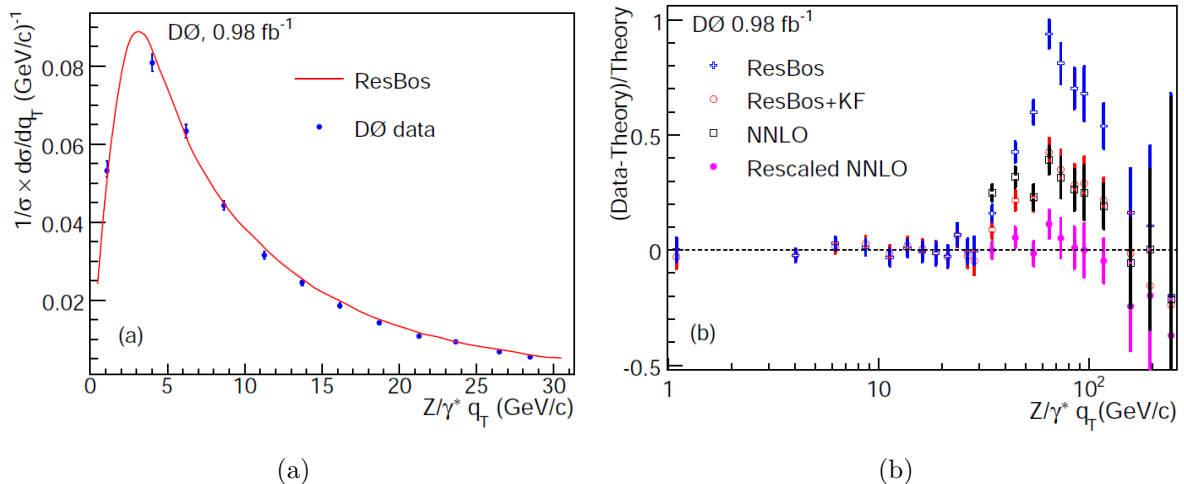
Figure 6.1: Shape of the transverse momentum distribution as measured by D0 for $p_T^Z < 30$ GeV (a), and comparison of data with theoretical predictions for the full range (b) [1].

p_T^Z values with past measurements, the value of the measurement becomes clear. The significant increase in precision can be used to test theoretical predictions with an unprecedented accuracy, and tune phenomenological models that can be compared to other observables afterwards.

6.2 Theoretical models

We compare the measurement with theoretical calculations based on perturbative QCD and resummation schemes, as described in section 1.2.

6.2.1 ResBos

The ResBos program [80] generates predictions for several types of differential spectra (p_T and rapidity) of particles produced in pp collisions. It is based on a resummed cross-section, that contains NLO perturbative contributions matched with an all-order sum of large logarithmic terms. The resummation is done using the Collins-Soper-Sterman formalism, where the cross-section is expressed as a Fourier expansion on the impact parameter variable b, conjugate to the p_T^2 variable. The predictions contain a non-perturbative form factor, with parameters that have to be obtained from the comparison with data [81].

In figure 6.3 we show the comparison of the combined p_T^Z measurement with the ResBos prediction. The prediction uses the NNLO PDF set CT10, and the central values for the parameters of the model are tuned to Tevatron measurements. The uncertainties shown include the scale variations, which comes from the uncertainty in the parameters entering the resummation formalism, and PDF uncertainties, which contain variations around the CT10 eigenvectors [54].

The ResBos prediction shows a good agreement across the p_T^Z spectrum, within the uncertainties, except for a drop of 5 % in the prediction around $p_T^Z = 50$ GeV. A preliminary tuning exercise of one of the parameters entering the non-perturbative form factor has been done [82], showing that even with this tuning, the drop in the comparisons persists. A more complete tuning procedure is needed (including other parameters), in order to investigate if the tension can be absorbed by the tuning, or if a revision of the scheme is needed.

Notice that the ResBos prediction is not available for $p_T^Z > 300$ GeV. However, beyond this value the agreement is not expected to be good, as the spectrum at high p_T^Z is dominated by higher order perturbative amplitudes that are not included in the resummed prediction.
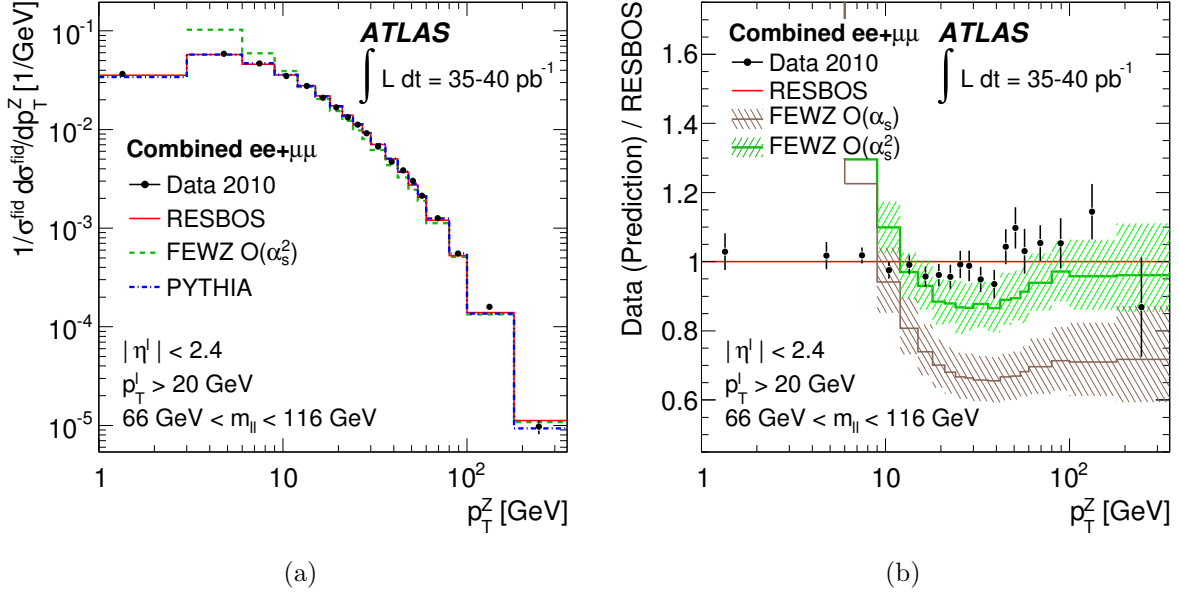
Figure 6.2: Results of the 2010 ATLAS p_T^Z measurement (Born level). (a) Shape of the transverse momentum distribution compared to ResBos, FEWZ and PYTHIA, (b) ratios of data and theoretical predictions to ResBos [2].

Small "x" broadening

The comparison of the resummed predictions to deep inelastic measurements with the HERA accelerator suggested that a modification of the non perturbative form factor was needed for processes involving small momentum fraction x, in order to reproduce the broadening of the distributions at high rapidity [81]. However, recent measurements of the p_T^Z spectrum at Tevatron concluded that the modification of the form factor was not needed [1][83]. The collisions at LHC probe higher energies thus smaller and larger values of x, so the measurements can be used to give insight on this issue.

Comparing the p_T^Z measurement done in different y^Z regions we can observe the behavior of the p_T^Z distribution for different values of the momentum fraction of the partons (c.f. equation (1.16)). In figure 6.4 we show the ratios of the p_T^Z measurements in different rapidity bins with the inclusive one. Notice the clear broadening of the distribution in the last rapidity bin.

The corresponding plot for the ResBos prediction is shown in figure 6.5. Notice that the broadening for high y^Z is well modeled. The ResBos prediction was done using the non perturbative form factor without the modification suggested by the HERA results, so this confirms what was concluded by the Tevatron measurements.

6.2.2 FEWZ

The FEWZ program [84] implements a numerical computation of differential and inclusive cross-sections for hadronic production of the Z boson, evaluating QCD amplitudes up to NNLO. In figure 6.6 we show the comparison of the p_T^Z measurement to two different FEWZ predictions, using two different sets of PDF: MSTW [13] and CT10 [54]. The prediction done with MSTW includes all the theoretical uncertainties: statistical from the numerical computation, PDF variations, and perturbative scales (renormalization and factorization scales, see section 1.2.1). The prediction done with CT10 contains only statistical and PDF uncertainties.

We notice that the prediction shows a strong disagreement with data, almost always outside the theoretical uncertainties. For low p_T^Z (below 20 GeV), the prediction shows instability, which is expected due to the fact that it does not include the resummation needed to describe
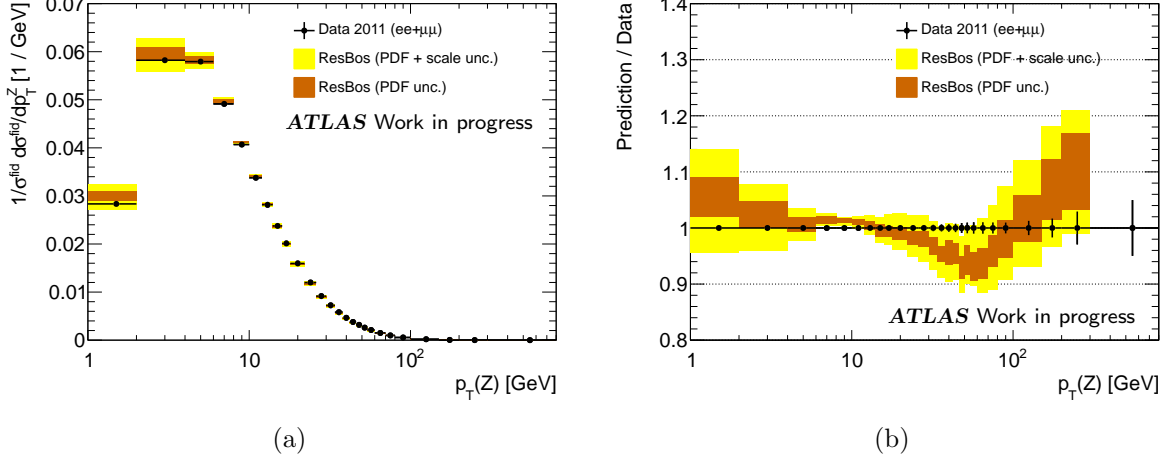
Figure 6.3: Combined p_T^Z measured cross-section, compared to the ResBos prediction, (a) shows the comparison of the shapes and (b) the ratio. The PDF uncertainties and total uncertainties (PDF + scale) are included in the comparison (the ResBos prediction is not available for $p_T^Z > 300$ GeV).
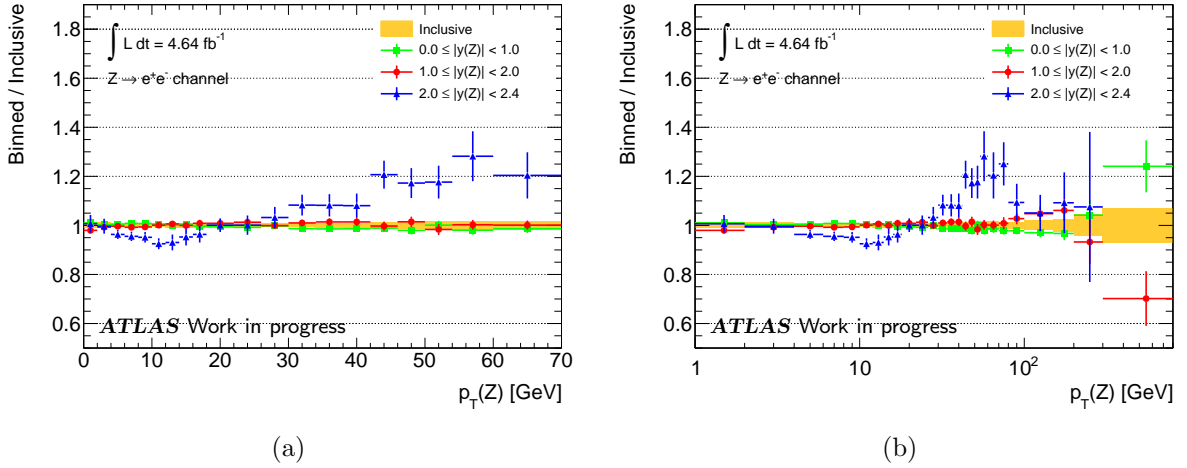

Figure 6.4: Comparison of the results in rapidity bins with the inclusive one. (a) low p_T^Z region, (b) full spectrum.

the spectrum at low p_T^Z. However, starting from 20 GeV, the prediction gets closer to data but underestimate it up to 200 GeV, and afterwards overestimates it. This could indicate that some effects have not been taken into account in the computation, for example higher order electroweak corrections.

6.2.3 Pure perturbative NNLL+NLO

A different resummation scheme has been presented in reference [85]. It includes NLO perturbative QCD, matched with resummation of logarithmic terms up to NNLL. Notice that this differs from the ResBos scheme, which includes a sum to all orders in the form of an integral which originates the non-perturbative form factor. This prediction does not include any form factor, only perturbative contributions to the resummation. In figure 6.7 we show the comparison of the p_T^Z measurement with the pure perturbative NNLO+NLO prediction.

The agreement obtained is fairly good, showing slight disagreements of up to 2 % near $p_T^Z = 5$ GeV. However, the theoretical uncertainties, due to the perturbative scales, are higher than those of the ResBos prediction. In addition, the low p_T^Z description is better in ResBos, which may be due to missing contributions in the resummation of the logarithmic terms.
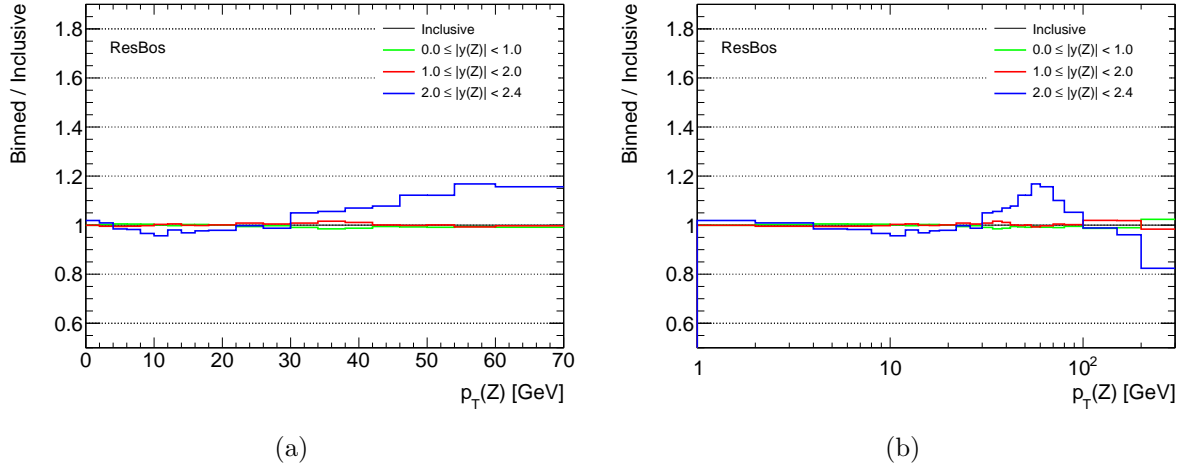
Figure 6.5: Comparison of ResBos predicted p_T^Z shapes in different rapidity bins. (a) low p_T^Z region, (b) full spectrum.

6.3   Comparison with MC generator predictions

We compare our measurement with p_T^Z distributions obtained from different MC generators, using truth variables and electron kinematics at Born level (see section 1.4). The generators differ in the implementation of the different features of the QCD process, and the predictions have a considerable dependence on adjustable parameters. Figure 6.8 shows the p_T^Z distributions predicted by different MC, and the measurement (inclusive in y^Z). Notice the differences of up to 20 % in the peak description.

In figure 6.9 we show the ratio of the predicted shapes from different MC to the measurement, inclusive and in the three y^Z bins.

The features shown in the comparison plots of figure 6.9 can be summarized as follows:

- The PYTHIA prediction with the parton shower tune AMTB1 [60] based on Tevatron data, describes the spectrum within 10 % for low p_T^Z and up to 20 % in the last p_T^Z bin. On the other hand, the tune AUET2B [61] based on ATLAS data, does a worse description, with disagreements of up to 30 %. This reflects what was seen at reconstruction level (figure 5.3), and suggests that new tunings are important for the parton shower parameters of the PYTHIA implementation.

- ALPGEN overestimates the data above $p_T^Z = 90$ GeV, by an amount of 30 % to 40 %. This overestimation could be due to a mis-modeling of the events with multiple hard partons.

- MC@NLO does a description within 10 % of data, up to 30 GeV, where it goes off significantly. This suggests a revision of the mechanism used to match the NLO prediction with the parton shower, which involves the subtraction of events (events with negative weight).

- The POWHEG generator does a description within 20 % of data. The level of agreement at high p_T^Z looks similar to the PYTHIA one (for the AMTB1 tune), so at first there is no visible improvement with the introduction of NLO matrix elements (the improvements are visible in the angular description, see appendix C).

- The SHERPA prediction describes the data within 10 % up to $p_T^Z = 200$ GeV, giving the best MC based description.
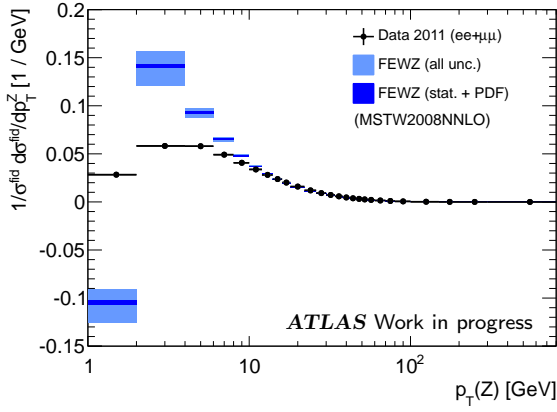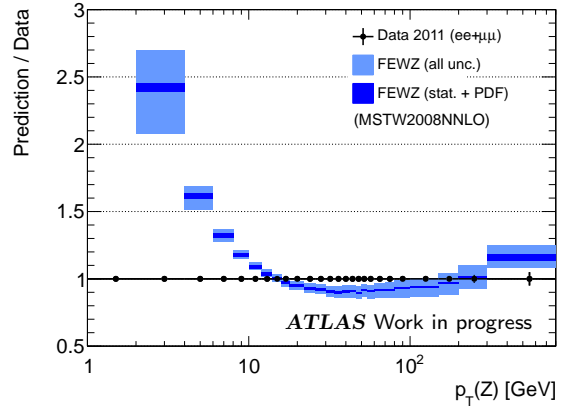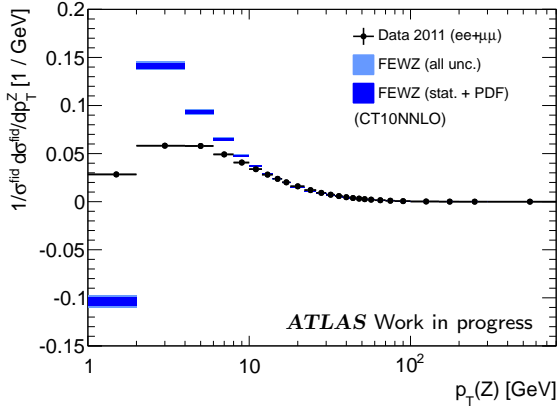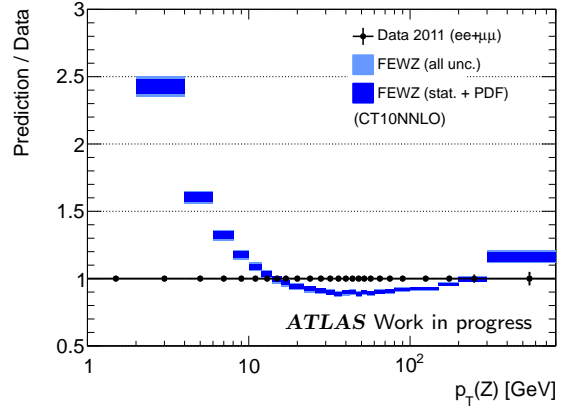
Figure 6.6: Combined p_T^Z measured cross-section, compared to FEWZ predictions. The left columns shows the comparison of the shapes, and the right column the ratios. a) and b) show the FEWZ prediction that use the MSTW PDF set, and c) and d) the FEWZ prediction obtained with CT10.
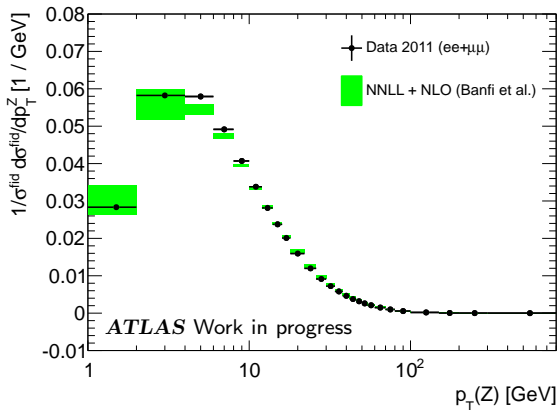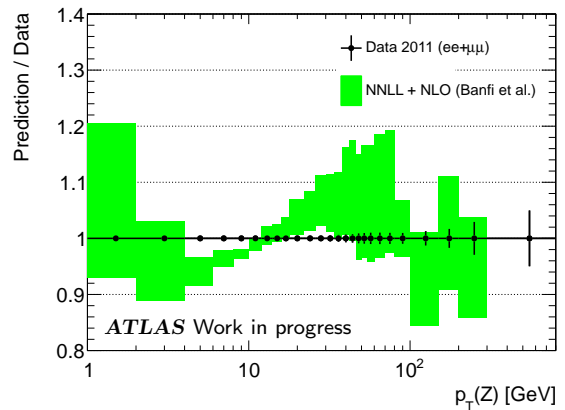
Figure 6.7: Combined p_T^Z measured cross-section, compared to the pure perturbative NNLL+NLO prediction, (a) shows the comparison of the shapes and (b) the ratio.
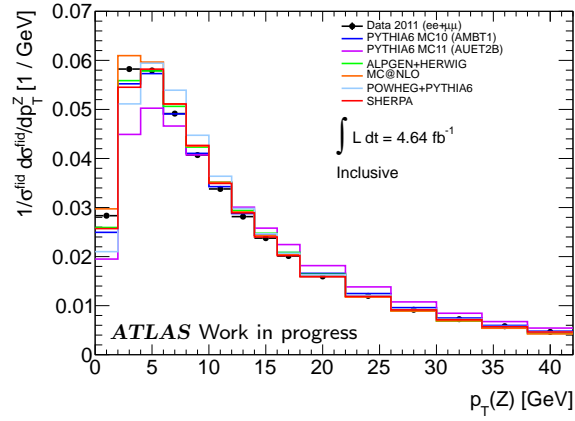
Figure 6.8: Comparison of predicted p_T^Z shapes from different MC generators and data (at Born level, and inclusive in y^Z).

(a)

(b)

(c)

(d)

Figure 6.9: Ratio of the p_T^Z distribution predicted by different generators to the combined measurement (at Born level), (a) over the whole y_Z range, (b) for $0.0 \leq |y^Z| < 1.0$, (c),for $1.0 \leq |y^Z| < 2.0$ and (d) for $2.0 \leq |y^Z| < 2.4$.

6.4 Parton shower tuning and compatibility with ϕ^* measurement

The high precision of the p_T^Z measurement makes it very sensitive to parton shower parameters. A preliminary parton shower tuning has been done [82], using samples generated with PYTHIA6 [15], PYTHIA8 [86] and POWHEG [21]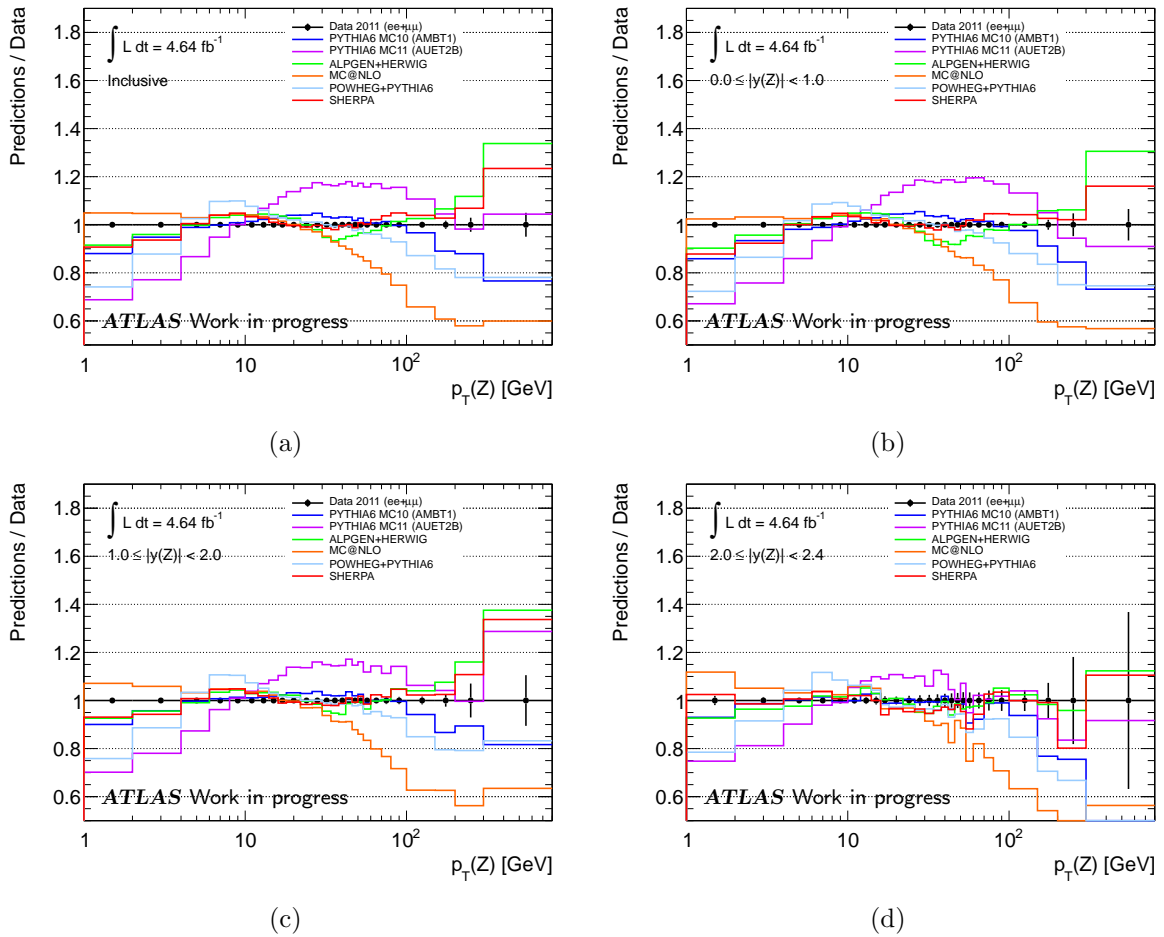 interfaced to both of them. The parameters tuned include those controlling the development of the ISR shower (ISR cut off), the primordial k_T (transverse momentum of original partons) and for the case of the POWHEG samples, a parameter controlling the matching of the matrix elements with the parton shower (cut off for parton emissions in POWHEG).

The tuning has been done using two experimental inputs: the p_T^Z and the ϕ^* measurements, both performed using the same dataset (final state of leptons at "dressed" level). The ϕ^* variable is defined in the following section.

6.4.1 The ϕ^* variable

It is possible to introduce alternative variables to p_T^Z that can probe the same physics. One of this variables is ϕ^*, which is defined using the lepton pair kinematic variables as [87]:

$$\phi^* \equiv \tan\left(\frac{\pi - \Delta\phi_{12}}{2}\right) \sin \Delta\theta_{12}^* \tag{6.1}$$

where $\Delta\phi_{12}$ is the azimuthal opening angle of the lepton pair, and $\Delta\theta_{12}^*$ is the opening polar angle measured in the rest frame of the dilepton system. It can be computed from the relationship:

$$\cos(\Delta\theta_{12}^*) = \tanh\left(\frac{\eta_1 - \eta_2}{2}\right) \tag{6.2}$$

where η_1 and η_2 are the pseudorapidities of the leptons. Notice that the definition of ϕ^* only involves angular variables. It can be shown that:

$$\phi^* \approx \frac{a_T}{m_{l_1 l_2}} \tag{6.3}$$

where a_T is the component of p_T^Z orthogonal to the axis defined by the unitary vector: $\hat{\mathbf{t}} = (\mathbf{p_T^{(1)}} - \mathbf{p_T^{(2)}})/|\mathbf{p_T^{(1)}} - \mathbf{p_T^{(2)}}|$, with $p_T^{(1)}$ and $p_T^{(2)}$ the transverse momentum vector of the leptons, and $m_{l_1 l_2}$ is their invariant mass. In figure 6.10 the definition of the variables is shown.
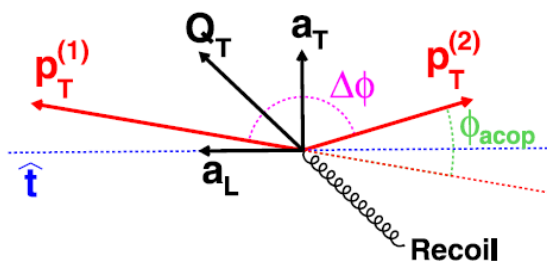
Figure 6.10: Scheme showing the geometrical variables used in the definition of the ϕ^* variable. In this figure, $Q_T = p_T^Z$.

Equation 6.3 expresses the relationship between the angular variables and the transverse momentum of the pair of leptons. It also shows that, as uncertainties in the momentum measurement enter both a_T and $m_{l_1 l_2}$ in the same way, the variable ϕ^* is less sensitive to those uncertainties [87]. For this reason, this variable have been proposed as an alternative way of probing the same physics that p_T^Z, but using only angular measurements, which are normally affected by less uncertainties than the energy and momentum measurements.

However, the ϕ^* is affected by other sources of uncertainties, among them the description made by the MC samples of the angular distributions (since MC samples are used to unfold the measurement). Moreover, even though ϕ^* and p_T^Z probe the same physics, the sensitivity to the dynamical aspects of the interaction is direct in the case of the p_T^Z, and only partial for the case of ϕ^*. For this reason, we consider both variables as complementary in the study of QCD dynamics. In figure 6.11 we show the correlation between both variables, obtained using the 2011 dataset. Values of ϕ^* ranging from 0 to 1 probe the p_T^Z distribution up to ~ 100 GeV.

Figure 6.11: Correlation for the variables p_T^Z and ϕ^*, obtained from the dataset used in the p_T^Z measurement.

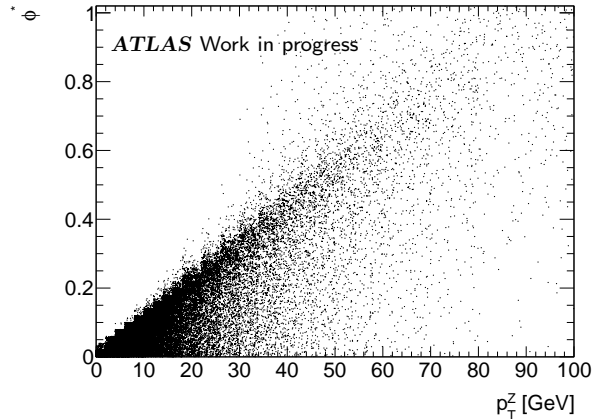The ϕ^* differential cross-section for the Z boson has been measured in ATLAS [88] using the same dataset used for the p_T^Z measurement presented in this work. The precision obtained goes from 0.35 % to 2.5 %, in a range of values from 0 to 3.2.

6.4.2 Results of the parton shower tuning

The results of the parton shower tunings are shown for PYTHIA6 and POWHEGPYTHIA6 in figure 6.12, and for PYTHIA8 and POWHEGPYTHIA8 in figure 6.13 [82]. The ratios MC / data are shown for both variables (p_T^Z and ϕ^*), before and after the new tuning. The original samples used the tunes AUET2B, based on ATLAS 2010 data [61] (PYTHIA6 and POWHEGPYTHIA6), and the more recent tunes 4C (Tevatron data) and AU2-CT10 (ATLAS 2010 data) for PYTHIA8 and POWHEGPYTHIA8 respectively [62].

The tuning of PYTHIA6 shows that the original tension of 20 % for the low p_T^Z region can be reduced to 3 % - 4 %, but the agreement at high p_T^Z does not improve (this is expected, as the low p_T^Z region is the most sensitive to the parton shower). The tuning of POWHEGPYTHIA6 shows similar features at low p_T^Z, with a level of disagreement at high p_T^Z comparable to the PYTHIA6 one, which can indicate some problems in the matrix element computation of POWHEG. The tunings improve simultaneously the agreement to p_T^Z and ϕ^*, showing the compatibility of the measurements.

The tuning of PYTHIA8 improves the agreement at low p_T^Z, up to the 3 % level, better than the one achieved with the PYTHIA6 tuning. At high p_T^Z, the tension remains around the 10 % level after the tuning, however also improved with respect to PYTHIA6. The tuning to POWHEG-PYTHIA8 is globally better than the one to POWHEGPYTHIA6, but shows the same issues at high p_T^Z. Similarly to what was observed for the tunings of PYTHIA6 and POWHEGPYTHIA6, these tunings allow to improve simultaneously the agreement to both p_T^Z and ϕ^* variables, which shows their compatibility.

Figure 6.12: Results of the parton shower tuning. Showing the ratios between the MC predicted distributions and p_T^Z (left) and ϕ^* (right) data, before and after the tuning, for PYTHIA6 (a) and (b), and POWHEGPYTHIA6 (c) and (d).

6.5 Summary

In this chapter we have shown some of the many possible applications of the p_T^Z measurement. The high precision and large p_T^Z range explored makes this measurement very sensitive to many different theoretical inputs, including parton showers and resummation at low p_T^Z, and matrix element calculations and pQCD at high p_T^Z. The preliminary tuning studies done for ResBos and MC parton showers show how the measurement can be used to constrain and improve the models. These tunings will have an strong impact on the precision of analyses that rely on MC descriptions, like the W mass measurement.

We foresee among the possible applications further studies of ResBos tuning, tests to evaluate the effect of more electroweak contributions at NNLO for high p_T^Z, tuning studies including further MC models like MC@NLO and SHERPA, and also PDF fits using the results in y^Z bins.
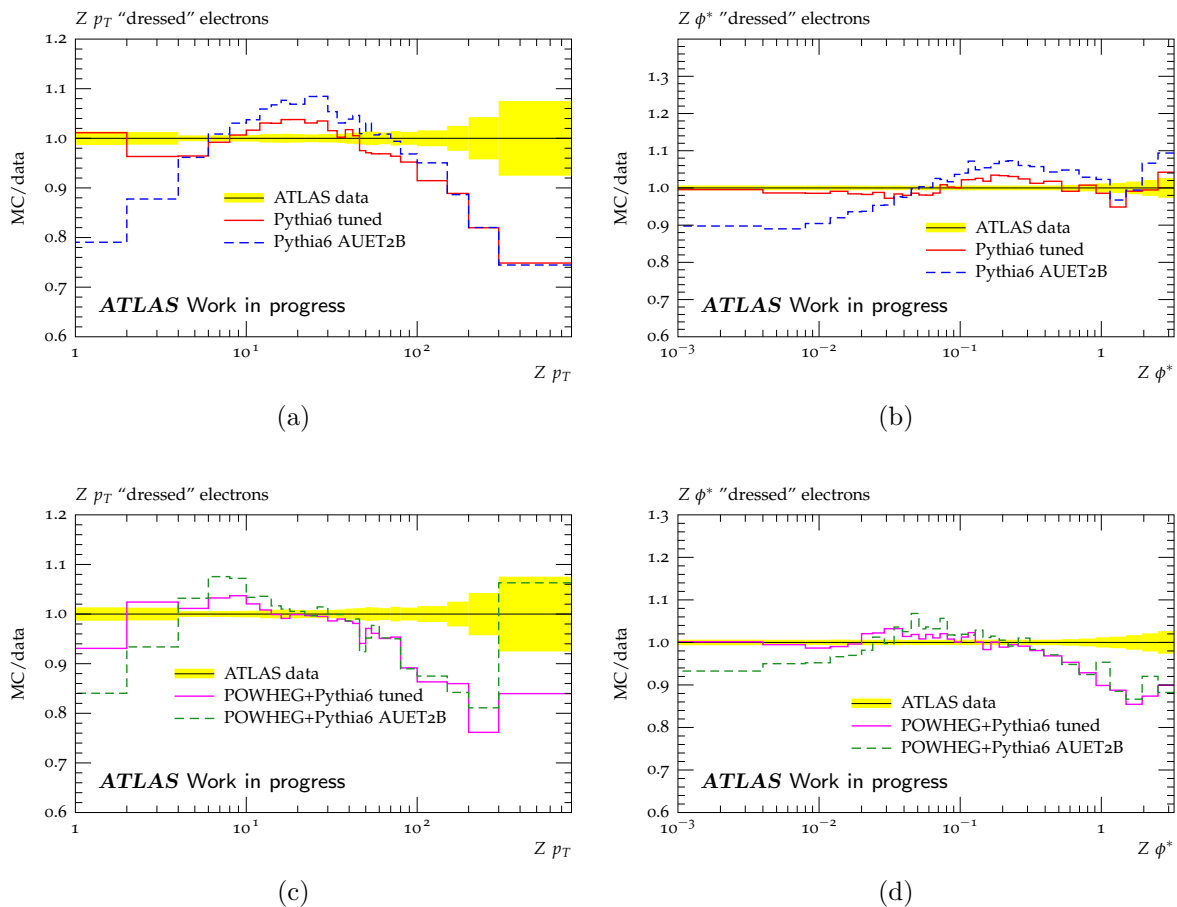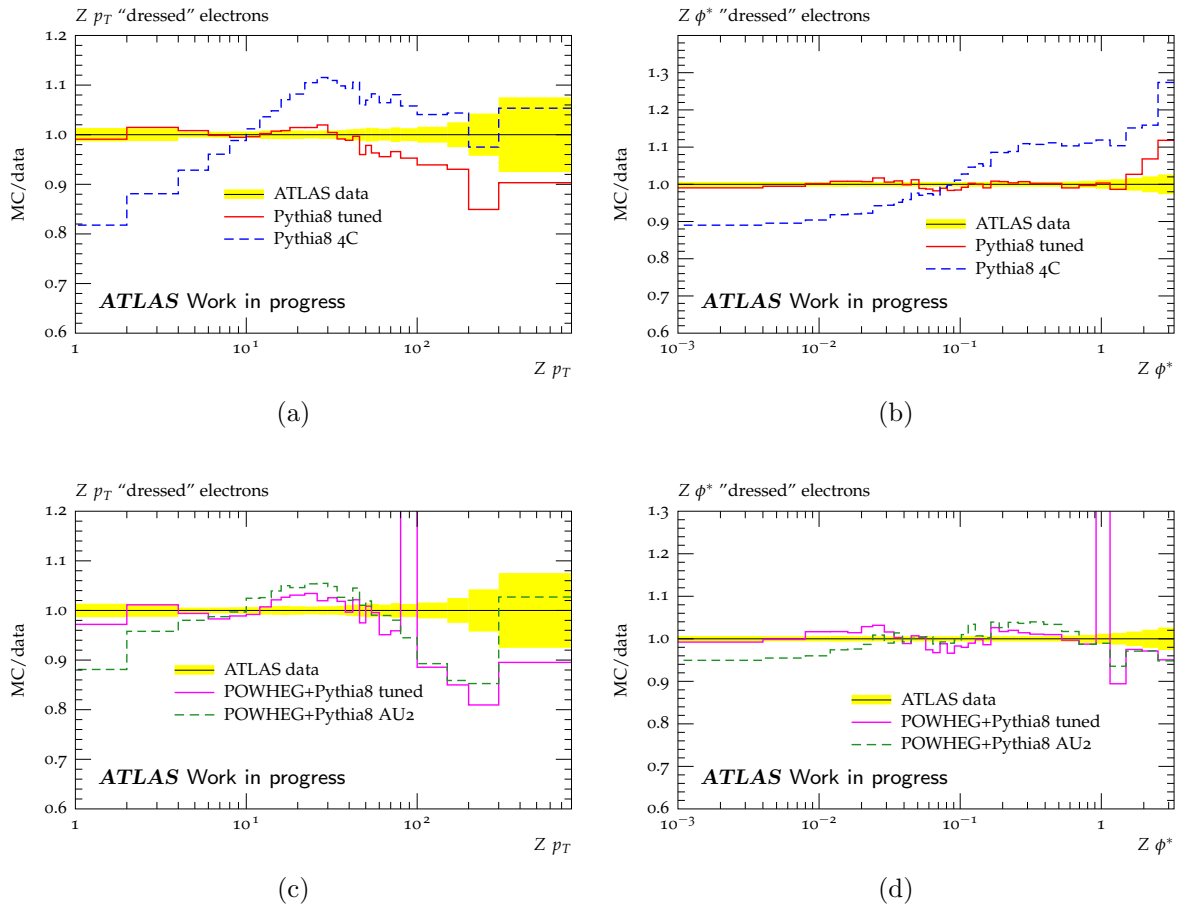
Figure 6.13: Results of the parton shower tuning. Showing the ratios between the MC predicted distributions and p_T^Z (left) and ϕ^* (right) data, before and after the tuning, for PYTHIA8 (a) and (b), and POWHEGPYTHIA8 (c) and (d).

Conclusions

In this thesis we have presented the measurement of the Z boson transverse momentum spectrum, in the electron decay channel, using ATLAS proton-proton collision data at a center-of-mass energy of 7 TeV, collected by the LHC in 2011. The amount of data analyzed corresponds to an integrated luminosity of 4.64 fb^{-1}. The normalized spectrum was measured in a fiducial region defined by lepton kinematic cuts and by an invariant mass of the electron pair between 66 and 116 GeV. The result is combined with the measurement done in the muon channel using the same data set. The high amount of statistics allows for a fine granularity in the p_{T}^Z variable, with a typical uncertainty of 0.5 % for $p_{\text{T}}^Z < 60$ GeV for the combined measurement, rising up to 5 % towards the end of the spectrum. The measurement is repeated independently in three bins of Z boson rapidity, defined as $0.0 \leq |y^Z| < 1.0$, $1.0 \leq |y^Z| < 2.0$ and $2.0 \leq |y^Z| < 2.4$, reaching typical precisions of 0.7 %, 0.8 % and 2.0 % for $p_{\text{T}}^Z < 60$ GeV, respectively.

The combined measurement was compared to different theoretical predictions, including re-summed models at low p_{T}^Z, perturbative computations up to NNLO, and several MC generators that implement parton showers models. The unprecedented precision reached by the measurement makes it very useful in constraining the models, allowing the different parameters involved in the theoretical calculations to be tuned. We presented a preliminary MC parton shower tuning exercise, which shows the sensitivity of the result to the underlying QCD dynamics and the parton shower parameters, and at the same time the compatibility of the p_{T}^Z and ϕ^* measurements.

This measurement could become even more constraining if the huge amount of statistics collected by ATLAS in 2012 is included. In addition, the systematic uncertainties will benefit from an improved understanding of the detector and the MC generators tuned to the precise 2011 data.

Notice that at the time of the presentation of this thesis, the results were still being reviewed by the ATLAS collaboration, before becoming public. Updates of the efficiency corrections were being implemented, and the estimation of some systematics, specially the ones associated to the GEANT4 detector description and the hard process matrix element, were still being discussed. These updates introduced small changes in the central result (of the order of 0.1 % for $p_{\text{T}}^Z < 100$ GeV, and up to 1 % above, but well within the uncertainties presented in this document), and reduction of the systematics (changing the total uncertainty by an amount of the order of 0.1 % in the p_{T}^Z bins near 10 GeV and 20 GeV). For these reasons, the updated result does not change the physics conclusions discussed here.

Appendix A

Appendix: Detailed errors for the measurement in Z boson rapidity bins

In this appendix we present the detailed uncertainties for the p_T^Z measurement in rapidity bins. Tables A.1, A.2 and A.3 show the uncertainties for the measurement in the rapidity regions defined by $0.0 \leq |y^Z| < 1.0$, $1.0 \leq |y^Z| < 2.0$ and $2.0 \leq |y^Z| < 2.4$, respectively.

Figure A.1 shows the evolution of the uncertainties across the p_T^Z spectrum, for the measurements in the three rapidity regions.

Uncertainty (%)

Bin limits (GeV)	Data Stat.	EW backg. Xsec.	EW backg. Lumi.	QCD backg. Frac.	QCD backg. Shape	E. scale. Scale	E. scale. Mat.	E. scale. Pres.	E. Resol.	Scale factors Reco.	Scale factors Id.	Scale factors Trig.	Cha. Id.	G4 Fix	FSR	PDF CT10	PDF Ext.	Unfolding p_T^Z	Unfolding Mat.	MC stat.	Total sys.	Total
0 - 2	0.54	0.02	0.01	0.06	0.00	0.16	0.35	0.16	0.38	0.02	0.01	0.00	0.08	0.53	0.20	0.02	0.01	0.04	0.52	0.26	0.99	1.13
2 - 4	0.33	0.02	0.01	0.05	0.00	0.16	0.35	0.16	0.38	0.01	0.01	0.00	0.08	0.53	0.20	0.02	0.00	0.04	0.52	0.16	0.97	1.03
4 - 6	0.34	0.02	0.01	0.04	0.00	0.12	0.19	0.12	0.04	0.02	0.03	0.00	0.01	0.58	0.20	0.03	0.02	0.06	0.17	0.16	0.71	0.79
6 - 8	0.38	0.02	0.01	0.02	0.00	0.12	0.19	0.12	0.04	0.01	0.03	0.00	0.01	0.58	0.20	0.01	0.01	0.06	0.17	0.18	0.72	0.81
8 - 10	0.42	0.02	0.00	0.00	0.00	0.03	0.05	0.01	0.24	0.01	0.03	0.00	0.10	0.20	0.20	0.01	0.01	0.01	0.20	0.20	0.48	0.64
10 - 12	0.46	0.02	0.00	0.01	0.00	0.03	0.05	0.01	0.24	0.01	0.02	0.00	0.10	0.20	0.20	0.05	0.02	0.01	0.20	0.22	0.50	0.67
12 - 14	0.51	0.01	0.00	0.02	0.00	0.06	0.15	0.09	0.03	0.00	0.02	0.00	0.02	0.63	0.20	0.05	0.02	0.02	0.24	0.23	0.77	0.92
14 - 16	0.56	0.01	0.00	0.03	0.00	0.06	0.15	0.09	0.03	0.00	0.02	0.00	0.02	0.63	0.20	0.04	0.02	0.02	0.24	0.25	0.77	0.95
16 - 18	0.62	0.01	0.00	0.04	0.01	0.06	0.12	0.07	0.12	0.00	0.01	0.00	0.01	0.55	0.20	0.05	0.01	0.02	0.26	0.27	0.72	0.95
18 - 22	0.53	0.01	0.00	0.05	0.00	0.06	0.12	0.07	0.12	0.01	0.01	0.00	0.01	0.55	0.20	0.02	0.01	0.02	0.26	0.21	0.70	0.88
22 - 26	0.60	0.00	0.00	0.06	0.01	0.10	0.15	0.07	0.02	0.01	0.00	0.00	0.00	0.33	0.20	0.01	0.01	0.07	0.76	0.24	0.92	1.10
26 - 30	0.68	0.01	0.00	0.06	0.00	0.10	0.15	0.07	0.02	0.02	0.01	0.00	0.00	0.33	0.20	0.02	0.00	0.07	0.76	0.28	0.93	1.15
30 - 34	0.80	0.02	0.01	0.06	0.00	0.07	0.18	0.09	0.04	0.02	0.02	0.00	0.02	0.18	0.20	0.07	0.03	0.02	0.34	0.33	0.60	1.00
34 - 38	0.89	0.03	0.01	0.05	0.01	0.07	0.18	0.09	0.04	0.02	0.04	0.00	0.02	0.18	0.20	0.01	0.03	0.02	0.34	0.37	0.62	1.08
38 - 42	0.99	0.03	0.01	0.05	0.00	0.21	0.21	0.13	0.04	0.03	0.07	0.00	0.11	0.46	0.20	0.05	0.03	0.01	0.43	0.41	0.85	1.30
42 - 46	1.11	0.05	0.01	0.05	0.00	0.21	0.21	0.13	0.04	0.03	0.09	0.00	0.11	0.46	0.20	0.05	0.02	0.01	0.43	0.45	0.88	1.41
46 - 50	1.22	0.06	0.02	0.04	0.00	0.11	0.12	0.07	0.02	0.03	0.12	0.01	0.00	0.06	0.20	0.14	0.07	0.04	1.06	0.49	1.22	1.73
50 - 54	1.33	0.07	0.02	0.03	0.01	0.11	0.12	0.07	0.02	0.03	0.14	0.01	0.00	0.06	0.20	0.02	0.01	0.04	1.06	0.54	1.23	1.82
54 - 60	1.20	0.08	0.02	0.01	0.00	0.10	0.15	0.09	0.02	0.03	0.16	0.01	0.06	0.35	0.20	0.08	0.04	0.00	1.22	0.47	1.40	1.84
60 - 70	1.10	0.11	0.03	0.01	0.00	0.10	0.15	0.09	0.02	0.03	0.19	0.01	0.06	0.35	0.20	0.07	0.01	0.00	1.22	0.40	1.39	1.77
70 - 80	1.38	0.13	0.03	0.03	0.00	0.14	0.16	0.06	0.03	0.03	0.16	0.01	0.07	0.35	0.20	0.04	0.00	0.15	0.50	0.50	0.88	1.64
80 - 100	1.22	0.17	0.04	0.05	0.00	0.14	0.16	0.06	0.03	0.03	0.08	0.01	0.07	0.35	0.20	0.03	0.00	0.15	0.50	0.41	0.84	1.48
100 - 150	1.22	0.17	0.05	0.07	0.00	0.20	0.48	0.22	0.02	0.06	0.04	0.01	0.04	0.80	0.20	0.01	0.00	0.36	0.89	0.37	1.45	1.89
150 - 200	2.38	0.12	0.03	0.09	0.01	0.20	0.48	0.22	0.02	0.08	0.13	0.01	0.04	0.80	0.20	0.04	0.03	0.36	0.89	0.73	1.58	2.86
200 - 300	3.25	0.10	0.03	0.09	0.00	0.63	1.60	0.88	0.02	0.10	0.17	0.01	0.08	0.68	0.20	0.02	0.02	1.37	4.03	0.97	4.84	5.82
300 - 800	6.82	0.09	0.02	0.09	0.00	0.63	1.60	0.88	0.02	0.12	0.22	0.01	0.08	0.68	0.20	0.40	0.14	1.37	4.03	1.95	5.14	8.54
Avg.	1.19	0.05	0.01	0.04	0.00	0.15	0.30	0.16	0.08	0.03	0.07	0.00	0.05	0.44	0.20	0.05	0.02	0.17	0.82	0.42	1.23	1.74
Avg. (< 60)	0.71	0.03	0.01	0.04	0.00	0.10	0.17	0.09	0.10	0.02	0.04	0.00	0.04	0.39	0.20	0.04	0.02	0.03	0.48	0.30	0.84	1.12

Table A.1: Detailed uncertainties, given in percent with respect to the bin content, for the measurement in the rapidity region defined by $0.0 \leq |y^Z| < 1.0$. The last two rows show the average errors, for the whole p_T^Z range and for $p_T^Z < 60$ GeV.

Uncertainty (%)

Bin limits (GeV)	Data Stat.	EW backg. Xsec.	EW backg. Lumi.	QCD backg. Frac.	QCD backg. Shape	E. scale. Scale	E. scale. Mat.	Pres.	E. Resol.	Scale factors Reco.	Scale factors Id.	Scale factors Trig.	Cha. Id.	G4 Fix	FSR	PDF CT10	PDF Ext.	Unfolding p_T^Z	Unfolding Mat.	MC stat.	Total sys.	Total
0 - 2	0.67	0.02	0.00	0.07	0.00	0.18	0.56	0.16	0.58	0.02	0.05	0.01	0.15	0.76	0.20	0.02	0.01	0.09	0.24	0.32	1.24	1.41
2 - 4	0.42	0.02	0.01	0.06	0.00	0.18	0.56	0.16	0.58	0.02	0.05	0.01	0.15	0.76	0.20	0.02	0.01	0.09	0.24	0.20	1.21	1.28
4 - 6	0.40	0.02	0.00	0.05	0.00	0.14	0.27	0.11	0.01	0.02	0.05	0.01	0.01	0.22	0.20	0.02	0.00	0.18	0.21	0.20	0.57	0.69
6 - 8	0.46	0.02	0.00	0.04	0.00	0.14	0.27	0.11	0.01	0.01	0.05	0.00	0.01	0.22	0.20	0.01	0.01	0.18	0.21	0.22	0.57	0.73
8 - 10	0.52	0.01	0.00	0.02	0.00	0.05	0.09	0.06	0.28	0.01	0.04	0.00	0.14	0.40	0.20	0.03	0.01	0.04	0.35	0.24	0.71	0.88
10 - 12	0.57	0.01	0.00	0.00	0.00	0.05	0.09	0.06	0.28	0.00	0.03	0.00	0.14	0.40	0.20	0.02	0.00	0.04	0.35	0.27	0.71	0.91
12 - 14	0.61	0.01	0.00	0.01	0.00	0.07	0.17	0.09	0.16	0.00	0.01	0.00	0.08	0.79	0.20	0.04	0.01	0.04	0.49	0.29	1.03	1.19
14 - 16	0.66	0.01	0.00	0.03	0.00	0.07	0.17	0.09	0.16	0.00	0.00	0.00	0.08	0.79	0.20	0.02	0.01	0.04	0.49	0.33	1.04	1.23
16 - 18	0.70	0.00	0.00	0.04	0.00	0.07	0.19	0.08	0.24	0.00	0.01	0.00	0.08	0.10	0.20	0.08	0.05	0.03	1.13	0.36	1.26	1.44
18 - 22	0.64	0.01	0.00	0.06	0.00	0.07	0.19	0.08	0.24	0.01	0.02	0.00	0.08	0.10	0.20	0.05	0.02	0.03	1.13	0.29	1.24	1.40
22 - 26	0.80	0.01	0.00	0.07	0.00	0.11	0.30	0.11	0.06	0.01	0.04	0.00	0.03	0.10	0.20	0.05	0.03	0.11	0.36	0.34	0.66	1.03
26 - 30	0.87	0.01	0.00	0.08	0.00	0.11	0.30	0.11	0.06	0.02	0.05	0.00	0.03	0.10	0.20	0.01	0.02	0.11	0.36	0.38	0.68	1.10
30 - 34	0.99	0.02	0.01	0.09	0.01	0.26	0.38	0.15	0.25	0.02	0.08	0.01	0.03	0.17	0.20	0.04	0.02	0.07	0.46	0.43	0.89	1.33
34 - 38	1.13	0.02	0.01	0.07	0.00	0.26	0.38	0.15	0.25	0.03	0.09	0.01	0.03	0.17	0.20	0.05	0.04	0.07	0.46	0.48	0.91	1.46
38 - 42	1.22	0.03	0.01	0.07	0.01	0.34	0.37	0.28	0.11	0.03	0.12	0.01	0.16	0.37	0.20	0.05	0.03	0.07	0.58	0.55	1.11	1.65
42 - 46	1.41	0.04	0.01	0.06	0.00	0.34	0.37	0.28	0.11	0.04	0.13	0.01	0.16	0.37	0.20	0.13	0.08	0.07	0.58	0.61	1.14	1.82
46 - 50	1.49	0.05	0.01	0.05	0.01	0.24	0.58	0.06	0.02	0.04	0.16	0.01	0.40	0.57	0.20	0.03	0.04	0.11	0.73	0.67	1.40	2.05
50 - 54	1.76	0.06	0.02	0.05	0.01	0.24	0.58	0.06	0.02	0.04	0.17	0.01	0.40	0.57	0.20	0.04	0.02	0.11	0.73	0.75	1.44	2.27
54 - 60	1.55	0.07	0.02	0.04	0.01	0.19	0.55	0.13	0.12	0.03	0.19	0.02	0.00	0.09	0.20	0.06	0.01	0.03	0.68	0.69	1.19	1.96
60 - 70	1.47	0.08	0.02	0.02	0.00	0.19	0.55	0.13	0.12	0.03	0.21	0.02	0.00	0.09	0.20	0.14	0.06	0.03	0.68	0.60	1.15	1.87
70 - 80	1.84	0.10	0.03	0.00	0.00	0.45	0.68	0.29	0.01	0.02	0.16	0.02	0.01	0.70	0.20	0.15	0.05	0.08	0.82	0.75	1.61	2.45
80 - 100	1.61	0.12	0.03	0.01	0.01	0.45	0.68	0.29	0.01	0.02	0.11	0.02	0.01	0.70	0.20	0.25	0.10	0.08	0.82	0.64	1.57	2.25
100 - 150	1.68	0.12	0.03	0.03	0.00	0.30	0.86	0.17	0.02	0.04	0.00	0.02	0.27	1.62	0.20	0.14	0.06	0.57	0.79	0.60	2.22	2.78
150 - 200	3.20	0.08	0.02	0.05	0.01	0.30	0.86	0.17	0.02	0.10	0.11	0.02	0.27	1.62	0.20	0.08	0.06	0.57	0.79	1.24	2.47	4.04
200 - 300	5.06	0.09	0.02	0.06	0.01	0.99	4.10	1.33	0.52	0.14	0.20	0.02	0.90	2.29	0.20	0.44	0.20	1.08	6.21	1.86	8.33	9.75
300 - 800	12.91	0.13	0.03	0.07	0.01	0.99	4.10	1.33	0.52	0.17	0.29	0.03	0.90	2.29	0.20	0.21	0.15	1.08	6.21	4.50	9.28	15.90
Avg.	1.72	0.04	0.01	0.05	0.00	0.26	0.70	0.23	0.18	0.03	0.09	0.01	0.17	0.63	0.20	0.08	0.04	0.19	1.00	0.69	1.75	2.50
Avg. (< 60)	0.89	0.02	0.01	0.05	0.00	0.16	0.34	0.12	0.19	0.02	0.07	0.01	0.11	0.37	0.20	0.04	0.02	0.08	0.52	0.40	1.00	1.36

Table A.2: Detailed uncertainties, given in percent with respect to the bin content, for the measurement in the rapidity region defined by $1.0 \leq |y^Z| < 2.0$. The last two rows show the average errors, for the whole p_T^Z range and for $p_T^Z < 60$ GeV.
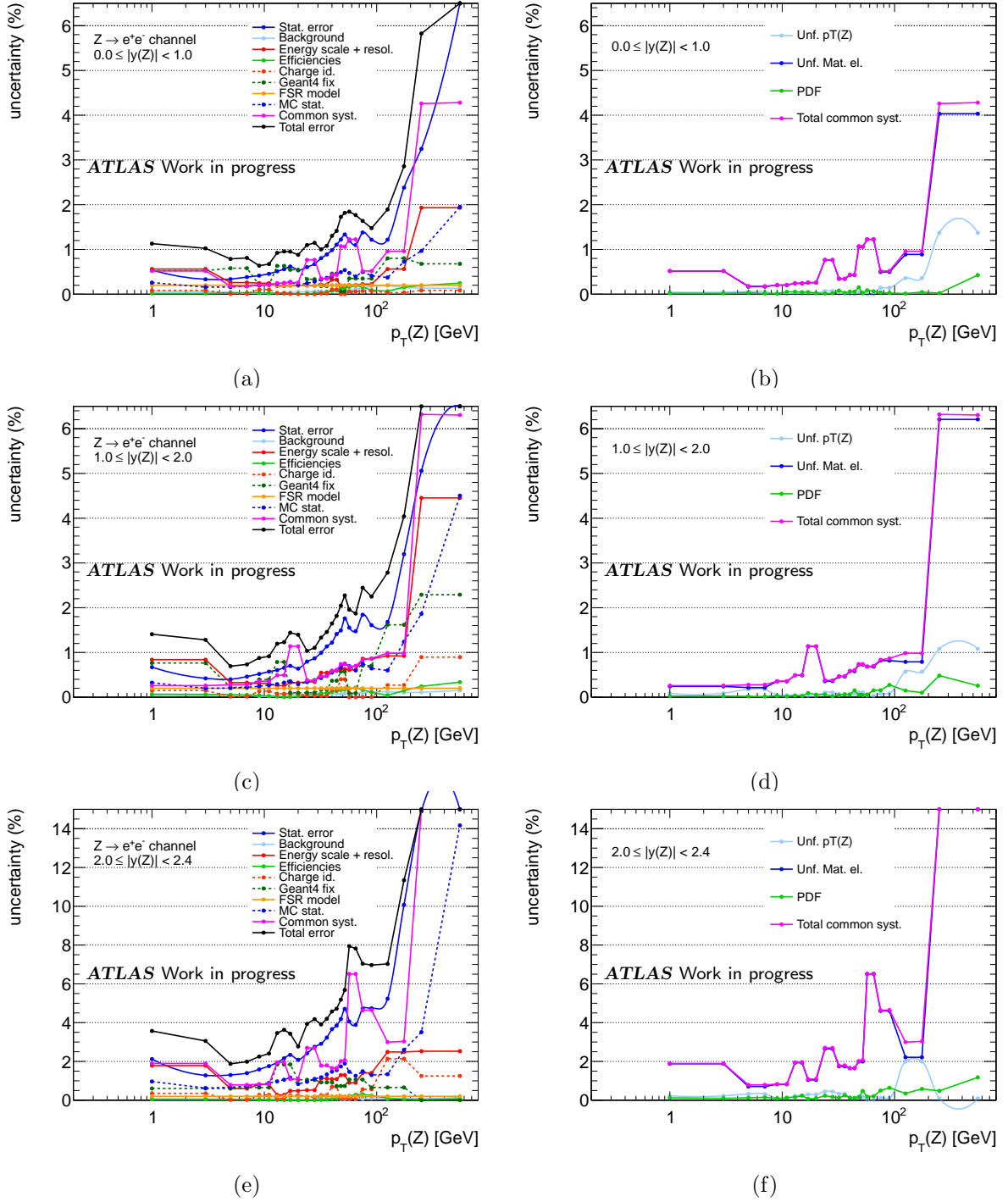
Bin		Uncertainty (%)																			
			EW backg.		QCD backg.		E. scale.				Scale factors						PDF		Unfolding				
limits (GeV)	Data Stat.	Xsec.	Lumi.	Frac.	Shape	Scale	Mat.	Pres.	E. Resol.	Reco.	Id.	Trig.	Cha. Id.	G4 Fix	FSR	CT10	Ext.	p_T^Z	Mat.	MC stat.	Total sys.	Total
0 - 2	2.12	0.02	0.01	0.05	0.00	0.41	1.09	0.29	1.33	0.00	0.05	0.00	0.35	0.60	0.20	0.11	0.04	0.22	1.88	0.97	2.87	3.57
2 - 4	1.28	0.01	0.00	0.05	0.00	0.41	1.09	0.29	1.33	0.00	0.05	0.00	0.35	0.60	0.20	0.09	0.04	0.22	1.88	0.63	2.77	3.06
4 - 6	1.30	0.02	0.01	0.04	0.00	0.25	0.46	0.21	0.21	0.00	0.05	0.00	0.02	0.60	0.20	0.12	0.04	0.32	0.71	0.66	1.35	1.88
6 - 8	1.40	0.02	0.01	0.04	0.00	0.25	0.46	0.21	0.21	0.00	0.04	0.00	0.02	0.65	0.20	0.14	0.05	0.32	0.71	0.73	1.41	1.99
8 - 10	1.59	0.02	0.01	0.03	0.00	0.22	0.22	0.17	0.74	0.00	0.03	0.00	0.27	0.65	0.20	0.08	0.05	0.09	0.82	0.80	1.59	2.25
10 - 12	1.76	0.02	0.01	0.02	0.00	0.22	0.22	0.17	0.74	0.00	0.03	0.01	0.27	0.65	0.20	0.13	0.03	0.09	0.82	0.89	1.64	2.41
12 - 14	1.93	0.02	0.00	0.00	0.01	0.15	0.10	0.10	0.17	0.00	0.02	0.01	0.09	1.84	0.20	0.13	0.08	0.23	1.93	0.97	2.88	3.46
14 - 16	2.16	0.01	0.00	0.02	0.02	0.15	0.10	0.10	0.17	0.00	0.02	0.01	0.09	1.84	0.20	0.23	0.07	0.23	1.93	1.06	2.91	3.63
16 - 18	2.34	0.01	0.00	0.03	0.01	0.21	0.36	0.21	0.14	0.00	0.02	0.00	0.26	1.84	0.20	0.06	0.03	0.30	1.05	1.17	2.51	3.43
18 - 22	2.08	0.00	0.00	0.03	0.00	0.21	0.36	0.21	0.14	0.00	0.00	0.01	0.26	1.05	0.20	0.09	0.04	0.30	1.05	0.84	1.83	2.77
22 - 26	2.42	0.01	0.00	0.05	0.01	0.10	0.39	0.11	0.30	0.00	0.00	0.01	0.16	1.05	0.20	0.21	0.11	0.45	2.65	0.95	3.10	3.93
26 - 30	2.75	0.01	0.00	0.06	0.02	0.10	0.39	0.11	0.30	0.00	0.00	0.01	0.16	1.05	0.20	0.17	0.02	0.45	2.65	1.10	3.15	4.18
30 - 34	2.91	0.06	0.02	0.06	0.01	0.41	0.99	0.32	0.00	0.00	0.02	0.00	0.26	0.92	0.20	0.11	0.07	0.33	1.75	1.18	2.61	3.91
34 - 38	3.23	0.06	0.02	0.07	0.01	0.41	0.99	0.32	0.00	0.00	0.03	0.00	0.26	0.92	0.20	0.19	0.02	0.33	1.75	1.33	2.68	4.20
38 - 42	3.66	0.05	0.01	0.09	0.01	0.46	0.78	0.44	0.41	0.00	0.07	0.00	0.69	0.92	0.20	0.13	0.02	0.09	1.65	1.48	2.74	4.57
42 - 46	3.85	0.03	0.01	0.08	0.04	0.46	0.78	0.44	0.41	0.00	0.11	0.01	0.69	0.73	0.20	0.11	0.06	0.09	1.65	1.55	2.72	4.72
46 - 50	4.19	0.05	0.01	0.05	0.03	0.22	1.23	0.11	0.31	0.00	0.11	0.01	0.10	0.73	0.20	0.11	0.11	0.18	2.00	1.74	3.06	5.18
50 - 54	4.71	0.05	0.01	0.03	0.02	0.22	1.23	0.11	0.31	0.00	0.15	0.02	0.10	0.73	0.20	0.48	0.03	0.18	2.00	1.89	3.18	5.68
54 - 60	4.06	0.05	0.01	0.04	0.02	0.27	0.77	0.38	0.04	0.00	0.22	0.03	0.08	1.06	0.20	0.13	0.13	0.02	6.51	1.47	6.83	7.94
60 - 70	3.89	0.05	0.01	0.04	0.01	0.27	0.77	0.38	0.04	0.00	0.28	0.04	0.08	1.06	0.20	0.20	0.06	0.02	6.51	1.26	6.79	7.82
70 - 80	4.72	0.05	0.01	0.05	0.02	0.45	1.31	0.21	0.11	0.01	0.31	0.05	0.56	1.06	0.20	0.49	0.08	0.12	4.60	1.49	5.22	7.04
80 - 100	4.74	0.10	0.03	0.04	0.01	0.45	1.31	0.21	0.11	0.00	0.24	0.04	0.56	0.66	0.20	0.63	0.09	0.12	4.60	1.30	5.11	6.97
100 - 150	5.23	0.08	0.02	0.00	0.01	0.86	2.31	0.33	0.14	0.01	0.11	0.03	2.14	0.66	0.20	0.26	0.23	1.99	2.21	1.34	4.69	7.03
150 - 200	10.08	0.10	0.02	0.01	0.01	0.86	2.31	0.33	0.14	0.02	0.01	0.04	2.14	0.66	0.20	0.45	0.38	1.99	2.21	2.59	5.21	11.34
200 - 300	14.89	0.06	0.01	0.03	0.03	1.48	1.74	1.01	0.38	0.01	0.00	0.03	1.25	0.00	0.20	0.45	0.16	0.10	23.81	3.51	24.24	28.45
300 - 800	70.26	0.11	0.03	0.05	0.00	1.48	1.74	1.01	0.38	0.00	0.07	0.01	1.25	0.00	0.20	1.18	0.04	0.10	23.81	14.17	27.88	75.59
Avg.	6.29	0.04	0.01	0.04	0.01	0.42	0.90	0.30	0.33	0.00	0.08	0.01	0.48	0.87	0.20	0.25	0.09	0.34	3.97	1.81	5.04	8.35
Avg. (< 60)	2.62	0.03	0.01	0.04	0.01	0.27	0.63	0.22	0.38	0.00	0.05	0.01	0.24	0.97	0.20	0.15	0.06	0.23	1.86	1.13	2.73	3.83

Table A.3: Detailed uncertainties, given in percent with respect to the bin content, for the measurement in the rapidity region defined by $2.0 \leq |y^Z| < 2.4$. The last two rows show the average errors, for the whole p_T^Z range and for $p_T^Z < 60$ GeV.

Figure A.1: Summary of uncertainties, given in percent of the central value of the bin, as a function of p_{T}^Z. The left column shows all the uncertainties and the right one the splitting of the uncertainties that are common with the muon channel measurement. (a) and (b) show the uncertainties for the rapidity region defined by $0.0 \leq |y^Z| < 1.0$, (c) and (d) for $1.0 \leq |y^Z| < 2.0$ and (e) and (f) for $2.0 \leq |y^Z| < 2.4$.

Appendix B

Appendix: Some technical details of the analysis

In this appendix we give some technical details of the analysis, about the data and MC samples used, and the variables that enter the selection cuts.

Data and MC samples

The collision data is read from the datasets:

```
data11_7TeV.{run number}.physics_Egamma.merge.NTUP_SMZEE.{tags}
```

where "run number" identifies the run the dataset comes from (a run is defined as a period of time where data taking conditions in the ATLAS detector are stable, and it has a typical duration of few hours). The total number of runs processed is 235, with numbers going from 179710 to 191933. The runs are grouped together in data periods, organized as shown in table B.1. The "tags" are identifiers that allow to recognize the different versions of the software used in the reconstruction chain up to the final D3PD (see section 2.3.1).

Data period	Run number range	Integrated luminosity (fb^{-1})
D	179710 - 180481	0.182
E	180614 -180776	0.052
F	182013 - 182519	0.156
G	182726 - 183462	0.566
H	183544 - 184169	0.283
I	185353 - 186493	0.406
J	186516 - 186755	0.237
K	186873 - 187815	0.676
L	188902 - 190343	1.599
M	190503 - 191933	1.160

Table B.1: ATLAS data taking periods in 2011.

The main signal MC sample used is:

```
mc11_7TeV.108303.PowHegZePythia.merge.NTUP_SMWZ.e825_s1372_s1370_r3043_r2993_p1035
```

and the auxiliary signal samples, used in the evaluation of systematic uncertainties, are:

```
mc11_7TeV.106046.PythiaZee_no_filter.merge.NTUP_SMWZ.e815_s1272_s1274_r3043_r2993_p1035
mc11_7TeV.147770.Sherpa_CT10_Zee.merge.NTUP_SMWZ.e1443_s1372_s1370_r3108_r3109_p1035
mc11_7TeV.106087.McAtNloZee_no_filter.merge.NTUP_SMWZ.e1096_s1372_s1370_r3043_r2993_p833
mc11_7TeV.129913.McAtNloZee_M60.merge.NTUP_SMWZ.e1514_s1372_s1370_r3108_r3109_p1035
mc11_7TeV.108303.PowHegZePythia.merge.NTUP_SMWZ.e825_s1662_s1704_r3108_r3109_p1035
```

The background samples are:

```
mc11_7TeV.106043.PythiaWenu_no_filter.merge.NTUP_SMWZ.e815_s1272_s1274_r3043_r2993_p1035
mc11_7TeV.107054.PythiaWtaunu_incl.merge.NTUP_SMWZ.e825_s1349_s1300_r3043_r2993_p1035
mc11_7TeV.105200.T1_McAtNlo_Jimmy.merge.NTUP_SMWZ.e835_s1272_s1274_r3043_r2993_p1035
mc11_7TeV.106052.PythiaZtautau.merge.NTUP_SMWZ.e825_s1349_s1300_r3043_r2993_p1035
mc11_7TeV.105985.WW_Herwig.merge.NTUP_SMWZ.e825_s1310_s1300_r3043_r2993_p1035
mc11_7TeV.105986.ZZ_Herwig.merge.NTUP_SMWZ.e825_s1310_s1300_r3043_r2993_p1035
mc11_7TeV.105987.WZ_Herwig.merge.NTUP_SMWZ.e825_s1310_s1300_r3043_r2993_p1035
```

Details of the event selection

The data quality requirements are encoded in the good run list (GRL):

```
data11_7TeV.periodAllYear_DetStatus-v36-pro10_CoolRunQuery-00-04-08_WZjets_allchannels_DtoM.xml
```

The trigger cut is done using the variables `EF_2e12_medium` for data periods D to J, `EF_2e12T_medium` for period K and `EF_2e12Tvh_medium` for periods L to M. As explained in section 5.1.2 these variables allow to select events where the EF (see section 2.2.6) has identified two electrons with p_T above the threshold of 12 GeV, and passing medium identification criteria. However, the LVL1 criteria used by these triggers differ. The LVL1 requirements are summarized in table B.2.

Trigger name	LVL1 seed
EF_2e12_medium	L1_2EM7
EF_2e12T_medium	L1_2EM10
EF_2e12Tvh_medium	L1_2EM10VH

Table B.2: Summary of LVL1 requirements used in the trigger selection.

The `L1_2EM7` and `L1_2EM10` LVL1 seeds require two signals in the ECAL with $E_T > 7$ GeV and $E_T > 10$ GeV, respectively. `L1_2EM10VH` requires two electromagnetic signals in the ECAL, and additionally isolation requirements in the hadronic towers, and a correction for dead material. For more details see [89][90].

The LAr error cleaning is done requiring the variable "larError" to be < 2. The areas with local hardware problems are removed using the variable "el_OQ", and the selection of objects passing the electron reconstruction algorithm in the central region is done using the variable "author", which is required to be either 1 or 3.

Appendix C

Appendix: Control plots POWHEG vs PYTHIA

In this appendix we show plots of pseudorapidity distributions of electrons at reconstruction level, comparing data with the expected distributions obtained from signal MC and the background estimation. We compare the performances of the main signal sample (PowhegPythia) and the auxiliary Pythia sample (see table 5.1). The distributions shown are taken for events in two different kinematic regions defined according to the values of the reconstructed p_{T}^Z. Figure C.1 shows distributions in the region defined by 12 GeV $\leq p_{\mathrm{T}}^Z < 30$ GeV and $1.0 \leq |y^Z| < 2.0$. Figure C.2 shows distributions in the region defined by 30 GeV $\leq p_{\mathrm{T}}^Z < 800$ GeV and $1.0 \leq |y^Z| < 2.0$. Both figures show the improvement obtained in the modeling of angular distributions when moving from Pythia to PowhegPythia, the level of agreement improving from 1 % to 0.5 % in some cases, and from 2 % to 1 % in other cases.
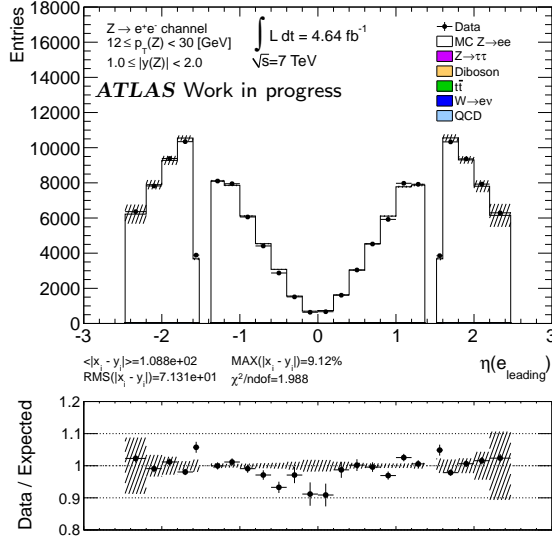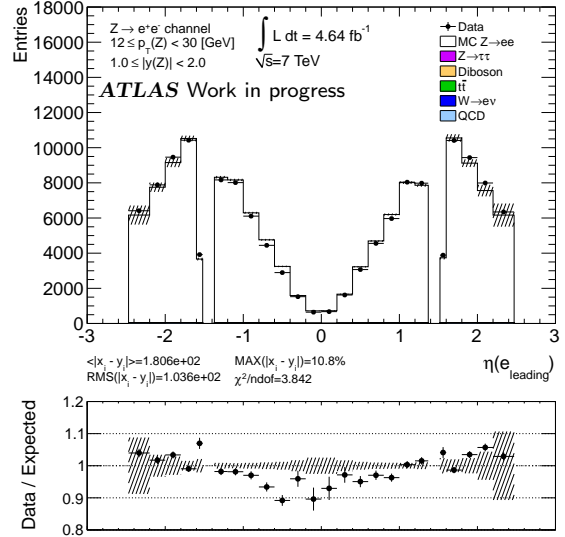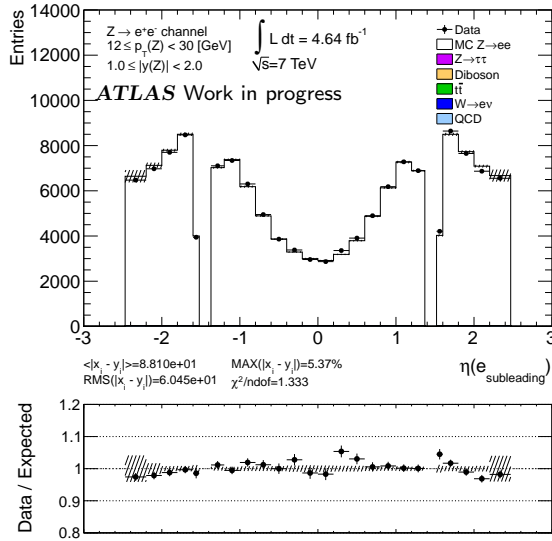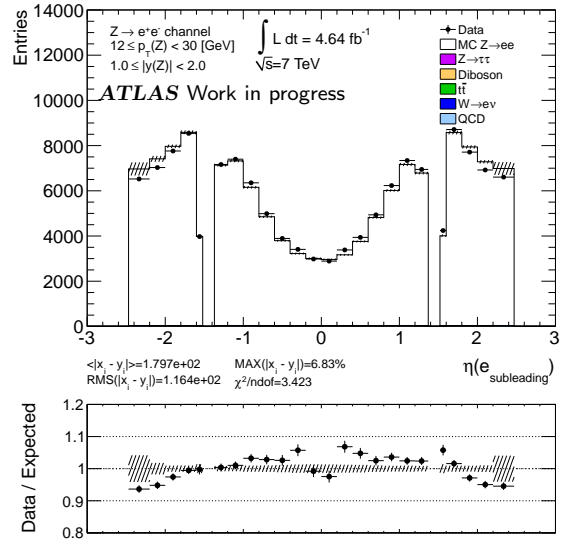
Figure C.1: Pseudorapidity distributions of electrons selected in $Z \to e^+e^-$ events, in the kinematic region defined by 12 GeV $\leq p_T^Z <$ 30 GeV and $1.0 \leq |y^Z| < 2.0$. (a) leading electron using POWHEGPYTHIA sample, (b) leading electron using PYTHIA sample, (c) subleading electron using POWHEGPYTHIA sample, (d) subleading electron using PYTHIA sample.
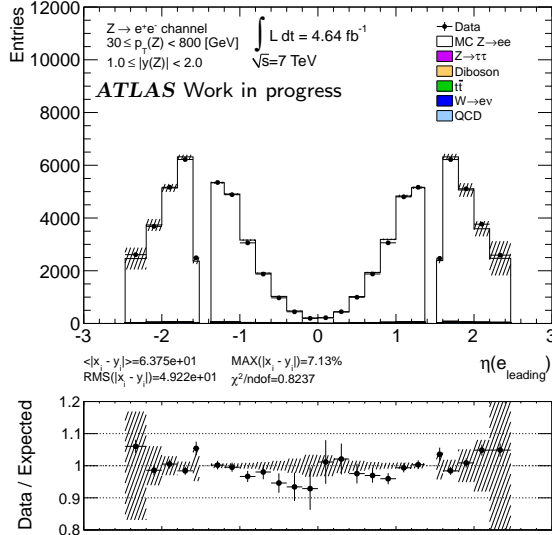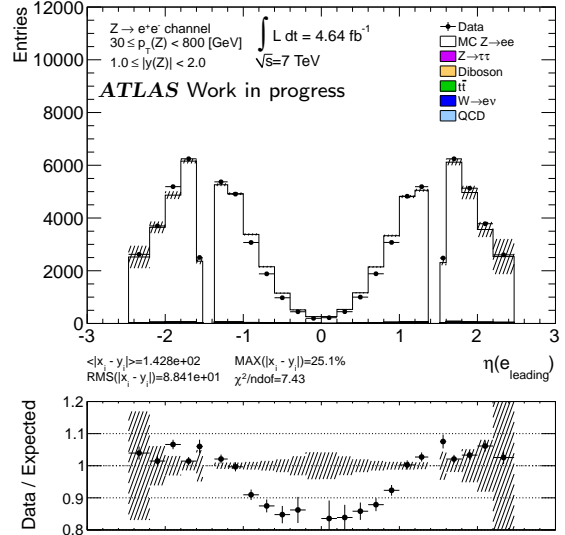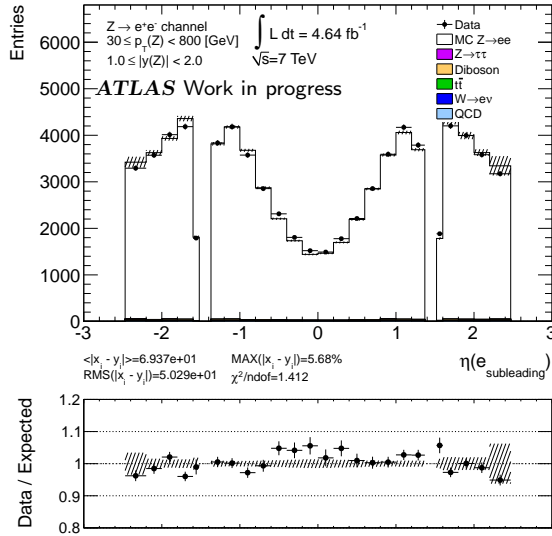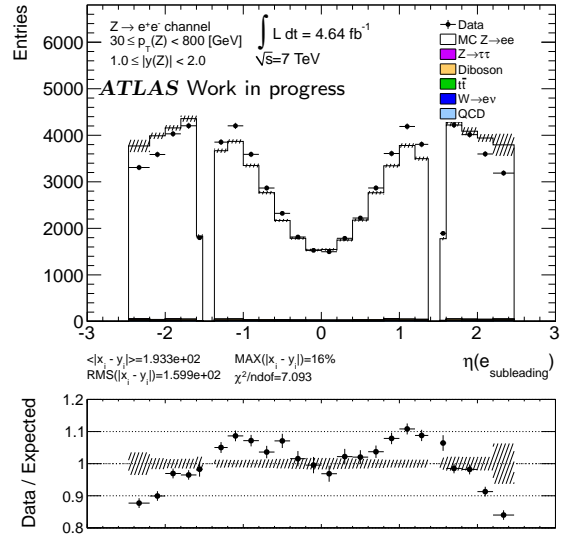
Figure C.2: Pseudorapidity distributions of electrons selected in $Z \to e^+e^-$ events, in the kinematic region defined by 30 GeV $\leq p_T^Z <$ 800 GeV and 1.0 $\leq |y^Z| <$ 2.0. (a) leading electron using POWHEGPYTHIA sample, (b) leading electron using PYTHIA sample, (c) subleading electron using POWHEGPYTHIA sample, (d) subleading electron using PYTHIA sample.

Appendix D

Appendix: Detailed results of the BCID validation study

In this appendix we give detailed results for the BCID validation study (presented in chapter 4). We show the overlap of the transverse energy ranges for the two BCID algorithms $(E_T^{FIR}(MAX) - E_T^{THR}(MIN))$, and the maximum energy of the threshold algorithm ($E^{THR}(MAX)$), for each run analyzed an for each trigger tower. These results are shown in figures D.1, D.2, D.3 and D.4.

(a) Run 178044

(b) Run 178044

(c) Run 179710

(d) Run 179710
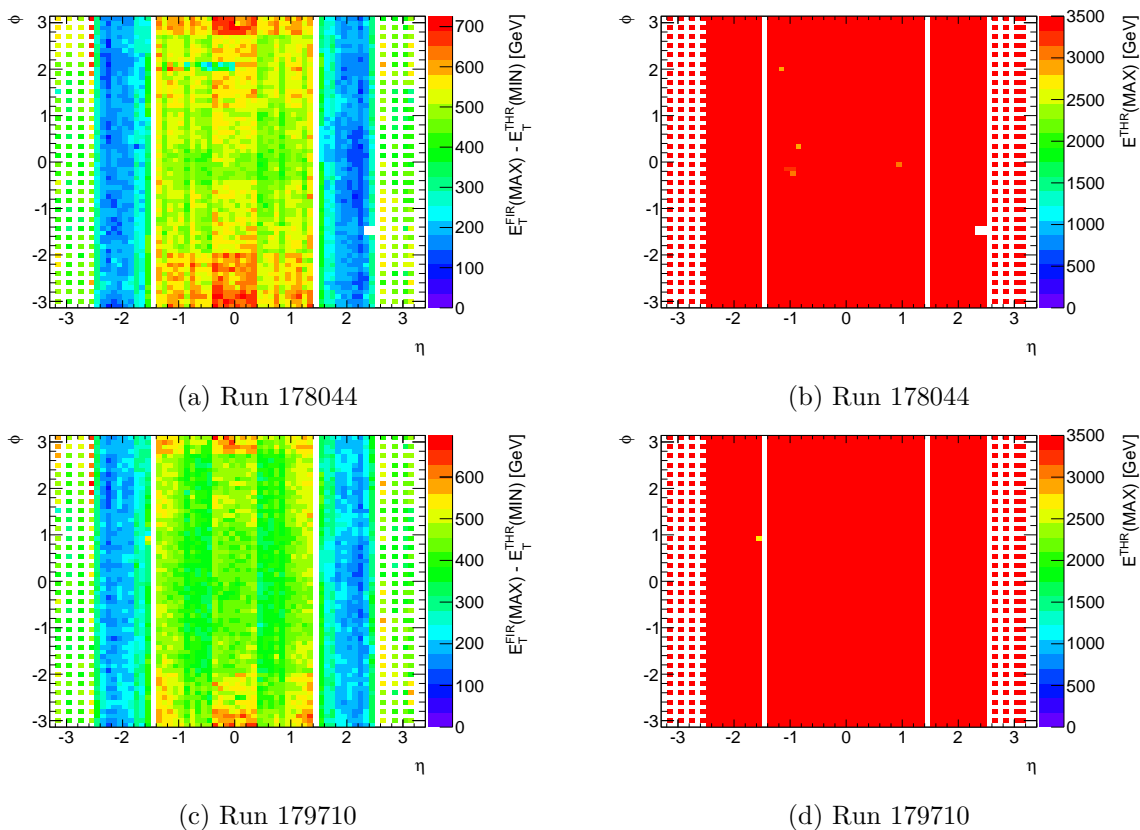
Figure D.1: Detailed results of the BCID validation study. Left column: overlap of the two algorithms, right column: maximum energy of the threshold algorithm.

(a) Runs 180481-180636-180710

(b) Runs 180481-180636-180710

(c) Runs 183081

(d) Runs 183081

(e) Run 185649

(f) Run 185649

(g) Run 186217

(h) Run 186217
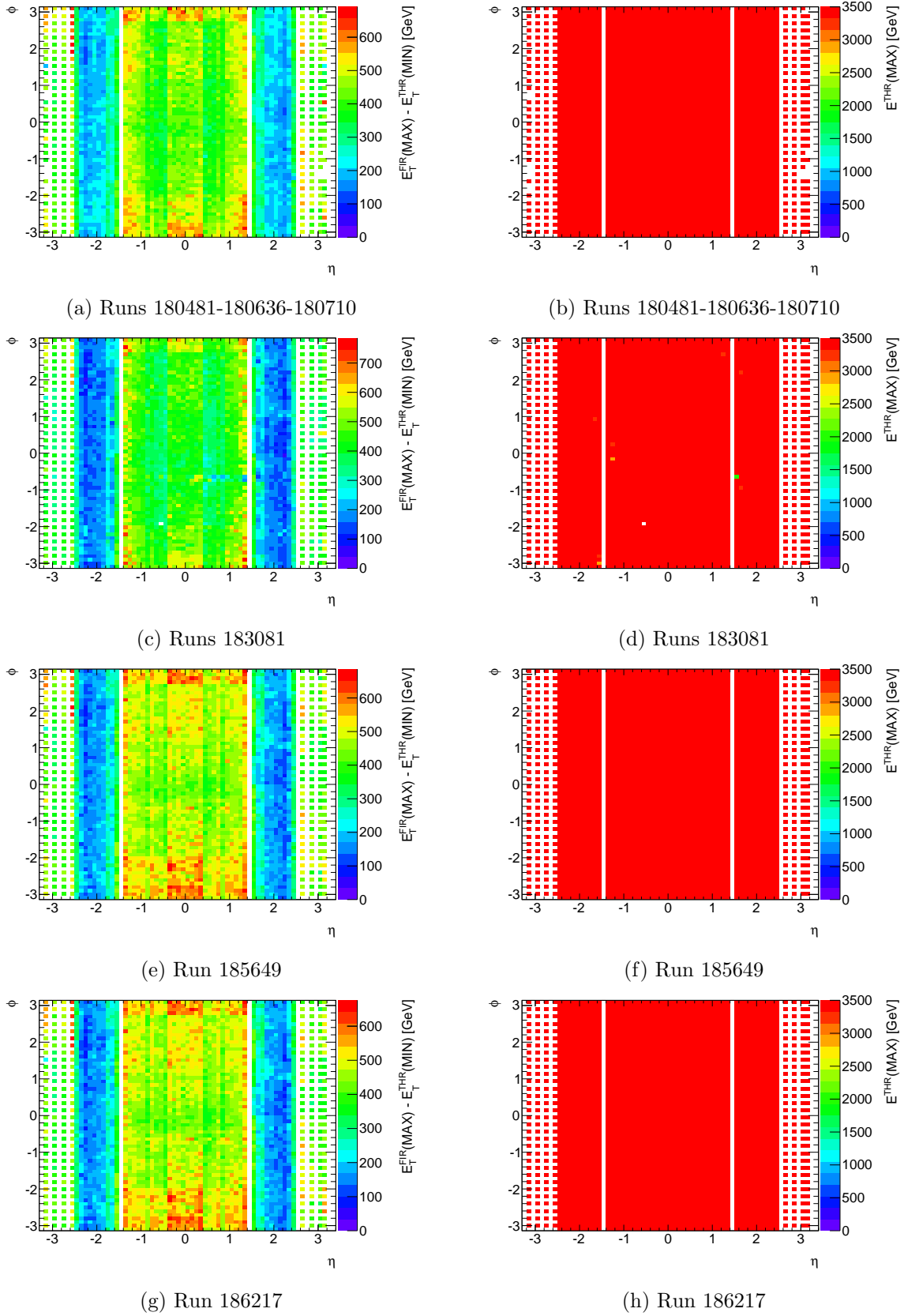
Figure D.2: Detailed results of the BCID validation study. Left column: overlap of the two algorithms, right column: maximum energy of the threshold algorithm.
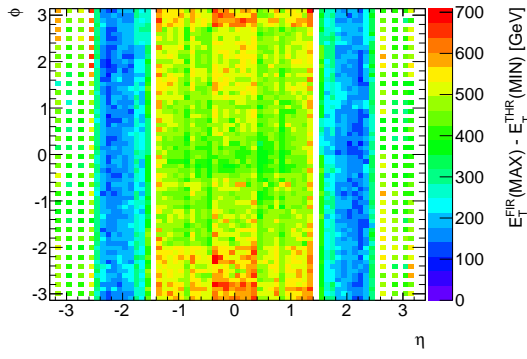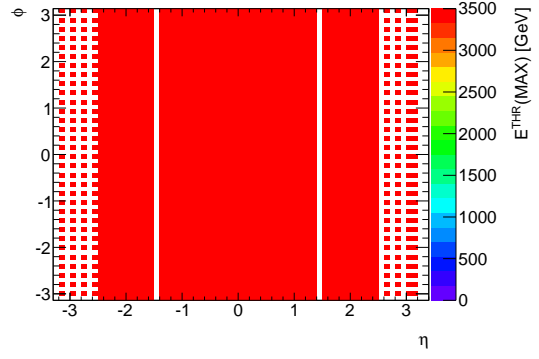
(a) Run 186533   (b) Run 186533
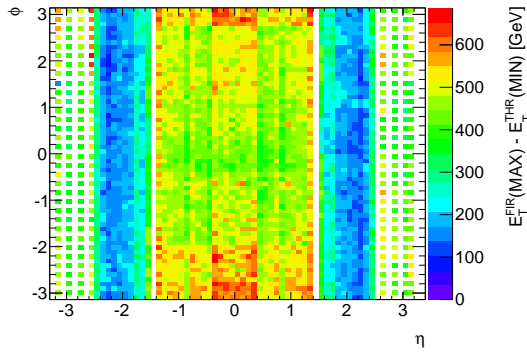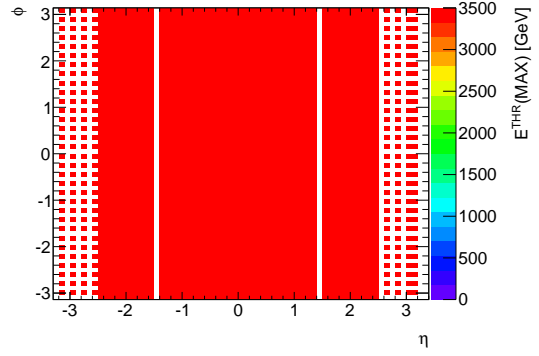
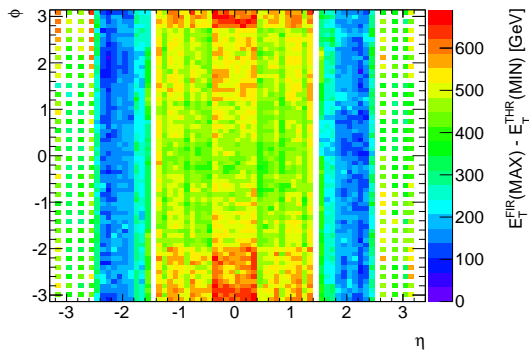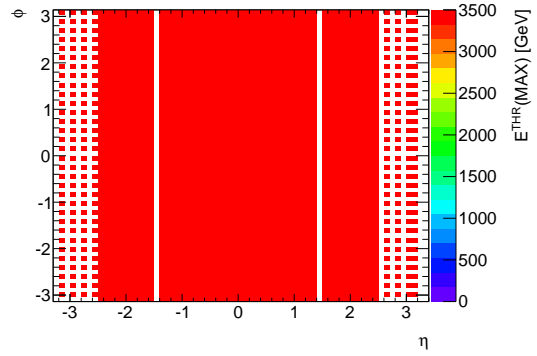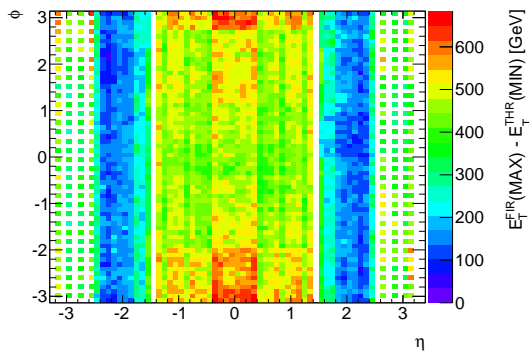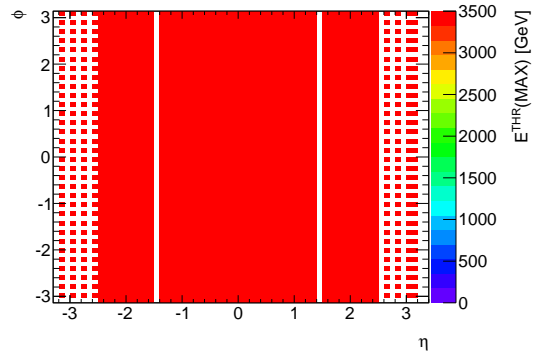(c) Run 187014   (d) Run 187014
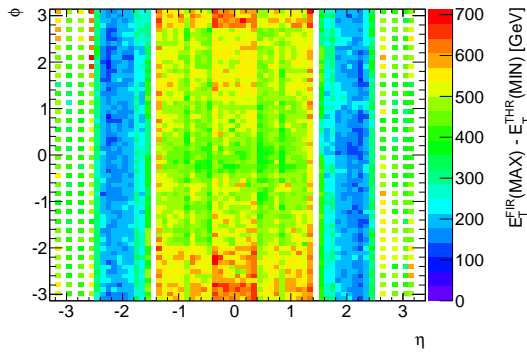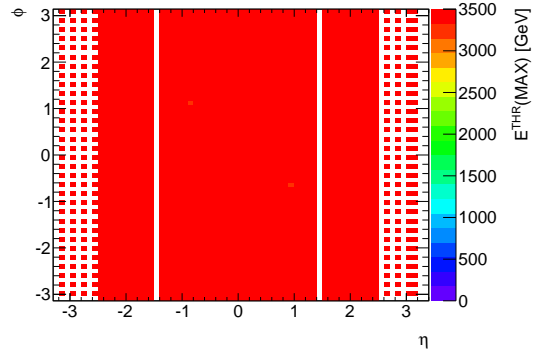
(e) Run 187763   (f) Run 187763
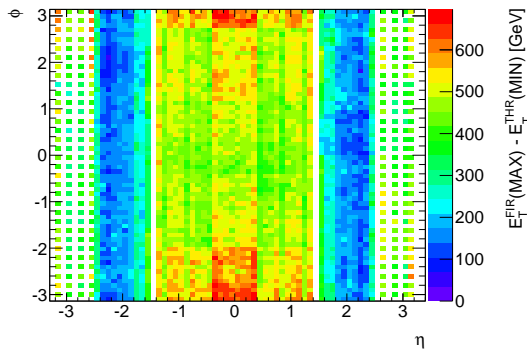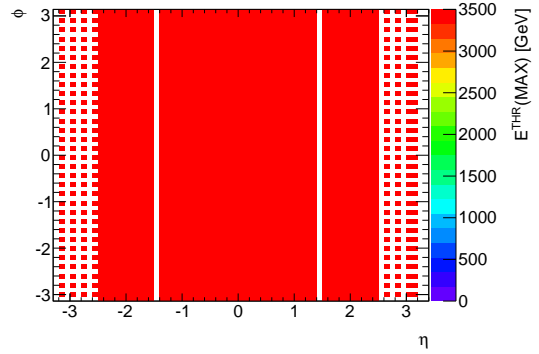
(g) Run 189483   (h) Run 189483

Figure D.3: Detailed results of the BCID validation study. Left column: overlap of the two algorithms, right column: maximum energy of the threshold algorithm.

(a) Run 190300

(b) Run 190300

(c) Run 191517

(d) Run 191517

Figure D.4: Detailed results of the BCID validation study. Left column: overlap of the two algorithms, right column: maximum energy of the threshold algorithm.

Bibliography

[1] D0 Collaboration, V. Abazov et al., *Measurement of the shape of the boson transverse momentum distribution in $p\bar{p} \to Z/\gamma^* \to e^+e^- + X$ events produced at $\sqrt{s}$=1.96-TeV*, Phys.Rev.Lett. **100** (2008) 102002, `arXiv:0712.0803 [hep-ex]`.

[2] ATLAS Collaboration, G. Aad et al., *Measurement of the transverse momentum distribution of Z/gamma* bosons in proton-proton collisions at sqrt(s)=7 TeV with the ATLAS detector*, Phys.Lett. **B705** (2011) 415–434, `arXiv:1107.2381 [hep-ex]`.

[3] CMS Collaboration, S. Chatrchyan et al., *Measurement of the Rapidity and Transverse Momentum Distributions of Z Bosons in pp Collisions at sqrt(s)=7 TeV*, Phys.Rev. **D85** (2012) 032002, `arXiv:1110.4973 [hep-ex]`.

[4] J. L. Hewett, *The Standard model and why we believe it*, `arXiv:hep-ph/9810316`.

[5] J. Griffiths, *An introduction to the elementary particles*. John Wiley & Sons, New York (USA), 1999.

[6] Planck Collaboration, P. Ade et al., *Planck 2013 results. I. Overview of products and scientific results*, `arXiv:1303.5062 [astro-ph.CO]`.

[7] ATLAS Collaboration, G. Aad et al., *Observation of a new particle in the search for the Standard Model Higgs boson with the ATLAS detector at the LHC*, Phys.Lett. **B716** (2012) 1–29, `arXiv:1207.7214 [hep-ex]`.

[8] Super Proton Synchrotron (SPS) Project, *First Proton Anti-Proton Collisions In The Cern SPS Collider*, Phys.Lett. **B107** (1981) 306–309.

[9] J. Beringer and others (Particle Data Group) Phys. Rev. **D86** (2012) 010001.

[10] T.-P. Cheng and L. Ling-Fong, *Gauge Theory of Elementary Particle Physics*. Clarendon Press, Oxford, 1982.

[11] J. M. Campbell, J. W. Huston, and W. J. Stirling, *Hard Interactions of Quarks and Gluons: a Primer for LHC Physics*, `arXiv:hep-ph/0611148`.

[12] A. Buckley et al., *General-purpose event generators for LHC physics*, `arXiv:1101.2599`.

[13] A. D. Martin et al., *Parton distributions for the LHC*, `arXiv:0901.0002 [hep-ph]`.

[14] G. Bozzi, S. Catani, G. Ferrera, D. de Florian, and M. Grazzini, *Production of Drell-Yan lepton pairs in hadron collisions: Transverse-momentum resummation at next-to-next-to-leading logarithmic accuracy*, Phys.Lett. **B696** (2011) 207–213, `arXiv:1007.2351 [hep-ph]`.

[15] T. Sjöstrand and others, *PYTHIA 6.4 physics and manual*, JHEP 05 **026** (2006), `arXiv:hep-ph/0603175`.

[16] M. Brandt and M. Klasen, *Parton densities from LHC vector boson production at small and large transverse momenta*, `arXiv:1305.5677 [hep-ph]`.

[17] S. Drell and T.-M. Yan, *Massive Lepton Pair Production in Hadron-Hadron Collisions at High-Energies*, Phys.Rev.Lett. **25** (1970) 316–320.

[18] P. B. Arnold and M. H. Reno, *The Complete Computation of High p(t) W and Z Production in 2nd Order QCD*, Nucl.Phys. **B319** (1989) 37.

[19] S. Frixione and B. R. Webber, *Matching NLO QCD computations and parton shower simulations*, `arXiv:hep-ph/0204244`.

[20] M. Bahr et al., *Herwig++ Physics and Manual*, `arXiv:0803.0883`.

[21] S. Alioli et al., *NLO vector-boson production matched with shower in POWHEG*, JHEP 07 **060** (2008), `arXiv:0805.4802 [hep-ph]`.

[22] T. Gleisberg, S. Hoeche, F. Krauss, M. Schoenherr, S. Schumann, F. Siegert, and J. Winter, *Event generation with SHERPA 1.1*, `arXiv:0811.4622`.

[23] L. Evans and P. Bryant, *LHC Machine*, JINST **3** (2008) S08001.

[24] D. Perkins, *Introduction to high energy physics*. Addison-Wesley Publishing company, Reading (USA), 1987.

[25] T. S. Pettersson and P. Lefevre, *The Large Hadron Collider: conceptual design*, Tech. Rep. CERN-AC-95-05 LHC, CERN, Geneva, Oct, 1995.

[26] D. A. Edwards and M. J. Syphers, *An Introduction to the Physics of High Energy Accelerators*. John Wiley & Sons, New York (USA), 1993.

[27] *Expected Performance of the ATLAS Experiment*. CERN, Geneva, 2008.

[28] ATLAS Collaboration, G. Aad et al., *The ATLAS Experiment at the CERN Large Hadron Collider*, JINST **3** (2008) S08003.

[29] *ATLAS detector and physics performance: Technical Design Report, 1.* Technical Design Report ATLAS. CERN, Geneva, 1999.

[30] V. A. Schegelsky et al., *A note on rapidity distributions at the LHC*, `arXiv:arXiv:1010.2051`.

[31] D. Green, *High pT Physics at Hadron Colliders*. Cambridge University Press, Cambridge (UK), 2005.

[32] C. Grupen and B. Schwartz, *Particle detectors*. Cambridge University Press, Cambridge (UK), 2008.

[33] S. Haywood, L. Rossi, R. Nickerson, and A. Romaniouk, *ATLAS inner detector: Technical Design Report, 2.* Technical Design Report ATLAS. CERN, Geneva, 1997.

[34] T. Lenz, *Vertex Fitting in the ATLAS Inner Detector*, tech. rep., University of Wuppertal, Germany, June, 2006.

[35] "Root - an object oriented data analysis framework,." `http://root.cern.ch/`.

[36] W. Richard, *Calorimetry: Energy measurement in Particle Physics*. Oxford University Press, Oxford (USA), 2000.

[37] *ATLAS liquid-argon calorimeter: Technical Design Report*. Technical Design Report ATLAS. CERN, Geneva, 1996.

[38] ATLAS Collaboration, A. Bazan et al., *The ATLAS Liquid Argon Calorimeter Read-Out System*, IEEE TRANSACTIONS ON NUCLEAR SCIENCE **53** (2006).

[39] W. Lampl et al., *Calorimeter Clustering Algorithms: Description and Performance*, Tech. Rep. ATL-LARG-PUB-2008-002. ATL-COM-LARG-2008-003, CERN, Geneva, Apr, 2008.

[40] ATLAS Collaboration, M. Aharrouche et al., *Response Uniformity of the ATLAS Liquid Argon Electromagnetic Calorimeter*, `arXiv:0709.1094 [physics.ins-det]`.

[41] ATLAS Collaboration, M. Aharrouche et al., *Energy Linearity and Resolution of the ATLAS Electromagnetic Barrel Calorimeter in an Electron Test-Beam*, `arXiv:0608012v1 [physics.ins-det]`.

[42] ATLAS Collaboration, G. Aad et al., *Electron performance measurements with the ATLAS detector using the 2010 LHC proton-proton collision data*, `arXiv:1110.3174 [hep-ex]`.

[43] M. Aharrouche et al., *Expected electron performance in the ATLAS experiment*, Tech. Rep. ATL-PHYS-INT-2010-126, CERN, Geneva, Nov, 2010.

[44] ATLAS Collaboration, N. Besson, M. Boonekamp, E. Klinkby, S. Mehlhase, and T. Petersen, *Re-evaluation of the LHC potential for the measurement of Mw*, Eur.Phys.J. **C57** (2008) 627–651, `arXiv:0805.2093 [hep-ex]`.

[45] P. Borgeaud, X. De la Broise, E. Ferrer-Ribas, A. Le Coguie, B. Mansoulie, and J. Pascual, *The LArg Tower Builder Board: calculation, simulation, measurements.*, Tech. Rep. ATL-LARG-2002-001, CERN, Geneva, May, 2002.

[46] *ATLAS level-1 trigger: Technical Design Report*. Technical Design Report ATLAS. CERN, Geneva, 1998.

[47] N. Morange, J. T. Childers, S. Hillier, and B. Mansoulie, *Study and validation of the BCID of the L1Calo at very high transverse energies*, Tech. Rep. ATL-DAQ-INT-2011-001, CERN, Geneva, May, 2011.

[48] Bazan, A. et al., *ATLAS liquid argon calorimeter back end electronics*, JINST 2 **P06002** (2007).

[49] "ATLAS L1Calo Commisioning Changes." `https://twiki.cern.ch/twiki/bin/viewauth/Atlas/L1CaloCommissioningChanges`.

[50] "ATLAS muon combined performance working group." `https://twiki.cern.ch/twiki/bin/viewauth/AtlasProtected/MuonPerformance`.

[51] GEANT4 Collaboration, S. Agostinelli et al., *GEANT4: A simulation toolkit*, Nucl. Instrum. Meth. **A506** (2003) 250–303.

[52] J. Butterworth et al., *Single Boson and Diboson Production Cross Sections in pp Collisions at sqrts=7 TeV*, Tech. Rep. ATL-COM-PHYS-2010-695, CERN, Geneva, Aug, 2010.

[53] M. Aharrouche et al., *Total and differential Wlnu and Zll cross-sections measurements in proton-proton collisions at sqrts =7 TeV with the ATLAS Detector*, Tech. Rep. ATL-COM-PHYS-2011-751, CERN, Geneva, Jun, 2011.

[54] H. L. Lai et al., *New parton distributions for collider physics*, Phys.Rev. **D82** (2010) 074024, `arXiv:1007.2241 [hep-ph]`.

[55] M. Warsinsky et al., *ATLAS Minimum Bias Tune 1: Documentation to support tuning CONF note*, Tech. Rep. ATL-COM-PHYS-2010-267, CERN, Geneva, May, 2010.

[56] P. Golonka et al., *PHOTOS Monte Carlo: A Precision tool for QED corrections in Z and W decays*, Eur. Phys. J. **C45** (2006) 97–107, `arXiv:hep-ph/0506026`.

[57] "ATLAS W/Z and Electroweak Common Topics (2011)." `https://twiki.cern.ch/twiki/bin/viewauth/AtlasProtected/WZElectroweakCommonTopics2011`.

[58] "ATLAS MC 2011 setup." `https://twiki.cern.ch/twiki/bin/viewauth/Atlas/MC11b`.

[59] "ATLAS Extended Pile-up Reweighting." `https://twiki.cern.ch/twiki/bin/viewauth/AtlasProtected/ExtendedPileupReweighting`.

[60] A. Buckley et al., *ATLAS Monte Carlo Tunes for MC09*, Tech. Rep. ATL-PHYS-INT-2010-005, CERN, Geneva, Jan, 2010.

[61] *ATLAS tunes of PYTHIA 6 and Pythia 8 for MC11*, Tech. Rep. ATL-PHYS-PUB-2011-009, CERN, Geneva, Jul, 2011.

[62] *Further ATLAS tunes of PYTHIA6 and Pythia 8*, Tech. Rep. ATL-PHYS-PUB-2011-014, CERN, Geneva, Nov, 2011.

[63] *Studies of vector boson transverse momentum simulation in Monte Carlo event generators*, Tech. Rep. ATL-PHYS-PUB-2011-015, CERN, Geneva, Nov, 2011.

[64] "ATLAS Energy Scale Resolution Recommendations (for electrons, photons)." `https://twiki.cern.ch/twiki/bin/viewauth/AtlasProtected/EnergyScaleResolutionRecommendations`.

[65] "ATLAS Efficiency Measurements (for electrons, photons)." `https://twiki.cern.ch/twiki/bin/viewauth/AtlasProtected/EfficiencyMeasurements`.

[66] "ATLAS Egamma Isolation." `https://twiki.cern.ch/twiki/bin/viewauth/AtlasProtected/EgammaIsolation`.

[67] G. Cowan, *Statistical Data Analysis.* Clarendon Press Oxford, Oxford, 1998.

[68] G. D'Agostini, *A Multidimensional unfolding method based on Bayes' theorem*, Nucl.Instrum.Meth. **A362** (1995) 487–498.

[69] G. D'Agostini, *Improved iterative Bayesian unfolding*, Oct., 2010.

[70] T. Adye, *Unfolding algorithms and tests using RooUnfold*, `arXiv:1105.1160 [physics.data-an]`.

[71] T. Adye, "Roounfold: Root unfolding framework." `http://hepunx.rl.ac.uk/~adye/software/unfold/RooUnfold.html`.

[72] ATLAS Collaboration, G. Aad et al., *Luminosity Determination in pp Collisions at sqrt(s)=7 TeV Using the ATLAS Detector at the LHC*, Eur.Phys.J.**C71** 1630, `arXiv:1101.2185 [hep-ex]`.

[73] "ATLAS LAr Cleaning and Object Quality." `https://twiki.cern.ch/twiki/bin/viewauth/AtlasProtected/LArCleaningAndObjectQuality`.

[74] "LHAPDF: the Les Houches Accord PDF Interface." `https://lhapdf.hepforge.org/`.

[75] K. Müller, *Measurement of the transverse momentum distribution of Z bosons in proton-proton collisions at* $\sqrt{s} = 7$ *TeV using the ATLAS detector*. PhD thesis, Universität Bonn, 2013.

[76] A. Valassi, *Combining correlated measurements of several different physical quantities*, Nuclear Instruments and Methods in Physics Research Section A: Accelerators, Spectrometers, Detectors and Associated Equipment **500** no. 13, (2003) 391 – 405. `http://www.sciencedirect.com/science/article/pii/S0168900203003292`.

[77] "Minuit minimization program." `http://seal.web.cern.ch/seal/work-packages/mathlibs/minuit/`.

[78] F. Landry, R. Brock, P. M. Nadolsky, and C. Yuan, *Tevatron Run-1 Z boson data and Collins-Soper-Sterman resummation formalism*, Phys.Rev. **D67** (2003) 073016, `arXiv:hep-ph/0212159 [hep-ph]`.

[79] K. Melnikov and F. Petriello, *Electroweak gauge boson production at hadron colliders through O(alpha(s)**2)*, Phys.Rev. **D74** (2006) 114017, `arXiv:hep-ph/0609070 [hep-ph]`.

[80] C. P. Y. C. Balazs, *Soft gluon effects on lepton pairs at hadron colliders*, Phys. Rev **D56** (1997) 5558–5583.

[81] S. Berge, P. M. Nadolsky, F. Olness, and C.-P. Yuan, *Transverse momentum resummation at small x for the Tevatron and CERN LHC*, Phys.Rev. **D72** (2005) 033015, `arXiv:hep-ph/0410375 [hep-ph]`.

[82] N. Besson et al., *Measurement of the transverse momentum distribution of Z/* bosons in proton-proton collisions at roots = 7 TeV with the ATLAS detector: Update with 4.7 fb-1 of the previous measurement at this energy.*, Tech. Rep. ATL-COM-PHYS-2013-117, CERN, Geneva, Feb, 2013.

[83] D0 Collaboration, V. M. Abazov et al., *Precise study of the Z/γ^* boson transverse momentum distribution in $p\bar{p}$ collisions using a novel technique*, Phys.Rev.Lett. **106** (2011) 122001, `arXiv:1010.0262 [hep-ex]`.

[84] R. Gavin et al., *FEWZ 2.0: A code for hadronic Z production at next-to-next-to-leading order*, Comput.Phys.Commun **182** (2011) 23882403, `arXiv:1011.3540 [hep-ph]`.

[85] A. Banfi, M. Dasgupta, S. Marzani, and L. Tomlinson, *Predictions for Drell-Yan ϕ^* and Q_T observables at the LHC*, Phys.Lett. **B715** (2012) 152–156, `arXiv:1205.4760 [hep-ph]`.

[86] T. Sjöstrand, S. Mrenna, and P. Z. Skands, *A Brief Introduction to PYTHIA 8.1*, Comput.Phys.Commun. **178** (2008) 852–867, `arXiv:0710.3820 [hep-ph]`.

[87] A. Banfi, S. Redford, M. Vesterinen, P. Waller, and T. Wyatt, *Optimisation of variables for studying dilepton transverse momentum distributions at hadron colliders*, Eur.Phys.J. **C71** (2011) 1600, `arXiv:1009.1580 [hep-ex]`.

[88] ATLAS Collaboration, G. Aad et al., *Measurement of angular correlations in Drell-Yan lepton pairs to probe Z/gamma* boson transverse momentum at sqrt(s)=7 TeV with the ATLAS detector*, `arXiv:1211.6899 [hep-ex]`.

[89] "ATLAS Egamma Trigger Signature Group."
https://twiki.cern.ch/twiki/bin/viewauth/Atlas/TrigEgamma.

[90] "ATLAS Egamma 2012 Analyses."
https://twiki.cern.ch/twiki/bin/viewauth/AtlasProtected/Egamma2012Analyses.

Acknowledgements